Biomechanical assessment of distal tibia fracture reduction devices for supramalleolar corrective osteotomy fixation

Julia Greenfield

N°d'ordre NNT : 2018LYSE1215

THESE de DOCTORAT DE L'UNIVERSITE DE LYON
opérée au sein de
l'Université Claude Bernard Lyon 1

Ecole Doctorale N° 162
Mécanique, Energétique, Génie Civile, et Acoustique

Spécialité de doctorat : Biomécanique
Discipline : Orthopédie

Soutenue publiquement le 04/11/2019, par :

Julia Greenfield

Biomechanical assessment of distal tibia fracture reduction devices for supramalleolar corrective osteotomy fixation

Devant le jury composé de :

Lustig, Sebastien	Professeur des Universités - Praticien Hospitalier, LBMC UMR T_9406, UCBL-IFSTTAR, Lyon, France	Examinateur
Kuhn, Sebastian	Professeur associé - Praticien Hospitalier, UMC Mainz, Allemagne	Examinateur
Terrier, Alexandre	Professeur des Universités, LBO EPFL – Lausanne, Suisse	Rapporteur
Pithioux, Martine	Professeure des Universités, UMR 7287 CNRS & Aix-Marseille Université, Marseille, France	Rapporteuse
Bruyère, Karine	Directrice de recherche, LBMC UMR T_9406, UCBL-IFSTTAR, Lyon, France	Directrice de thèse
Lafon, Yoann	Maître de Conférences, LBMC UMR T_9406, UCBL-IFSTTAR, Lyon, France	Co-directeur de thèse
Rommens, Pol Maria	Professeur des Universités - Praticien Hospitalier, UMC Mainz, Allemagne	Invité
Appelmann, Philipp	Praticien Hospitalier, UMC Mainz, Allemagne	Invité

Biomechanical assessment of distal tibia fracture reduction devices for supramalleolar corrective osteotomy fixation

Thèse préparée au Laboratoire de Biomécanique et Mécanique des Chocs (LBMC)
LBMC UMR_T9406 IFSTTAR – Université Claude Bernard Lyon 1
25 avenue François Mitterrand, Case 24, 69675 Bron Cedex, France

Abstract (EN)

Introduction: Supra-malleolar corrective osteotomies (SMOT) are a common surgical procedure for the prevention of early onset of ankle arthritis. The Distal Tibia Nail (DTN; Mizuho®), was previously developed for the reduction of distal tibia fractures. The aim of this project was to identify error sources in biomechanical testing, and to test the feasibility of the DTN for SMOT performed using the medial wedge opening (MWO) technique. **Methods**: Sixteen Sawbones® were each implanted with either a DTN or medial distal tibia plate (MDTP; Synthes®), and a MWO simulated. Four testing phases were defined: Phase-0, testing of Sawbones® without implant/osteotomy; Phase-1, samples with MWO and implant; Phase-2, Phase-1 samples with lateral cortex fractured; Phase-3, samples with an A3 type fracture. Stiffness construct and interfragmentary movement (IFM) were analysed. CT scans were taken of the samples at Phases 0 and 1. **Results**: Up to 80% difference was noticed between Sawbones® samples in Phase-0; in Phases 1 and 2 significant differences were found between stiffness constructs of the implant groups but this amounted to <2 mm IFM. The DTN was significantly more resistant to compression and torsion when supporting an A3 fractures (Phase-3). Elements such as original Sawbones® stiffness construct, implant position, potting material, loading axis, and sample positioning can have a high influence on measured stiffness and bias the results. **Conclusion:** The DTN is a viable option for the fixation of SMOT performed with a MWO technique. Future studies should pay careful attention to boundary conditions affecting outcomes measures and drawn conclusions.

Keywords: Biomechanics, orthopaedics, Implants, Digital image correlation, Distal tibia,

Résume (FR)

Introduction: Une procédure fréquente pour la prévention de l'arthrose à la cheville est une ostéotomie corrective du tibia distal (SMOT). Le Distal Tibia Nail (DTN ; Mizuho®), a été développé pour la réduction des fractures du tibia distal. L'objectif de ce projet était d'analyser la faisabilité du DTN pour des procédures SMOT effectuées avec une ouverture médiale (MWO). **Méthodes :** Seize Sawbones® ont été instrumentés par un DTN ou une plaque (MDTP, Synthes®), suivi par la simulation d'une MWO. Quatre phases d'expérimentation étaient définies : Phase-0, Sawbones sans implant ni MWO ; Phase-1, échantillons avec un implant et MWO. Phase-2, les échantillons de la Phase-1 avec le cortex latéral fracturé ; Phase-3, simulation d'une fracture de type A3. La raideur et le mouvement inter-fragmentaire (IFM) étaient analysés. Des tomographies des échantillons ont été prises à Phases 0 et 1. **Résultats :** Jusqu'à 80% de différence était présente enter les Sawbones® de Phase-0 ; dans les Phases 1 et 2, des différences importantes se sont montrées entre des implants mais équivalent à <2 mm d'IFM. Le DTN a démontré une résistance très élevée aux charges de compression et de torsion appliquées en comparaison avec le MDTP pour la fixation des fractures A3. Des facteurs expérimentaux tels que la raideur initiale des Sawbones®, l'axe de chargement, et le positionnement de l'échantillon dans la machine d'essai, peuvent tous avoir une influence importante sur la raideur mesurée. **Conclusion :** Le DTN peut être considéré comme option pour la fixation des SMOT effectués avec un MWO. Des études futures doivent faire attention aux conditions limites ayant un effet sur des critères d'évaluation et des conclusions tirées.

Mots clés : Biomécanique, Orthopédie, Implants, Stéréocorrélation, Tibia distal,

Acknowledgements / Remerciements / Danksagungen

I firstly wish to thank my parents – for your unconditional support in all that I do, for letting me run away to chase the French dream (it's in the shape of a croissant), and letting me make all the right mistakes to learn to be a better person. Not forgetting Aunty Frances who has allowed me to decorate my office walls with postcards from all over England – it makes for the most interesting office in the lab and I often receive complements!

My next thank-you goes back to University days in Leeds where I met two people who could be considered as the pioneers of my biomechanical enthusiasm. To Daniella Strauss and Neil Messenger, I wish to thank you for answering every question I ever asked (there were a lot, and this hasn't changed), for never sending me away after asking a stupid question, and for starting the process of moulding me into the student/researcher that I am today. A good part of this thesis is written in your name.

En allemand on utilise deux mots que l'on peut traduire comme « mère de thèse » et « père de thèse » pour définir ses encadrant.e.s de thèse. Karine et Yoann, vous avez été plus que des encadrants, vous avez assumé ce rôle de mes « parents de thèse » et je peux moi-même voir la progression que j'ai faite, toute grâce à vous. J'espère que dans l'avenir je vais continuer à m'appuyer sur les compétences que vous m'avez apportées. J'espère aussi que je serai capable de montrer la patience que vous m'avez montrée, le jour où je me retrouve à votre place – à encadrer des étudiantes débutantes dans leur carrière de recherche. Ç'a été un vrai plaisir de travailler avec vous, je vous remercie pour tout, et je vous regretterai.

Et si Yoann et Karine ont été mes parents de thèse, c'est Léo, mon cher collègue de bureau qui en est mon frère. Merci à toi Léo pour tout le soutien que tu m'as apporté. Tu as su assumer chaque cri de joie et de déception poussée, chaque larme versée, chaque tasse de thé partagé, et chaque pas couru autour du fort de Bron. Nos séances tennis me manqueront en particulier – je te remercie de m'avoir laissée gagner… Plusieurs fois… Je pense que j'aurai du mal à trouver un collègue de bureau pareil. J'espère que l'on restera en contact.

Sur les activités physiques du labo, je me serai rendue folle toute seule s'il n'y avait pas eu l'équipe des coureurs les mardis et les jeudis midis. A -15° on court, à +40° on court. Merci à François (notamment pour chaque mail arrivé à 08h précis le jour-J !), Marie-Christine, Sabine, Patrick, Michelle, Léo (encore), Laura, et Sonia. Heureusement que vous étiez là pour vous défouler avec moi.

Ich darf bestimmt nicht allen Kollegen in Mainz vergessen, und auch mein ganz liebe Familie bei wen ich immer bleiben könnte. Ein besonderes herzlichen Dank an meine Tante Renate und mein Onkel Wolfgang, dass ich immer bei euch eine Unterkunft hatte ob ich nur zwei Wochen blieb, oder zwei Monate. Und jedes Mal, dass ich um 23Uhr nach Hause kam, war das Essen immer fertig, das Bett immer bereit, und freundliches Lächeln immer anwesend. Ohne euch, wäre es nicht möglich gewesen. Vielen, vielen Dank für alles.

Lieber/liebe Sebastian, Philipp, Dorothé, Felix, und Prof. Rommens: seit 2014 arbeiten wir zusammen und ich habe sehr viel von euch gelernt. Ich hoffe, dass alle Projekte und Zusammenarbeite auch so

angenehm für euch war. Am Anfang, hätte ich nur zwei Monate lang Master-Praktikum machen sollten, fünf Jahre später bin ich endlich fertig mit Master und Doktorarbeit! Ein besonderes Dankeschön an Sebastian, danke für jedes Mittagsessen, und wenn du diese Seite liest - dann habe *ich* dir hoffentlich endlich mal zum Essen eingeladen.

Thank you to all of my colleagues for making the long hours more bearable, in particular the fellow PhD students at LBMC, just to name a few – but it's true for everyone: Yuliia, Tomas, Mingming, Mehdi, Kevin, Michelle, Mohammed, Cyrille, Léo, and Ilias.

Sans oublier de remercier chaleureusement Leila, Stéphane, Jean-Luc, et Richard. Vous n'avez jamais répondu « non » à toutes mes demandes de manips à faire et pièces à fabriquer. J'ai pris beaucoup de plaisir à travailler avec vous (ça change du bureau !) et un mot spécial à Stéphane : Je pense que Karine ne sera jamais contente de nos manips, mais au moins on a bien rigolé !

Un grand merci à mon (premier) stagiaire, Benjamin, c'est grâce à toi que j'ai pu exploiter toutes les données décrites dans chapitre 5, si je pouvais dédier ce chapitre à quelqu'un, ce serait à toi ! Je te souhaite bon courage pour la suite de tes études à l'INSA même si je suis confiante que tu vas très bien t'en sortir ! Si jamais la segmentation te manque… Call me !

Etre loin de sa famille et ses proches n'est pas toujours facile, mais j'ai eu de la chance à être adoptée par le #LFCfamily. A tous les membres du Lyon Floorball Club, surtout aux filles, merci pour tout. Mon séjour à Lyon n'aurait pas été pareil sans vous et heureusement que vous avez été là pour moi pendant tous les trois ans. Un jour Pirate, toujours Pirate ! J'ai été fière de porter les couleurs du club.

PIRATES DU RHÔNE… A L'ABORDAGE !

Table of Contents

Table 1: Table of commonly used abbreviations.

Abbreviation	Full name
AO foundation	Arbeitsgemeinschaft für Osteosynthesenfragen
C	Compression
CT scan	Computer Tomography scan
DIC	Digital Image Correlation
DTN	Distal Tibia Nail
ETN	Expert Tibia Nail
IFM	InterFragmentary Movement
IMN	IntraMedullary Nail
K	Stiffness
LCWO	Lateral Closing Wedge Osteotomy
LDTA	Lateral Distal Tibia Angle
Lin. Elas. Iso	Linear Elastic Isotropic
MDTP	Medial Distal Tibial Plate
MM	Medial Malleolus
MOWO	Medial Opening Wedge Osteotomy
OA	Osteoarthritis
OO	Oblique Osteotomy
ROM	Range of Motion
SD	Standard Deviation
SMOT	Supramalleolar Osteotomy
T	Torsion
TAS	Tibial Anterior Surface angle
TLS	Tibial Lateral Surface angle
TT	Talar Tilt

Table of Illustrations

Table of tables

Chapter 1: General introduction and literature review

1. Basic principles of anatomy

1.1. Anatomical reference system

The anatomical reference system (Figure 1) is based upon the outline of a man with feet shoulder-width apart and palms facing forward. From this position, reference planes, axes and a range of movements can be defined. An imaginary line running down the central axis of the body is visualised to define the fundamental movements of human motion, known as the midline.

1.1.1. Axes and Planes

There are three principal planes of human movement (Figure 1) and each movement involves displacing a body part in one or more planes. The planes include: the frontal plane which cuts the body medio-laterally following the x axis; the sagittal plane which cuts the body antero-posteriorly, following the z axis; and the transverse plane which cuts the body proximo-distally, following the y axis.

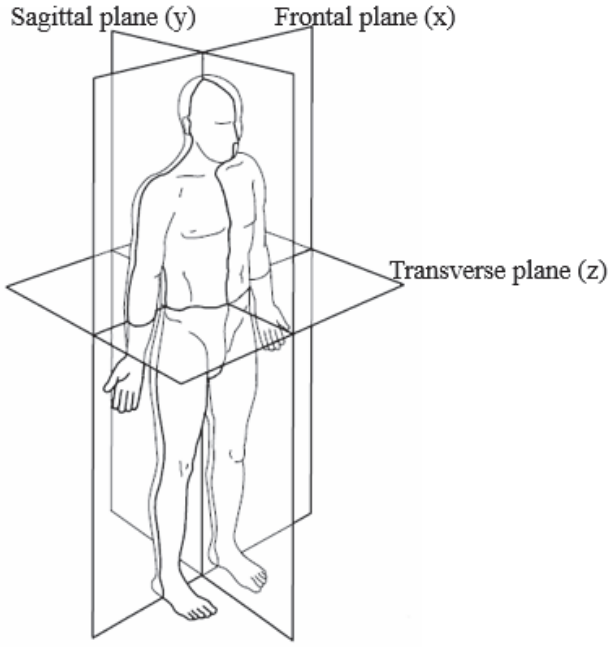

2.

Figure 1: The human anatomical reference position with the three planes each allowing movement in two directions (adapted from Human Walking, by V. T. Inman et al., 1981, Baltimore: Williams & Wilkins).

1.2. Anatomy of the lower leg

The tibia belongs to the long bone family and is the primary bone of the lower leg with proximal and distal articulating surfaces at the knee and ankle, respectively (Figure 2). Looking at the tibia along

its axis from proximal to distal (from the diaphysis through to the metaphysis), the first portion of the bone section takes on a triangular form before adopting a more circular shape. The anteromedial surface becomes concave during this transition (Trafton, 2009). The medullar cavity of the tibia has the form of an hourglass, indicating a wide medullar cavity at the epiphyses and a narrower cavity at the diaphysis.

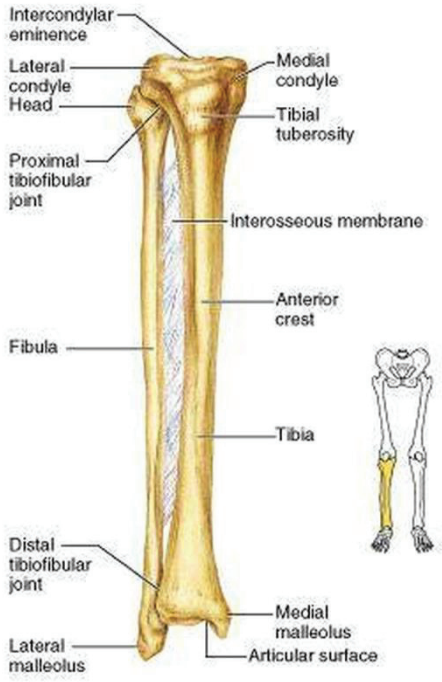

Figure 2: Basic anatomy of the lower leg.
Image adapted from http://sansu.rabionetassociats.com/

1.1.2 Tibial proximal epiphysis

This section of the tibia is anatomically characterised by the tibial plateau which contains the medial and lateral condyles. These bony landmarks are separated by the intercondylar eminence to which the cruciate ligaments and menisci of the knee are attached. The tibial tuberosity is found on the anterior surface below the tibial plateau, it is the attachment point for the patellar ligament.

1.1.3 Tibial diaphysis

The mid-section of the tibia contains the muscular insertion points for the tibialis anterior, soleus, and a number of other muscles allowing movement of the foot. The posterior surface of the diaphysis is marked by the soleal line, and the lateral surface serves as an attachment area for the interosseous membrane which connects the tibia and fibula.

1.1.4 Tibial distal epiphysis

The distal portion of the tibia is split in to two parts according to its anatomy: the medial malleolus and the pilon. These latter two bony landmarks, along with the lateral malleolus form three edges of a square which accommodates the talus bone, creating the ankle joint.

1.1.5 Fibula

The fibula is the secondary bone in the leg. It is smaller in size and plays a less important role in the structure of the leg. Its main job is to provide origin and insertion points for surrounding muscles as well as the interosseous membrane connecting the fibula and the tibia. The distal articulating surface of the fibula is at the lateral malleolus where it helps to form the ankle joint. It is subjected to only around 10% of the ground reaction force that passes through the leg from the foot, whereas the tibia compensates for the remaining 90% (Hammil and Knutzen, 2008).

2. Anatomical description of the tibia: Bone architecture and structure

2.1. Cortical Bone

Cortical bone is dense and makes up the outer layer of long bones with a varying thickness. This thickness also changes over a lifetime depending on the use of the bones and the type of activity solicited. Cortical bone is most commonly found in the diaphysis of long bones and is made up of osteons, which are essentially columns of lamellae made from collagen fibres and minerals that are grouped around a central canal known as the Haversian Canals. Running perpendicular to the Haversian Canals are Volkmann's Canals that connect the osteons together. This entire system is enveloped in a surrounding fibrous layer called the Periosteum that contains progenitor cells that transform into osteoblasts and chondroblasts, which generate bone reconstruction post rupture. Cortical bone is relatively tough and rigid helping to protect the inner part of the bone.

2.1. Trabecular Bone

Trabecular bone is a network of porous bone tissue separated from cortical bone by a fibrous layer known as the endosteum; it is relatively weak when compared to cortical bone, for example according to Rho et al. (1993), with a Young's modulus of around 1 GPa compared to 18 GPa for cortical bone. The role of trabecular bone role is linked to metabolic activity such as haematopoiesis (the production of red blood cells) thanks to a high level of vascularisation. It is also important in the transmission of loads across joints, hence its location in long bone epiphyses.

2.2. Bone Fractures

Bone fractures occur as a result of either a sudden impact or several micro-traumas. A fracture occurs when the level of stress or strain is higher than the bone's failure point. As with many materials, bone has two yielding thresholds linked to its level of elasticity: and plastic yield point and a failure yield point. These yield points are based on the fact that bone is made up of both cortical (strong but brittle) and trabecular (weak but flexible) bone. If the level of deformation exceeds that of the plastic yield point, plastic deformation occurs which generates micro-damage; if the level of deformation exceeds the failure yield point, failure (fracture) occurs (Figure 3).

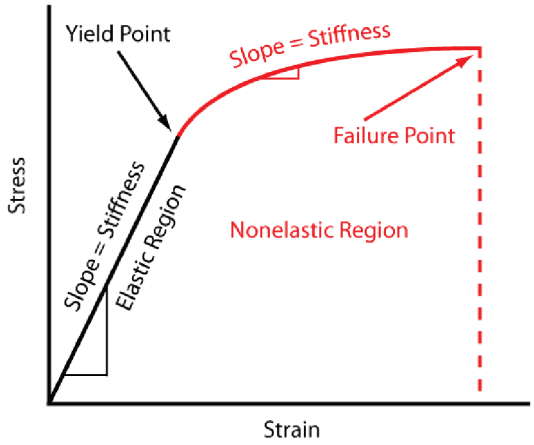

Figure 3: Graphical representation of a stress-strain curve of an object with its elastic deformation zone, plastic zone, followed by failure point. Image adapted from the University of texas, USA (www.utexas.edu).

The resulting Young's compressive modulus of long bones is around 16 GPa (Reilly and Burnstein, 1975) but this figure can vary depending on the measurement method, the type of bone tested, and the characteristics of that bone. For example, bone has a higher resistance towards compressive forces than tensile forces and shear forces are much less well tolerated leading to facture at an earlier stage of stress application (Ashman et al., 1989)

2.3. Bone remodelling post-fracture

Following a fracture, bone will work to regenerate itself and fill in any gaps within the bone matrix, this process is different to that of initial bone modelling for example in the development and growth of the human skeleton. Post-fracture remodelling can be broken down into four stages (Clarke, 2008):

1) Haematoma. Post-facture a haematoma is formed at the fracture site and is then steadily converted to granulation tissue. This haematoma causes the initial inflammation. White blood cells clear the fracture site of debris and the formation of new blood cells is triggered. A healthy blood supply and ease of blood circulation is important for cell removal following apoptosis and also to promote the generation of new blood vessels which later nourish the fracture site with the relevant enzymes and other molecules necessary for total fracture repair.
2) A soft callus is then developed thanks to the deposit of collagen and fibrocartilage which replaces the granulation tissue (Marsell and Einhorn, 2011). The recruitment of mesenchymal stem cells (MSC) for proliferation and differentiation towards bone cells is paramount for the generation of new bone. The MSCs aid the development of callus tissue which in turn gives an initial stability to the fracture site.
3) The primary soft callus is absorbed to leave space for the formation of a new, harder callus which will be more beneficial in terms of weight bearing. Apatite crystals are formed from prior deposits of calcium and phosphate and with time this new callus increases in solidity and rigidity (Raisz et al., 2005).

4) The new callus is later reabsorbed by osteoclasts and any unwanted bone fragments are removed. Lamellar bone is put down by osteoblasts which progressively constitute the new, solid bone through ossification (Crocket et al., 2011).

The process of bone remodelling is promoted through weight-bearing and micro-motion of the bone fragments which act as a mechanical stimulus for the generation of new bone (Prendergast, 1997).

3. Osteoarthritis (OA)

Osteoarthritis is a degenerative disease affecting articular cartilage (Martel-Pelletier, 1999) consisting of multifactorial pathomechanisms leading to its onset, such as obesity, genetics, age, joint alignment, applied mechanical stress to an area, past injury, and bone density which in itself is related to genetic and environmental factors (Takakura et al., 1995; Egloff et al., 2012). According to the World Health Organisation (WHO, 2019; https://www.who.int/chp/topics/rheumatic/en/) it is in the top 10% of the most disabling diseases in developed countries.

Osteoarthritis is characterised through active modification of bone, deterioration of hyaline cartilage and swelling of the synovial lining of a joint (Aaron and Racine, 2013) leading to the development of osteophytes – bone formation linked to the degeneration of cartilage; the consequences of which include loss of mobility and joint incongruence.

Primary OA is the rarer of the two forms of osteoarthritis; this form of the condition is related to aging and its effect on the lubrication properties of cartilage which, in turn trigger a thickening of the subchondral plate and therefore reduces the joint space. The joint space narrowing causes friction and pain between the articulating bones. Secondary OA presents the same symptoms with the same causes; but the onset of this condition is linked to a past trauma which triggers the early onset of cartilage degeneration. Such traumas include shocks related to high-impact injuries.

When a bone is broken, no matter how small the fracture, its repairing process consists of bone remodelling through the development of new bone (Bennel and Brukner, 2005). As arthritis is caused by inflammation from friction between tissues, and abnormal remodelling pattern or over-remodelling, a history of bone fractures may lead to the development of OA through aggravation of surrounding tissues to the affected area.

Reports from the literature (Takakura et al., 1995; Tanaka et al., 2006) have identified four main stages of OA based upon joint space narrowing between the inferior tibial surface and the superior talar surface:

- Stage 1: osteophyte formation, but no joint space narrowing,
- Stage 2: medial joint space narrowing,
- Stage 3: joint space eradication and subchondral bone contact across the former joint space,

– Stage 4: complete joint space eradication and subchondral bone contact,

3.1. Socio-economic impact of OA

No literature was found that specifically studied the economic impact of ankle osteoarthritis; studies regarding hip and knee arthritis are prioritised are these are by far the most common types of OA. Data on hip and knee OA costs in Europe range from 1000€ to 5000€ per patient per year and observed a constant increase in OA prevalence over the course of the recent decades (Chen et al., 2012; Salmon et al., 2016). The cost of arthritis includes not only the direct cost of hospitalisation and pharmaceutical treatment, but also that of post-operative costs such as absenteeism at work, loss of productivity and disability benefits. Other costs unable to be quantified are patient-specific, for example: decreased quality of life, suffering, and potential depression (Chen et al., 2012; Hunter et al., 2014). Therefore, the pre-empting of OA and the relatively basic surgical procedures that can attenuate or even immobilise the progression of this disease are a very popular option for both patients and national health systems.

3.2. Lower limb joint misalignment

Lower limb joint misalignment can be a result of genetic disposition, as is the case in people with bowed legs as a birth deformity (Beaman et al., 2012); however this problem can also be related to post-operative misalignments due to the operative procedure or fragment malunion.

Individuals with a predisposition to joint misalignment are at greater risk of OA at the joint concerned. Joint malalignment leads to an imbalance in load transmission across the joint surface resulting in increased impact and compressive loads. An example of ankle OA is shown in Figure 4 where an obvious difference can be observed between image A and image B; the latter shows flagrant evidence of joint narrowing and subchondral bone contact between the tibial pilon and the proximal surface of the talus.

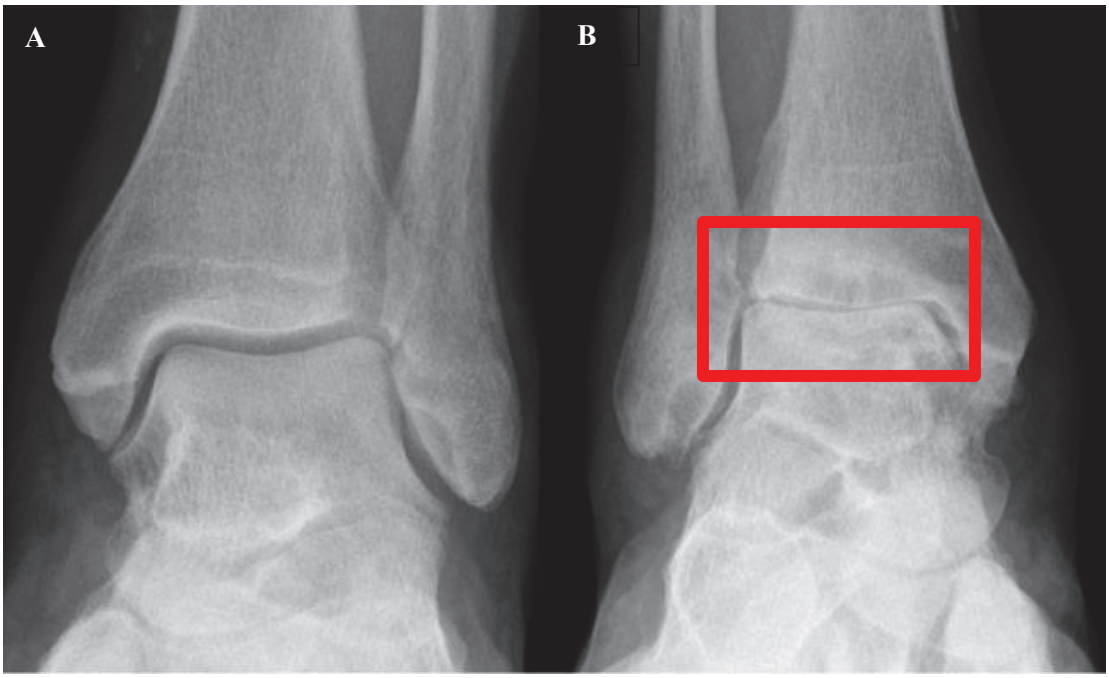

Figure 4: Radiographs of a healthy ankle joint (a) and an arthritic ankle joint (b). In red, the area of subchondral bone contact due to joint space narrowing. Images adapted from the TARVA study: www.anklearthritis.co.uk

4. Corrective osteotomies

A corrective osteotomy is a surgical technique used to straighten the axis of a long bone in order to improve joint congruency at its proximal and/or distal end. In the case of the tibia, a SupraMalleolar OsteoTomy (SMOT) is carried out to realign the ankle joint where the tibial pilon meet the superior surface of the talus bone.

The main objectives of corrective osteotomies include (Knupp et al., 2008) 1) the realignment of the joint axis of the ankle joint with the aim of distributing the load forces across a zone with intact cartilage remaining. 2) An improvement in joint congruency increases the joint contact surface results in a reduction of peak intra-articular pressure. 3) relieving zones of advanced cartilage degradation with the aim of reducing pain.

Anthropometrical studies (Lee et al., 2011; Colin et al., 2013; Kobayashi et al., 2016) across large populations have been used to define what a “normal” joint axis should be in the lower limb. Their protocole involved tracing lines along the axes of the femur, tibia, and foot in a weight-bearing position (Probe et al., 2003), resulting in a tibial tilt in the range of 0-8° (in relation to the horizontal axis of the floor). The horizontal axis of the ankle joint is said to be “normal” if it is parallel to the ground. Despite the widespread studies carried out in this domain, one widely used technique to assess lower limb joint alignment is to compare one side of the body to the other (Bauer et al., 1995).

4.1. Surgical principles and objectives

The process for correcting misalignment of the ankle joint through tibial osteotomy can be carried out using one of two techniques (Bauer et al., 1995). The first technique is known as a Medial Opening Wedge osteotomy (MWO; Figure 5a) and the second a Lateral Closing Wedge osteotomy (LCW; Figure 5b).

The former (MWO) involves making an incision on the medial side of the tibia using a Kirschner wire (K-wire), angle and insertion depth should be verified using fluoroscopy. The tibia is then medial to lateral leaving approximately 5 mm of the lateral cortex intact. A surgical chisel is then used to prize open the tibia and realign the distal joint.

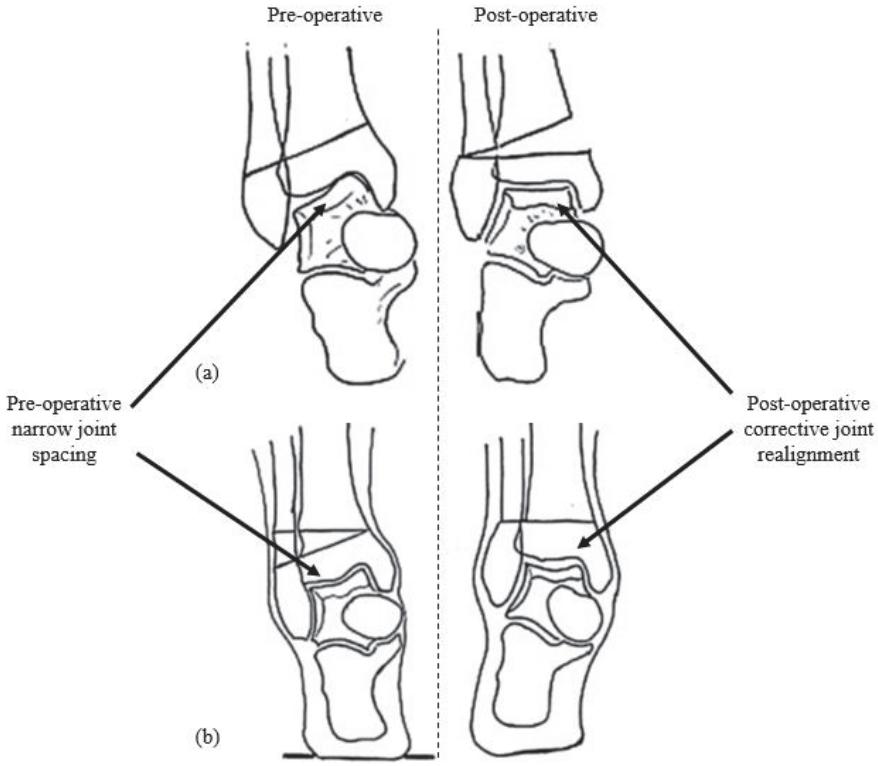

Figure 5: Examples of Medial Opening Wedge (MWO) (a) and Lateral Closing Wedge (LCW; b) -osteotomy techniques. Image adapted from Colin et al. (2013).

The latter technique (LCW) requires the dissection and post-operative resection of a portion of the distal fibula in order to gain access to the lateral cortex of the tibia. A wedge in the frontal plane is then outlined by inserting two K-wires, this is verified using fluoroscopy. The wedge is then dissected and the gap closed.

Corrective osteotomies are stabilised using a locking compression plate screwed to the exterior of the tibia. For the medial opening wedge osteotomy, the gap left by the opening is either left for natural bone remodelling to take place; or, depending on the size of the wedge, a bone graft often take from the

iliac crest is inserted (Tanaka et al., 2006; Colin et al., 2013). In the case of a lateral closing wedge osteotomy, the fibula is also plated to reconsolidate its two fragments.

In both cases, careful pre-operative planning is required which involves the determination of the osteotomy angle. The aim of realigning the joint axis is done by basing the “normal” joint angle on a divergence of 89° (range 86° - 92°; Takakura et al., 1995) between the anatomic axis of the tibia and a line parallel to the lateral distal tibia plafond (Beaman and Gellman, 2012). This is known as the Lateral Distal Tibia Angle (LDTA). The measuring of the LDTA is calculated from antero-posterior radiographs in a standing, weight-bearing, position in an anterior (TAS) and lateral view (TLS) (Figure 6).

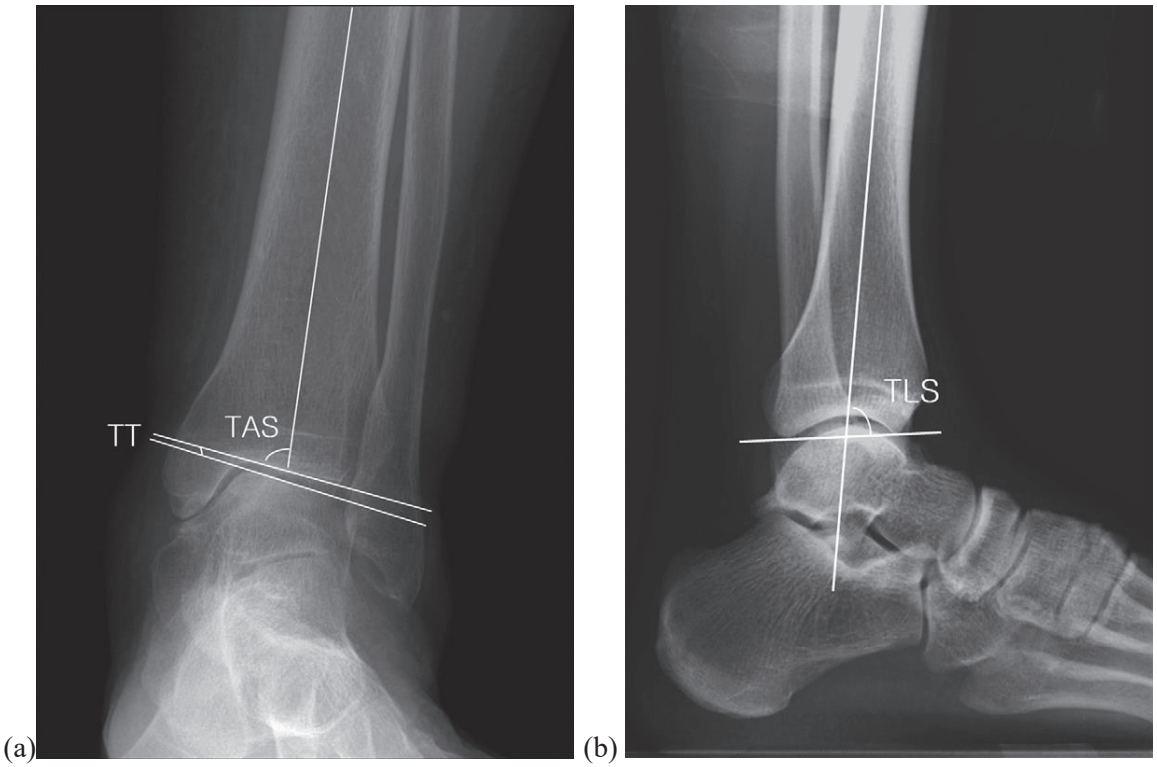

Figure 6: Example measurements of (a) Tibial-Ankle-Surface (TAS), Talar-Tilt angle (TT), and (b) Tibial-Lateral-Surface (TLS) angle (adapted from Lee et al., 2011)

4.2. Surgical aims

The goals of this intervention are to neutralise TAS, TT and TLS angle, attenuate the progression of OA, increase ankle mobility and reduce pain (Pagenstert et al. (2007), Lee et al. (2011), Colin et al., 2013). However, the outcome of corrective osteotomies in the distal tibia depends on a number of influential factors related to patient history, and post-operative therapy. In particular, the pre-operative tilt angle has been cited to be a good indicator of the level of post-operative improvement that can be expected. Pre-operative TT angles greater of 10° show little improvement and have little effect on ankle OA (Tanaka et al., 2006).

4.3. Existing research on corrective supramalleolar osteotomies

There is limited research available for the biomechanical analysis of supramalleolar osteotomies and osteosynthesis, the majority of the existing research is based on clinical case studies and observe the post-operative outcome of different surgical techniques in in-vivo situations (Table 2).

A large part of the literature surrounding corrective osteotomies is centred on high tibial osteotomies where the surgical aim is to realign the knee joint (Miller et al., 2005; Agneskirchner et al., 2006; Spahn et al., 2006; Pape et al., 2010; Choi et al., 2017). Two studies (Table 3) have conducted biomechanical analyses on the surgical techniques possible for corrective osteotomies with respect to contact between the proximal and distal fragments of the lateral cortex (Nha et al., 2016) and choice of external plate fixation (Ettinger et al., 2018).

The case studies often cited to support surgical techniques relating to SMOT involve the presentation of the patient's deformity, the surgical procedure carried out, any surgical complications and finally the measures used in the follow-up in order to assess the success of the surgical intervention. Such studies are interesting if the deformity being treated is uncommon or if a new surgical technique is being analysed. Otherwise, cohort studies collecting data over a number of months or years can provide more concrete information, such as methods and outcome measures that globally address a large number of cases.

Kitoaka et al. (1994) developed an ankle-hind foot scale adopted by the American Orthopaedic Foot and Ankle Society (AOFAS) and commonly used in study to evaluate pain, joint mobility, walking endurance, walking surface adaptation, gait abnormalities and joint alignment. The report to be completed is a questionnaire with patient-subjective criteria (e.g. pain, walking endurance) and clinician-objective criteria (e.g. joint alignment and mobility). This scale has become the standardised method for assessing ankle stability before and after surgical intervention. A more detailed method of measuring ankle mobility and pain is the Takakura scale; this approach may be adopted as it provides a more detailed examination of ankle mobility (Takakura et al., 1995).

Nha et al. (2015) carried out a cadaver study to determine a "safe zone" for medial open-wedge supramalleolar osteotomies based on the osteotomy plane in relation to the intrasyndesmotic ligament (Figure 7). Their outcome criterion was the presence or absence of a lateral cortical fracture appearance; in an ideal situation, the lateral cortex should remain intact. The study concluded that osteotomies carried out in the proximal third of the syndesmotic ligament (intrasyndesmotic osteotomy) are more stable than those conducted proximal to this range (suprasyndesmotic osteotomy).

Figure 7: Intrasyndesmotic ligament safe zone for SMOT identified by Nha et al. (2016)

Ettinger et al. (2018) compared the biomechanical performance of five different plate-based implants. Sawbones® models were used to simulate a supramalleolar osteotomy which was then fixed with one of the five chosen plates (n=5 samples/plate); all plates were externally fixed to the sample on its medial side. The samples were then subjected to biomechanical testing (150 N and 800 N compression, and 5 Nm torsion) and stiffness constructs were calculated to compare the two implants. A higher stiffness was considered to offer greater stability and therefore seen as the better option.

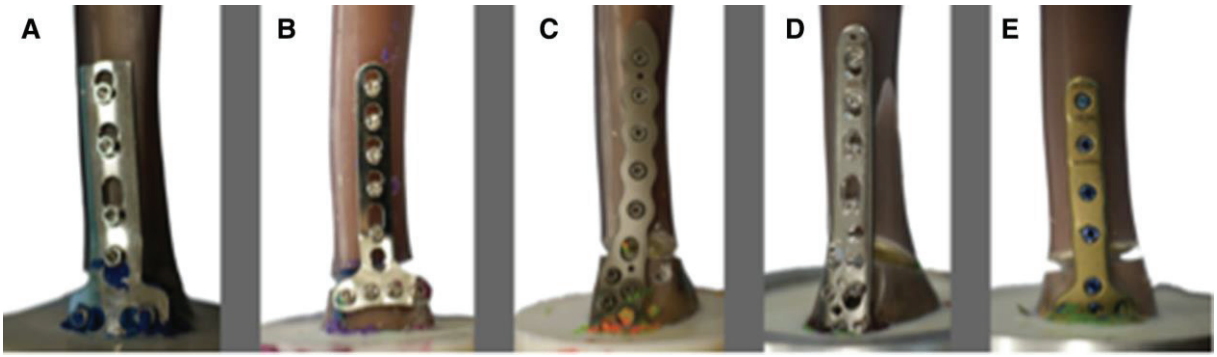

Figure 8: Different plates used in the study by Ettinger et al. (2018). DePuy Synthes© 4.5 mm LCP Medial Proximal Tibia Plate (a); DePuy Synthes© 3.5 mm LCP Distal Radius Plate; Stryker© AxSOS® Distal Medial Tibia (c); DePuy Synthes© 3.5 mm LCP low bend medial distal tibia plate (d); Integra® TIBIAXYS® distal tibia osteotomy medial plate (e)

Results from Ettinger et al. demonstrate high axial stiffness values in the range of 20-26 $kN.mm^{-1}$, and relatively high rotational stiffness between 3.5 and 4.2 $Nm.deg^{-1}$. Although cited as such, we consider these overly high axial stiffness values to be an error in publication and that the real range was from 2-2.6 $kN.mm^{-1}$. Axial and rotational failure were also measured, showing large differences between the plates tested with plate failure occurring at 1206 N for the Integra® TIBIAXYS® plate, against 6462 N for the Stryker AxSOS® plate. Although not detailed in their study, we can only assume that the force levels cited here are the forces at which failure occurred.

These differences are not elucidated in the article but may be related to plate geometry and boundary conditions such as screw insertion torque and the number of screws used. The high axial force 800 N compression was considered to simulate in-vivo loads during full weight-bearing. Torsional stability of the implants was attributed to the importance of leaving the lateral cortex intact, offering greater stability to the bone-implant construct. No other biomechanical studies (as opposed to case studies) relating to SMOT were found.

The use of a SMOT technique to improve stability is tested using the AOFAS is numerous studies (Pagenstert et al., 2007; Lee et al., 2011; Colin et al., 2013; Kobayashi et al., 2016).. Complementary procedures to SMOT were also highlighted in this study, where SMOT through MWO osteotomies sometimes also require lengthening of the Achilles tendon to account for increase in total leg length.

Biomechanical studies have highlighted the importance of the intact lateral cortex thickness on bone-implant stability; yet this is seldom measured or cited in the clinically-based literature. The lateral cortex is commonly also fractured during wedge opening techniques due to the stiffness of the bone. Similarly, the “safe zone” defined by Nha et al. (2015) in the intrasyndesmotic area compared to the suprasyndesmotic zone may be of great interest to surgeons regarding surgical planning and influential factors linked to post-operative outcome, such as lateral cortex preservation. Nonetheless, again this information is rarely stated, possibly due to the lack of concrete research in this area. Only Colin et al. (2013) stated that osteotomies were carried out at 10-15 mm above the joint space for lateral closing wedge osteotomies and 15 mm for medial opening wedge osteotomies.

To date, only external compression plates have been considered for the fixation of supramalleolar osteotomies as the sole nailing option would be the Expert Tibia Nail (ETN), destined for proximal, diaphyseal and some (but not all) distal tibia fractures. Supramalleolar osteotomies tend to encroach into the distal most 30 mm of the tibia (Colin et al., 2013) where the ETN is no longer a suitable option due to its length and screw placement.

In all studies aforementioned and later cited, the term stability is related to the stiffness of the bone-implant construct, and in some cases also the interfragmentary movement (IFM). A more stable construct is considered to present a higher stiffness value and allow less IFM.

Table 2: Medical studies relating to corrective osteotomies in a clinical setting

Authors	Study parameters			Outcome measures			
	Surgical technique applied	Number of patients	Average follow-up time (months) [range]	AOFAS	Takakura score	Medical imaging	Other
Takakura et al. (1995)	MOWO (n=12) LCWO (n=5) OO (n=1)	18	81m [33-154m]		Yes	Radiographs TAS, TLS, TMM	
Stamatis et al. (2003)	MOWO (n=6) LCWO (n=7)	13	33.6m [12-59m]	Yes	Yes	Radiographs TAS, TLS	Time to operative union Arthritis progression (Takakura classification)
Tanaka et al. (2006)	MOWO (n=26)	25	79m [27-215m]		Yes	Radiographs TAS, TLS Varus tilt angle	
Pagenstert et al. (2007)	MCWO (n=18) MOWO (n=8) LCWO (n=7) LOWO (n=2)	35	60m [36-126m]	Yes	Yes	TAS, TLS, TMM, TT Dorsi and plantar -flexion ROM	Pain Calcaneocrural angle Arthroscopy (arthritis assessment)
Lee et al. (2011)	MOWO (n=16)	16	28m (median) [12-78]	Yes	Yes	Radiographs TAS, TLS, TT Heel alignment angle	Arthritis progression (Takakura classification)
Colin et al. (2013)	MOWO (n=21) MCWO (n=12) LOWO (n=9) LCWO (n=41)	83	42m [12-144m]	Yes	Yes	Radiographs TAS, TLS, TT Meary angle	Pain walking across an incline Arthritis progression (Takakura classification)

MOWO = medial opening wedge osteotomy; LCWO = lateral closing wedge osteotomy; OO = oblique osteotomy; TAS = Tibia anterior surface angle; TLS = Tibia lateral surface angle; TMM = Tibia / medial malleolus angle; TT = Tibio-talar tilt angle; ROM = range of motion

Table 3: Biomechanical studies relating to corrective osteotomies in a research setting

MWO = medial wedge osteotomy; MM = Medial malleolus

Authors	Study parameters					Loads applied		Outcome measures
	Implant	Bone sample	Surgical technique applied	Osteotomy site	Intact lateral cortex	Extra-axial compression	Torsion	
Nha et al. (2016)	None	Cadaver (n=10)	MWO	40 mm proximal to MM	5 mm	None		Presence of lateral cortex fracture
Ettinger et al. (2018)	External medial plate (5 types)	Sawbones (n=25)	MWO	45 mm proximal to MM	5 mm	150 N 800 N	5 Nm	Construct stiffness

5. Distal tibia fractures

A high rate of distal tibial fractures are caused by a direct trauma often relating to a road accident, a sporting injury, or a fall (Cowie and Court-Brown, 2012); such fractures are far from being the most prevalent incidents but they have a high impact on both the economy and the quality of life of the patient.

5.1. Economic impact of tibia fractures

Tibia fractures are strongly associated with post-operative complications such as non-union or mal-union, both of which require secondary surgical treatment (Heckman and Sarasohn-Kahn, 1997). As a consequence, the economic impacts on a health service are high with supplementary costs related to radiology and physiotherapy during and post –treatment (Dahabreh et al., 2009). One major factor affecting the economic impact of a tibia fracture is the post-operative outcome. A secondary surgery required to fix non-union can be costly depending on the chosen treatment. In the UK, tibial non-union surgery can cost up to £16,000 (14,500€ in Germany; Kanakaris and Giannoudis, 2007). The choice of implant and its repercussions on surgical outcome are therefore an important aspect in the primary treatment of distal tibia fractures.

5.2. Fracture classification

In Europe, the AO foundation (Arbeitsgemeinschaft für Osteosynthesenfragen, Davos, Switzerland; www.aofoundation.org) has developed a widely accepted classification system which categorises fractures based on the area and the stability of the fracture (Figure 9).

The code 43 relates to the distal tibia; type A fractures indicate an extra-articular fracture and the number 1, 2, or 3 associates a simple, wedge, or complex fracture, respectively. The A3 type fractures in the distal tibia are the most common (Court-brown and McBirnie, 1995) and also the most severe of the extra-articular fractures.

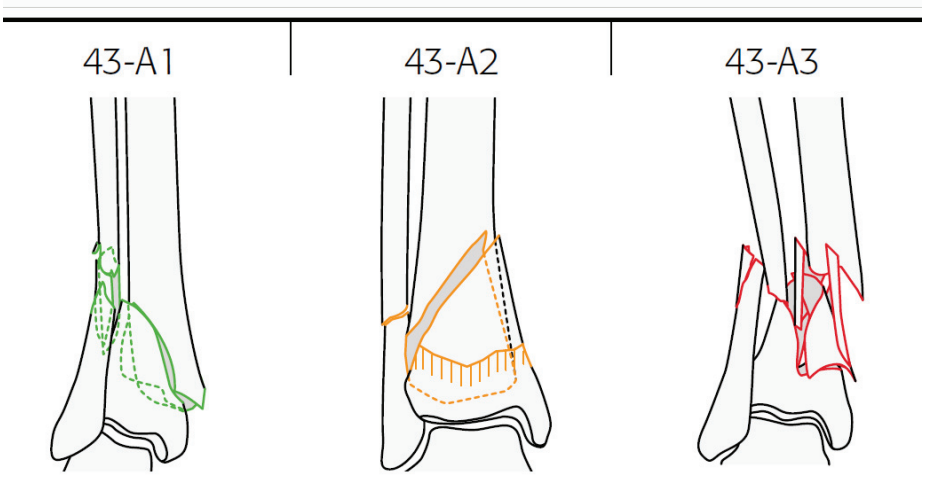

Figure 9 Type-A fracture classification for distal tibia fractures

5.3. Anatomical reduction of distal tibia fractures

The most important factor in the treatment of distal tibia fractures is the anatomical reduction of the fracture and the realignment of the bone fragments; the latter being an aspect difficult to achieve.

Misalignment problems stem from two main causes: a poor anatomical reduction during surgery before implant insertion which leaves the fracture in a compromising position with regards to restoring normal tibia function. The second cause develops post-operatively and is due to an unstable fixation of the implant to the bone increasing the chances of implant failure (Kuhn et al., 2012). Soft tissue damage, bone loss during injury, compromised blood supply, and fracture of the ipsilateral fibula are all injury-related factors that can slow down fracture healing and fragment reunion. Similarly, patient-related factors for example: pre-existing medical conditions, smoking, and diabetes will also have a negative influence on fragment union.

There are currently two implant models available on the European market for distal tibia fracture treatment: an intramedullary nail (IM nail) or a locking compression plate (LCP). The concept of an intramedullary nail is that to insert the nail into the medullar cavity which places it in the central axis of the tibia allowing for a high resistance to compressive and tensile forces. The LCP is attached to the exterior of the tibia on the medial side. Both implants are stabilised using a certain number of screws.

5.3.1. Locking Compression Plate (MDTP; Figure 10a)

One commonly used LCP for distal tibia fracture repair is the Medial Distal Tibia Plate (MDTP; Depuy-Synthes®, Switzerland) which is inserted beneath the skin on the medial side of the ipsilateral tibia (Hessmann et al., 2015). The plate is fixed in place with one screw proximal to the fracture site and a second screw distal to the fracture site. Additional screws are added in relation to the severity of the

fracture and the health of the patient; those with osteoporosis, for example, will have a greater number of screws inserted in order to distribute the mechanical strains more evenly across the injured area and to improve the hold of the plate to the bone.

5.3.2. Intramedullary Nailing

Expert Tibia Nail (ETN)

To date, the Expert Tibia Nail (ETN; Depuy-Synthes®, Switzerland) is the only IM nailing option available for the reduction distal of tibia fractures. The nail measures approximately 30 cm in length and is inserted at the tibial plateau. The nail descends the entire length of the tibia to reach the fracture site in the distal tibia. Depending on the patient morphology, three difference nail lengths are available; despite this concept, however, the ETN is not an option for very distal fractures in the distal 30 mm of the tibia (Figure 10b) due to nail length and the necessity of having two screws to block distal nail translation.

Following insertion, the ETN is proximally fixed to the bone using a guide that is attached to the proximal end of the nail and allows for the accurate screw insertion at two sites. The distal screw holes are then drilled using fluoroscopy to verify the position, such a technique can easily induce error if the surgeon does not correctly check the radiographs and drill in the correct plane.

Distal Tibia Nail (DTN)

A new concept of IM nailing has been developed: the Distal Tibia Nail (DTN, Mizuho®, Japan) has a distal insertion point which means that it is an intramedullary nailing possibility for very distal fractures that the ETN cannot reach (Figure 10b). This product is currently in clinical trials in Japan. The surgical technique of the DTN involves drilling an insertion site at the medial malleolus along with supplementary reaming around the insertion site until the nail can be fully inserted (Figure 10c). The nail is then locked in place by five screws; two screws proximal to the fracture site and three distal. The distal screws are designed such that the far part of the screw has a thinner body and deeper threading to increase its purchase in the trabecular bone.

(a) 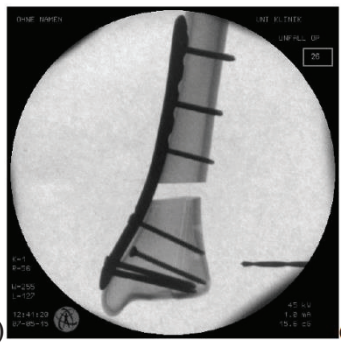 (b) 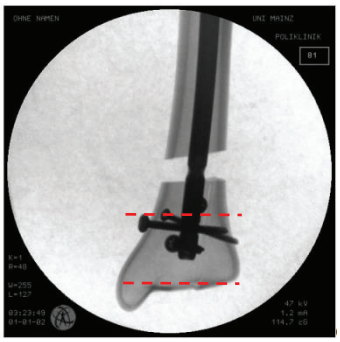 (c) 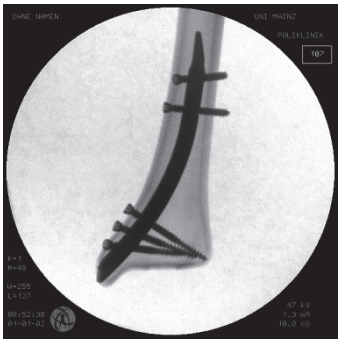

Figure 10: Radiographic images of the LCP (a), ETN (b; in red the very distal area that the ETN cannot reach) and DTN (c). (source: University Medical Centre, Mainz, Germany; unpublished images).

5.4. Comparison of implant options

The choice of implant is largely patient-based. In elderly patients the ETN is favoured over the MDTP as it has less impact on soft tissues around the fracture site and therefore this and vascularisation are not compromised decreasing the risk of co-morbidities (Casstevens et al., 2012; Parion et al., 2015).

The geometric characteristics of the MDTP and its positioning make it more susceptible to bending forces during compression of the tibia in weight-bearing activities (Mauffrey et al., 2012). As a consequence, screw loosening is a common post-operative problem (Hazarika et al., 2006; Hasenboeler et al., 2007) with the plate leading to implant instability and mechanical hardware protrusion through the skin. Furthermore, this procedure is generally avoided where possible in patients presenting an already compromised vascularisation around the distal tibia as the application of the plate only worsens this situation by squashing the peri-bone blood vessels. Nonetheless, this surgical technique is relatively easy to carry out and is less prone to error than the ETN; the plate can be inserted and fixed to the fracture site with minimal use of radiography leaving the patient and surgeons at less risk of radiation exposure.

Other post-operative problems stemming from the MDTP include incidences of pseudo-arthrosis where healing is largely delayed and an excess of fibrocartilage develops. In such cases, secondary operations must be carried out to remove the plate and extra bony matter around the fracture site (Hasenboehler et al., 2006).

The ETN has been associated with post-operative problems such as fragment mal-union and increased fibrocartilage at the fracture site which is a sign of slow bone remodelling often due to high levels of stress shielding from an implant (Khoury et al., 2002; Zelle et al., 2006; Ahmad et al., 2012; Li et al., 2015). Stress shielding is the term given to the effect of a metal implant having a significantly higher Young's modulus than bone, leading it to absorb the necessary stress to the bone to provoke remodelling. While, in certain cases, this may protect the bone, lack of remodelling and repetitive loading can lead to implant deformation and later failure. Its surgical technique however is more prone to error – in severe cases leading to secondary surgery, and can have a detrimental effect on the health of the knee joint of the patient due to its proximal insertion site.

Retrospective studies (Katsoulis et al., 2006; Soraganvi et al., 2016; Bishop et al., 2018) report many cases of knee pain for patients implanted with the ETN which is ascribed to the distance between the proximal nail tip and the tibial plateau insertion site, and the antero-posterior distance from the tibial tuberosity. Muscle deconditioning has also been cited as a cause pain (Väistö et al., 2007), despite rehabilitation programmes and a significant amount of time between operation and post-op follow-up studies (up to 8 years), weaker knee musculature can be found on the operated leg.

To date no clinical studies are available for the DTN, as it is relatively new to the market and, for now, is exclusive to Japan for clinical usage. Biomechanical studies have been carried out to compare this implant to the ETN (Kuhn et al., 2014a) and MDTP (Kuhn et al., 2014b) for the reduction of distal tibia fractures and promising results were found. The DTN appears to have a similar (slightly lower) compressive stiffness construct to that of the ETN but demonstrates a significantly higher resistance to torsional loading. Furthermore, its distal insertion point allows it to cover the very distal zone not attainable by the ETN (Figure 10). In comparison with the MDTP, the DTN proves to be far stiffer for both compressive and torsional loading. Overall, it is thus far considered to be an advisable option for patients presenting distal tibia fractures where importance is drawn to the preservation of the knee joint and distal tibia vascularisation.

5.5. Implants and bone remodelling

As aforementioned, the remodelling process of human bone is dependent on external mechanical stimuli within a certain range: high enough to stimulate the need for bone redevelopment but not excessive so to further damage the bone.

Fractures reduced with an implant receive their necessary mechanical stimuli from the implant and its mechanical hardware which is in direct contact with the bone (often the screws rather than the implant itself). Increasing the number of screws, and therefore increasing the bone-implant contact area, the mechanical stimulus will be spread over a greater area and higher loads earlier in time post-operation can be tolerated.

On the contrary, the implants commonly used in orthopaedics are made from titanium (Ti-6Al-4V) which has a Young's modulus approximately five times higher than that of bone (Niinomi, 1998; Niinomi, 2008) (discrepancies originate from methods used to measure bone's elastic modulus; Rho et al., 1993; Heiner 2008). The difference in stiffness between the implant and the bone will cause stress shielding to occur and hinder the remodelling process.

5.6. Biomechanical testing of treatment options

In Europe for an implant to be accepted for production and clinical use, it is subjected to a 4-point bending test following the Europeans norms (ISO 5837). In a more clinical setting implants are subjected to biomechanical testing which replicates their usage in the human body. Tests often involve the use of cadaver or composite bone with a simulated fracture reduced with the implant in question. Samples are then evaluated through compression, bending, and/or torsion testing (Guerorguiev et al., 2011; Kuhn et al., 2014a,b,c). A summary is given in Table 3.

5.6.1. Composite bone for medical research

Composite bones, as a substitute for cadaver bones are increasing in popularity due to the reproducibility and reliability of such samples. Numerous studies to date have chosen to use composite

bones as they offer a stable alternative to anatomical specimens, which often differ in bone quality and size, making the unbiased testing of implants harder to achieve.

Fourth generation Sawbones® tibiae, made from epoxy resin, have been tested under various conditions and have been validated concerning their mechanical behaviour during compression, torsion and 4-point bending tests (Heiner, 2008; Gardner et al., 2010). This range of Sawbones represent a healthy male, under the age of 80, of 1.83 m in height and weighing 90.8 kg (890 N), the levels of cortical and trabecular volume are adapted accordingly (Figure 11).

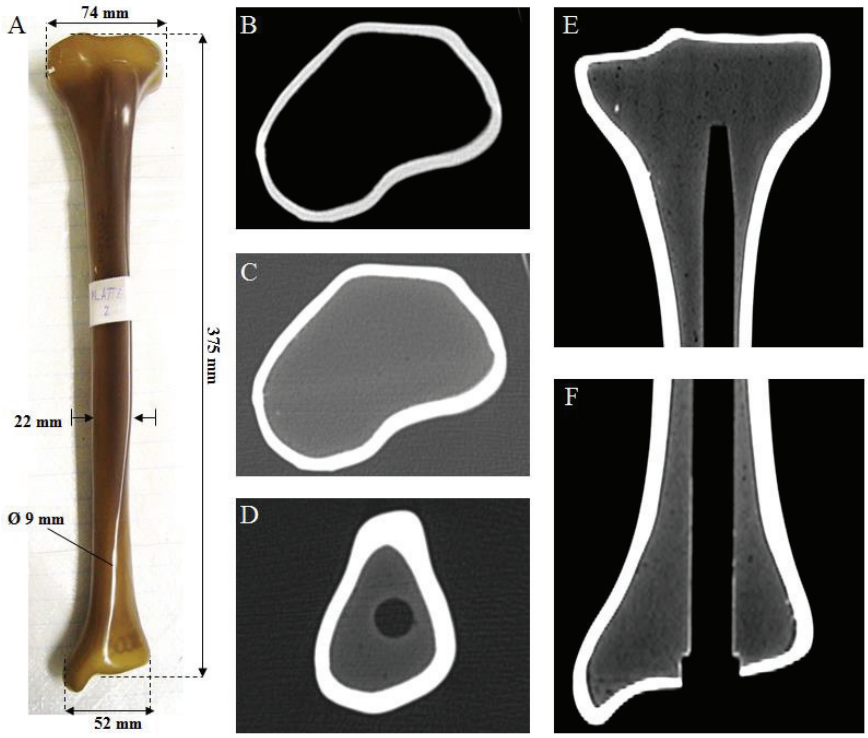

Figure 11 : Left medium-sizes tibia Sawbones sample (A); computer tomography scans of a Sawbones® tibia. Horizontal cuts of the tibial plateau (B,C), the diaphysis (D), frontal cuts of the proximal (E) and distal (F) tibia.

The composite tibia from Sawbones® differentiates between cortical and trabecular bone, which can be observed in Figure 11B for solely cortical bone and Figure 11C where the spongy bone of the tibial plateau is visible (shown as a light grey within the cortical shell). As the medullary cavity offers no mechanical stability, it is simply accounted for by an empty 9 mm cylinder within the trabecular bone ranging from the distal articular surface (Figure 11F) to the proximal epiphysis (Figure 11E). The diaphysis of the composite tibia (Figure 11D) therefore contains cortical and spongy bone, and the empty medullar cavity. Measurements of the medium sized Sawbones® tibia are displayed in (Figure 11A).

Sawbones® composite tibiae were used within the framework of this project; all testing was carried out using 4th generation left medium sized composite tibiae (item no: 3401). The mechanical validation studies from Heiner, 2008 and Gardner et al. (2010) have reported the following mechanical properties

for this Sawbones® model: Flexural rigidity (medio-lateral) = 146±5 Nm^2; Axial stiffness = 7.48±0.70 $N.\mu m^{-1}$; Torsional stiffness = 1.93±0.07 $Nm^2.deg^{-1}$.

5.6.2. Loading

The applied loads to instrumented samples vary, in particular with respect to compression testing. Authors justify their compression loads by stating that they represent physiological loads, however these loads differ depending on the study. Guerorguiev et al. (2011), Brinkman et al. (2014) and Horn et al. (2009) declared their loads to be based on physiological conditions, yet they vary by almost three-fold; Snow et al. (2008), loading just 50 N less than Horn et al. admitted that their loading conditions were not representative of those found in the human body. Nevertheless, none of the loads presented in Table 4 account for internal forces linked to muscle contraction and soft tissue tension (for example, Leupongsak et al. (2012) found 50% of body weight compressive forces across the knee joint linked to muscle forces during standing).

Similar discrepancies can be observed in the torsional loads and, again, little justification is provided for the choice of load magnitude. Wähnert et al. (2012) stated that their torsional loads were set at 5 Nm applied at 1 $Nm.s^{-1}$ so to assure the presence of deformation; but without causing damage to the bone-implant construct. Little literature is available on the torque applied to the ankle joint during walking, or other common activities. Wehner et al. (2009) used musculo-skeletal modelling to estimate the internal loads applied to the tibia during walking at 8 Nm – in agreement with levels used by Kuhn et al.

5.6.3. Stiffness measurement

The most common outcome measure used to asses implant stability is mechanical stiffness. Generally, a stiffness value of the instrumented sample in its test setup is determined and compared with other samples when analysing the stability between two implants. Such methods are simple to carry out and relatively efficient in terms of time consumption. A second method commonly used is the measurement of interfragmentary movement with the use of one or multiple cameras to film pre-defined points around the fracture gap. The threshold of allowing <2 mm interfragmentary movement is widely accepted as exemplifying implant stability (Billard et al. 2014; Gruszka et al., 2017, Nyary and Scammell, 2018).

Stiffness values cited in the literature are seldom comparable due to different test setups employed where the stiffness of the test setup is not subtracted from the sample stiffness (Guerorguiev et al., 2011; Helgason et al., 2014; Kuhn et al., 2014a,b). Other error sources include the use of potting materials (PolyUrethane: PU, or Poly(methyl methcralate: PMMA) and test setups which, in theory, should have a stiffness value infinitely higher than the test sample.

An important matter raised in a study by MacLeod et al. (2018) is the calculation of stiffness based upon interfragmentary movement, eliminating the displacement of the test setup detected by the displacement transducer; they keyed this term “gap stiffness”. Such influences linked to the test setup and data processing techniques help to explain the discrepancies found in the literature concerning bone-implant construct stiffness where displacement other than that carried out by the sample is detected and considered part of the bone-implant construct. The use of gap stiffness rather than sample construct stiffness is recommended as it provides values regarding the solely the sample and does not take into account the stiffness related to the boundary conditions.

5.6.4. Boundary conditions

The test setup boundary conditions have also shown to have a large influence on the outcome measures (Macleod et al., 2018). The study in question coupled experimental and numerical testing to analyse the effect of loading conditions on sample stiffness and interfragmentary movement around the simulated fracture gap. The use of pinned rather than clamped boundary conditions was concluded to be the advantageous concerning the freedom of the sample to rotate and increases the repeatability of results, not only in relation to calculated stiffness values but also stress and strain distribution. Samples subjected to loading under clamped conditions are likely to vary three-fold whereas under pinned conditions just by one order of magnitude.

Table 4: Research relating to experimental testing of distal tibia fracture reduction implants

Authors	Study parameters		Loads applied Pre-load‡ – main load [Cycle number]			Data acquisition		Outcome measures		
	Implant*	Bone sample	Extra-axial compression (N)	Torsion (Nm)	4-pt Bending (Nm)	Load cell	Marker tracking	Stiffness, elastic yield point &/ to rupture	IFM	Other /Imaging
Snow et al., 2008	LCP	Synbone (n=5)	0-450 [30,000]	0-3.5	0-3.5	✓		✓		
Horn et al., 2009	ETN	Cadaver (n=16)	0-500			✓	✓	✓	✓	✓ (pQCT)
Guerorguiev et al., 2011	ETN	Cadaver (n=16)	0-600 0-1200 0-1600 [to failure, <60,000]	1.5	3	✓	✓	✓	✓	✓ (pQCT)
Hogel et al., 2012	ETN	Sawbones (n=20)	0-350	+5 to -10		✓	✓	✓	✓	
Wähnert et al., 2012	ETN	Cadaver (n=8)	5-50 [10]	5		✓		✓		
Kuhn et al., 2014abc	ETN LCP DTN	Sawbones (n=14)	18-350 [4] 18-600 [4] 18-1200 [1]	±8 [4]		✓	✓	✓	✓	

‡ Pre-load is assumed to be 0 where no information is given by the authors

* LCP = Locking compression plate, DTN = Distal tibia nail; ETN = Expert Tibia Nail; IFM = InterFragmentary Movement

5.6.5. Digital Image Correlation (DIC) in orthopaedic research

The use of DIC in orthopaedics is interesting as it allows for a non-invasive, contactless technique for the measurement of displacement and strain fields across a surface (Grassi and Isaksson, 2015). This can supply information concerning stiffness calculations, bone remodelling (based on strain levels), bone fracture risk, and crack propagation (Palanca et al., 2014). Furthermore, Haddadi and Belhabib (2008) highlight the importance of being able to quantify the strain across an entire surface, rather than just a section, in order to account for the inhomogeneity and anisotropy of biological specimens - a criterion not possible with the use of strain gauges that are commonly used to directly asses strain. DIC also provides reliable data that can be used as a validation method for numerical simulations, such as displacement and strain fields (Väänänen et al., 2013). In some cases, DIC may be better adapted to research protocol than strain gauges for the identification of local peak strains and bone fracture characteristics such as the direction of crack propagation and location (Sztefek et al., 2010). An overview of the general principles of DIC is given in the appendix (§1).

The majority of the research concerning DIC on hard tissue whole segments of the human body concern the femur where compression and fall-imitation tests are carried out to predict bone failure compressive forces, implant-related behaviour, and fracture crack propagation (Tayton et al., 2010; Op Den Buijs and Dragomir-Daescu, 2011; Helgasson et al., 2014). Op Den Buijs and Dragomir-Daescu (2011) and Helgasson et al. (2014) both used DIC to validate FE models of the human femur during compression testing; whereas Tayton et al. (2010) observed the stress shielding effects of different hip prosthetics.

A summary of research carried out in an orthopaedic setting using DIC is given in Table 5; studies included in this summary contain whole hard tissue samples and are, for the most part, based on the femur or the tibia.

As was the case for research related to distal tibia research, the main test carried out is compression testing, often relating to fall situations. The only study to take into account rotational loads was Small et al. (2013) where 5° medial rotation was added to the specimens with the total knee arthrodesis component in full extension and 10° lateral rotation with the prosthetic component at a 90° flexion angle. The resultant torque transferred to the proximal tibia was measured.

DIC is mainly used for exploitation of strain variables, interfragmentary movement is analysed in two studies. Strain data is more complicated to obtain as the positioning and gluing of strain gauges, the otherwise-considered gold standard method for strain measurement, is complicated. DIC, on the contrary, rapidly calculates surface strain data. One could argue that the export of only IFM in studies by Billard (2014) and MacLeod et al. (2018) does not use DIC to its full potential, especially given that normal and von Mises strains present useful information to predict possible bone fracture and implant failure.

Table 5: Research relating to DIC in whole human hard tissue samples.

Author	Specimen		Research context	Mechanical test	2D/3D	DIC program	Outcome measures*	Complementary measures
	Composite bone	In-situ testing						
MacLeod et al. (2018)	Tibia (n=4)		Boundary conditions influence on outcome measures	200 N 500 N	2D	Matlab (v 7.6)	IFM	FEA
Op Den Buijs and Dragomir-Daescu, (2011)		Femur (n=22)	2D FEA validation	Test to failure at 100 $mm.s^{-1}$	2D	Matlab	ε_{xx}, ε_{yy}, ε_{zz}, ε_{xy}, ε_{xz}, ε_{yz}, ε_{vm}	2D FEA
Billard (2014)	Femur (n=3)		Implant behaviour	1000 N 2000 N 3000 N	**3D**	7D	IFM	3D FEA Construct stiffness
Grassi et al. (2014)		Femur (n=3)	Full-field strain during walking	Compressive test to failure at 15 $mm.s^{-1}$	**3D**	Vic 3D (2010)	ε_1, ε_2	Strain gauges
Helgason et al. (2014)		Femur (n=1)	Protocol development	16,500 N Impact/drop test	**3D**	DaVis and Strainmaster (v8)	ε_2	FEA
Small et al. (2013)	Tibia (n=24)		TKA	2500 N Axial compression 5°, 10° rotation	**3D**	Aramis (v6)	ε_{vm}, Torsional moment	Strain gauges
Tayton et al. (2010)	Femur (n=5)		Stress shielding of prostheses	1000 N Extra-axial compression	**3D**	Vic 3D (2006)	ε_2	None
Väänänen et al. (2013)	Femur (n=6)		Surface strain repeatability of DIC	Compressive test to failure at 1 $mm.min^{-1}$	**3D**	Vic 3D (2007)	Strain noise Strain variation	Construct stiffness

ε_1 = maximum principal strain; ε_2 = minimum principal strain; ε_{xx}, ε_{yy}, ε_{zz} = normal strain components; ε_{xy}, ε_{xz}, ε_{yz} = normal shear strain components; ε_{vm} = von Mises strain; FEA = finite element analysis; TKA = total knee arthroplasty; IFM = interfragmentary movement.

Vic-3D, Correlated Solutions Inc, USA
7d (Iméca, Université de Savoie, France; CTC, Lyon, France)
Aramis (Gom, Inc., Braunschweig, Germany)
DaVis and StrainMaster (LaVision, Goettingen, Germany)
Matlab (Mathworks, Cambridge, UK)

6. Numerical modelling and simulation in orthopaedics

One commonly used numerical modelling method in orthopaedics in the Finite Element Method (FEM) in which a structure is represented by a set of elements; these elements are interconnected at their points, known as nodes. An assembly of elements is known as a mesh and various material properties can be applied to this mesh in order to characterise its structural behaviour, such as stiffness, Poisson's ratio, thermal conductivity, etc.

The use of FEM in orthopaedics is advantageous as it gives information on the stress and strain parameters of modelled bone and soft tissue which are impossible to obtain via experimental methods. This is particularly helpful in the prediction and testing of new surgical techniques and orthopaedic implant design as stress and strain deformation patterns can be analysed throughout the different bone types and provide information related to bone remodelling potential, primary and secondary fracture risk, and implant behaviour.

Concerning distal tibia fractures and corrective osteotomies, there are a number of numerical studies related to the former especially with respect to implant choice (Table 6). As for supramalleolar corrective osteotomies there is, to date, no literature available on the numerical analysis of this problem. A summary of distal tibia fracture numerical model research can be found in the table below (Table 6). Across all the studies evaluated, only Oh et al. (2014) attempted to validate their work with a four-point bending test. Nourisa and Rouhi (2016) compared their results with experimental and numerical testing found in the literature. No other study has made an attempt to validate the numerical models with experimental research.

The most commonly used loading condition is axial compressive force ranging from 70 N (Kim et al., 2010) to 2500 N (Aizat et al., 2011). The differences in axial loading force can be attributed to the varying weight bearing positions of the human tibia; Kim et al. (2010), for example, considers 70 N to be equivalent to 10% body weight of a 70 kg person in a post-operative scenario where only partial weight bearing is recommended at first in order to stimulate fracture healing mechanisms. Zhang et al. (2016) based their loading forces on daily activities such as flat walking and stair walking.

Given that compression forces are most commonly applied in numerical studies of the human tibia, considering the elements as isotropic is relatively unproblematic. Human bone is known to be anisotropic with varying resistances depending on the axis of the force vector. The highest Young's modulus is in the longitudinal axis to support body weight and ground reaction forces during standing and walking/running activities. The only study to take this into account was Kim et al. (2010) who defined separate Young's moduli and Poisson's ratios in the longitudinal, transverse and radial axes for cortical bone. Zhang et al. (2015) considered the elements to be isotropic in their model of the tibia and

simulated axial compression and torsion simultaneously in order to evaluate the effect of the distance between an external plate fixation and the outer bone cortex on stress distribution during activity.

Von Mises' stresses (σ_{VM}) and interfragmentary movement (IFM) are the most frequently sought outcomes measures. The advantage of exploiting σ_{VM} is that this information and is also a predictor of bone/implant failure, and is not attainable through experimental techniques. On the other hand, IFM can be easily obtained during experimental procedures and could be used to validate, to a certain extent, numerical models. Many of the studies mentioned in Table 6 state that a limitation of their study is the absence of model evaluation. This may be due to the difficulty in controlling boundary conditions between numerical and experimental conditions where, in the latter, issues such as sample degrees of freedom, friction coefficients, and test configurations are often a source of error leading to incoherencies (albeit small) between data.

All but one article mention no use of a priori sensitivity analyses to optimise the effect of independent variables (mesh size, mesh type, contact type, boundary conditions, etc.) on defined dependent variables (σ_{VM}, IFM, etc.). As a result, for simulations carried out using the same solver (in this case Abaqus), large differences can be observed between the number and type of elements used to model the tibia. Kim et al. (2010) based their tibia model on 18,000 hexahedral elements, whereas Nourisa and Rouhi (2016) used 180,000 tetrahedral elements; both studies used CT imaging techniques to obtain the tibia geometry.

A recent article from Kluess et al., (2019) requested four different laboratories to develop a FE model from supplied experimental data of one human femur extra-axial compression testing. All necessary experimental setup and imaging data were supplied; however no results were given to evaluate the models. None of the four models used the same method to develop the numerical model. Mesh element number ranged from 72k to 1 million, computation time from 16 minutes to 6 days and two different applied boundary conditions were also observed. This again reiterates the level in discrepancies between models of identical experimental background.

Table 6: A summary of recent literature relating to numerical modelling and simulation of the human tibia

Authors	Model	Mesh			Loading conditions	Results			Evaluation	Sensitivity analysis
	Bone and implant	Element type	Material type	Solver	Compression	σ_{VM}	IFM	Other		
Aizat et al., 2011	Proximal tibia, LCP	Tetra	N/A	Marc	2500 N	Yes	Yes		No	
Fouad et al., 2010	Bone cylinder, LCP	Tetra (10-node)	N/A	Abaqus	2.5 MPa (800 N)	Yes	No	Fracture healing	No	
Golovakha et al., 2014	Proximal tibia, LCP	Tetra N_{total} = 35k	Lin. Elas. Iso	ANSYS	0.3 MPa (800 N)	Yes	Yes		Lit.	
Gomez-Benito et al., 2006	Proximal tibia, LCP	Hexa (shell) $N_{implant}$ = 14k	Lin. Elas. Iso	Abaqus	975 N	Yes	Yes	Implant strain	No	
Kim et al., 2010	Tibial diaphysis, LCP	Hexa N_{tibia} = 18k $N_{implant}$ = 6k N_{screw} = 380	Linear elastic anisotropic	Abaqus	Screw fastening 2000 N (tensile), Weight-bearing 10% BW*, 200% BW, 300% BW	No	No	Fracture gap strain, Bone healing rate	No	Contact analysis for screw fastening
Ma et al., 2013	Tibial diaphysis, LCP	N/A	Lin. Elas. Iso	ANSYS	600 N	No	Yes	Axial and bending stiffness	No	
Nourisa and Rouhi, 2016	Distal tibia, LCP + IM nail	Tetra N_{total} = 210k, N_{bone} = 184k, N_{LCP} = 22k, N_{IMN} = 18k	Lin. Elas. Iso	Abaqus	400 N, 800 N	Yes	Yes	Bone / implant shear movement	Lit.	
Oh et al., 2010	Bone cylinder, LCP, DCP	N/A	N/A	ANSYS	4-point bending test to failure at 1 mm/min	Yes	No	Stiffness construct	Yes	
Oken et al., 2017	Distal tibia, LCP		Lin. Elas. Iso	Fempro	400 N axial	Yes	Yes		No	
Zhang et al., 2015	Distal tibia, LCP	Tetra, N_{tibia} = 82k	Lin. Elas. Iso	Abaqus	2230 N axial, ±8Nm torsion	Yes	Yes		No	
Zhang et al., 2016	Proximal tibia arthroplasty	N_{total} = 750k	Lin. Elas. Iso		1960 N (walk) 2492 N (↘ stairs) 2280 N (↗stairs)	Yes (SS‡)	No	Bone strain, secondary fracture risk	No	

* BW = body weight for a 70kg person, according to Kim et al., 2010; DCP = Dynamic compression plate; IFM = Interfragmentary movement; SS = Stress Shielding; Lin. Elas. Iso = Linear Elastic isotropic; Lit. = literature comparison; ; LCP = Locking Compression Plate

7. Aim

The general aim of this thesis is to evaluate the feasibility of the Distal Tibia Nail as an intramedullary nailing alternative to external plating for the fixation of supramalleolar osteotomies. A secondary aim is also to further contribute to the little existing literature on supramalleolar corrective osteotomies and the identification influential parameters which can alter experimental results leading to differing results between tests within the laboratory and between published results from varying authors. The biomechanical analysis of the DTN in comparison to the MDTP for distal tibia A3 fractures has already been widely explored by the research group at the UMC Mainz; but changes to protocol and test setups require a revaluation of these analyses. In light of the changes made, the DTN and MDTP will be retested for A3 fractures simulations. Incidentally, analyses of the test conditions are also carried out and their influence on construct stiffness calculations is investigated.

This work comprises of multiple sub-studies which include the mechanical evaluation and testing of the test setup boundary conditions (chapter 2). The biomechanical testing of the DTN as an alternative for supramalleolar osteotomy fixation and the retesting of both implants for distal tibia A3 fractures (chapter 3). A posteriori analysis of the influential boundary conditions directly linked to the biomechanical testing of chapter 3 (chapter 4). The influence of implant screw geometry on bone surface deformation with consequences for bone remodelling and secondary fracture risk (chapter 5).

Chapter 2: Preliminary testing of biomechanical methods and setup

1. Introduction

As aforementioned in the study carried out by MacLeod et al. (2018) the influence of boundary conditions on the testing of orthopaedic devices can have a large influence on the results obtained. The work in this thesis is based upon previous studies carried out at the Biomechanics Laboratory of the University Medical Centre, Mainz, Germany, where no study to-date has sought to quantify the impact of the test setup and boundary conditions on stiffness construct results. The aim of the work presented in this chapter is to evaluate the effect of the materials and configurations used to create the boundary and loading conditions, and suggest improvements that can lead to the increase in the reliability of results as well as their accuracy.

The testing procedures described in this research project are carried out using either a servopneumatic testing machine at the Biomechanics Laboratory of the University Medical Centre (UMC), Mainz, Germany (http://www.unimedizin-mainz.de/); or the servohydraulic testing machine at the Biomechanics and Impact Mechanics Laboratory of the French Institute of Science and Technology for Transport, Development and Networks (www.ifsttar.org).

2. Compression testing configurations

2.1. Principle

In the human body the compression forces do not pass directly through the central axis of the tibia. They are shared across the tibial plateau with an estimated 60% passing through the medial condyle and 40% through the lateral condyle (Högel et al., 2013; Rastetter et al., 2016; Moewis et al., 2018); this force vector also passes posterior to the central axis. In light of this, a physiological loading setup is recreated by drilling a hole at 10 mm medial and posterior to the centre of the PMMA block to define the loading point (Figure 12).

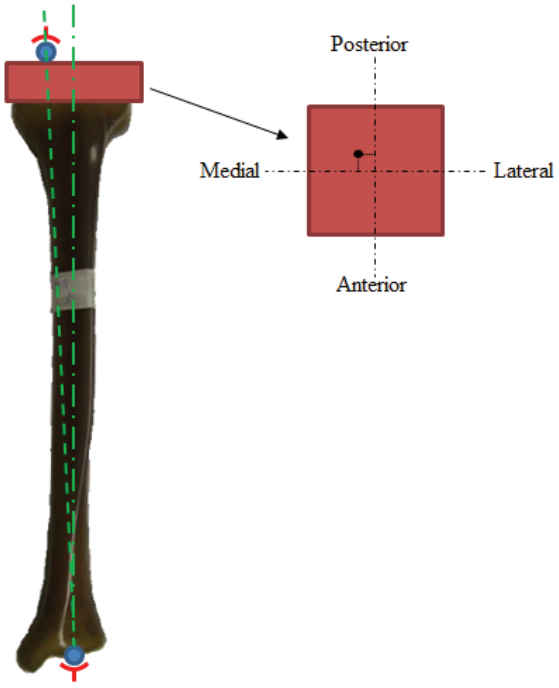

Figure 12: Compression test setup principle with an extra-axial loading point.

2.2. Existing test setup

The test setup habitually used in the biomechanics laboratory of the UMC Mainz consisted of a resin-based component attached directly to the force transducer in the superior half of the setup (Figure 12a). The inferior part of the setup was placed on an aluminium plate supported by four cylinders, used to protect the rotating table used during torsional testing. On the aluminium plate, a PMMA mould of the distal end of a Sawbones tibia (known as the pseudo-talus; Figure 13c) was positioned and held in place by a U-profile made from steel in diagonally opposing corners (Figure 13b).

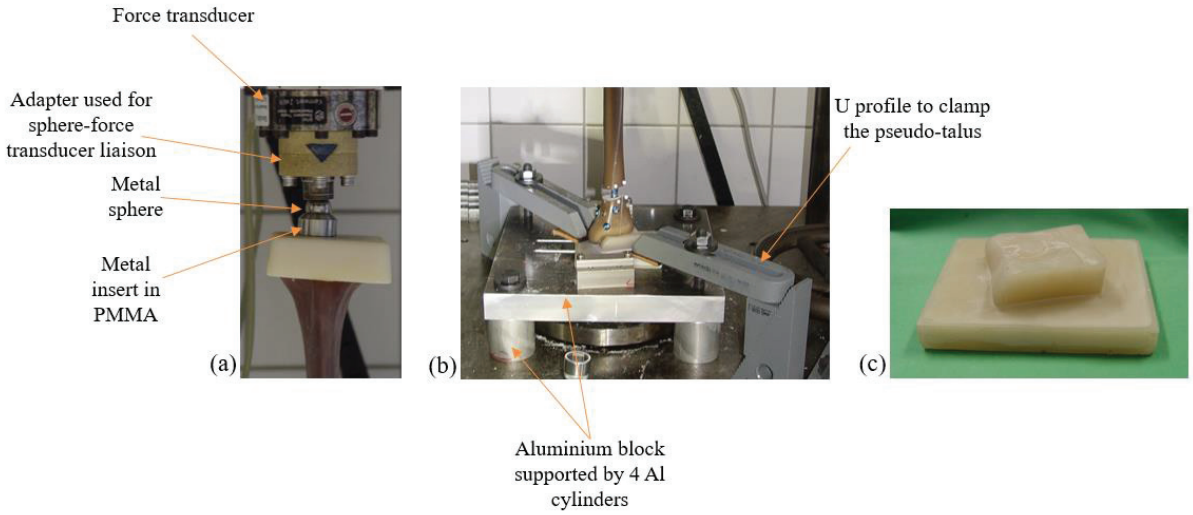

Figure 13: Example of the original test setup with a plastic component in contact with a metal sphere and hollowed piece (a); the distal setup with a pseudo-talus mounted onto an aluminium table (b); the pseudo-talus made from PMMA (c).

This original test setup left many factors open to error such as the alignment of the pseudo-talus in relation to the vertical axis of the machine. In this setup, the sample was blocked in all rotational degrees of freedom. The material of the resin-based superior clamp/adapter (Figure 13a) was unknown, and was thought to have a low stiffness.

2.2.1. Error assessment

No reliable method to date was used to embed the samples identically, nor had any research been undertaken into the mechanical properties of PMMA and the effect that these may have on the test results. Despite its unknown characteristics and influences in an orthopaedic setting, multiple studies employ the use of PMMA without accounting for it in their cited stiffness results (Horn et al., 2009; Helgason et al., 2014; Kuhn et al., 2014; Ettinger et al., 2018). A number of potential error sources were identified in the existing test setup (Figure 14) and investigated to measure their impact of sample construct stiffness.

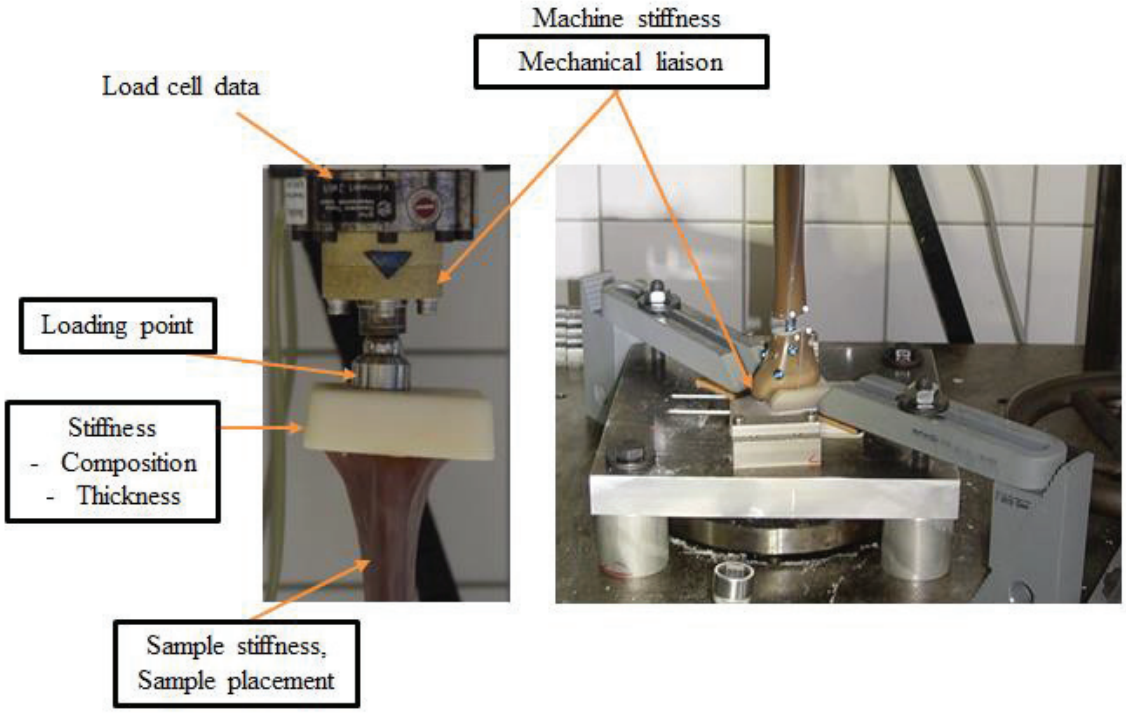

Figure 14: Identified error sources in the existing test setup. Outlined in black are the parameters taken into account in this study.

A series of preliminary studies were carried out which consisted of characterising the PMMA to calculate its elastic modulus and mechanical stiffness. The effects of the PMMA thickness, composition, and contact type were tested; as well as the loading point position and sample placement repeatability on sample total stiffness value. All tests were carried out using the servopneumatic testing machine at the UMC Mainz and one Sawbones® sample was used.

2.3. New setup

The compression test setup was then modified with the aim of eliminating the sources of error mentioned above. A double ball-joint setup was used to allow rotation in the vertical axis and both joints were correctly aligned using a repeatable method at the start of each test (Figure 15). The resin-based adapter was replaced by a steel part with an integrated steel ball that is in direct contact with the PMMA (Figure 15).

The advantages of this new setup included an increase in the degrees of freedom permitted to the sample thanks to the use of the two spherical jigs. The pieces used to maintain the sample and transmit the compressive forces to the sample were replaced by pieces made from steel and are therefore certain to have a higher stiffness than the sample. The use of steel pieces is to avoid force absorption before transmission to the sample; otherwise the calculated stiffness construct is based on the sample and its setup, rather than solely the sample.

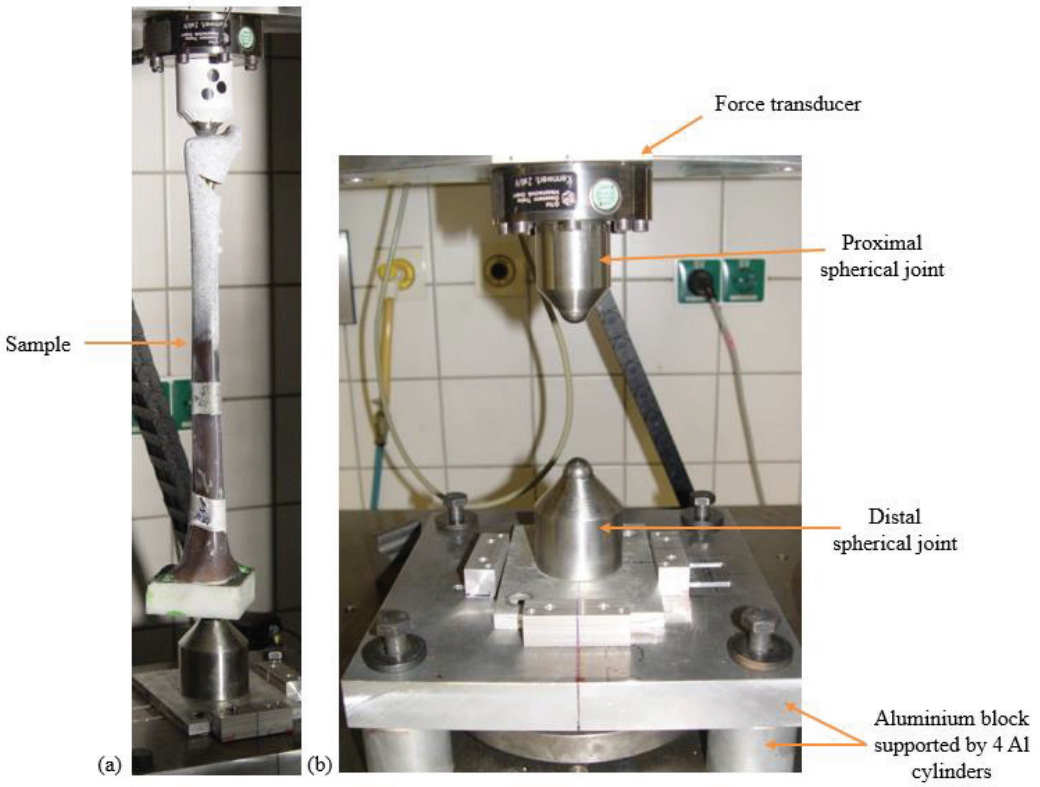

Figure 15: An improved setup for compression testing with a double ball-joint setup with (a) and without a sample (b).

The spherical joints are aligned and compressive forces are still applied in the theoretic mechanical axis which is located at 40% lateral of the medial condyle (Figure 13). Three opaque markers were fixed to the superior clamp (visible in Figure 15a) to record sample displacement using the cameras.

2.4. Sample preparation

Due to the uneven proximal and articular surfaces of the tibia, a widely used technique is to embed the surfaces in an artificial resin (PU or PMMA), improving the fit of the test sample in the testing machine. This is of particular interest for testing on anatomical specimens presenting no flat surface to which load can be applied.

At the biomechanics laboratory of the UMC, PMMA is the resin used for embedding the samples (Hansen et al., 2007; Kuhn et al., 2014a,b,c; Gruska et al., 2015, 2017). The PMMA is made by the experimenter following a 2:1 powder to liquid ratio as per the supplier recommendations; both the powder and the liquid were supplied by Suter-Kunststoffe AG (Fraubrunnen, Switzerland; www.swiss-composite.ch; powder: Beracryl powder D-28; liquid: Beracryl monomer).

Poly(methyl methacrylate) (also known as plexiglass or acrylic glass) is made from the polymerisation of methyl methacrylate and has the chemical formula $C_5H_8O_2$. Its popularity in orthopaedic testing comes from the fact that it offers a high impact resistance and can be easily produced and moulded to any desired form. It takes on the shape of its host form and does not have adhesive properties so can later be removed from the sample.

2.5. Outcome measures

In all test samples, the stiffness construct was calculated at 100 N, 300N and 600 N for loads up to 700 N. For tests where only 350 N compression was applied, sample stiffness was calculated at 100 N and 300 N only. This was done using data from the force and displacement transducers of the testing machine. For torsional testing, stiffness at 6.5 Nm was calculated from the torque/angle transducers. DIC was also carried out to measure sample displacement for the assessment of the effect of loading position, and sample placement-replacement (compression testing only).

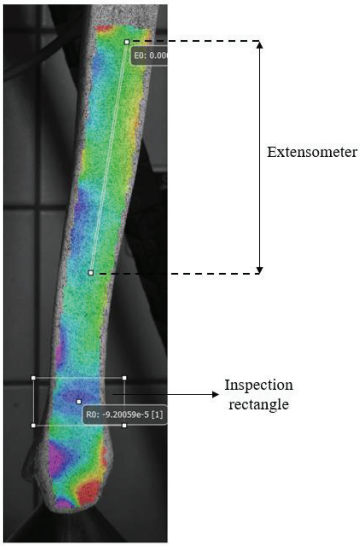

Figure 16: Extensometer and rectangle inspection tools used for measuring strain in the tibial diaphysis and metaphysis during loading position and placement-replacement testing.

The image data was analysed in Vic3D (version 8, Correlated Solutions, Inc, USA). Images from the last cycle of the load position and placement-replacement tests were identified and correlated. Inspection tools for measuring deformation along the tibial diaphysis and in the MWO zone (Figure 16) were employed and applied to the image corresponding to -690 N force application. The force-displacement acquired by the machine were resampled to match the image data (passing from 25 Hz to 10 Hz), in some cases this eliminated the points at which -700 N were applied.

Data Processing

An in-house script for Scilab (version 5.5.2) was written in order to calculate sample stiffness values from the machine data. Cycles were defined based on the known number of points per cycle - the testing machine was piloted through force application and therefore each cycle had a constant number of data points during acquisition (n = 500). Each cycle was set to start at zero and a 2nd order polynomial trend-line was applied to the raw force-displacement data; the stiffness of each cycle was calculated by taking the derivative of the displacement with respect to its force. The in-house code was also used to synchronise the image and machine data, and identify the image corresponding to -690 N; this level of force was chosen to ensure that an image could be identified.

Outlying stiffness values greater than two standard deviations from the mean were excluded from further analyses. Convergence of the stiffness values over the test cycles was fitted using the logarithmic displacement values.

2.6. Effect of boundary conditions

2.6.1. PMMA thickness

To assess the effect of the PMMA on sample stiffness, two square blocks of PMMA (proximal block: 88 x 88 x 20 mm; distal block: 88 x 88 x 10) were created. This was set to imitate the approximate thickness of the PMMA used to embed the proximal and distal end of a Sawbones sample, as per previous studies (see Kuhn et al., 2014a,b,c). No hole was drilled into the blocks; loading was directly applied onto the flat surface. Firstly, one single block was tested (Figure 17a), followed by two blocks to simulate an increase in total PMMA thickness (Figure 17b). Compression tests of 350 N over 40 cycles at a loading frequency of 0.05 Hz were carried out.

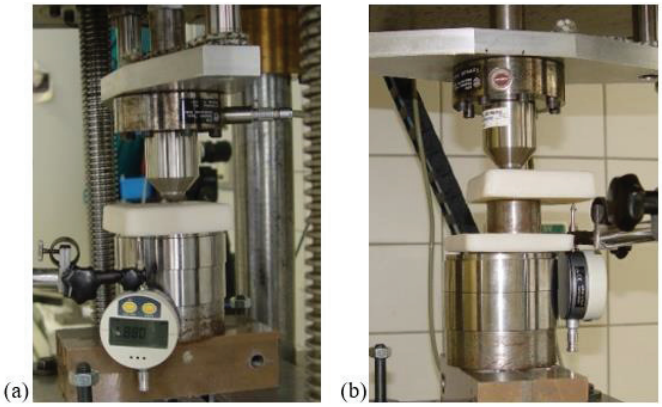

Figure 17: Stiffness testing for one PMMA block (a) and two PMMA blocks (b).

Force-displacement curves and stiffness per cycle convergence curves are presented in Figure 17. The first cycle of the force-displacement curves shows a curve of moderate steepness after which the rest of the cycles all seem to demonstrate a similar gradient (Figure 18). This is reinforced by stiffness per cycle data where a gradual increase in stiffness is observed between cycles 1-10. From cycle 20 onwards, the stiffness stabilises to 95% of the maximal observed stiffness.

Results and discussion

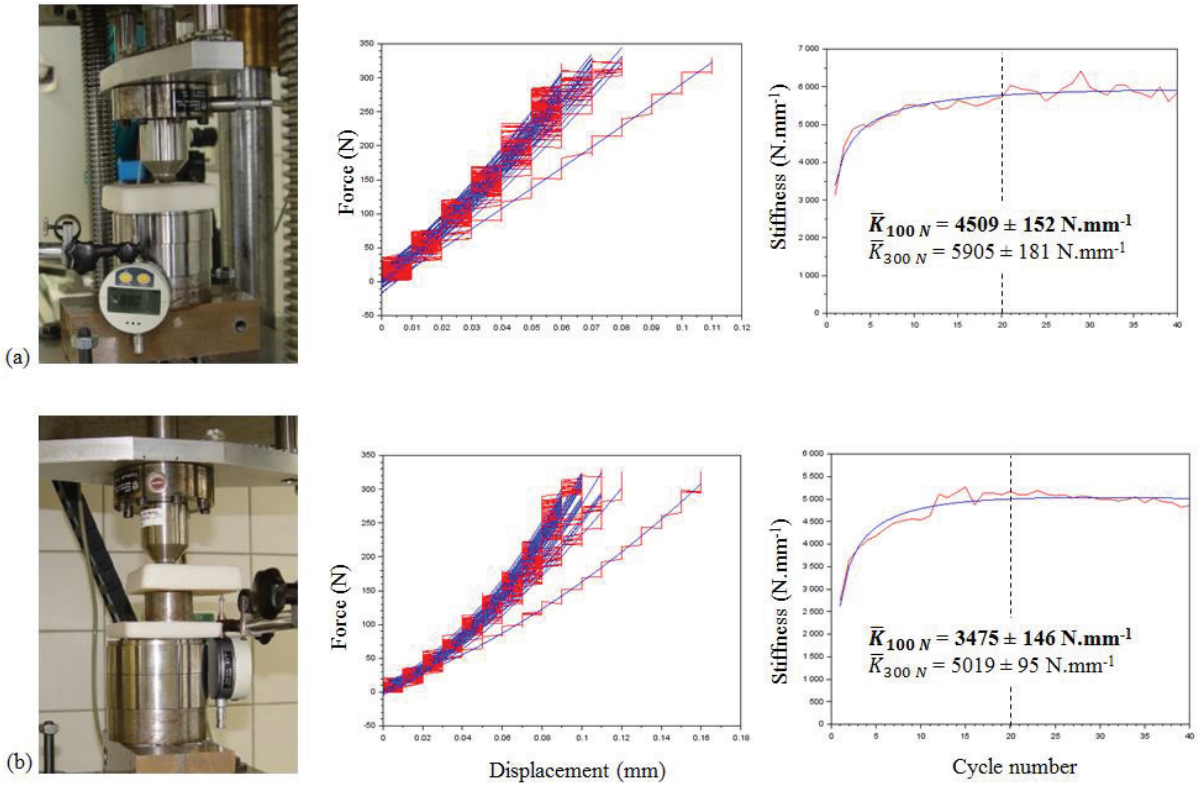

Figure 18: PMMA thickness results from one block (a) and two blocks of PMMA (b). The figure illustrates the force displacement curves for each cycle (middle) and the calculated stiffness for each cycle (right) with the raw stiffness in red and the interpolated stiffness curve in blue. Stiffness curves relate to 100 N force.

The specimen, the PMMA and the machine were considered as linear elastic springs in series (Symon, 1971) to calculate the stiffness (K) of each component. The test with one block of PMMA was used to calculate the resin stiffness. $K_{machine}$ corresponds to the machine stiffness, K_{setup} relates to the setup stiffness with the sample and K_{PMMA} is the calculated resin stiffness.

$$\frac{1}{K_{setup} = 3475} = \frac{1}{K_{machine} = 13041} + \frac{1}{K_{PMMA}} \leftrightarrow K_{PMMA} = \left(\frac{1}{3475} - \frac{1}{13041}\right)^{-1} = 4733\ N.mm^{-1}$$

Equation 1

$$\frac{1}{K_{total} = 2277} = \frac{1}{K_{tibia}} + \frac{1}{K_{setup} = 3475} \leftrightarrow K_{tibia} = \left(\frac{1}{2277} - \frac{1}{3475}\right)^{-1} = 6604\ N.mm^{-1}$$

Equation 2

Where K_{tibia} is the calculated sample stiffness for a Sawbones® tibia, K_{total} is the total calculated stiffness for the setup and sample, and K_{setup} is the same setup stiffness as described for Equation 1.

Equation 1 calculates the PMMA stiffness as being 4733 $N.mm^{-1}$; using this value, the stiffness of a Sawbones tibia is then calculated to be at 6604 $N.mm^{-1}$ (Equation 2). Ideally, the PMMA should have a stiffness value ratio to the composite tibia of at least 5:1; in this case, the ratio is 1:1.2.

Tests on the PMMA have shown that this material has a lower stiffness construct than a medium sized Sawbones® tibia meaning that during compression testing a large part of the strain is absorbed by the PMMA before being transferred to the composite bone sample. **Increasing the thickness of the PMMA prolongs the force transfer and reduces the overall stiffness.**

The use of PMMA and the control of its use are therefore questionable in orthopaedic research and may explain the disparity between results from different authors (as suggested by MacLeod et al., 2018). An average of 20 pre-cycles were required before stiffness curve convergence was reached; in light of these results, 30 cycles and a decrease in PMMA thickness will be performed in future testing.

2.6.2. PMMA composition

The influence of the PMMA composition on its stiffness construct by changing its powder to liquid ratio was measured by creating two cuboids of PMMA (2.6 x 2.6 x 12.8 mm). The first cuboid was created using the manufacture guidelines with a ratio of 2:1 powder to liquid, and the second one with a 2.5:1 ratio. The cuboids were tested by applying a force of 700 N at 0.05 Hz over 30 cycles, across the entire surface of the block (Figure 18), the stiffness of each block was analysed.

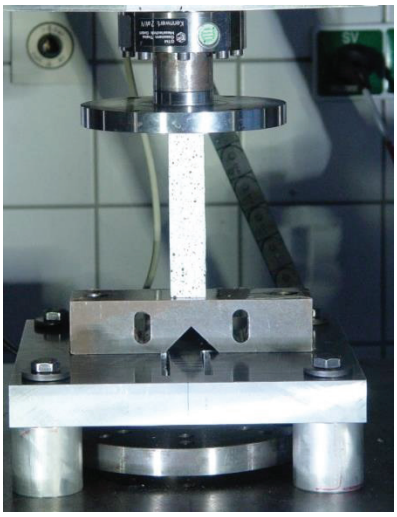

Figure 19: Test setup for the PMMA composition tests.

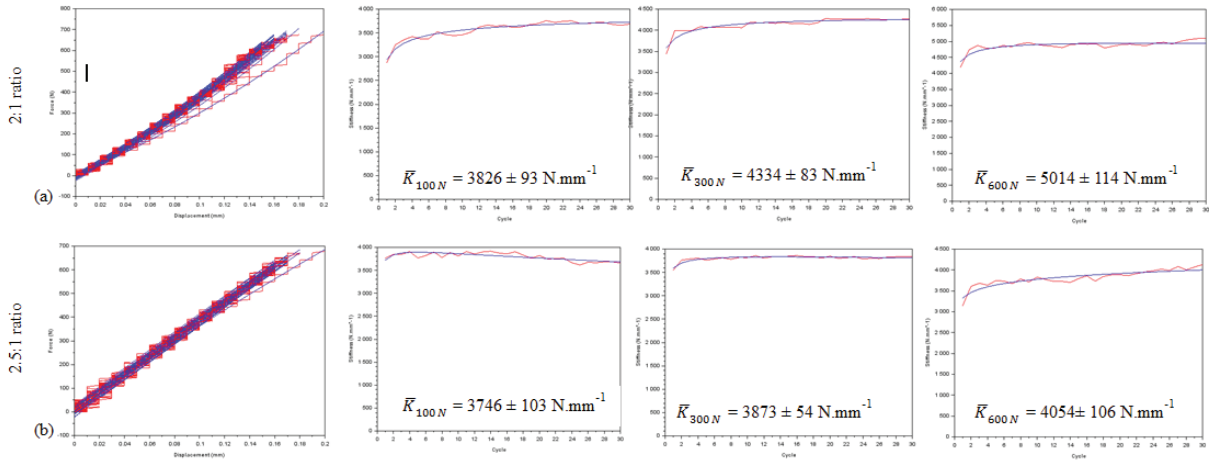

Figure 20: (left to right) Force-displacement curves for all cycles, 100 N stiffness curves per cycle at 100 N, 300 N, and 600 N compression; for the 2:1 ratio cuboid (a) and the 2.5:1 ratio cuboid (b). Ratio = powder:liquid in PMMA creation. Red lines = raw stiffness, blue lines = interpolated stiffness.

Although not large, there is nonetheless a disparity between the two samples (Figure 20). At 100 N of compression, there is a small difference of 80 N.mm^{-1} between the two samples, with the 2:1 ratio sample being higher; however, at 300 N the difference becomes more apparent and further data analysis goes on to show that this difference becomes greater with higher compressive loads. The 2:1 ratio PMMA demonstrates a higher stiffness at increasing compressive loads (3826 N.mm^{-1} at 100 N vs 5014 N.mm^{-1} at 300 N); whereas the 2.5:1 ratio increases by just ~300 N.mm^{-1} in comparison and therefore being more susceptible to deformation at greater loads.

Changing the composition of the PMMA was originally thought to increase its stiffness by increasing the powder to liquid ratio. **The application of higher loads results in lower stiffness for the 2.5:1 ratio**; furthermore, we noted that changing increasing the quantity of powder made the mixture difficult to work with. The conclusion was made that the composition of PMMA need not be altered.

2.6.3. Loading contact

The aim of the loading contact tests was to assess the influence of the contact surface conditions on the recorded stiffness. Load was applied via a spherical jig (Ø20 mm) to the flat superior surface (point contact) of the PMMA cuboid made from a 2:1 powder to liquid ratio (manufacturer guidelines); while the inferior surface was placed on a steel block covering the entire surface. Next, the same sample was re-tested but with an 8 mm hole was drilled into the superior surface and the spherical jig applied the load here (line contact; Figure 21). Loads of 700 N were applied to each sample at 0.05 Hz, over 30 cycles.

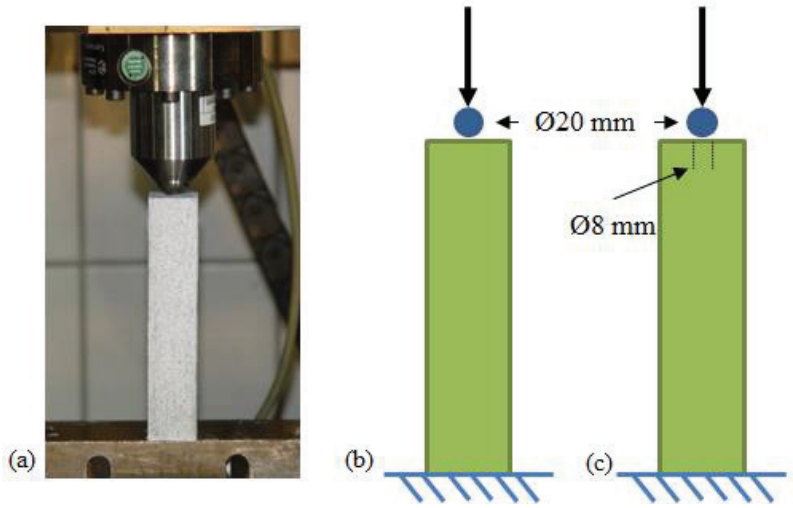

Figure 21: Loading contact setup (a) on a flat surface of PMMA (point of contact; b), a drilled surface (line of contact; c).

Results and discussion

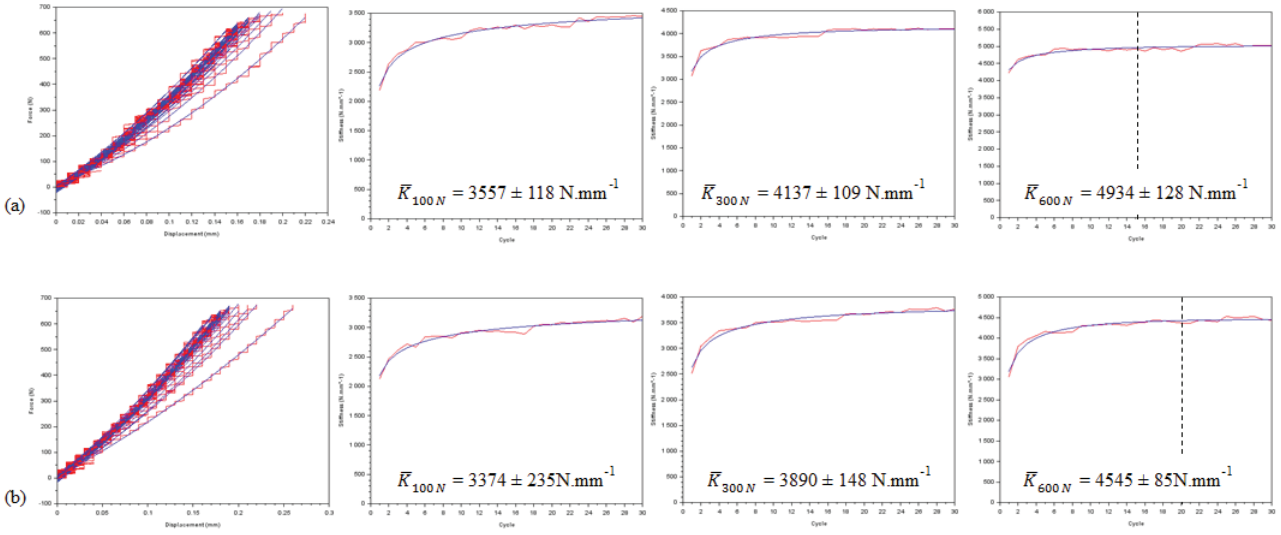

Figure 22: Force-displacement curves for all cycles, 100 N stiffness curves per cycle at 100 N, 300 N, and 600 N compression; for loading on a flat surface (a) and on the border of a drilled hole (b). Red lines = raw stiffness, blue lines = interpolated stiffness.

Compressive loading on a flat surface (Figure 22) displays greater values across all calculated stiffness constructs, the difference becoming more apparent with increasing loads. The first five cycles appear to be the most influential in lowering the global stiffness and increasing the range of stiffness values. Results from stiffness at 100 N and 300 N tend towards a continuous, albeit minor, increase in stiffness. At 600 N on the other hand, a plateau is reached after ~15 cycles for load applied on a flat surface and ~20 cycles for load applied to a drilled surface.

Previous experimenters at the UMC have consistently drilled a hole in the superior PMMA surface to support a metal sphere and increase the stability of the sample in the testing machine. Applying the force to a drilled hole resulted in lower stiffness. It is not certain that there was a difference in area over which the force was applied between the two loading situations; however, it is possible that for the load application to the drilled hole, the force was concentrated on the edges of the hole which consequently were greatly deformed.

Despite the observed differences in stiffness, the choice was made to keep the drilled hole in the PMMA for safety reasons (to avoid the sample rapidly exiting the testing machine when subjected to high loads) and also to ensure the repeatability of the loading point.

2.6.4. Loading position

These tests sought to measure the effect of changing the position of the load application point on calculated stiffness. One composite tibia was proximally embedded in PMMA and subjected to mechanical compression at 350 N and a loading frequency of 0.05 Hz over 40 cycles. The loading point position was tested by drilling five holes in the top of the PMMA (Figure 23a).

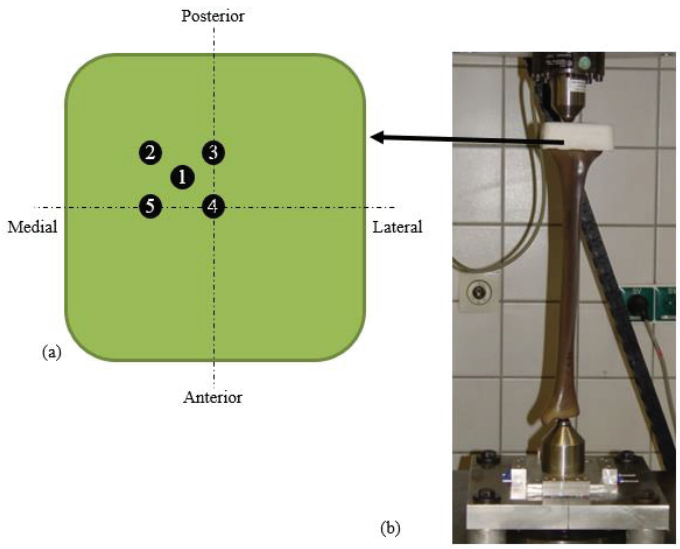

Figure 23: Five holes drilled in the proximal surface of the PMMA embedded on the proximal tibia (a) and the test setup (b).

The hole drilled at point 1 corresponds to the mean physiological loading point across the tibial plateau. The location of this point was found by identifying the centre of the PMMA block and tracing 10 mm medio-posterior from this centre. Point 4 is the centre of the PMMA block. All other points were drilled at 10 mm from point 1 and are 8 mm in diameter and 5 mm deep.

Results and discussion

Testing machine data

Loading position appears to have a higher influence on stiffness values with increasing loads. The difference between the highest (position 4) and lowest (position 3) stiffness is at 191 $N.mm^{-1}$ at 100 N, and at 300 $N.mm^{-1}$ (position 4 vs position 1) at 300 N and 600 N (Figure 24). Relatively high stiffness values are repeatedly present at positions 4 and 5, which correspond to the central and centre-medial axes, respectively. The lowest stiffness values are found in positions 1 and 3. Stiffness at position 1 decreases with increasing loads, while at position 3 it increases. Position 1 corresponds to the experimenter-defined physiological loading axis, position 3 relates to the centre-posterior axis. The highest stiffness constructs are observed at 600 N and belong to positions 4 and 5, at values of 1369 and 1379 $N.mm^{-1}$, respectively, while at position 1 this value is at 1019 $N.mm^{-1}$.

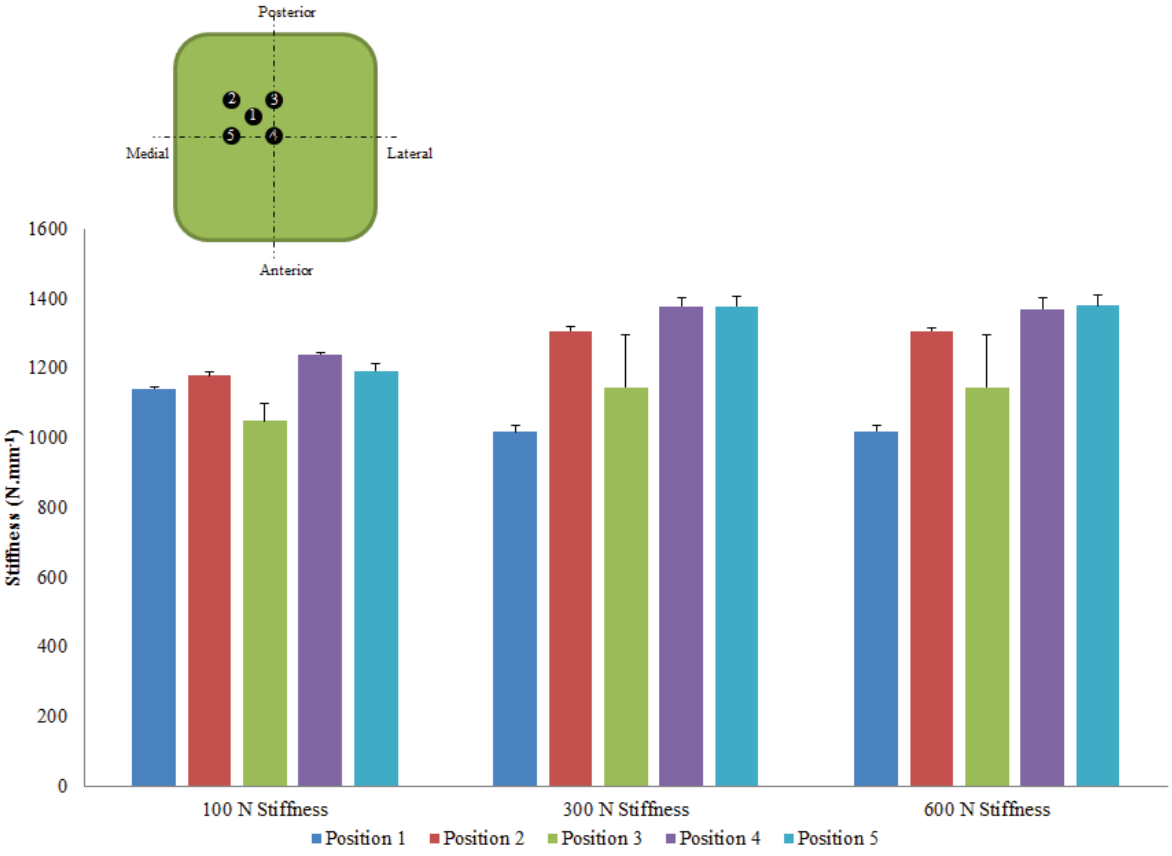

Figure 24: Stiffness constructs at 100 N, 300 N and 600 N compression for five difference proximal loading positions.

DIC data

Figure 25 illustrates the strain fields at 690 N compression for the difference loading point locations. The effect of altering the load application point on strain distribution was noticed in the tip of the medial malleolus where a mixture of tension and compression is witnessed. The spread of deformation in the tibial diaphysis generally remains negative (compression) towards the posterior part of the diaphysis, while the anterior portion is positive (tension). In all positions, the general strain in the diaphysis was measured as positive while in the metaphysis (the zone in which a MWO would take place), the strain is negative.

Position 1, relating to the physiological loading axis where the stiffness construct was calculated to be the lowest, sees relatively high tension in the diaphysis and a small amount of compression in the metaphysis. Position 2, being the most extra-axial loading point increases in negative strain towards the posterior section of the tibia, and position 3 (the most posterior loading point) increases the tension in the anterior diaphysis. The central axis is represented by position 4 and here the strain seems to be evenly distributed in the diaphysis but negative strain is concentrated in the medial malleolus. In the final loading position (in the central A-P axis but the furthest medial) an increase in overall negative strain can be observed.

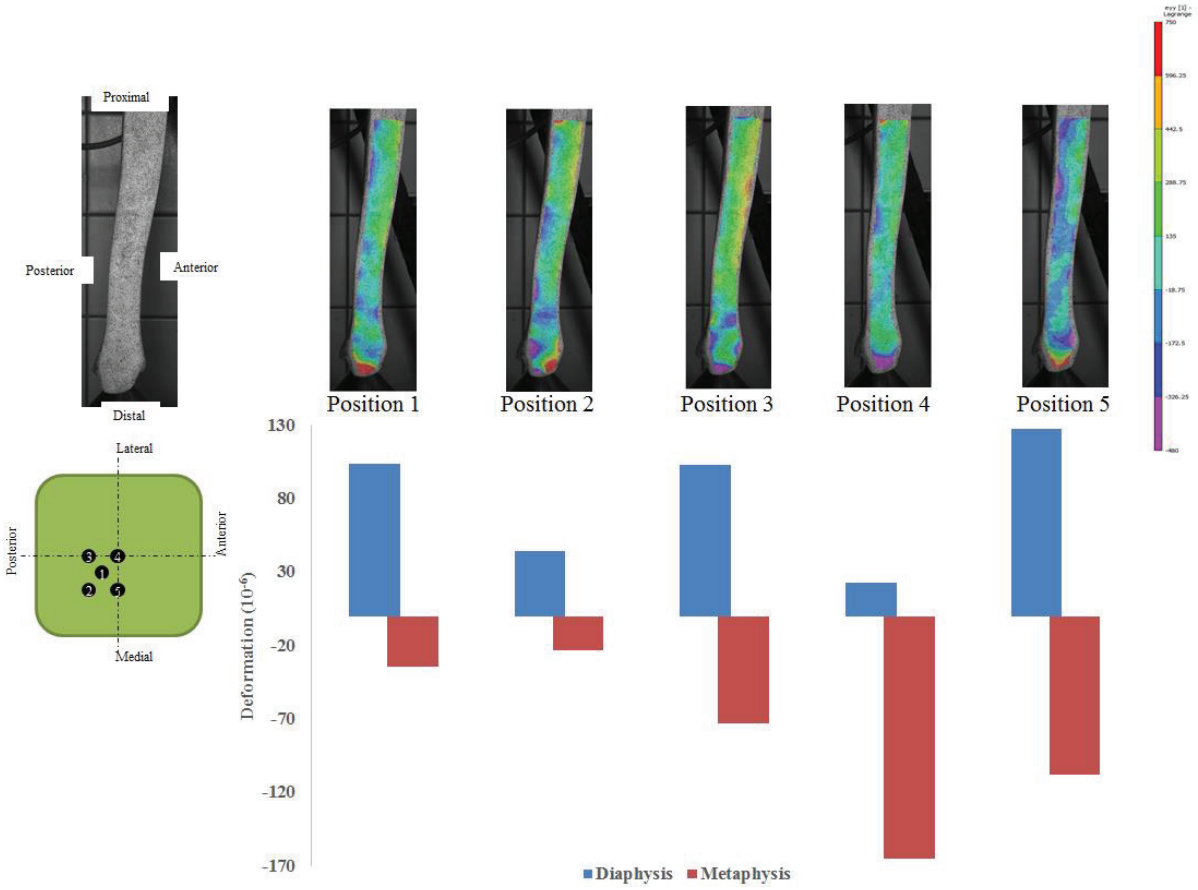

Figure 25: Measured deformation in the tibial diaphysis and metaphysis for five different loading positions and their respective strain distributions along the medial face of the distal tibia.

Strain values measured in this experiment remain relatively low, ranging from -165 to 127 (με) between the diaphysis and metaphysis. The concentration of negative strain in the metaphysis seems logical as this is the smallest section of the tibia and therefore the least stable. Metaphyseal strain ranged from -23 to -165 (με), an increase by 7-fold in Sawbones® - structures which are generally very mechanically stiff and one might therefore expect to see greater disparities in less stable constructs (such as a sample with a simulated fracture). One drawback of this series of test was that the sample was not embedded in an exact manner, it is therefore impossible to comment on whether position 4, for example, truly corresponds to the central axis.

The results from this preliminary study highlight the **disparities that can be present in stiffness construct when loading the sample in different axes**; this difference is more pronounced at higher loads. The importance of being able to reliably reproduce a loading axis point in all samples is emphasised to ensure that differences in calculated stiffness values do not come from factors other than the test sample.

2.6.5. Sample placement repeatability

One Sawbones® sample embedded in PMMA underwent compression testing of 700 N over 30 cycles at a loading frequency of 0.05 Hz. The sample was then removed from the testing machine for approximately two minutes and replaced in the same position with the same test boundary conditions applied. The load was applied medio-posterior in the calculated physiological loading axis (position 1 from Figure 23). The test setup was identical that demonstrated in Figure 25. The aim of this test was to assess the possible influence of removing the sample and replacing it in the test machine, without changing any other parameters.

Results and discussion

Results on stiffness are illustrated in Figure 26 and Figure 27 and those of strain field are given in Figure 28. The general tendency of these results is a slight increase in stiffness between placement 1 and placement 5 (Figure 26) from 1094 to 1332 $N.mm^{-1}$ (stiffness measured at 100 N), with Placement 4 demonstrating the highest stiffness construct at 1341 $N.mm^{-1}$.

Between placements 4 and 5 there is minimal difference in calculated stiffness at all levels. Stiffness at 100 N increases by almost 100 $N.mm^{-1}$ between placements 1 to 4; while at 300 N, the only sharp increase is noticeable between placements 1 and 2 (1330 to 1436 $N.mm^{-1}$). At 600 N, construct stiffness for placement 1 (1629 $N.mm^{-1}$) is slightly lower than the other placements, and it is placement 2 which demonstrates the highest stiffness construct (1741 $N.mm^{-1}$). The convergence graphs displayed in (Figure 27) show that as placement repetition increases, the convergence of the stiffness plateau occurs at an earlier stage.

Testing machine data

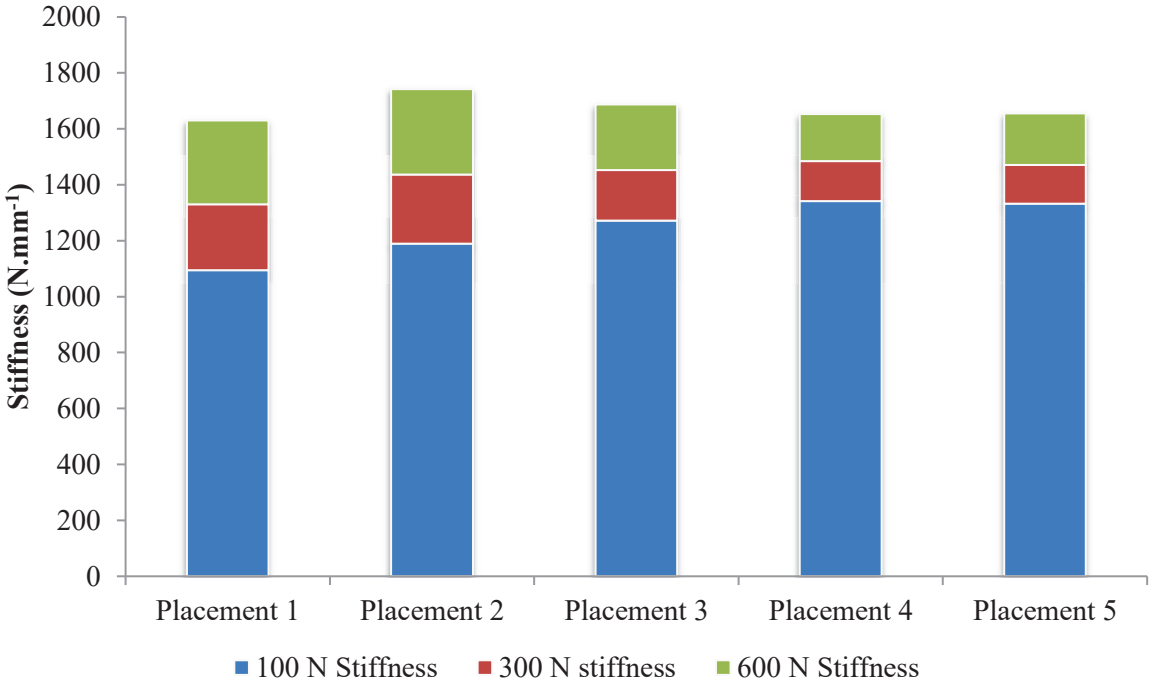

Figure 26: Stiffness constructs at 100 N, 300 N, and 600 N compression for one sample tested five times in the same test configuration after 30 cycles of compression testing at 700 N.

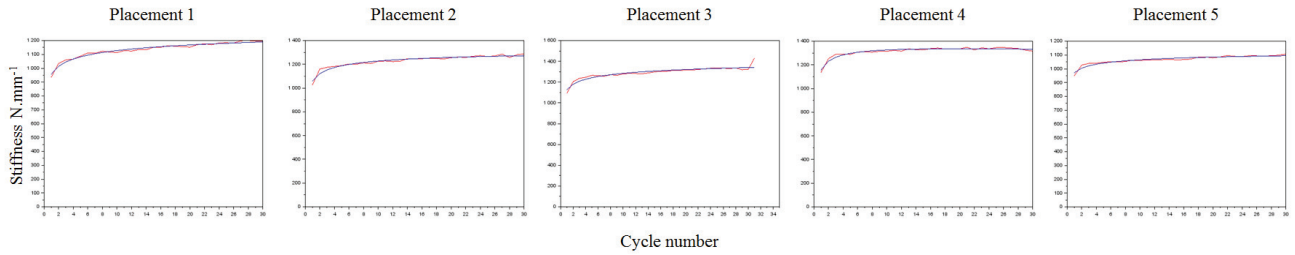

Figure 27: Stiffness convergence graphs for placements 1-5. The red line corresponds to raw data; the blue line is the interpolated stiffness at each cycle.

DIC data

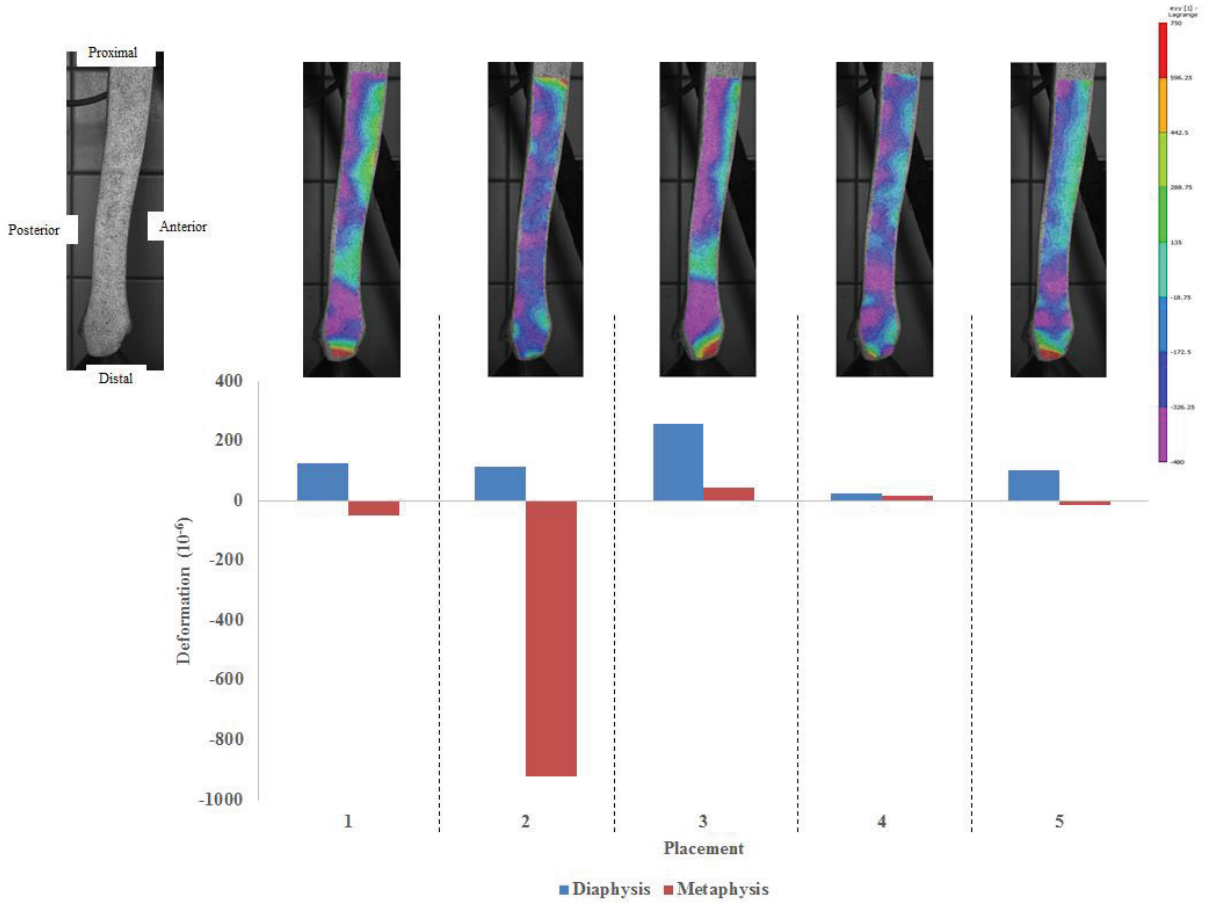

Figure 28: Measured deformation at 690 N compression in the tibial diaphysis and metaphysis for five placements of the sample in the same loading position, and the respective strain distributions along the medial face of the distal tibia.

All samples indicate a certain level of tensile vertical strain in the tip of the medial malleolus while the distal epiphysis and metaphysis demonstrate the highest levels of strain (Figure 28). Concentrated zones of negative strain are present in all samples except for Placement-2 where harmonious negative strain appears throughout. The posterior side of the tibia is subjected to high negative strain while the anterior side appears exhibit positive strain. This can be related to the loading point position lying medio-posterior and creating a slight bending moment.

Other than the high metaphyseal strain measured in placement 2 (ε_{yy} = -920), the strains recorded during testing remained relatively harmonious (Figure 26). None of the boundary conditions changed during the different tests and yet strain distribution seems to vary. Diaphyseal strain continues to be positive in all placements but ranges from 26 to 257 ($\mu\varepsilon$) while metaphyseal strain varies between positive and negative strain (ε_{yy} = +44 to -920). The increase in stiffness observed between placements 1 to 4 may be due to compression of the PMMA.

The decrease in cycles necessary before convergence implies that that a part of the total setup was compressed during cyclic loading and did not return to its original state before the start of the next test. Given its low stiffness constructs compared to the other test components; we assume that it is the

PMMA that is gradually compressed over the accumulation of cycles. The high negative strain observed in Placement 2 may be an anomaly due to incorrect positioning but this test was only performed on one sample and this therefore cannot be concluded.

In light of this, compression tests for 350 N and 700 N will be performed consecutively for each sample. However, it is evident that the effect of **removing and replacing the same sample in the testing machine under the same boundary conditions has little effect on strain distribution**.

3. Torsional testing configuration

The configuration for torsional testing involves the embedding of both the proximal and distal ends of the sample. The PMMA created are used to clamp the sample between two v-shaped steel blocks that are attached to the rotating disc of the testing machine (found in the inferior part). During testing, the disc rotates and consequently the v-shaped clamps turn the distal end of the sample while the proximal end remains fixed (Figure 29a).

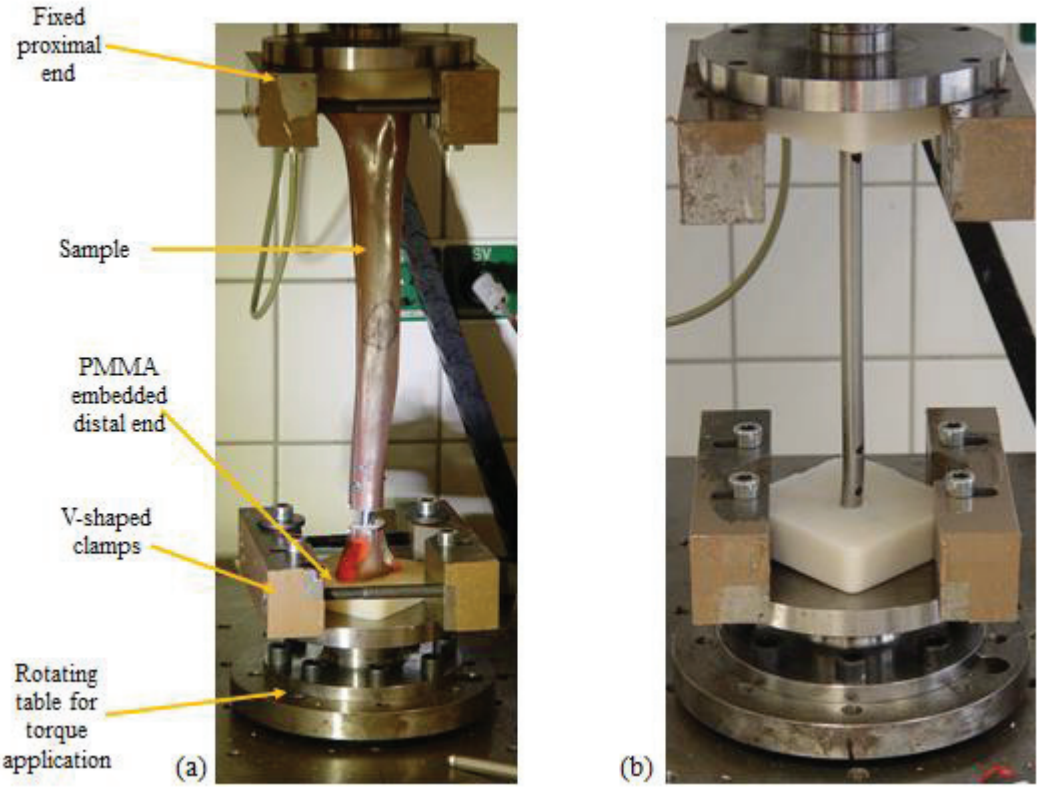

Figure 29: Existing torsion setup (a) and the test setup used to evaluate the influence of PMMA on torsional stiffness.

This setup for torsion testing (Figure 29a) was evaluated using a steel implant with both ends embedded in PMMA (proximal: 88 x 88 x 28 mm; distal: 88 x 88 x 22). The implant used was a T2 Stryker intramedullary nail measuring 210 mm in length and 12 mm in diameter Figure 29b). The nail was embedded in the PMMA with two screws through pre-drilled holes which served as extra

embedding attachments and to avoid the detachment of the nail from the PMMA. The sample was subjected to 20 loading cycles of ±8 Nm applied at 0.05 Hz. Moment and angle transducers collected torque and angle data, respectively.

A torque-angle graph was produced to observe the torsional stiffness of each cycle. A goodness-of-fit curve was generated by taking all points found at 6.5±1 Nm and calculating the barycentre of these points. The zero value in Figure 30b

Results and discussion

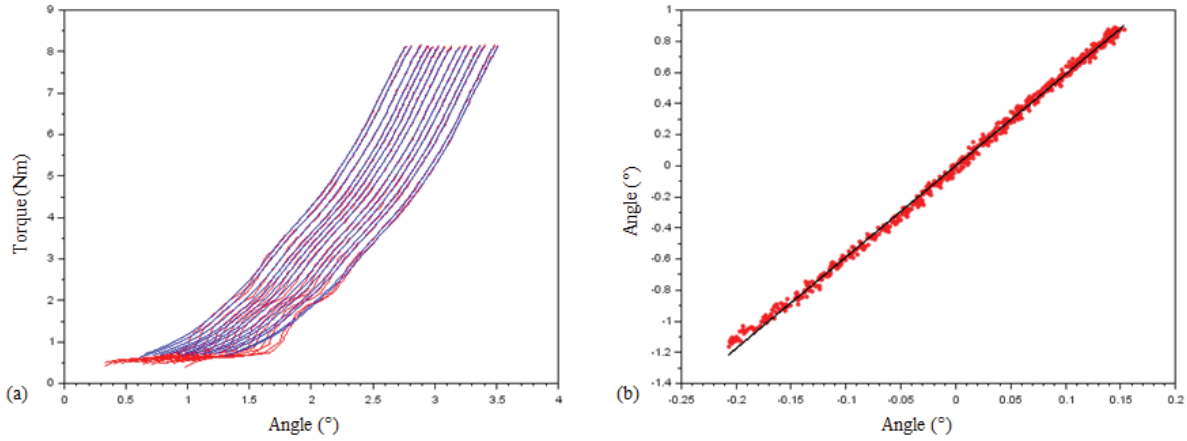

Figure 30: Torque-angle curves for all 20 cycles (a), points to fit for stiffness calculation compared to a linear trend-line (b).

The individual cycles displayed in Figure 30a appear homogenous throughout the 20 cycles with neither the first nor the last cycles seeming to have differing stiffness values. Likewise, the goodness of fit graph in Figure 28b shows the proximity of the points to the trend-line; only the first points diverge slightly from the start of the trend-line, but this is not apparent in the calculated stiffness values, or in quantitative data displayed in Figure 31.

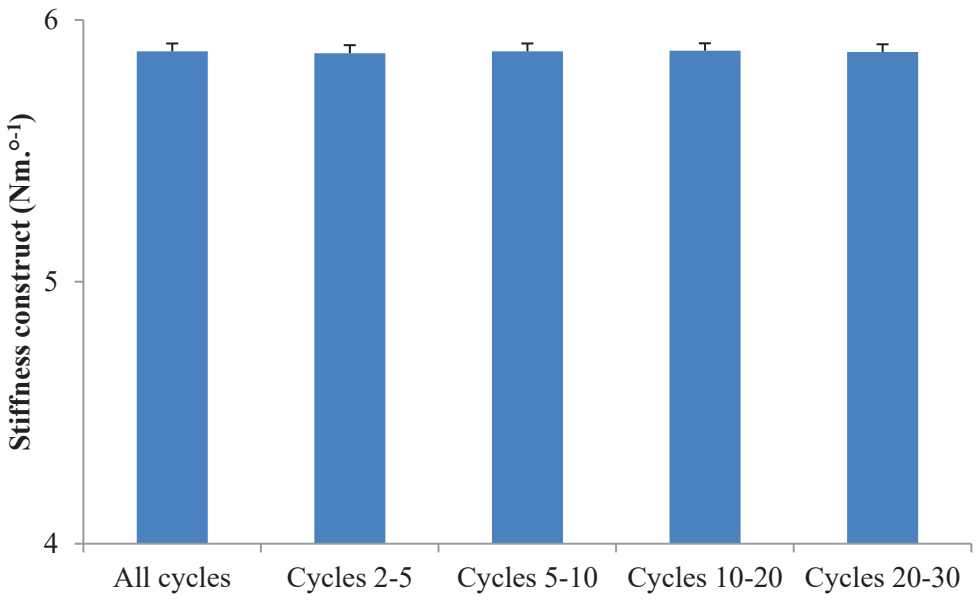

Figure 31: Mean torsional stiffness constructs calculated at 6.5 Nm.°$^{-1}$ over varying cycles.

The sample embedded in **PMMA undergoes little to no deformation during torsional testing** (Figure 29). Stiffness was calculated over all cycles, cycles 2-5, 5-10, 10-20, and 20-30 in order to assess the evolution of fluctuating stiffness constructs over the course of the test. The calculated stiffness values across all cycles remain constant at 5.87±0.004 Nm.°$^{-1}$ (range: 5.873 – 5.882), furthermore the calculated standard deviations for each batch of cycles range from 0.028 – 0.031.

Evaluation of the torsional test setup was neglected during the preliminary tests performed due to the nature of the setup and the materials available in the laboratory. Nonetheless, a small study on the torsional stiffness of PMMA was conducted and promising results were observed in that the resin is less influenced by torsional loads than compressive loads. Ideally, to correctly measure the stiffness of this machine test setup it would have been necessary to perform torsional tests with a block of material known to have high torsional resistance, such as steel or iron, as well as regulating the tightening of the clamps using a torque key. PMMA stiffness should also have been measured using a similar method, by creating a block of PMMA having a 1:5 minimum width to height ratio, and subjecting this sample to a ±8 Nm torsional test.

4. Template for PMMA embedding

Taking into account the multiple factors related to the sample's loading and boundary conditions being susceptible to influence the calculated stiffness value, a template was developed to ensure the potting of samples in PMMA through a reliable and repeatable method (Figure 32).

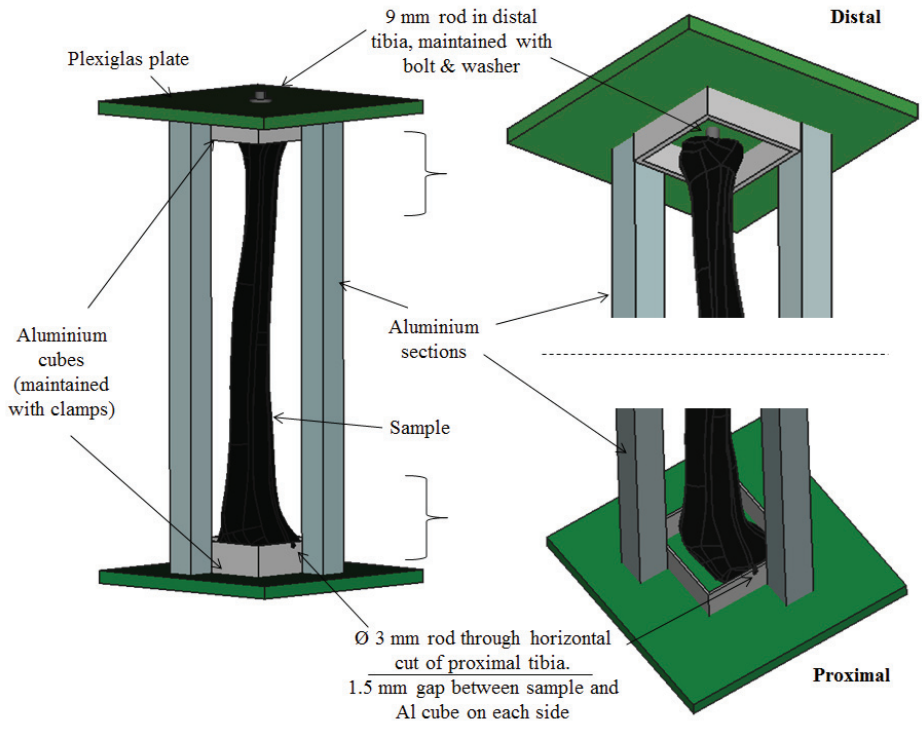

Figure 32: Template designed to ensure a reproducible method for sample embedding.

The template designed to provide a repeatable method for PMMA embedding was made such that it was possible to take it apart and reconstruct it, allowing for facilitated transport. The composite bone was placed proximal-end-down in a hollow aluminium cube of 80 x 80 x 30 mm. A 3 mm metal rod horizontally spanning the proximal tibia through a pre-defined hollow cylinder, present in all samples for manufacturing reasons, maintained its position. Similarly, the distal end was positioned using the 9 mm cavity in place from manufacturing: a 9 mm rod was held in position with the use of a bolt and washer on the superior Plexiglas plate. An aluminium cube was also placed around the distal end of the sample and held in place with clamps.

The PMMA liquid solution was poured into the proximal aluminium cube and left to set for 20 minutes. The device is then turned upside-down and the clamps are removed. The area around the medial malleolus was covered with play-dough to prevent PMMA contact. A distal mould is then created; one detachable distal mould for all samples was made (Figure 31b). The sample was covered in Vaseline and sprayed with silcone prior to PMMA embedding to ensure its easy removal from the cast. This mould was used during torsional testing in order to fix the distal end of the sample in the machine leaving the medial malleolus free for DIC analysis. During previous testing at UMC, the distal end of the sample was always embedded in PMMA and this part was tightened into the machine clamps. The advantage of creating a detachable distal PMMA block was so to leave the medial malleolus available for DIC.

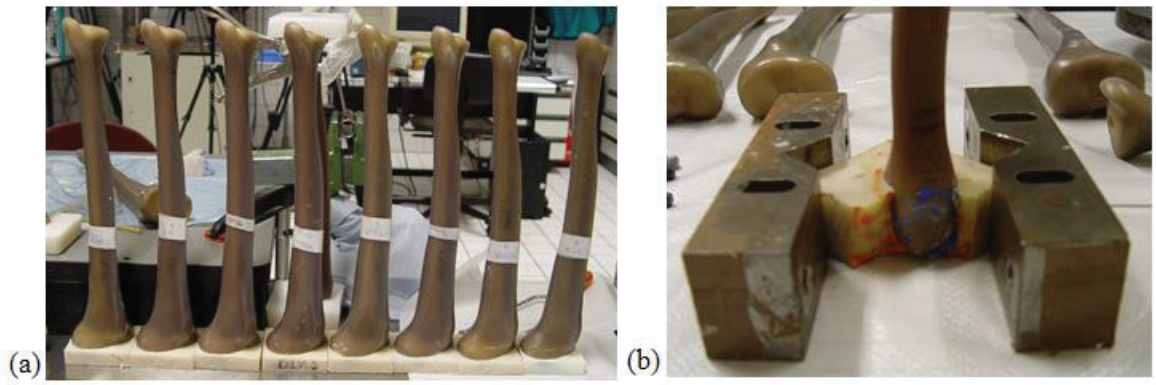

Figure 33: Embedded sample examples for the proximal (a) and distal (b) end of the composite tibiae.

5. Discussion

The tests carried out in this preliminary study were used to adapt the final test setup and protocol employed in Chapter 4, in order to reduce the parasitic influence of external factors on the collected displacement and calculated stiffness values. No statistical analyses were conducted due to small sample size. Throughout all tests, the first ~5 cycles tended to be very variable and can explain a large percentage of the standard deviations cited in the results; therefore the data processing of future testing for stiffness calculation will omit the first five cycles from analyses.

One further test was carried out with the use of steel flange sleeves (from here on referred to as 'inserts') inserted into the superior surface of the PMMA and the distal articular surface of the Sawbones® sample. The aim of this supplementary test was to test whether the collar around the insert (widened by the use of a washer) would help to distribute the compressive forces more equally, therefore reducing the overall deformation of the PMMA. Five different configurations with and without inserts were performed on two difference Sawbones® samples yet no differences in sample construct stiffness were observed with the use of inserts; this was therefore not integrated into the final protocol. Details on this experiment can be found in Appendix §2.

Results from this preliminary study highlight the importance of controlling boundary parameters so not to affect the main outcome measure of contact stiffness. The production of the embedding template in Figure 32 ensures a reproducible method for the potting of samples in PMMA. There are, however, still some elements open to error, such as the horizontal translation of the sample along the 3 mm metal rod spanning the tibial plateau. The freedom of movement along this axis can alter the position of the loading point with respect to the central axis of the tibia. Bearing this in mind, all samples will be subjected to a CT scan after embedding and before testing in order to later verify the loading position and the PMMA thickness.

The key elements from this work have been accepted for communication in the form of an academic poster at the 2018 World Congress of Biomechanics in Dublin (Ireland).

Influence of boundary conditions on the mechanical testing of orthopaedic devices

Julia Greenfield[1,2], Dorothea Mehler[2], Philipp Appelmann[2], Sebastian Kuhn[2], Pol Rommens[2], Karine Bruyère-Garnier[1], Yoann Lafon-Jalby[1]
[1]Claude Bernard University Lyon 1, IFSTTAR, LBMC UMR_T9406, F69622, Lyon, France
[2]Department of Orthopaedics and Traumatology, University Medical Centre, Mainz, Germany

Introduction

- The mechanical behaviour of bone with/without an implant is often evaluated through **total stiffness from compression testing** (e.g. tibial fracture reduction[1]).
- The **resin**[2] which is often used to position the sample in the testing machine, changes the **sample geometry** and **loading point**.
- **Aim**: to evaluate the influence of resin-based embeddings on the total stiffness of the experimental setup with application to tibial fracture reduction research

Figure 1. Initial compression testing setup

Method

- **Tested samples**: 1) composite tibia (Sawbones®) proximally embedded in PMMA (Fig 1) 2) two PMMA blocks of differing thickness and two types of contact surfaces (point and linear).
- **Loading**: extra-axial compression of 350 N using two spherical jigs[3] (0.05 Hz, 40 cycles), five positions for proximal tibial loading (Fig 2).
- **Outcome measures:** Set up stiffness at 100 N.
- **Hypothesis:** The specimen, the PMMA and the machine were considered as linear elastic springs to calculate the stiffness of each component

Figure 2. Five extra-axial loading positions

Results

- PMMA compressive stiffness plateaus (99%) after 20 cycles (ratio min/max: 1.5) (Fig 3)
  → **Need for high level of PMMA pre-cycling**
- Same magnitude for PMMA stiffness and tibial stiffness (ratio: 0.72 << ∞)
  → **Take PMMA into account in stiffness calculation**
- Proximal loading point influence (ratio min/max: 0.74) (Fig 4)
  → **Assure PMMA loading position repeatability**
- Point vs. linear contact (ratio : 1.09)
  → **Linear contact facilitates specimen positioning, but risk of PMMA matting**
- Sample placing repeatability: steady increase of stiffness (ratio: 1.22 for 5 placings)
  → **Avoid sample removal & replacement, risk of PMMA matting**
- **Conclusion: Consider and limit the use of PMMA in compressive mechanical testing for orthopaedic devices (Example stiffness ratio[1] between two implant types: 1.22).**

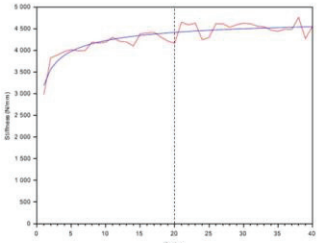

Figure 3. PMMA stiffness curve over 40 cycles. Stiffness of each cycle (red line), interpolation of stiffness results (blue line)

Figure 4. New experimental setup for compression testing

Acknowledgements

German Academic Exchange Service (DAAD): Research Grants - Short-Term Grants, 2017 (Grant No: 57314023)

References

[1] Kuhn et al. *Int Orthop* 2014, **38**(6):1255-1260; [2] Horn et al. *Injury Int J Care Injured* 2009, **40**:767-771; [3] Windolf et al. *BMC Musculoskelet Disord* 2010, **11**:95-101

Contact:
Yoann Lafon,
Lecturer
yoann.lafon@univ-lyon1.fr
www.ifsttar.lbmc.fr

Chapter 3: Biomechanical testing of a new implant option for supra-malleolar corrective osteotomies

1. Introduction

The standard treatment for supramallelor osteotomies is the use of a dynamic or a locking compression plate (Ettinger et al., 2018). All plates are minimally invasive and are fixed onto the medial or medio-anterior face of the the tibia. No other implant option is currently available; the other fixation method for the distal tibia is the Expert Tibia Nail (ETN) but, as mentioned in chapter 1, this is not a viable option as the nail does not cover the most distal 30 mm of the tibia and would result in a screw being placed in the osteotomy gap.

The development of the Distal Tibia Nail (DTN) has thus far only been considered for distal tibia fractures (Kuhn et al., 2014a,b). However its targeted design unique to the distal tibia is advantageous compared to the ETN with respect to the range of distal tibia covered.

The aim of this chapter is to investigate the possibility of using the DTN as an alternative treatment option to supramalleolar corrective osteotomy fixation, relative to the Medial Distal Tibia Plate (MDTP). A series of biomechanical tests and osteotomy/fracture configurations were simulated to test each implant. Test series have been separated into four different phases based on the simulated osteotomy/fracture in the sample. Low level compression corresponds to loads of 350 N, and high-level of 700 N; low-level torsion signifies ±4 Nm, while high-level means ±8 Nm.

Protocol (Figure 34)

Phase 0: Low-level compression and torsion testing of Sawbones® samples without implant, nor fracture

Phase 1: Low and high -level compression and torsion testing of implanted Sawbones® samples (n=8 for DTN and MDTP) with a supramalleolar osteotomy; the lateral cortex is kept intact.

Phase 2: Low and high -level compression and torsion testing of implanted Sawbones® with supramalleolar osteotomy and a simulated fracture in the lateral cortex.

Phase 3: Low and high level compression testing, high level torsion testing of implanted Sawbones® with a simulated A3 fracture.

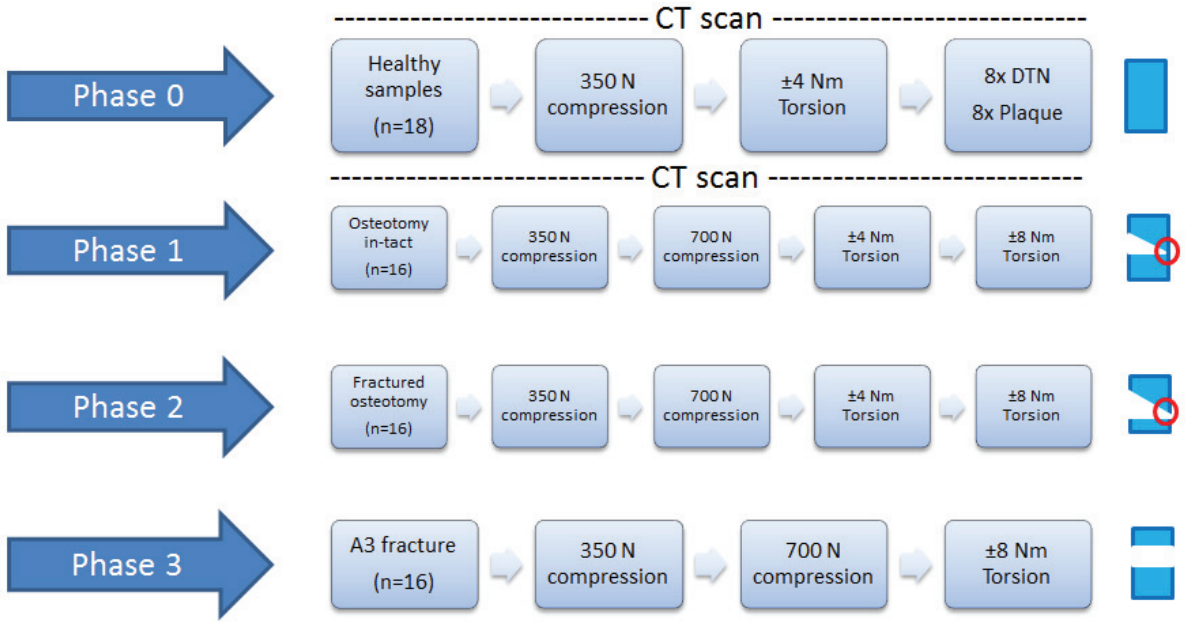

Figure 34: Schemas of the different testing phases and their respective boundary conditions (a), and a schema diagram of osteotomy/fracture phases 1-3.

2. Materials

2.1. Composite tibiae

Eighteen composite left medium-sized tibiae (article #3401, Sawbones®, Malmö, Sweden) were used for testing. Eight composite tibias were assigned to an implant, either the Distal Tibia Nail (DTN; Mizuho®, Japan) or the Medial Distal Tibial Plate (MDTP; Synthes®, Switzerland), leaving two samples as spares in case of failure during implant insertion or phase 0 of testing.

Four of the 18 samples had previously been embedded in PolyMethylMethcralate (PMMA) resin, standardly used for improving the samples' fit in the testing machine), and had also previously undergone compression testing of up to 700 N quasi-static compression (loading frequency: 0.05 Hz). These four samples were equally distributed to the DTN and MDTP sample groups in order to avoid bias. All other samples were randomly assigned to a sample group.

2.2. Sample Preparation

The samples were all embedded in 80x80x28 mm (width x length x height) PMMA cubes leaving minimal PMMA thickness above the intercondylar eminence. A 6 mm hole of approximately 3 mm depth was formed in the PMMA embedding for proximal loading application; this was then increased to 8 mm diameter using a manual drill. All samples were embedded in the same position using the custom-made template described in chapter 2.

A random speckle pattern was applied to the distal portion of all samples using white clown face-paint and black matt spray paint, both of which were applied manually; this was used for digital image correlation.

Following observations from preliminary testing, the testing machine and air pressure were both switched on at least 30 minutes before testing began and three compression tests of 350 N at 0.1 Hz over 30 cycles were run through using a test sample before sample testing started so to "warm-up" the machine for the compression tests. Torsional "warm-ups" were carried out with a test sample being put through two ±4 Nm torsion tests at 0.1 Hz. The machine acquisition frequency for all transducers was set at 25 Hz. Black markers were placed on the testing machine to track linear and angular displacement during the compression and torsion tests, respectively. There were placed on the superior spherical jig of compression testing (Figure 35a), and onto a custom made plate attached to the inferior clamps for torsional testing (Figure 35b).

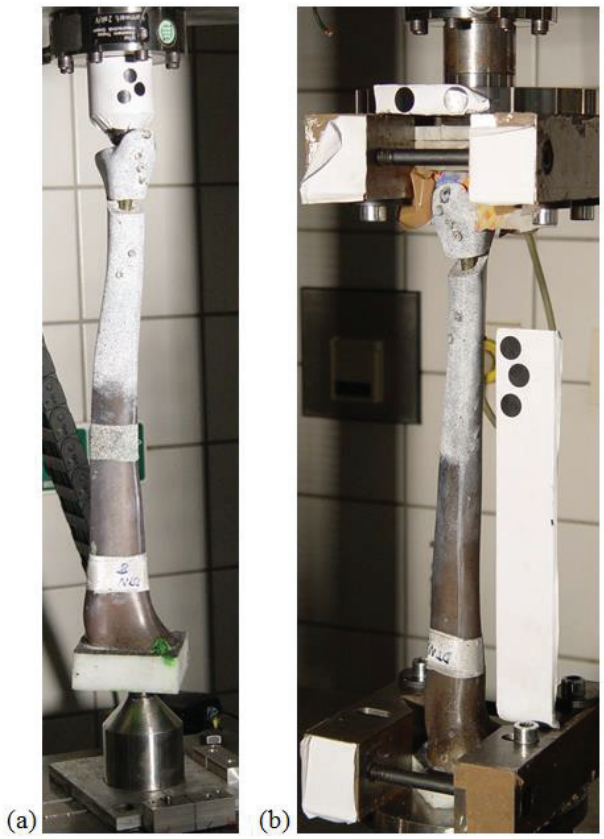

Figure 35: Marker placing on the machine clamps for tracking during compression (a) and torsional (b) testing.

The samples were placed in the testing machine with the medial side facing the cameras. The test setup was identical that described in chapter 2.

2.3. Implantation

Distal tibia nail

For DTN insertion, the surgical procedure was the same as that used in previous studies (Kuhn et al., 2014a,b,c). A Kirschner wire (K-wire) is used to plan the insertion angle in the medial malleolus (MM). The K-wire should lie in a central position between the anterior and posterior sides of the MM and should be inserted parallel to the superior medial cortex of the MM. The K-wire's position is verified using fluoroscopy (Figure 36).

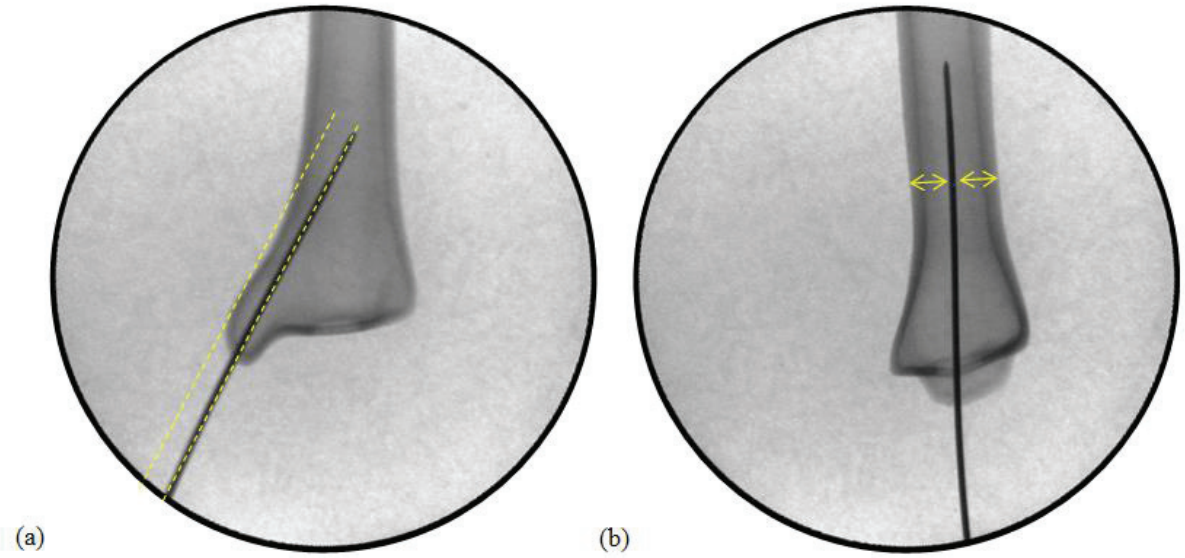

Figure 36: Fluoroscopy images of the K-wire insertion for guiding the cannulated drill. The K-wire lies parallel to the superior medial cortex of the MM (a), and in a centre position when visualised from a lateral view (b).

A 8.5 mm cannulated drill is used to create an opening around the K-wire and following this, extra remaining is carried out up to a diameter of 9 mm. For samples receiving a DTN, the MM was opened and nail insertion verified before osteotomy simulation. This was to ensure that the DTN could later easily be inserted without fracturing the lateral cortex – a procedure that could well be replicated in living patients.

Osteotomy simulation took place (described later) and the DTN was attached to the insertion guide used for screw placement. The nail is completely inserted into the MM until just the lower tip of the nail is at the edge of the insertion site. 3.2 mm diameter holes are drilled for the insertion of five 4 mm screws. Two screws are inserted proximal to the osteotomy and three screws, in an angle-locking configuration are placed distal to the osteotomy gap.

The proximal screws are of a standard length of 32 mm and are always bi-cortically inserted. The length of the three distal screws is measured and an appropriate screw length is chosen to ensure that the screw tip does not exit the lateral side of the tibia as in reality this would damage the tibio-fibular joint and syndesmosis. The distal screws differ from the proximal screws as they contain two

thread types: a proximal thread with a thick screw body and little thread depth, and a distal thread in which the screw body is thinner increasing the thread depth. The advantage of a greater thread depth is to improve screw purchase in trabecular bone. Finally, the guide is detached from the DTN and an end-piece is inserted into the inferior end of the nail.

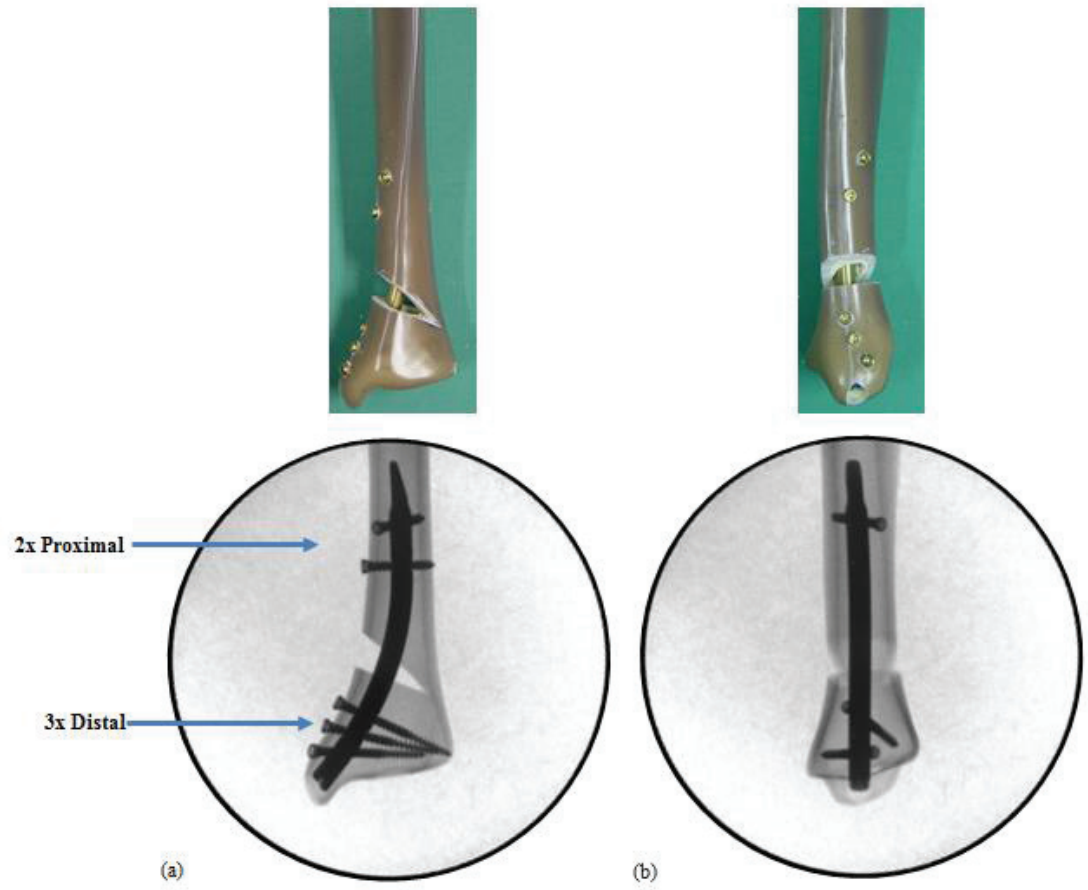

Figure 37: Photo and radio -graphs of the DTN with all screws inserted into a Sawbones® with a simulated MWO, in the sagittal (a) and frontal (b) plane.

Medial Distal Tibia Plate

The MDTP is manually held to the medial side of the sample and a first 2.8 mm hole for 3.5 mm diameter cortical screw insertion is drilled. The plate is aligned along the vertical axis of the sample and the first cortical screw is inserted to and tightened fix the plate to the sample. A second cortical screw is inserted distal to the osteotomy. A further five screws are inserted, two proximal to the osteotomy and three distal to the osteotomy. These five screws are locking screws and are tightened into tapped holes in the plate at a toque of 1.5 Nm.

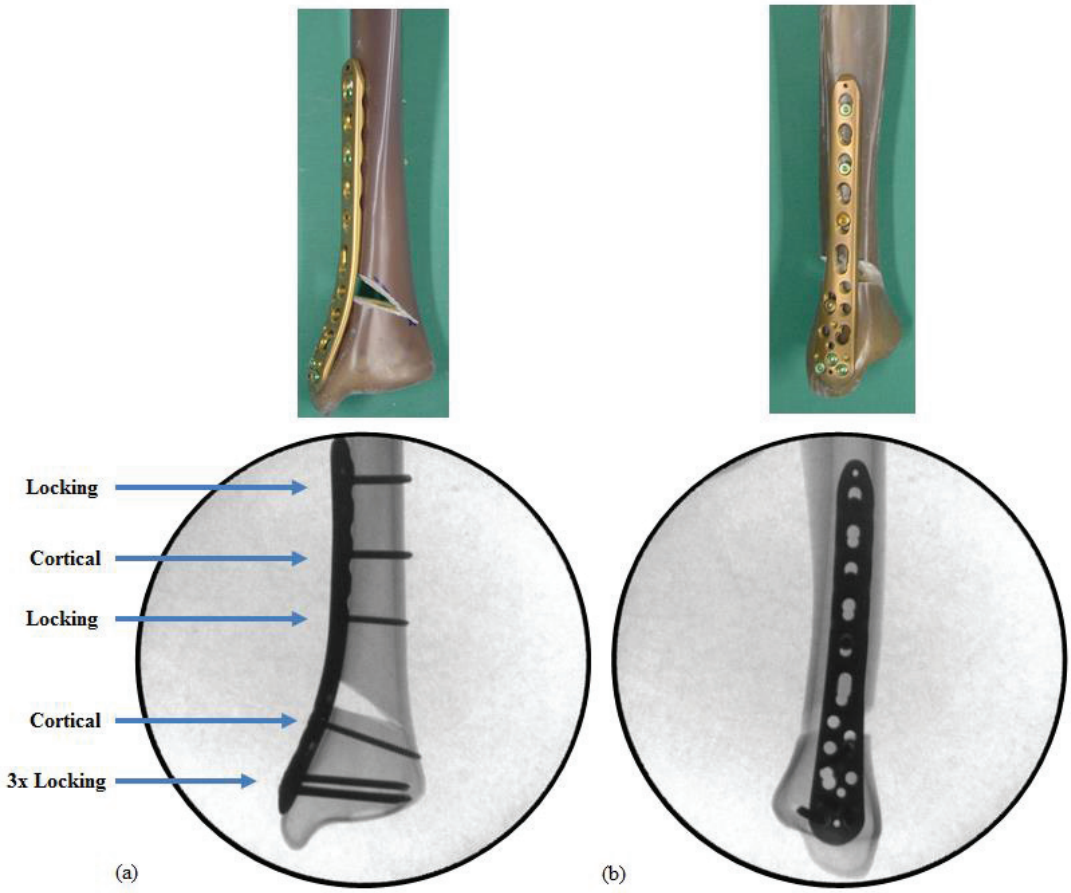

Figure 38: Radiographs of the MDTP with all screws inserted into a Sawbones® with a simulated MWO, in the sagittal (a) and frontal (b) plane.

The goal of the angle-stable locking screws in both implants is to prohibit post-operative screw loosening and, for the DTN rotation of the implant creating an unstable construct which allows for shear stress to be placed upon the bone fragments and can hinder the healing process.

2.4. Osteotomy simulation

A medial wedge osteotomy was simulated in all of the samples; this was performed by removing a wedge of material from the medial side of the bone. All osteotomies were planned to follow the measurement presented in Figure 39; the distal edge of the osteotomy situated at 35 mm from the distal articular surface and the proximal edge at 45 mm from this surface. The meeting point of the two cuts was planned to lie at 25 mm from the articular surface and 5 mm medial from the outer lateral cortex.

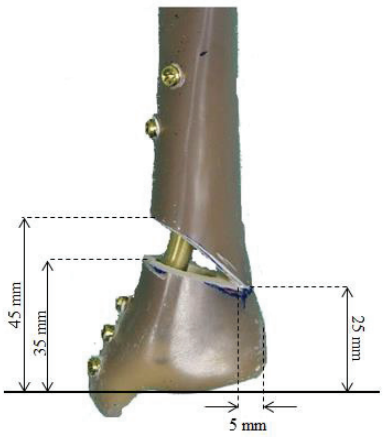

Figure 39: Planned measurements for the medial wedge osteotomy used in this study.

Osteotomies were manually implemented by a senior orthopaedic surgeon without the use of a template meaning that the osteotomies differed in angle and remaining lateral cortex area. The osteotomy simulation was carried out prior to implantation for the DTN samples and post-implantation for the MDTP samples.

3. Methods

3.1. Testing configurations

3.1.1. Compression

The samples were placed in the testing machine for two configurations: 1/ with the anterior side of the composite tibia facing the cameras so to observe the movement at the fracture gap, and 2/ with the medial side of the sample facing the cameras so to observe the implant and/or its screws (Figure 40). Tests of 350 N at 0.1 Hz over 30 cycles and 700 N at 0.05 Hz over 30 cycles were performed.

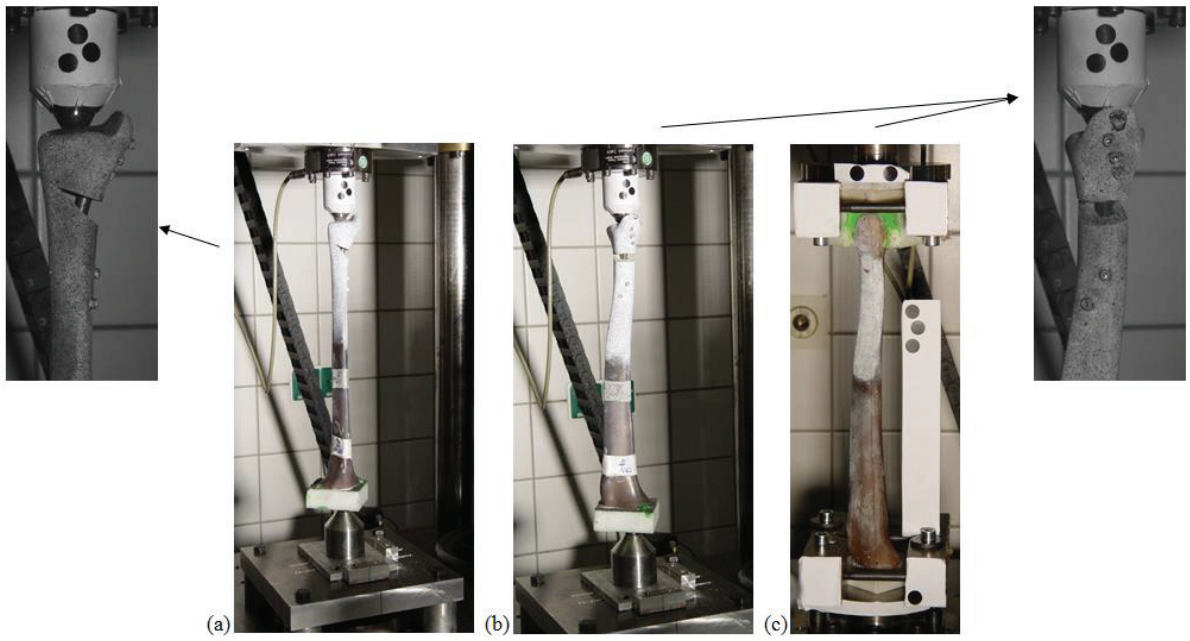

Figure 40: Testing configurations to visualise the lateral cortex of the osteotomy (a) and the implant (b) during compressive loading. Test configuration for torsional loading (c).

3.1.2. Torsion

Two levels of torsion were applied to the samples. First, bidirectional torsion of ±4 Nm at a loading frequency of 0.1 Hz was applied, followed by bidirectional torsion of ±8 Nm at a loading frequency of 0.05 Hz. All torsional tests were carried out for 30 cycles and a cyclic pre-load of 5-6 N was simultaneously applied to the sample at the same loading frequency as the torsional load being applied.

3.2. Data collection

Data were collected from the displacement transducer and the camera system that had a field of view including the superior clamps of the testing machine and the distal 50% of the sample.

At the start of the tests, the machine sends out a +5 V signal that acts as a trigger to begin data collection for both the connected computer and the cameras. Data were collected for the entire duration of the test.

Two identical cameras were used for all experimental procedures. A summary of the cameras properties can be found in Table 7. The JAI-GO cameras offer a high image quality at a sampling frequency adequate for the quasi-static tests carried out. Average pixel size for all recorded images was 0.07 mm². A summary of camera settings for all tests can be found in the appendix §3.

Table 7: Main specifications for the cameras used in this study.

Camera	Type	Sensor	Maximum resolution	Maximum sampling frequency (frames per second)
JAI-GO-5000-USB	Reflex	CMOS (1 inch)	2560 x 2048	62 (at maximum resolution) 75 (using binning)

Samples were tested in two configurations for compression testing: first the sample was placed in the testing machine with the anterior surface of the Sawbones® facing the cameras; this was to record deformation around the fracture gap and anterior portion of the lateral cortex (Figure 40a). Next the sample was rotated by 90deg to record its medial surface with the aim of analysing the effect of the compressive loads on the implant (Figure 40b). During torsional testing, only the medial side of the sample was recorded due to the nature of the detachable distal PMMA block.

As stated at the beginning of the chapter, testing was separated into four different phases. **Phase 0** included only the **Sawbones®** and their proximal PMMA embedding.

Phase 1 consisted of **a supramalleolar osteotomy** in which the **lateral cortex was preserved**. A thickness of 5 mm lateral cortex was aimed to remain constant between samples; however, the osteotomies were carried out without a template and therefore are of varying areas (Figure 41).

The **complete osteotomy cut** in **phase 2** of testing was done using a coping saw and following the distal edge of the osteotomy to traverse the lateral cortex. The thickness of the saw blade was 0.5 mm, theoretically leaving a gap between the proximal and distal fragments; however in many cases of Sawbones® instrumented with the locking plate, the tension of the screws on the plate forced the fragments into contact. This was less frequent in the DTN samples.

The simulated **A3 fracture** tested in **phase 3** of testing was carried out by sawing horizontally from the most medial part of the osteotomy's proximal edge to leave approximately a **10 mm gap** between the proximal and distal fragments.

All samples used in the scope of this thesis underwent two CT scans, the first of which involved only the Sawbones embedded in their proximal PMMA resin. The second scan took place after implant insertion and osteotomy simulation.

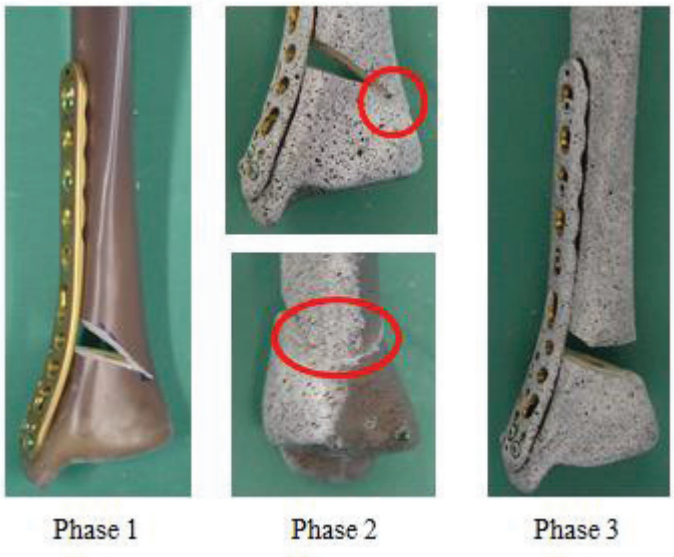

Figure 41: Visual differences between phases 1-3, the example is taken from a MDTP sample.

3.3. Data processing and statistics

Sample displacement and stiffness were defined as the chosen outcome measures in this study. This decision was based upon the literature, in which the majority of studies conducting mechanical testing report either stiffness or displacement values. Stiffness construct is used as an indicator of sample

stability, while displacement offers an insight into fracture healing potential. The outcome measures were calculated from the testing machine's force (/torque) and displacement (/angle) transducer data.

3.3.1. Stiffness data

An in-house code was written to process the data. Only cycles 6-28 were processed as the first 1-5 and last two cycles were often erroneous leading to altered means and high standard deviations. For torsion, only positive values were used for stiffness calculations; it was supposed that the positive and negative torsional stiffness constructs would be equal in all samples.

Data were first smoothed with a factor calculated by taking the number of data points through the entire test and dividing this by 15; as a result, a smoothing factor of ~1000 was applied to each sample. Each cycle was identified using the force or torque data, depending on the test performed, by locating the maximum values of the derivative of the force data.

Cycle start and end points were located (Figure 42) and any located points after 30 cycles were deleted. A cycle corresponds to one incremental load followed by incremental unloading. This was decided based on the trigger for the testing machine and the cameras sending out a punctual signal at the start of testing and that a total of 30 cycles had been pre-defined. Any cycles detected after 30 were therefore considered erroneous and linked to the random movement of the actuator to return to its neutral position at the end of testing. An example of one erroneous start and end point can be seen in the figure below, circled in black (Figure 42).

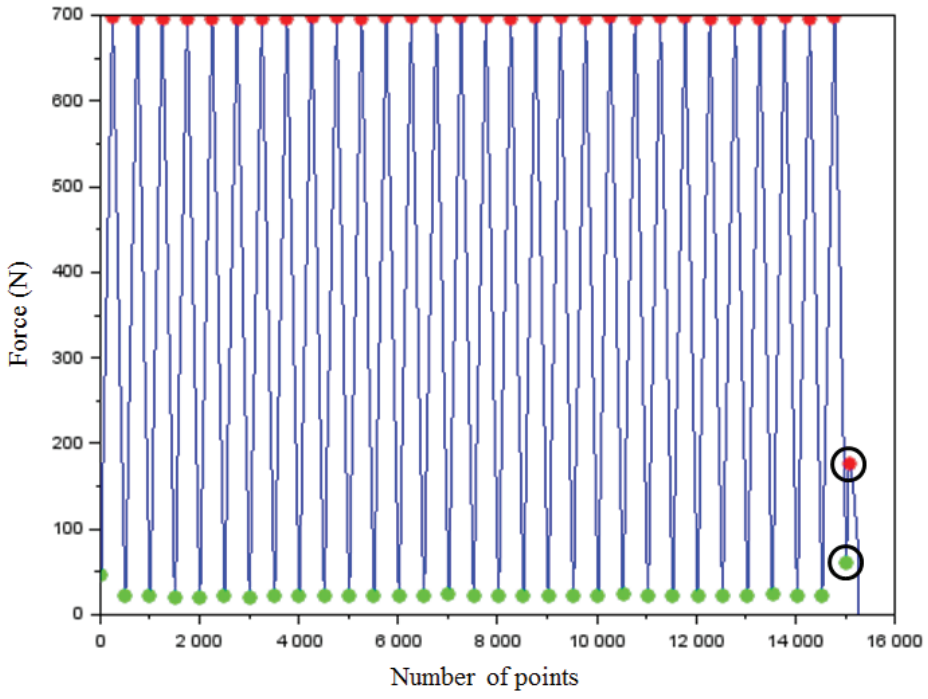

Figure 42: Plot of all points collected by the force transducer and used for cycle definition. Points in green correspond to the starting point of each cycle, in red the maximum force value points.

The force/torque and displacement/angle points in each cycle were then separately smoothed again with a factor of 20 and the points from each cycle used for stiffness calculations (Compression testing: points between 100N and 300 N; torsion testing: points between 5.5 Nm and 7.5 Nm) were plotted and fitted with a trend line calculated using the Theil-Sen estimator (Peng et al., 2008). For points corresponding to cycles: 5-28, 8-11; 11-16, 16-26, and 21-28; all points are displayed with error bars corresponding to ±2 standard deviations. In the results section, the cycle numbers take on their relative values based on the total number of cycles used for stiffness calculation (Table 8). The first four and last two cycles are not considered.

Table 8: Cycles used for stiffness calculations.

Protocol	Used for stiffness calculation
Total = 30 cycles	Total = 23 cycles
Cycles 1:4	Not considered
Cycles 5:8	Cycles 2:5
Cycles 8:12	Cycles 5:10
Cycles 12:22	Cycles 10:20
Cycles 22:28	Cycles 20:30
All cycles (robust) 1:30	Cycles 5:28

The partitioning of the cycles allowed for a closer analysis of the evolution of stiffness during the testing cycles; it also facilitated the identification of any errors or anomalies displayed through high standard deviations.

For comparison, the Theil-Sen estimator and the least squares method were used to calculate the stiffness across cycles 6-28, named “all cycles”. More information on the calculation of the Theil-Sen estimator can be found in the appendix (§3.1)

In cases where samples are analysed, the habitual curves exploited from the data are the force-displacement (or torque-angle) curves for the sample in question (Figure 43a) and the points used for

stiffness calculation around the line of best fit from the Theil-Sen estimator (Figure 43b). The graph in Figure 43b will hereafter be known as the goodness of fit curve. Points are plotted around an origin relating to the barycentre of the selected data points for both force (/torque) and displacement (/angle). The zero value for force corresponds to the chosen value at which stiffness should be calculated (200 N or 6.5 Nm) and the points within a specified threshold around that stiffness value (compression: 200 ± 100 N, torsion: 2.5± 0.5 Nm, 6.5 ± 1 Nm).

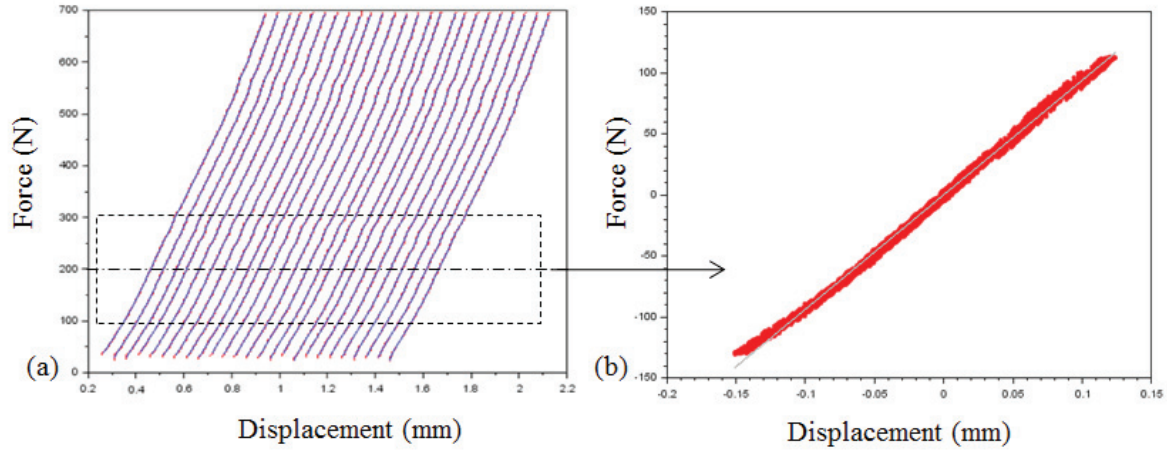

Figure 43: Force-displacement curves for individual cycles (a) and the points used for stiffness calculation grouped around a line of best fit based on the Theil-Sen estimator (b). The data enclosed in the dashed box indicate those used to calculate the data barycentre.

Tests for difference were performed for the two sample groups over 350 N and 700 N compression tests, as well as ±4 Nm and ±8 Nm torsion tests. The stiffness value used for statistical difference tests is the robust stiffness calculated across all cycles (6-28) using the Theil-Sen estimator. Where abnormal standard deviations are observed, the cycle-by-cycle graphs are analysed (see appendix §3)

3.3.2. DIC data

The images collected during all tests were semi-automatically renamed and reduced in number using an in-house python script; in order to decrease the volume of data, only one in every four images was retained for DIC. The images were imported into Vic3D (version 2010, Correlated Solution, Inc, USA) the marker tracking, whereas version 8 of the same software was employed for image correlation.

Images are used from the anterior facing samples only (visualising the fracture gap) except for the DTN samples for compression testing during Phase-3 where only one set of tests was carried out with the implant screws facing the cameras (medial tibia). In this scenario, it was considered that the fracture gap movement would be equal across the entire circumference of the sample and it was of greater interest to analyse the effect of force transmission to the bone from the screw heads. No images

are presented for the MDTP samples during torsional testing, as it was not possible to create a clear correlation of the implant on the medial side of the sample.

The given facet size for each given speckle pattern was chosen based on the minimal possible facet size which maintains a correlation error of less than 5%. DIC error was analysed for each type and phase of testing by duplicating the reference image for a given sample and running it through DIC; the vertical and shear strain was measured for compression and torsion testing, respectively. Error was found to be negligible for all correlations (<10 με).

DIC was carried out for the samples presenting the **highest and lowest stiffness constructs for each implant**. Vertical strain was measured for compression testing while shear strain was collected for torsional testing. In Phase-0 the samples with the highest and lowest measured compression and torsional stiffness constructs are presented; whereas in Phases 1-3 two samples (highest and lowest stiffness) are presented for each implant. Fracture gap movement was also calculated using the extensometer tool in Vic3D (Figure 44) to measure the gap movement in the mid-fracture/osteotomy gap region, and over the lateral cortex.

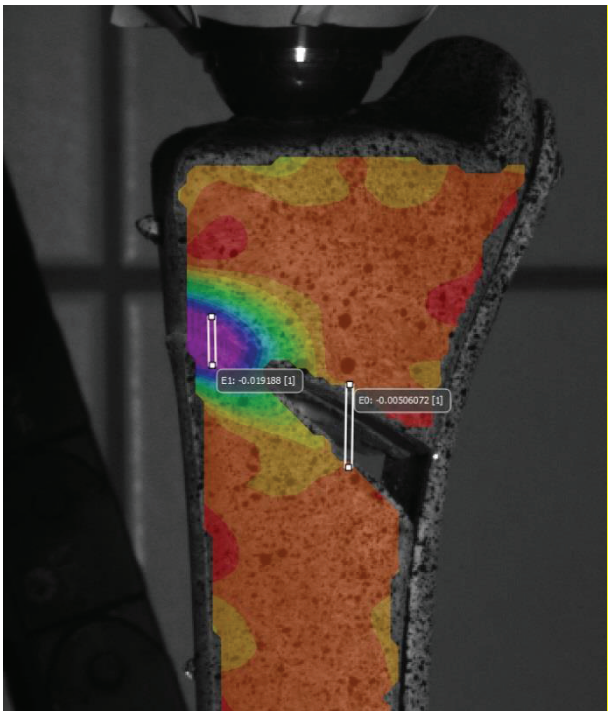

Figure 44: Extensometer placements for measurement of fracture gap displacement

The images presented in the results correspond to the maximum detected negative vertical and shear strain for compression and torsion testing, respectively. Colour scales to represent the deformation are harmonised across test type and test phase, which in some cases may depict an over–estimation of the strain mapping.

Sample-corresponding stiffness constructs are noted with K while vertical and shear deformation are represented with ε_{yy} and ε_{xy}, respectively; fracture gap movement is symbolised with Δl and measured in millimetres.

3.3.3. Statistics

Tests for normality (Shapiro-Wilk) and homoscedasticity (Levene's test) were carried out prior to all difference tests. Non-normal and/or heteroscedastic data were compared with the Mann Whitney-U test; otherwise, a standard two-tailed Student's t-test was employed. Student *t*-tests results are reported stating the t-statistic, (degrees of freedom), and *P*-value. Mann Whitney-U tests are reported stating the *U*-statistic and the *P*-value. Sample sizes are always equal between the two groups, (n_1=n_2=8).

Tests for difference were performed for the two sample groups during 350 N and 700 N compression tests, as well as ±4 Nm and ±8 Nm torsion tests. Results from the ±8 Nm torsion tests were calculated at 6.5±1 Nm so to take into account only the second stiffness slope, the first stiffness gradient appearing unstable up to ~4 Nm (Figure 45). All statistical analyses were undertaken in Statgraphics Centurion 18 (version 18.1.09, Statgraphics Technologies, Inc., Virginia, USA).

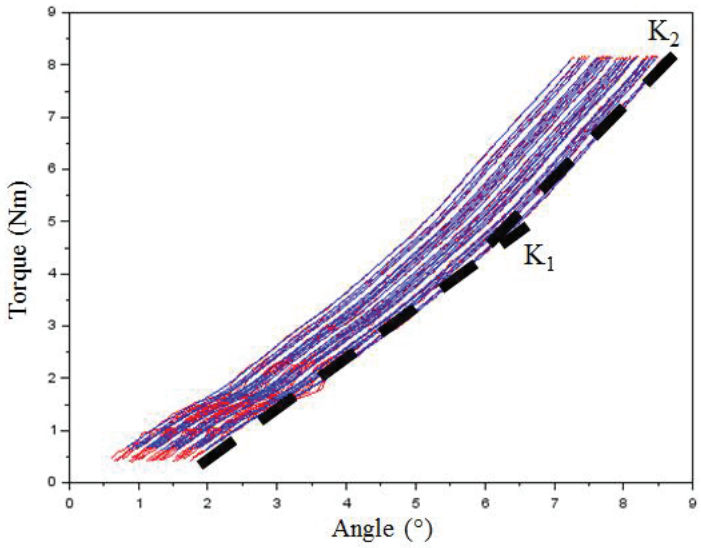

Figure 45: Example of a non-linear stiffness curve with two stiffness constructs present, identified as K1 and K2. The red line represents raw data; the blue line is the interpolated stiffness data.

4. Results

A summary of all results from all testing phases, loads and implant are displayed in Figure 46 for compression and Figure 48 for torsion. The DTN's average stiffness construct is higher than the MDTP during compression testing in all phases but phase 2 where the plate demonstrates a significantly higher stiffness. Despite the significant differences in samples stiffness, on analysing the level of displacement of each sample there appears to be very little movement permitted across all samples,

except for the MDTP during Phase-3 of testing. By comparing Figure 46 and Figure 47 for the stiffness and displacement values of each implant-group, we notice that an increase in stiffness is coupled with (and results from) a decrease in displacement. However, the significant differences indicated for stiffness constructs are not reflected in the displacement values for Phase-2.

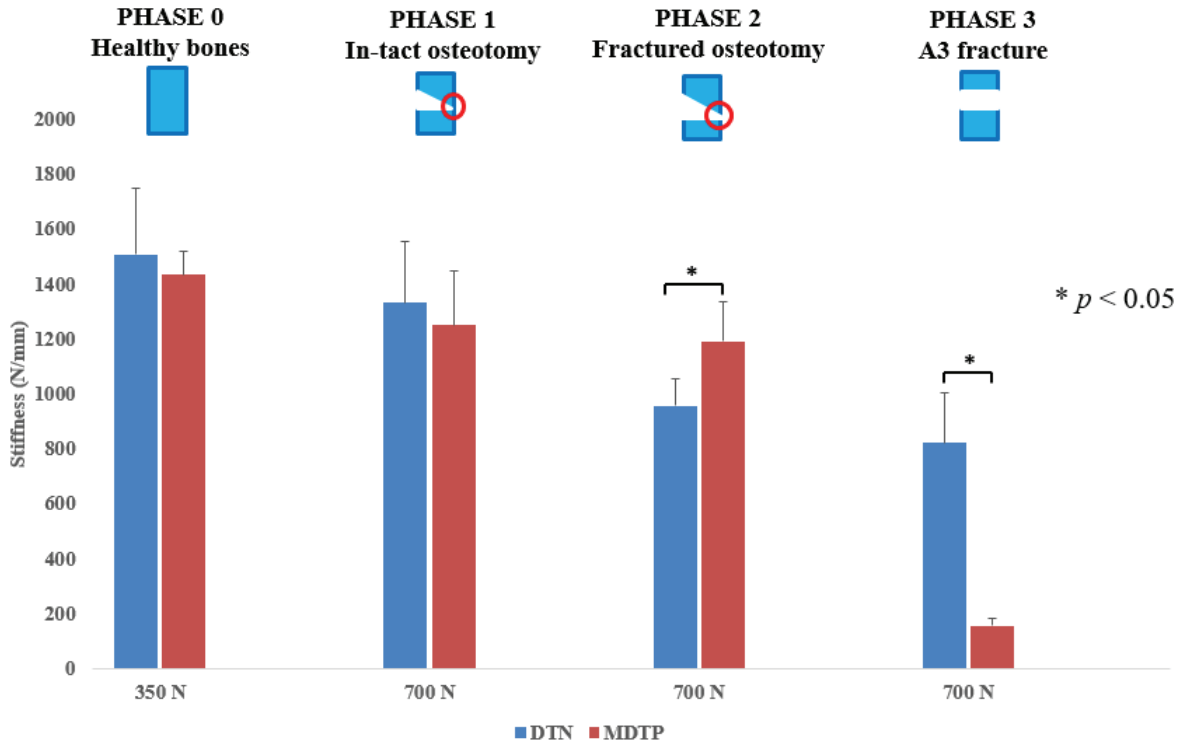

Figure 46: Mean ±2SD compression stiffness results for all testing phases, levels of loading and implants.

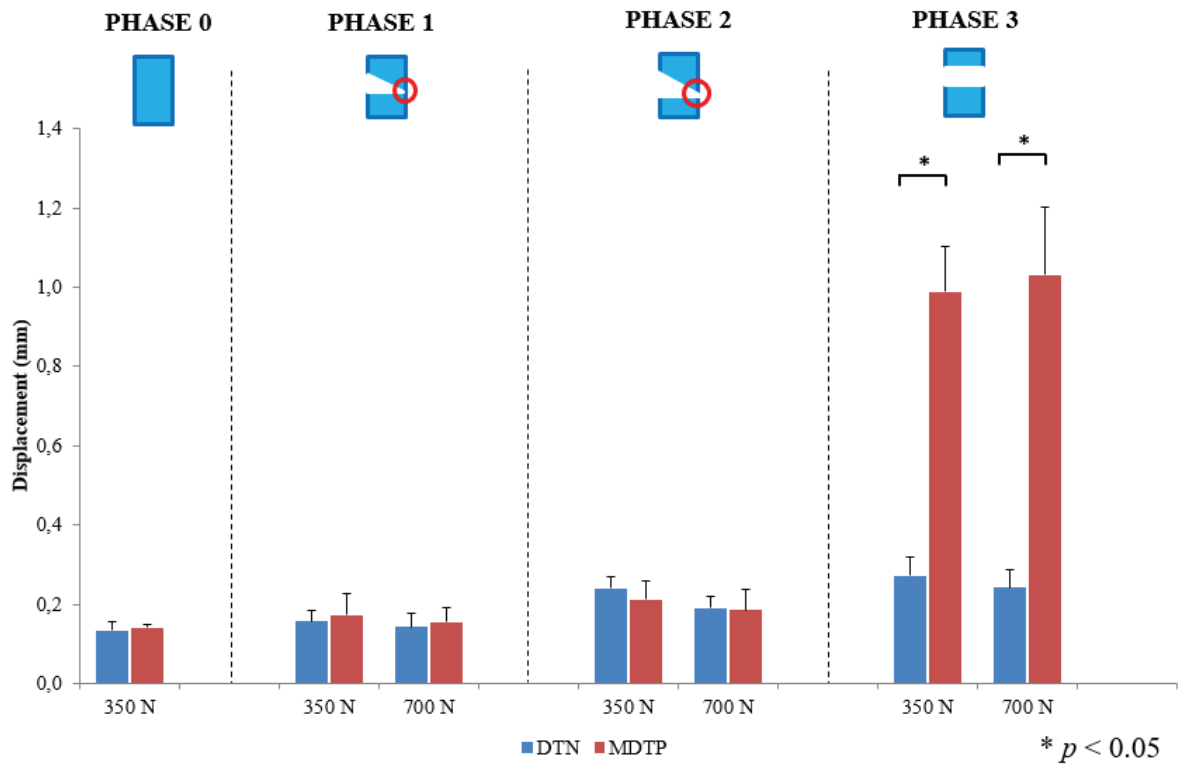

Figure 47: Mean ±2SD sample displacement results for all testing phases, levels of loading and implants for compression testing.

During torsional testing, again the DTN group displays higher stiffness constructs, in particular in phases 2 and 3; during phase 1, however, the plate exhibits significantly higher stiffness at low level ±4 Nm torsion. With respect to angular displacement (Figure 49), all samples remain below 1° of movement in Phases 0 and 1 whereas the levels and difference between samples increase for phases 2-3, as per the torsional stiffness graph (Figure 48). The significant difference observed between stiffness constructs in Phase-1 4 Nm testing, amounts to just a 0.16° difference in rotation. The mean angular displacement measured in Phase-2 remains below 2° for the DTN but is closer to 3° for the MDTP samples. In Phase-3, there is a difference of 2° between the sample groups (DTN average: 1.97°, MDTP average: 3.98°). Where differences in torsional stiffness were found to be significant between the implant groups, differences in angular displacement were also found to be significant.

All results from all phases are explained in more detail through this section.

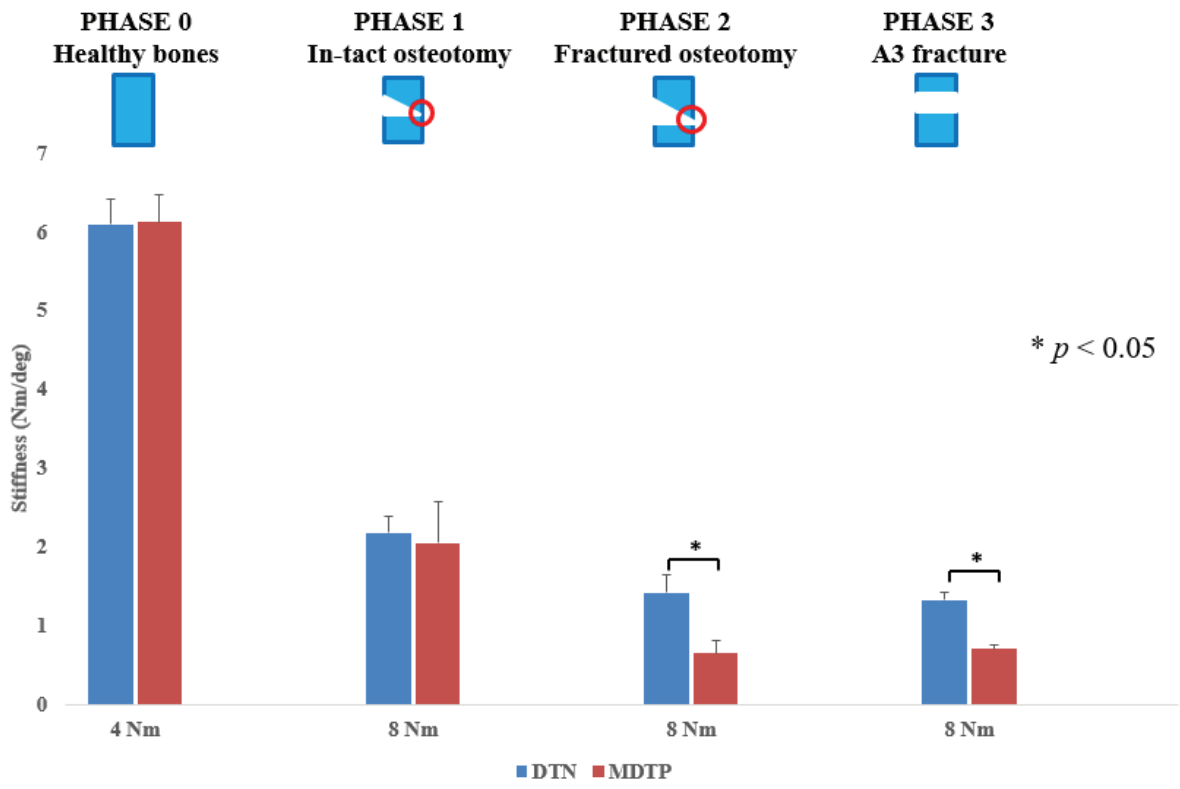

Figure 48: Mean ±2SD torsion results for all testing phases, levels of loading and implants.

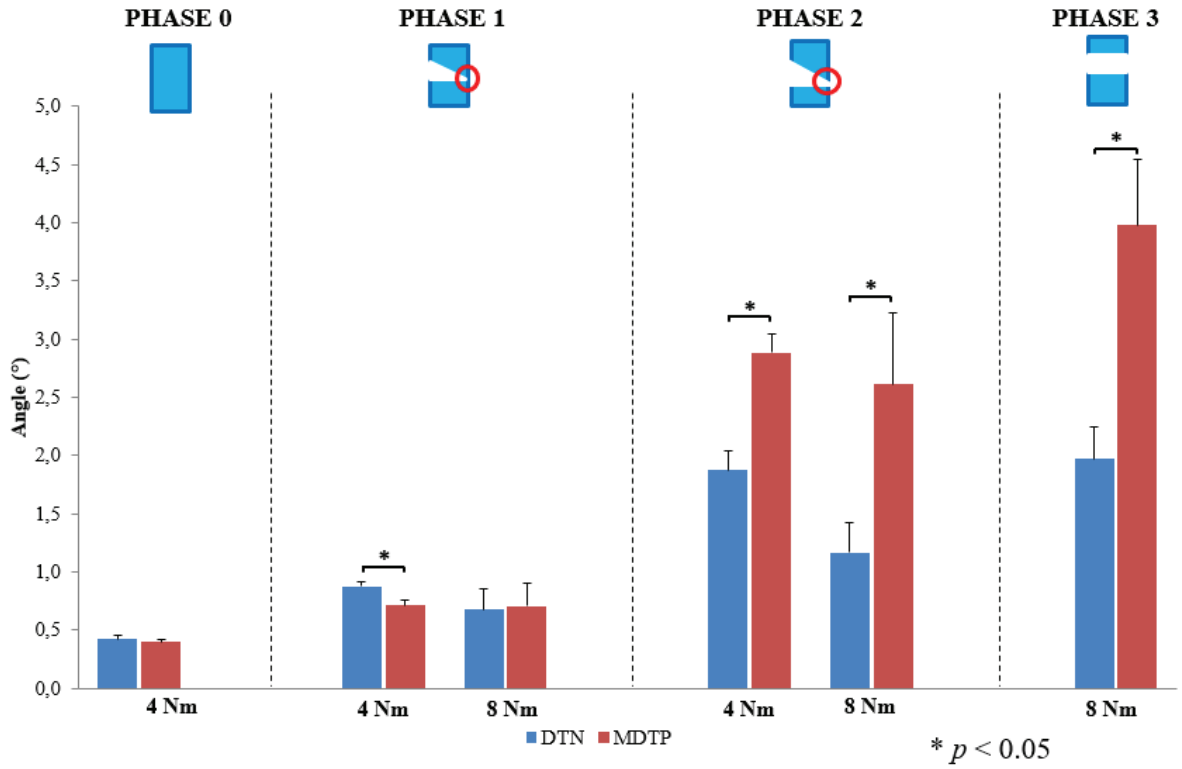

Figure 49: Mean ±2SD sample angular displacement results for all testing phases, levels of loading and implants for torsion testing.

4.1. Phase 0 – Composite bone testing

350 N Compression (phase-0)

Varying values in compressive (Figure 51) stiffness can be observed across all samples ranging from around 1125 to 1950 N.mm^{-1}. Although no significant differences are seen between the composite bone allocated to DTN and MDTP sample groups, a high disparity between certain samples can be observed.

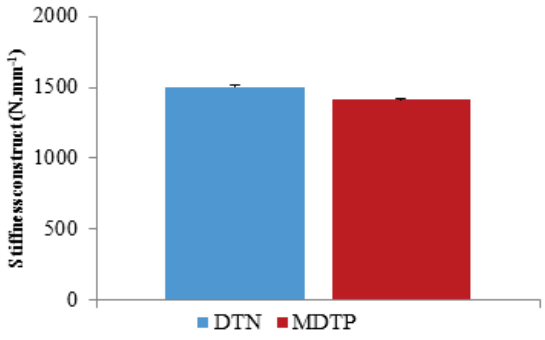

Figure 50: Mean±2SD compressive sample stiffness construct for all composite bones (n=18) assigned to the DTN and MDTP implants (Phase 0 of testing).

At 350 N compression, the stiffness calculated at 200 N for the samples assigned to the DTN group was 1508 ± 10 N.mm^{-1}; while for the MDTP group is was 1434 ± 10 N.mm^{-1}. No significant differences were found between the allocated DTN and MDTP groups.

The lowest calculated stiffness is for the DTN-1 sample which rises to just 1142 N.mm^{-1} while the DTN-4 sample displays a stiffness construct of 1968 N.mm^{-1}, an increase of almost two-fold. This increase in stiffness relates to a decrease in displacement tolerated by the sample which has a difference of 0.07 mm between the two samples. Average compressive stiffness across all samples is 1459 ± 191 N.mm^{-1}.

Standard deviations are relatively low, especially once the first five cycles are omitted from analyses. When comparing DTN-5 to DTN-6, for example, the cycles selected for stiffness calculation influence the resulting stiffness. Stiffness constructs calculated between cycles 5-10 and 10-20 appear lower than among other cycles. Nonetheless, in reality this variability between cycle groups amounts to 34 N.mm^{-1} for the DTN-5, against 9 N.mm^{-1} for the DTN-6 sample; such small differences in stiffness can be neglected as they relate to <5% of the total respective stiffness for the sample in question.

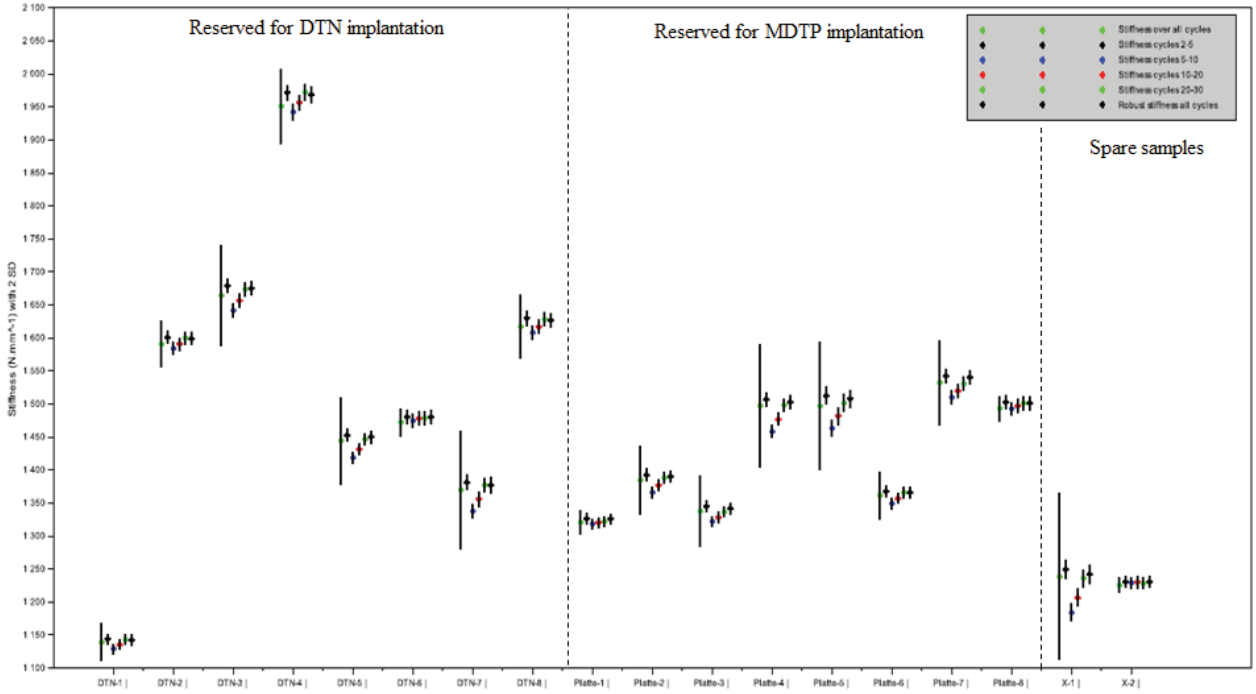

Figure 51: Mean±2SD compressive stiffness construct values for all samples over all cycles, cycles 2-5, cycles 5-10, cycles 10-20, cycles 20-30, and the robust stiffness calculation (over all cycles) during phase 0 of testing.

The 18 Sawbones® samples were randomly assigned to each implant group (DTN or MDTP) as well as two spare samples (X1 and X2) in case of failure during implant insertion. Both compression and torsion data tested as normal ($P > 0.05$) and therefore a t-test was carried out to compare the two groups. Digital image correlation was performed on the samples demonstrating the highest and lowest compressive and torsional stiffness constructs and can be consulted in the appendix (§3).

4 Nm Torsion (phase-0)

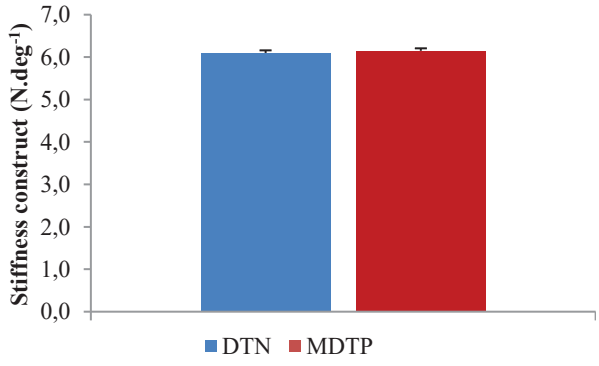

Figure 52: Mean±2SD torsional sample stiffness construct for all composite bones (n=18) assigned to the DTN and MDTP implants (Phase 0 of testing).

Torsional testing of ±4 Nm resulted in a mean torsional stiffness of 6.1 ± 0.06 $Nm.deg^{-1}$ for the DTN assigned group and 6.13 ± 0.06 $Nm.deg^{-1}$ for the MDTP group. No significant difference was identified between the two groups ($t(16)$ = 1.16, P = 0.26) or for torsion ($t(16)$ = -0.20, P = 0.84).

Torsional stiffness constructs for all samples appear to be randomly allocated throughout the samples. Highs of 6.83 Nm.deg^{-1} are observed in the Plate-7 sample, and lows of 5.42 Nm.deg^{-1} in the Plate-2 sample, resulting in a variation of 1.4 Nm.deg^{-1}, a difference is less important than during compression testing. Average torsional stiffness across all samples is 6.12 ± 0.05 Nm.deg^{-1}.

As with the compression tests, a dip in calculated torsional stiffness is observed for cycles 5-10 and 10-20 whereas for cycles 2-5, 20-30 and the robust stiffness calculation exhibit higher stiffness constructs. Taking the DTN-1 sample as an example, the maximum difference in torsional stiffness is 0.03 Nm.deg^{-1} between cycles 5-10 and cycles 20-30, amounting to <1% of the total stiffness and can therefore be considered negligible.

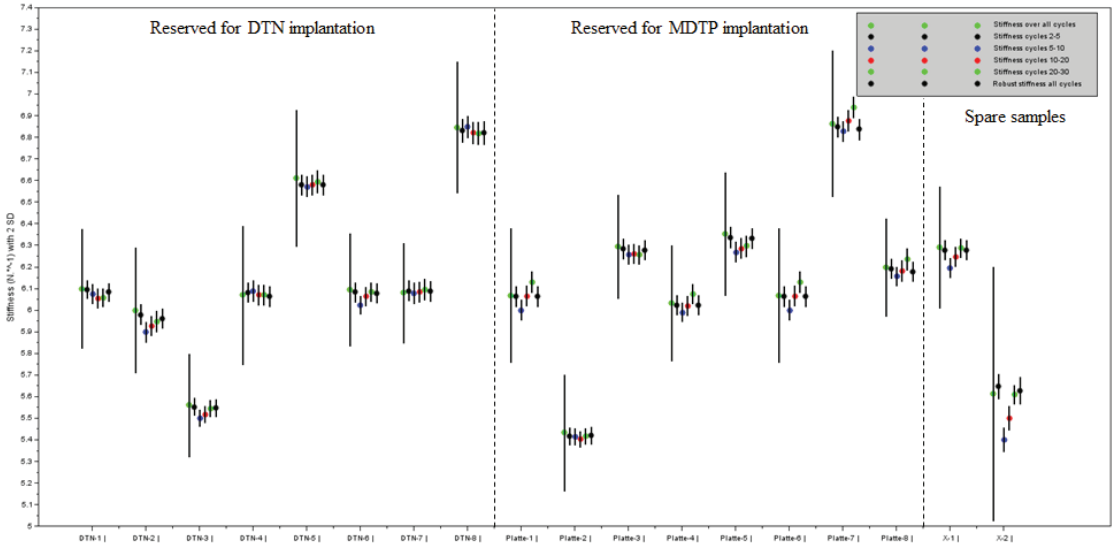

Figure 53: Mean±2SD torsional stiffness construct values for all samples over all cycles, cycles 2-5, cycles 5-10, cycles 10-20, cycles 20-30, and the robust stiffness calculation (over all cycles) during phase 0 of testing.

In Phase-0 of testing, no significant differences were found between the assigned sample groups; however, a large variability within sample groups (in particular for the DTN) was observed during compression testing.

4.2. Phase 1

Phase-1 relates to the simulation of the medial wedge osteotomy in all Sawbones® samples with the lateral cortex still intact: A best-case scenario supramalleolar osteotomy.

350 N compression testing (phase-1)

Machine data

Phase 1 of testing involved the simulation of a supramalleolar osteotomy and the placing of an implant to stabilise the construct. During implantation of the DTN, two samples experienced a rupture at the lateral cortex and the DTN-6 sample was eventually replaced by the X-2 sample. In total, eight samples were implanted with a DTN, and eight with a MDTP.

The results displayed for compression testing at 350 N after the simulation of a MWO and fixation with an implant follow a similar trend to those for the healthy samples with DTN-4 demonstrating the highest stiffness levels (1734 $N.mm^{-1}$), the Plate-1 sample exhibits the lowest stiffness construct (860 $N.mm^{-1}$).

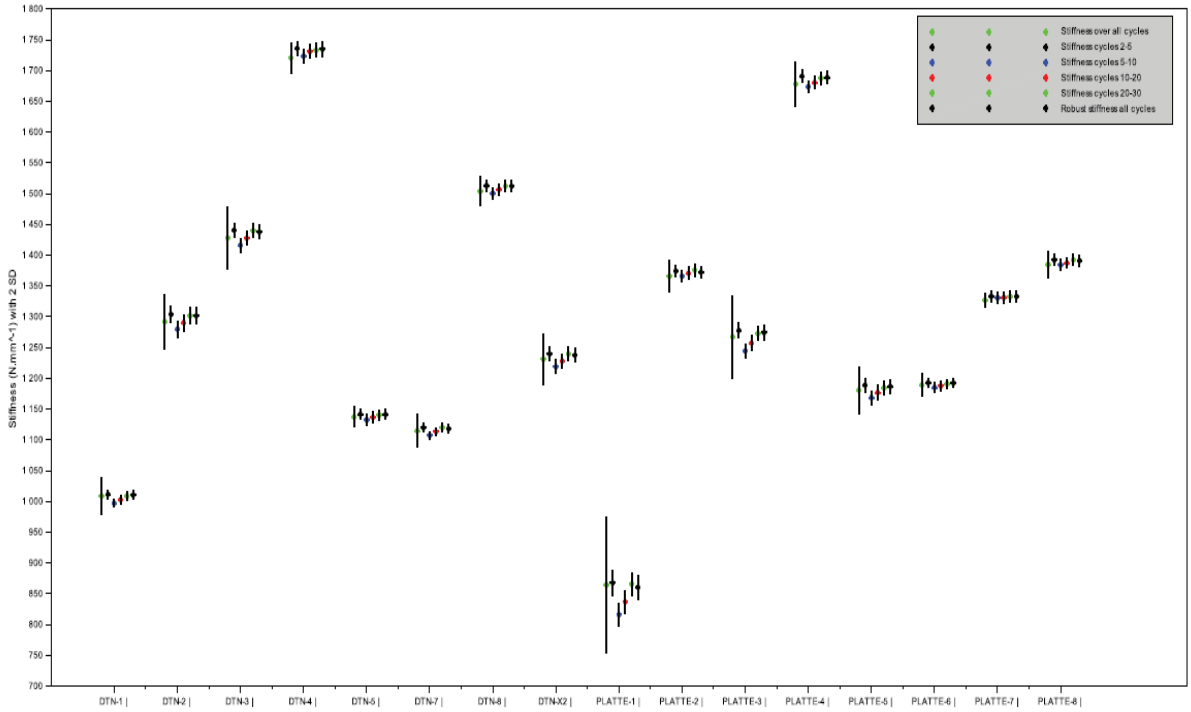

Figure 54: Mean±2SD compressive stiffness construct values for all samples over all cycles, cycles 2-5, cycles 5-10, cycles 10-20, cycles 20-30, and the robust stiffness calculation (over all cycles) during phase 1 of testing at 350 N (stiffness calculated at 200±100 N).

Most samples demonstrate a decrease in stiffness with the osteotomy simulation; others, however, increase in stiffness by up to 186 $N.mm^{-1}$ (for the Plate-4 sample), this is also the case for the DTN-8 sample, which increases in stiffness from 1368 to 1512 $N.mm^{-1}$. All testing parameters, including the test order, were maintained between phase-0 to phase-1, such differences may be explained by factors relating to the surgical technique.

700 N Compression (phase-1)

Stiffness constructs at 700 N range from 943 to 1641 $N.mm^{-1}$, these values belong to the Plate-1 and DTN-4 samples, respectively. The trend of the results follows the same as that demonstrated in Figure 55 for 350 N compression. Plate-6 shows a particularly high standard deviation for the all-cycles group and the stiffness calculated between cycles 10-20 is below average for this sample. A breakdown of this sample cycle-by-cycle can be referred to the appendix (§3).

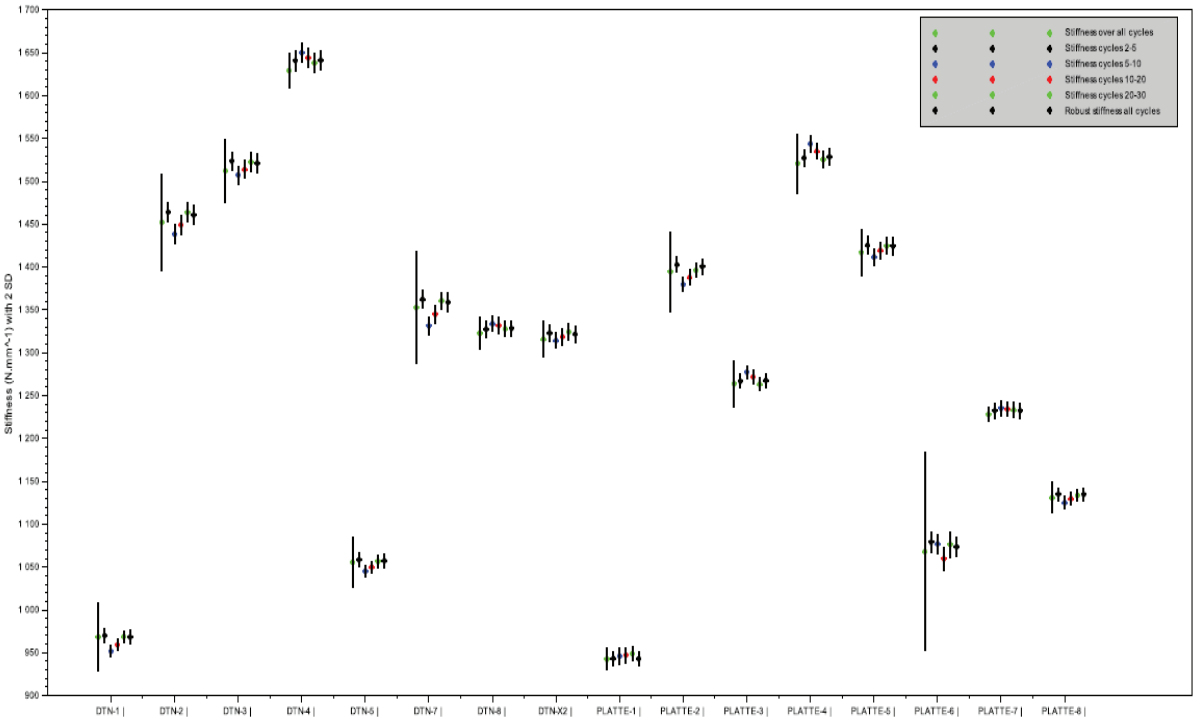

Figure 55: Mean±2SD compressive stiffness construct values for all samples over all cycles, cycles 2-5, cycles 5-10, cycles 10-20, cycles 20-30, and the robust stiffness calculation (over all cycles) during phase 1 of testing at 700 N (stiffness calculated at 200±100 N).

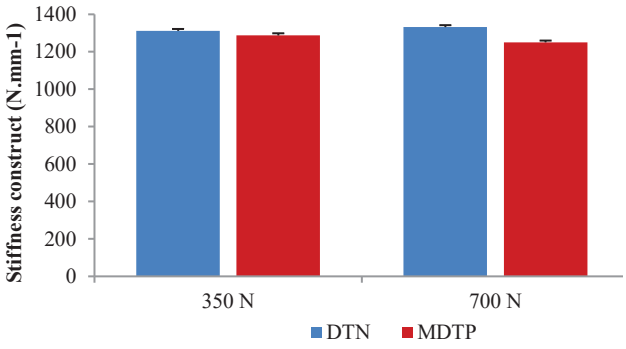

Figure 56: Mean±2SD compressive stiffness values for the implant groups at 350 N and 700 N during Phase-1 of testing.

Exported data for the compression tests respected the laws of normality and equal variance. Average compressive stiffness was higher in the DTN group during both 350 N and 700 N tests (Figure 54). Mean stiffness constructs were measured to be 1311 ± 10 $N.mm^{-1}$ for the DTN group during 350 N tests, and 1287 ± 11 $N.mm^{-1}$ for the MDTP implanted group. At 700 N, there was a greater difference between the groups (DTN: 1332 ± 10 $N.mm^{-1}$, MDTP: 1250 ± 9 $N.mm^{-1}$); however, no significant differences were observed between groups for the compression tests (350N: $t(14) = 0.20$, $P = 0.84$; 700N: $t(14) = 0.77$, $P = 0.45$).

Digital image correlation (phase-1 compression)

At 700 N compression, the DTN samples exhibit negative strain in the distal fragment of the sample but not necessarily around the osteotomy – this area lends itself more towards tensile strain. In the MDTP samples, the area around the osteotomy is dominated by negative ε_{yy} particularly proximal to the osteotomy. In the MDTP-1 sample, this zone extends to the distal side of the osteotomy also. The

DTN samples demonstrate higher levels of fracture gap movement, but this value remains minimal (<0.1 mm).

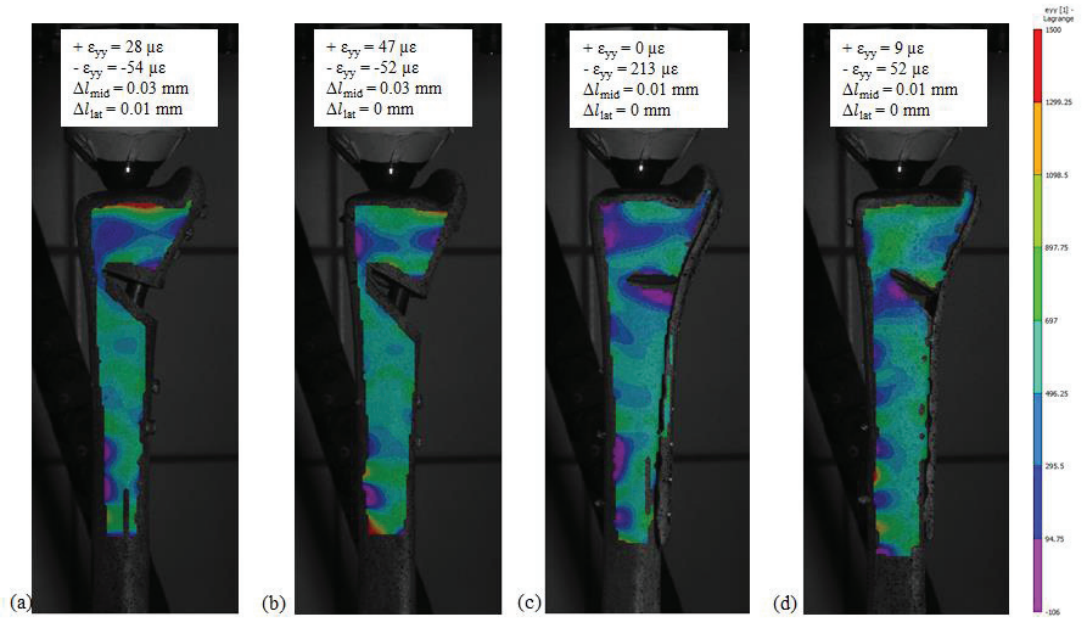

Figure 57: Vertical strain distribution of the DTN-1, DTN-4, MDTP-1, and MDTP-4 samples during 700 N of Phase-1 of testing. Images are taken at -650 N of loading.

±4 Nm torsion (phase-1)

The lowest measured torsional stiffness is observed in the DTN-1 sample at 2.27 Nm.deg^{-1} while the highest is seen in the MDTP-1 sample (3.88 Nm.deg^{-1}). Within the DTN samples, torsional stiffness varies from 2.27 Nm.deg^{-1} to 3.24 Nm.deg^{-1} (DTN-2); in the MDTP samples the range of stiffness is also around 1 Nm.deg^{-1}, varying from 2.95 Nm.deg^{-1} (MDTP-6) to 3.88 Nm.deg^{-1}.

Particularly high standard deviations can be seen in the Plate-7 sample when compared to other samples and a breakdown of this sample's performance can be seen in the appendix (§3).

Figure 58: Mean±2SD torsional stiffness construct values for all samples over all cycles, cycles 2-5, cycles 5-10, cycles 10-20, cycles 20-30, and the robust stiffness calculation (over all cycles) during phase 1 of testing at ±4 Nm (stiffness calculated at 2.5±0.5 Nm).

±8 Nm torsion (phase-1)

At 8 Nm torsional loading, the gap between the most and least stable samples remains at a similar magnitude as when testing as 4 Nm (~1.6 $Nm.deg^{-1}$). Plate-1 maintains the highest torsional stiffness at 3 $Nm.deg^{-1}$, while the Plate-6 sample exhibits the lowest resistance to torsional loading (1.4 $Nm.deg^{-1}$. At higher torsional loads, the MDTP decreased on average its torsional stability from 3.4 to 2.1 $Nm.deg^{-1}$; the DTN also showed lower average stiffness, but of a smaller magnitude, reducing from 2.7 to 2.2 $Nm.deg^{-1}$. This indicates that the DTN may offer greater reproducibility against high torsional loads whereas the MDTP does not perform as well. None of the samples demonstrate abnormal standard deviations.

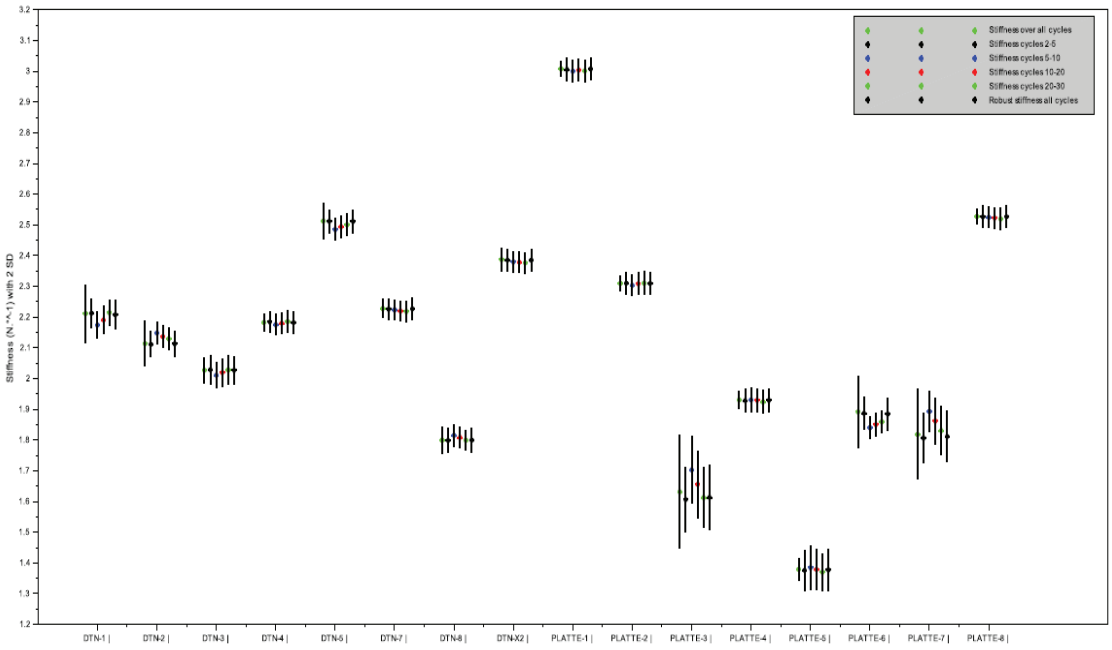

Figure 59: Mean±2SD torsional stiffness construct values for all samples over all cycles, cycles 2-5, cycles 5-10, cycles 10-20, cycles 20-30, and the robust stiffness calculation (over all cycles) during phase 1 of testing at ±8 Nm (stiffness calculated at 6.5±1 Nm).

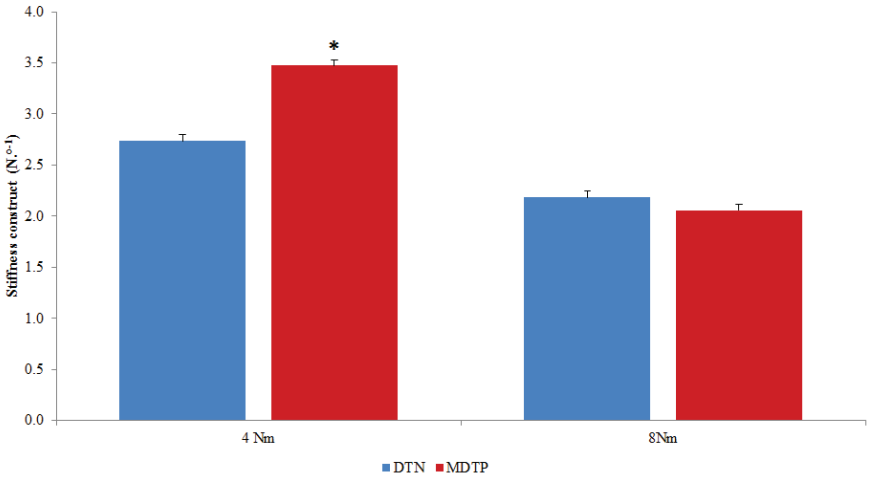

Figure 60: Mean±2SD torsional stiffness values for the DTN and MDTP groups at ±4 Nm and ±8 Nm loading during Phase-1 of testing.

Mean torsional stiffness during 4Nm testing was at 2.74 ± 0.06 Nm.deg-1 for the DTN, and significantly higher for the MDTP group at 3.47 ± 0.07 Nm.deg-1 ($t(14) = -4.51$, $P < 0.001$). Data was found to deviate from normality for results collected for the ±8 Nm and therefore a Mann-Whitney U test was applied. Nonetheless no significant differences were found between the sample groups ($U = 0.61$, $P = 0.55$).

Digital image correlation (phase-1 torsion)

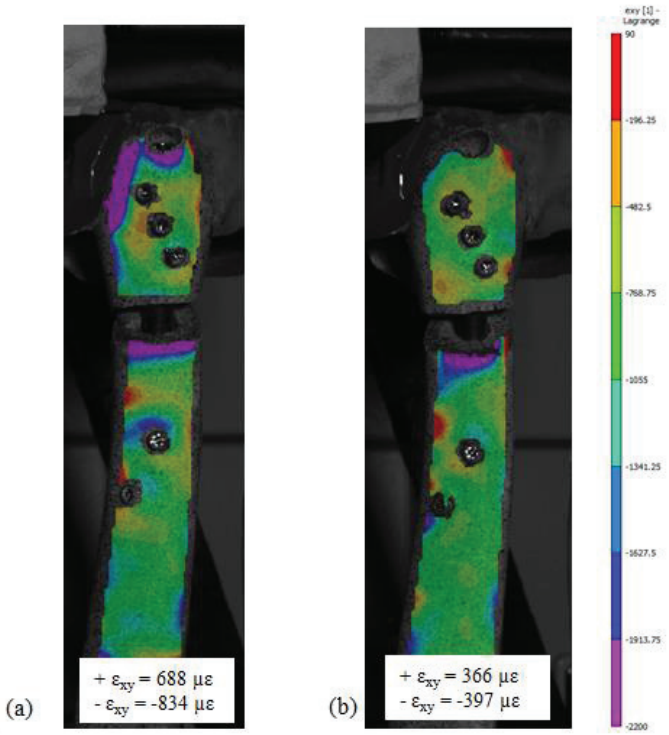

Figure 61: Shear strain distribution of the DTN-8 and DTN-5 samples during Phase-1 of testing at ±8 Nm torsion. Images are taken at +7.5 Nm.

Between the two DTN samples presented for ±8 Nm torsion, differences of at least 2-fold are observed between measured ε_{xy} values for both positive and negative shear strain. For the strain distributions displayed across the medial surface of the tibia, a consistent negative ε_{xy} is noticed proximal to the osteotomy. A large zone of negative ε_{xy} is witnessed in the DTN-8 sample (±8 Nm testing) at the anterior side of the medial malleolus whereas in the DTN-5 sample this zone appears to be much smaller.

In Phase-2 of testing, the DTN demonstrated higher levels of compression but this was not significant. The MDTP showed a significantly higher resistance to torsional loading at ±4 Nm but at ±8 Nm the DTN proved to be more resistant.

4.3. Phase-2

Phase-2 of testing relates to a worst-case scenario MWO where the later cortex of the osteotomy is fractured during the opening of the medial tibia in the course of the surgery.

350 N Compression (phase-2)

Plate-1 demonstrates the lowest levels of stiffness against compression (721 $N.mm^{-1}$), and Plate-4 displays the highest stiffness construct (1354 $N.mm^{-1}$), although the differences between the lowest and highest stiffness constructs are less apparent, this follows the same pattern as witnessed by 350 N in Phase 1.

Figure 62: Mean±2SD compressive stiffness construct values for all samples over all cycles, cycles 2-5, cycles 5-10, cycles 10-20, cycles 20-30, and the robust stiffness calculation (over all cycles) during phase 2 of testing at 350 N (stiffness calculated at 200±100 N).

700 N Compresion (phase-2)

The difference in stiffness constructs between the groups is less obvious during 700 N compression (compared to 350 N compression tests) with an average difference of just 236 $N.mm^{-1}$ between the two groups. Absolute minimum and maximum stiffness constructs are displayed in the DTN-3 and Plate-4 groups at 778 and 1392 $N.mm^{-1}$, respectively. The Plate-1 sample consistently demonstrates the lowest resistance (913 $N.mm^{-1}$) to compressive loading among all of the samples implanted with a MDTP.

The DTN-7 sample in the fracture configuration for the cameras displayed very high standard deviations and this is investigated further in the appendix (§4). These data were replaced with the implant configuration data (implant facing the cameras) for this sample. However, for the statistical analyses, the robust stiffness construct (6^{th} point) was taken and this point maintains a high stiffness where other points present lower stiffness values possibly due to error on the machine data.

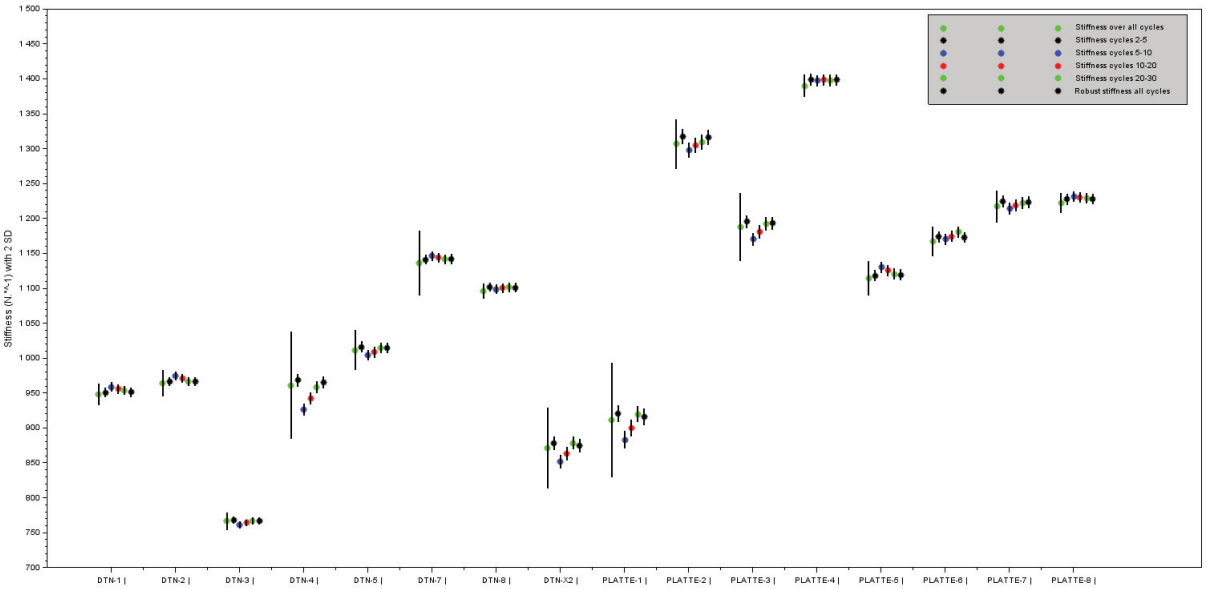

Figure 63: Mean±2SD compressive stiffness construct values for all samples over all cycles, cycles 2-5, cycles 5-10, cycles 10-20, cycles 20-30, and the robust stiffness calculation (over all cycles) during phase 2 of testing at 700 N (stiffness calculated at 200±100 N).

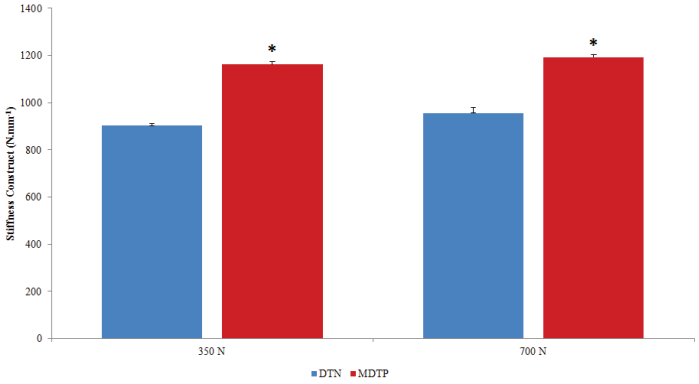

Figure 64: Mean±2SD compressive stiffness constructs for the DTN and MDTP sample groups at 350 N and 700 N during Phase-2 of testing.

Phase 2 of testing involved cutting through the lateral cortex in all samples. Data did not respect the laws of normality ($P = 0.02$) and there was a significant difference between implanted groups with the MDTP demonstrating higher levels of compressive stiffness (1162 N.mm^{-1} against 903 N.mm^{-1}; U = 56, $P = 0.01$). A significant difference between implant groups was also observed for 700 N compression test (1193 vs 957 N.mm-1 for the MDTP and DTN, respectively; t(14) = -3.87, $P = 0.002$).

Digital image correlation (phase-2 compression)

In Phase-2 of testing where the lateral cortex is fractured, large zones of negative ε_{yy} can be observed in the lateral cortex area for both 350 N and 700 N. For all samples, the negative ε_{yy} appears to cover a larger area at 700 N; however when deformation values are compared, the maximum level of ε_{yy} does not double despite the doubling of the force applied. Fracture gap movement is greatest in the MDTP-4 sample despite this sample presenting the highest stiffness construct (K = 1392 N.mm^{-1}).

Fracture gap movement varied between the location at which it was measured and higher IFM was detected on the lateral side for all samples. The greatest movement is identified in the DTN-4 and DTN-3 samples; these correspond to the DTN samples with the lowest construct stiffness at 350 N and 700 N, respectively.

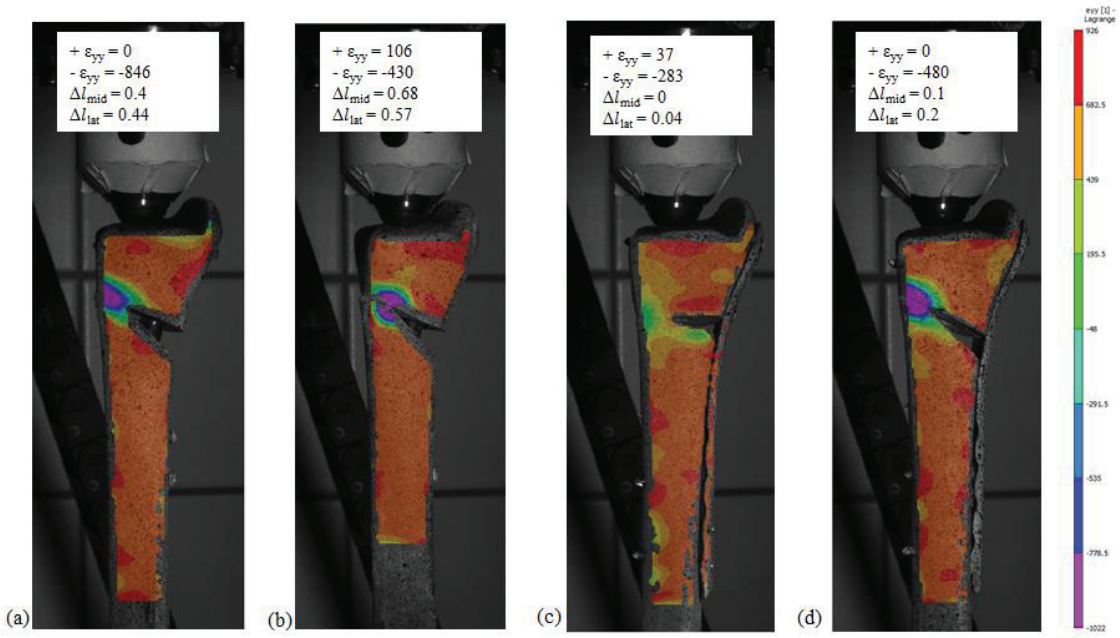

Figure 65: Vertical strain distribution of the DTN-3, DTN-8, MDTP-1, and MDTP-4 samples during 700 N of Phase-2 of testing. Images are taken at -650 N of loading.

±4 Nm torsion (phase-2)

The highest measured torsional stiffness construct was for the DTN-2 sample (1.23 Nm.deg^{-1}) while the lowest stiffness construct was in Plate-5 (0.45 Nm.deg^{-1}). Torsional stiffness construct ranged from 0.63 to 1.23 Nm.deg^{-1} in the DTN samples, a difference of almost two-fold. In the MDTP samples this range was from 0.45 to 0.85 Nm.deg^{-1}. Overly high standard deviations are detected for the DTN-1, -2, and -5 samples and the global picture shows high deviations in all samples. Closer investigation of these three samples is shown in the appendix (§3).

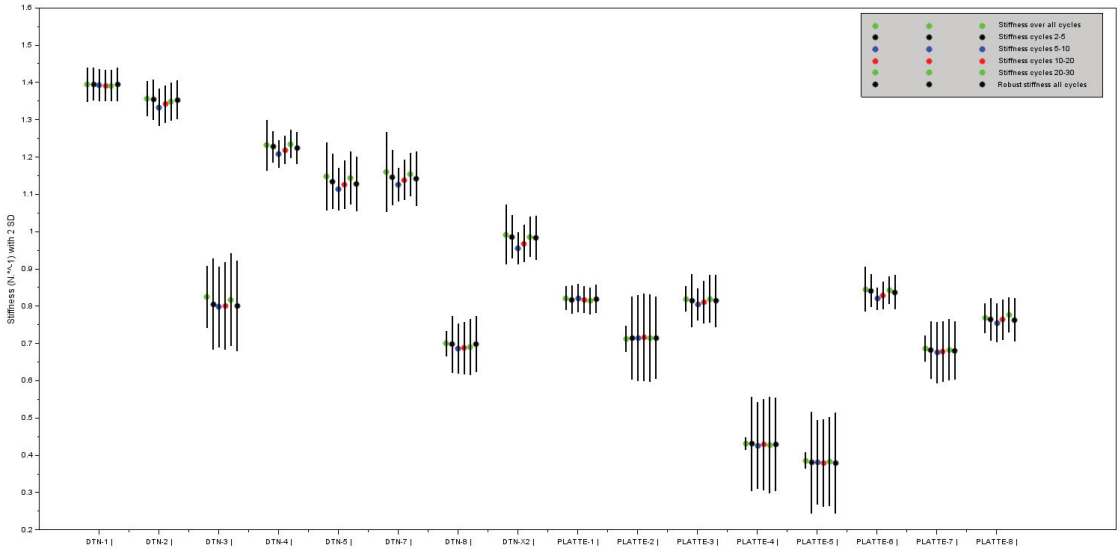

Figure 66: Mean±2SD torsional stiffness construct values for all samples over all cycles, cycles 2-5, cycles 5-10, cycles 10-20, cycles 20-30, and the robust stiffness calculation (over all cycles) during phase 2 of testing at ±4 Nm (stiffness calculated at 2.5±0.5 Nm).

±8 Nm torsion (phase-2)

The highest torsional stiffness is recorded for the DTN-1 sample at 1.76 Nm.deg^{-1} and the lowest at 0.5 Nm.deg^{-1} for Plate-5. A global difference can be seen between the two samples groups with the MDTP samples have generally lower torsional stiffness constructs compared to the DTN samples. MDTP sample stiffness values range from 0.5 Nm.deg^{-1} (MDTP-5) to 0.1 Nm.deg^{-1} (MDTP-8); while DTN samples range by the same amount but exhibiting higher stiffness constructs, from 1.42 Nm.deg^{-1} (DTN-8) to 1.76 Nm.deg^{-1} (DTN-1). No extra-ordinary standard deviations are observed.

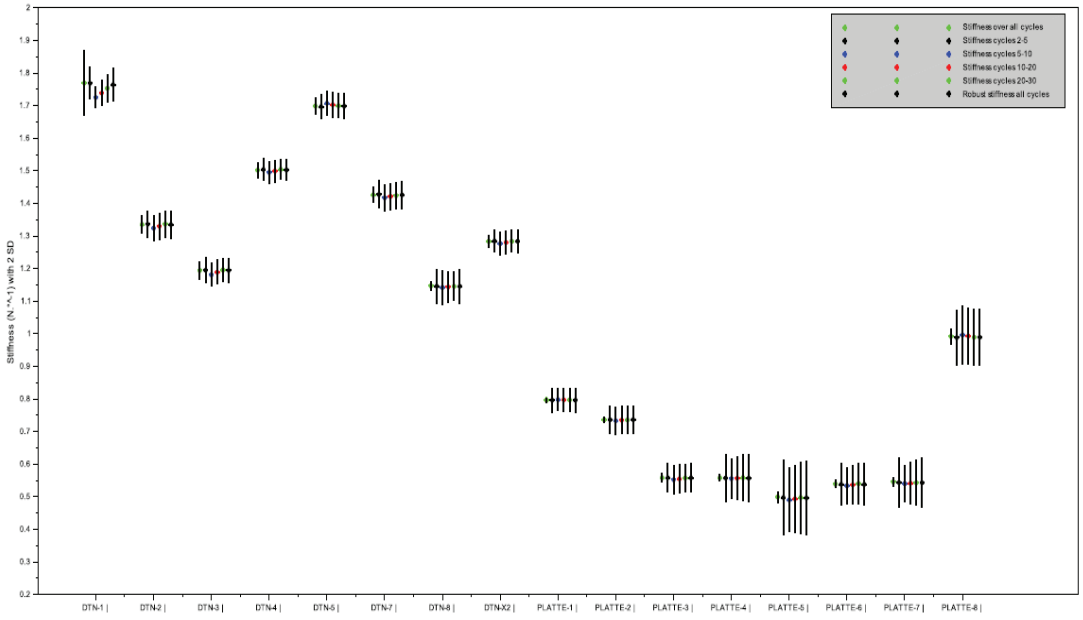

Figure 67: Mean±2SD torsional stiffness construct values for all samples over all cycles, cycles 2-5, cycles 5-10, cycles 10-20, cycles 20-30, and the robust stiffness calculation (over all cycles) during phase 2 of testing at ±8 Nm (stiffness calculated at 6.5±1 Nm).

Torsion data during 4 Nm testing did not conform to the laws of normality ($P < 0.05$) and a Mann Whitney-U test found the DTN to be more resistant, displaying higher average torsional stiffness at ±4 Nm (DTN: 0.96 Nm.deg^{-1} against MDTP: 0.71 Nm.deg^{-1}, U = 11, $P = 0.03$). This was also true at ±8 Nm (1.42 Nm.deg^{-1} against 0.65 Nm.deg^{-1}, for the DTN and MDTP, respectively).

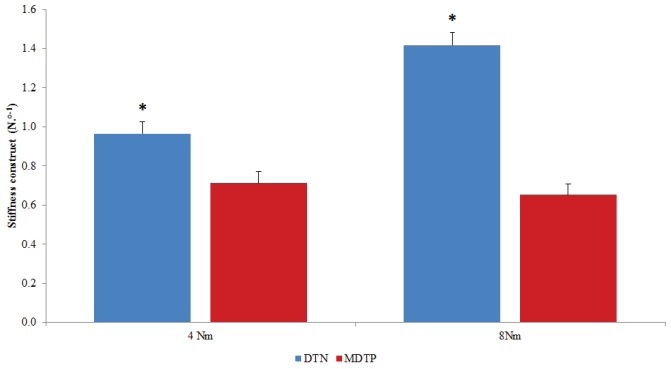

Figure 68: Mean±2SD torsional stiffness for the DTN and MDTP at ±4 Nm and ±8 Nm loads during Phase-2 of testing.

Digital image correlation (phase-2 torsion)

The shear strain measured for testing in Phase-2 is globally very small for both positive and negative ε_{xy}. It is interesting to note that in the DTN-8 sample (with a lower torsional stiffness, K = 1.14 Nm.deg^{-1}), the positive ε_{xy} is presented further proximally in the medial malleolus than in the DTN-1 sample (K = 1.76 Nm.deg-1). The area surrounding the most proximal screw of the DTN-1 displays high levels of negative ε_{xy} while in the DTN-8 no particular strain pattern can be observed.

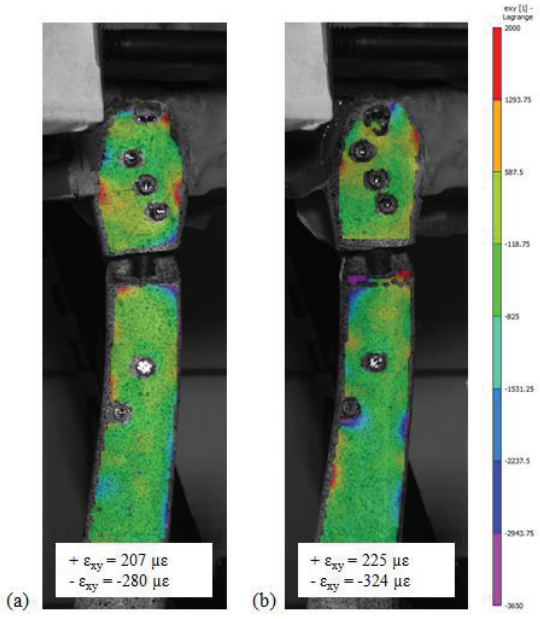

Figure 69: Shear strain distributions of samples DTN-8 and DTN-1 during Phase-2 of testing at ±8 Nm. Images are taken at +7.5 Nm loading.

To summarise Phase-2 of testing, the MDTP proved to be significantly more resistant against compressive loads compared to the DTN and this is also reflected in the levels of minimum

strain observed at the lateral cortex. For torsional testing, on the other hand, the DTN demonstrated significantly higher stiffness constructs.

4.4. Phase 3

Phase-3 of testing is the simulation of an A3 distal tibia fracture which corresponds to an extra-articular, mechanically unstable facture. The same samples were used as for the corrective osteotomy simulations.

350 N Compression (phase-3)

Stiffness values range from 937 N.mm-1 (DTN-8) to 139 N.mm^{-1} (Plate-5). There appears to be a relatively high disparity among the DTN samples with 352 N.mm^{-1} difference between the DTN-8 and DTN-X2 samples. MDTP fitted samples vary between 139 and 187 N.mm^{-1}. Standard deviations in all samples appeared normal.

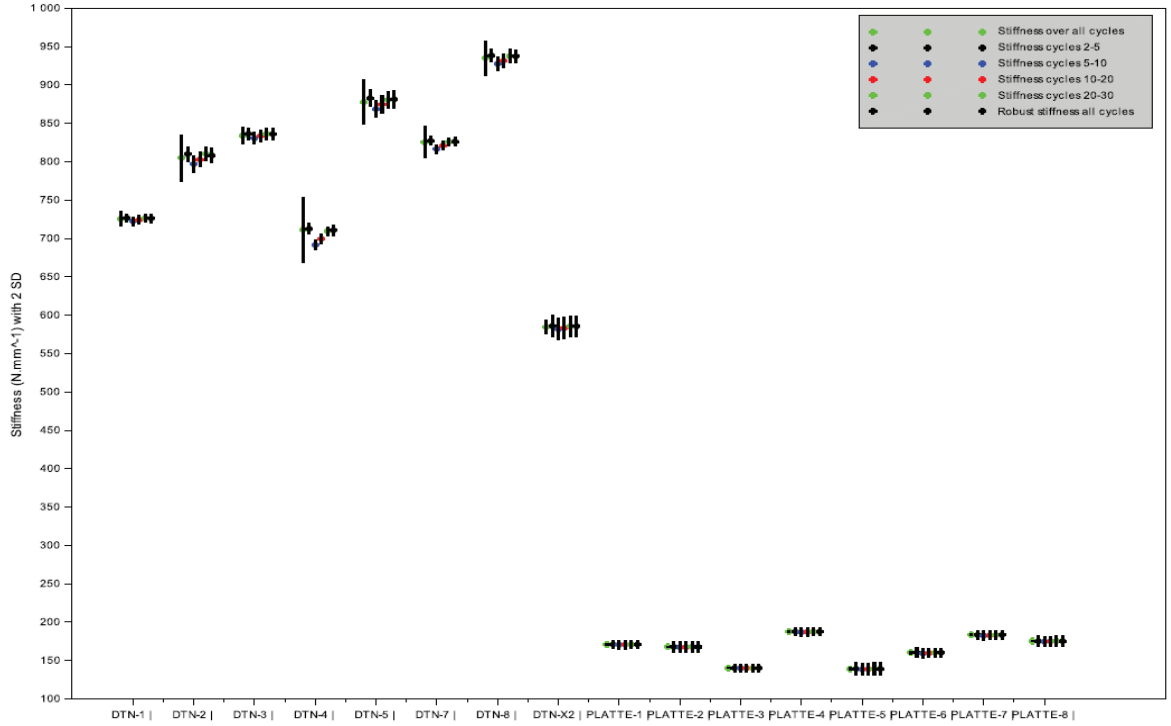

Figure 70: Mean±2SD compressive stiffness construct values for all samples over all cycles, cycles 2-5, cycles 5-10, cycles 10-20, cycles 20-30, and the robust stiffness calculation (over all cycles) during phase 3 of testing at 350 N (stiffness calculated at 200±100 N).

700 N Compression (phase-3)

Highest stiffness values are again observed in the DTN-8 sample (1138 N.mm^{-1}) and lowest in the Plate-5 sample (104 N.mm^{-1}). Stiffness constructs within the DTN samples continue to vary with the lowest calculated construct being at 562 N.mm-1 (DTN-X2), less than half of the greatest construct (DTN-8). Variations among the DMTP samples are relatively small in comparison, lying between 104 and 189 N.mm^{-1}. Standard deviations are low in all samples except the points accounting for all cycles

for certain DTN samples; nonetheless, this is not considered extra-ordinary as the points referring to the partitioning of cycles present very low standard deviations.

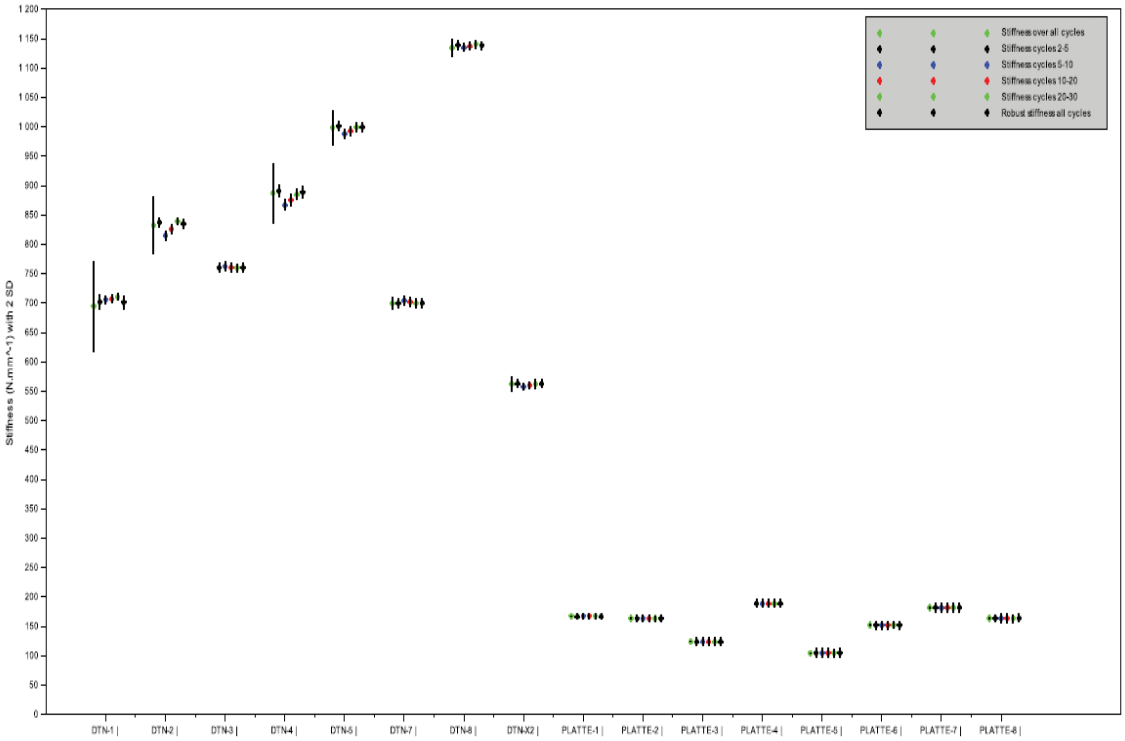

Figure 71: Mean±2SD compressive stiffness construct values for all samples over all cycles, cycles 2-5, cycles 5-10, cycles 10-20, cycles 20-30, and the robust stiffness calculation (over all cycles) during phase 3 of testing at 350 N (stiffness calculated at 500±100 N).

Phase 3 of testing (simulating an A3 fracture) presented non-normal data for both compression tests (Levene's test $P < 0.05$). In these tests, the DTN exhibited significantly higher stiffness levels than the plate for both 350 N and 700 N compression levels (350N: 789 N.mm^{-1} vs 165 N.mm^{-1}, U = 0, $P < 0.001$; 700 N: 823 N.mm^{-1} vs 155 N.mm^{-1}, U = 0, $P < 0.01$).

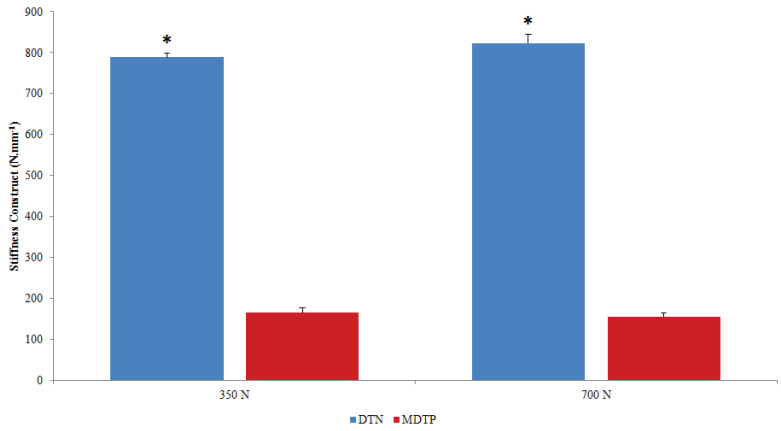

Figure 72: Mean±2SD compressive stiffness for the DTN and MDTP –implanted samples at 350 N and 700 N loading during Phase-3 of testing.

Digital image correlation (Phase-3 compression)

Correlated images were used to assess the **vertical displacement** in the samples displaying the lowest stiffness values for each implant group. The images presented display no displacement followed by maximum displacement for the DTN-X2 (Figure 73 a-b) and MDTP-5 (Figure 73 c-d) samples. In the DTN sample, the fracture gap does not close on the medial side but gap closing appears to be greater towards the anterior face of the tibia while the posterior part of the medial malleolus moves slightly upwards, representing a tilting motion.

For the MDTP sample, gap closure occurs, stemming from the lateral part of the distal fragment, while the medial part remains fixed. It is interesting to note the change in shape of the MDTP implant between 0 N and 650 N compression. In the absence of loading, the plate maintains its original form; however, at 650 N it appears to take on an almost vertical shape.

The medial side movement of the DTN samples remains below 1 mm whereas for the MDTP samples, the IFM measured on the lateral side of the sample was seen to be -2.5 mm and -3.4 mm at 350 N and, -5.2 mm and -9.8 mm at 700 N, for the MDTP-4 and -5 respectively.

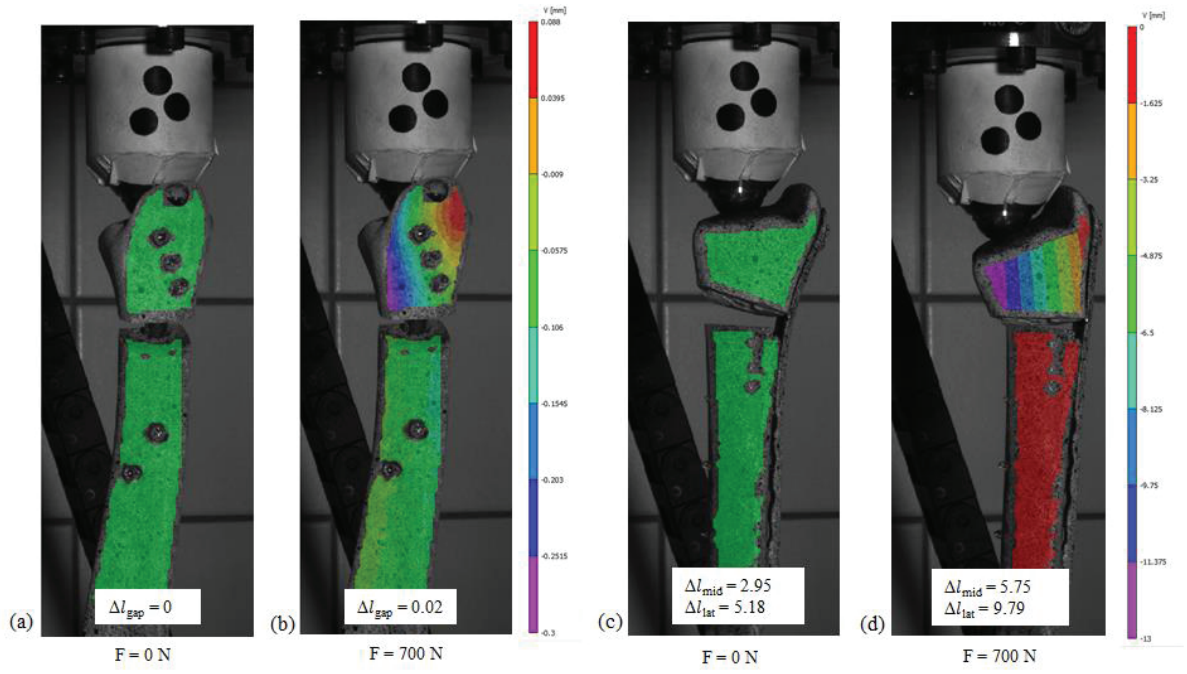

Figure 73: Still images at 0 N (a,c) and -350 N (b,d) for the DTN-X2 (a-b) and MDTP-5 (c-d) to demonstrate gap closing and maximum vertical displacement. Phase-3 of testing, 700 N compression.

The vertical strain around the screw heads of the DTN samples was assessed to identify any differences between the samples with the lowest stiffness (DTN-X2, K = 563 N.mm^{-1}) and highest stiffness (DTN-8, K = 1138 N.mm^{-1}). Differences can be observed in the distal fragment where in the DTN-X2 more negative strain is present around the DTN entry site and the most distal screw, in the DTN-8 sample, this entire region appears to exhibit positive ε_{yy}. Similarly, the DTN-X2 sample demonstrates greater areas of negative ε_{yy} around the proximal screws.

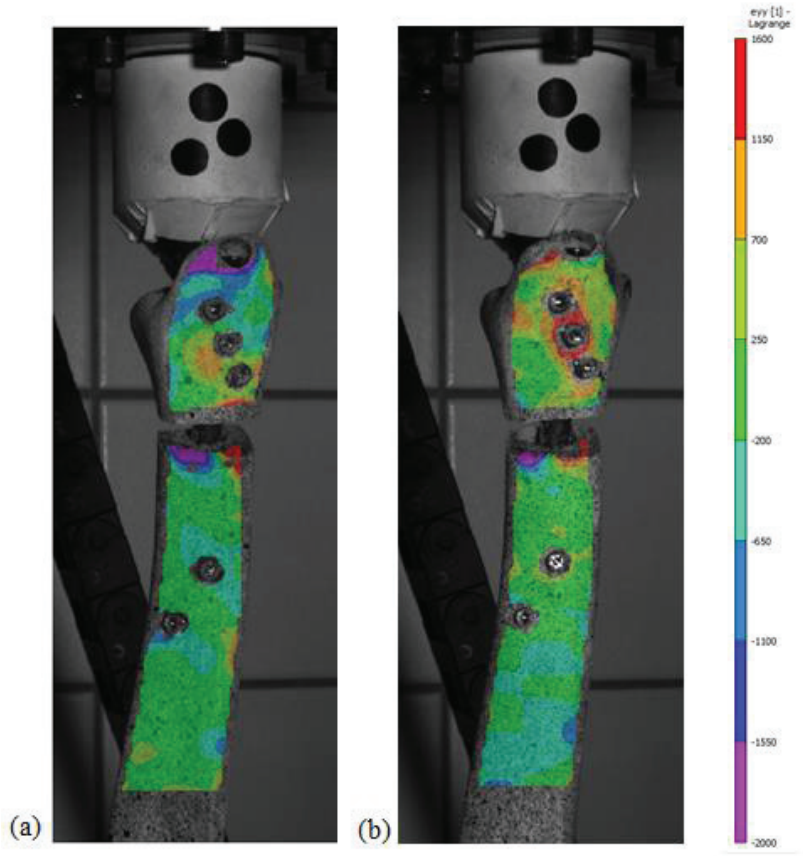

Figure 74: Vertical deformation on the medial side of the samples DTN-X2 (a) and DTN-8 (b) during Phase-3 700 N compression testing. Images are taken at 650 N compression.

±8Nm torsion (phase-3)

As with compression testing, the DTN proved again to have a higher resistance to torsional stiffness (1.33 Nm.deg^{-1} vs 0.71 Nm.deg^{-1}, $t(14) = 16.3$, $P < 0.001$). In particular, the DTN-5 sample demonstrates a high stiffness construct at 1.47 Nm.deg^{-1} while the Plate-7 shows the lowest stiffness at 0.65 Nm.deg^{-}

[1]; this latter value, however does not deviate much from the average MDTP stiffness value, nor from the maximum (0.8 Nm.deg^{-1}, Plate-2).

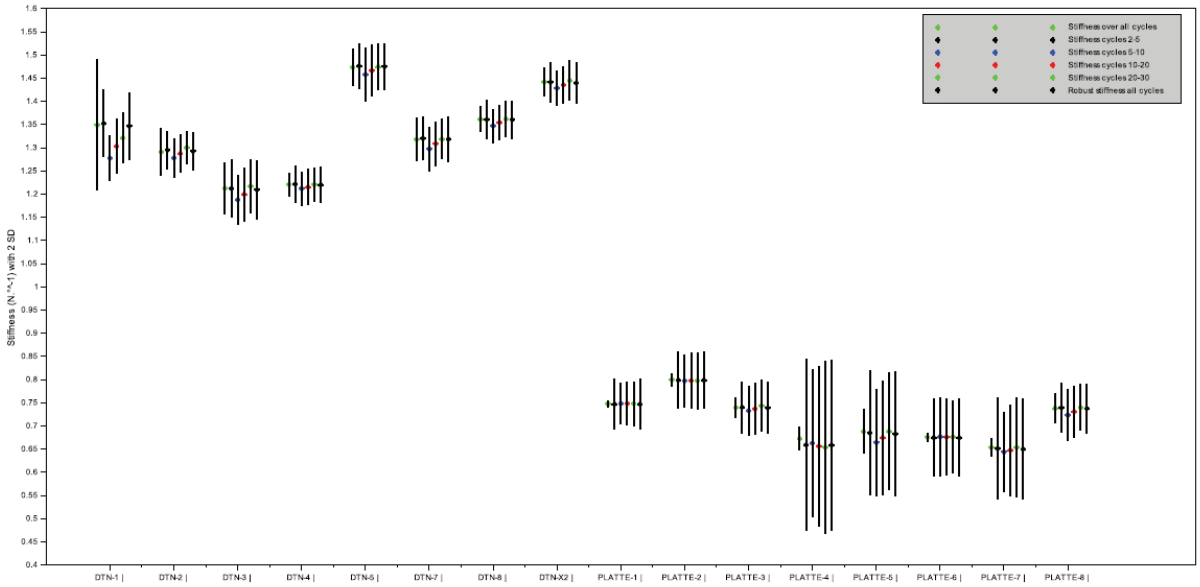

Figure 75: Mean±2SD torsional stiffness construct values for all samples over all cycles, cycles 2-5, cycles 5-10, cycles 10-20, cycles 20-30, and the robust stiffness calculation (over all cycles) during phase 3 of testing at ±8 Nm (stiffness calculated at 6.5±1 Nm).

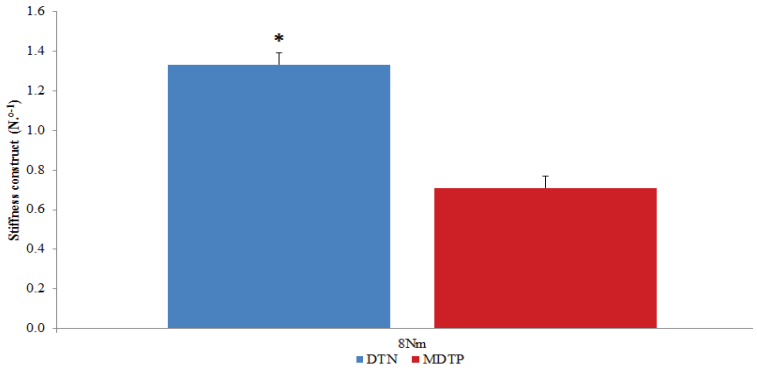

Figure 76: Mean±2SD torsional stiffness for the DTN and MDTP during Phase-3 of testing.

Digital image correlation (Phase-3 torsion)

Shear strain around the fracture gap from the DTN-3 sample appears to have a larger zone of negative ε_{xy} and a greater zone of positive ε_{xy} around the second most distal screw. Positive ε_{xy} increases from 228 to 264 micro-strains between the DTN-3 and DTN-5, in the latter case it appears to be centred on the DTN entry point at the tip of the medial malleolus. Negative ε_{xy} on the other hand, is greater in the

DTN-3 sample (267 micro-strains) compared to 182 micro-strains in the DTN-5 sample. In the DTN-3 sample the most proximal screw head is encompassing by positive ε_{xy} above the screw head and negative ε_{xy} below; in the DTN-5 sample, the opposite pattern is observed.

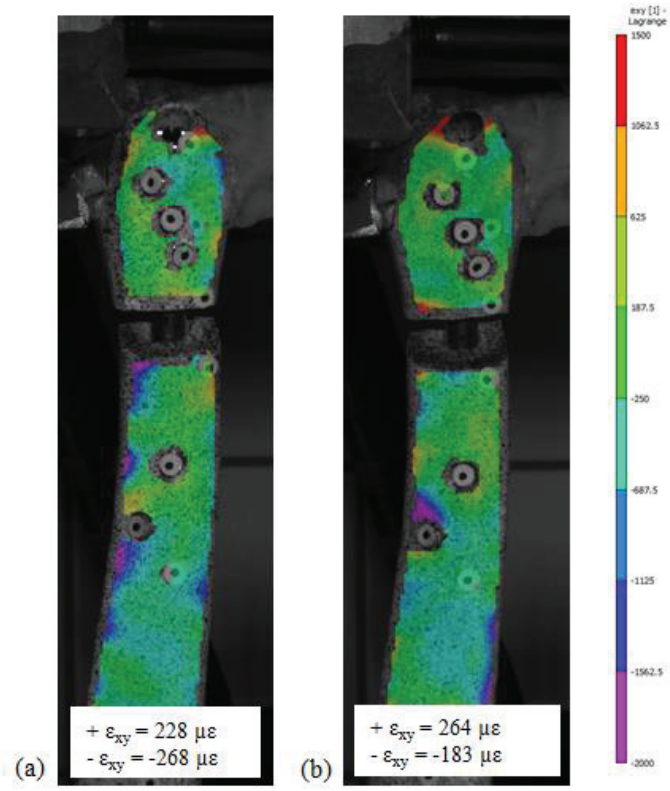

Figure 77: Shear strain distributions during ±8 Nm torsion in Phase-3 of testing for the DTN-3 (a) and DTN-5 (b) samples.

Phase-3 of testing simulates an A3 fracture and the DTN shows significantly higher stiffness constructs for both compressive and torsional testing. This is mirrored in the recorded IFM where the DTN's movement remains <1 mm while the MDTP's was very high, leading to fracture gap closure in some cases.

5. Discussion

Phase-0

Eighteen samples were tested to observe the possible differences between Sawbones® compressive and torsional stiffness constructs. Differences of up to 826 $N.mm^{-1}$ (SD = 13%) in composite bone stiffness for compression testing and 1.2 $N.deg^{-1}$ for torsion were found between samples, suggesting that Sawbones® are not necessarily equal with respect to their mechanical properties. Heiner et al. (2008) and Gardner et al. (2010) performed axial stiffness tests on Sawbones®

4th generation composite tibiae (Heiner et al., medium sized Sawbones®; Gardner et al., large sized Sawbones®). Heiner et al. reported a standard deviation of 9.3% between samples for axial stiffness; in our study we have a standard deviation of 13%.

Heiner however, did report axial and torsional stiffness levels for Sawbones® tibiae stating 7480 $N.mm^{-1}$ for compressive stiffness and 6.13 $Nm.deg^{-1}$ for torsional rigidity. Axial stiffness values are up to six times higher than those measured in the current study. No images and few details were given by Heiner et al, and it is hence difficult to explain from where this contrast originates. Loading conditions (maximal force and loading frequency) were similar to those used in this study, 600 N and 60 $N.s^{-1}$, respectively.

Possible explanations for the difference in results include the loading axis: our study loaded the tibiae in the physiological axis whereas Heiner loaded the samples in the vertical axis. The preliminary study described in Chapter 2 showed increases up to 34% when loading in the vertical axis compared to the physiological axis; while this does not fully explain the 6-fold increase between our results and those of Heiner, it may contribute.

A second possible explanation for the disparity between results is the method used for stiffness calculation. In the present study, very little of the sample was potted in PMMA and therefore it was considered that the calculated stiffness represented the entire length of the sample. Heiner et al. state that samples were distally potted up to 80 mm. No information is given on the potting material, or whether this material was accounted for in calculations; but if the distal portion of the sawbones® is not included in the stiffness calculation, this may increase the stiffness construct as the proximal and distal ends contain the lowest cortical thickness. Eliminating one of these weaker areas will increase stiffness. The disparity between the results of our study and that of Heiner support the notion by MacLeod et al. (2018) that varying boundary conditions can have a substantial effect on reported outcome measures. The latter study reported differences of up to 750 $N.mm^{-1}$ (223%) for the same implant used for the same fracture simulation but with different loading conditions (clamped vs. pinned).

Previous literature (Cristofolini and Viceconti, 2000; Heiner et al., 2001; Gardner et al., 2010) have avoided reporting axial stiffness values for composite Sawbones® tibiae based on the fact that the test setup is prone to induce bending and will not yield reproducible results. The results presented in the present study demonstrate high variations between samples but there is a high level of reproducibility within samples with low standard deviations seen throughout.

Concerning torsional stiffness, again Heiner et al. (2008) are the sole authors to have carried out experiments on medium sized Sawbones® tibiae under torsional loads. They reported a torsional rigidity of 1.93 $Nm^2.deg^{-1}$ - taking into account the length of the sample in the unembedded area (315 mm), this results in a torsional stiffness (irrespective of length) of 6.13 $Nm.deg^{-1}$, falling perfectly into the stiffness

range measured in the present study (5.5 to 6.7 Nm.deg^{-1}). The standard deviation for torsional stiffness reported by Heiner was of 3.6% while in our study, it is of <1%.

Standard deviations in torsional testing at Phase-0 remain relatively unchanged between the different cycles analysed. Preliminary results presented in Chapter 3 put forward the notion that the test setup for torsion is less influenced by external experimental factors (such as PMMA embedding) compared to the compression test setup. The standard deviations presented here may therefore be linked to another factor that was not controlled for in the test setup, such as machine clamp tightening torque, which can place a pre-strain on the sample.

Phase-1

Ettinger et al. (2018) are the only authors to have conducted biomechanical tests on implants used for MWO in-situ. The MDTP was one of the implants (fixed to Sawbones® samples) used in their study and the authors reported an axial stiffness construct of 2182 N.mm^{-1} (2182 kN.mm^{-1} is reported in their article but this is an error of units used and the disparity is evident between the reults and dicussion sections), compared to 1641 N.mm^{-1} – the maximum calculated stiffness value in the present study. This 1.3-fold increase may have been influenced by the 11-fold difference in loading frequency, our study loaded samples at 0.05 Hz to 700 N (70 N.s^{-1}) while Ettinger et al. loaded up to 800 N at 0.5 Hz (800 N.s^{-1}). Furthermore, Ettinger et al. controlled for the amount of lateral cortex remaining post-osteotomy and set this to be 5 mm. In our study, the lateral cortex area was not regulated but it is estimated to be less than 5 mm. Nonetheless, the figures reported by Ettinger et al. fall into a similar order of magnitude as in the current study.

Measured torsional stiffness by Ettinger et al. agrees with data presented in the current study (Ettinger: 3.53 Nm.deg^{-1} for loading at 0.25 Hz to 5 Nm; present study: 3.64 Nm.deg^{-1} for loading at 0.1 Hz to 4 Nm). In this scenario, the difference in loading frequency (Ettinger: 2.5 Nm.s^{-1}; current study: 0.8 Nm.s^{-1}) did not appear to affect recorded stiffness values.

The present study compared the DTN to the MDTP in compressive and torsional testing for supramalleolar osteotomy fixation. The MDTP proved to be significantly higher in torsional stiffness construct at 4 Nm but at 8 Nm and during compression testing, no statistically significant differences were found. Differences in interfragmentary movement (IFM) for each sample group are low in Phase-1 of testing with differences of 0.02 and 0.01 at 350 N and 700 N compression, respectively. In light of these results, the DTN can be considered as a fixation option for supramalleolar osteotomy (SMOT) where the medial wedge opening osteotomy (MWO) surgical approach is used. The DTN may offer additional advantages to the MDTP as its intramedullary position preserves vascularisation on the medial tibia – an area often damaged by the MDTP.

Phase-2

During Phase-2 of testing, a fracture was simulated in the lateral cortex to imitate a worst-case scenario for MWO. In many cases for the samples instrumented with a MDTP, no gap was left between the proximal and distal fragments due to the compression created by the plate; the fragments were nonetheless free to move independently. When placed in the torsion test setup, the tightening of the clamps around the sample often resulted in placing a tensile force on the sample and pulling the fragments apart, leaving no contact between the fragments.

The significant differences in stiffness constructs between the MDTP and DTN amount to differences in displacement of 0.03 mm at 350 N and 0.01 mm at 700 N in Phase-2 of testing where the lateral cortex is fractured; these differences are minimal and suggest that the DTN offers equal construct stability to MWO than does the MDTP. Furthermore, the allowance of greater vertical IFM may be advantageous to the bone remodelling of the osteotomy. As demonstrated using DIC, the DTN samples demonstrate higher compressive ε_{yy} levels to the fractured lateral cortex and these levels of vertical strain remain within the cited physiological zone for bone remodelling (500 – 2000 micro-strains; Duncan and Turner, 1983). The MDTP samples display, at the most, only half of this strain. Likewise, torsional stiffness is greater in the DTN samples – being more valuable in preventing shear strain. Shear movements are known to be harmful to bone remodelling if they exceed axial strain levels (Epari et al., 2006).

Attention is drawn to the MDTP-1 sample, which displayed the lowest stiffness among all MDTP samples and yet less IFM was detected here than in the MDTP-4 sample (having demonstrated the highest stiffness construct). Consequently, it would appear that the high displacement detected by the testing machine transducer does not stem from the fracture gap but from another experimental parameter linked to the implant or the test setup.

Phase-3

During Phase-3 of testing, all MDTP samples demonstrate very low stiffness and little difference is shown between the sample stiffness constructs. These results are in agreement with previous studies comparing the DTN and MDTP for A3 fractures (Kuhn et al. 2014) and highlight the unsuitability of the MDTP for unstable extra-articular fractures both with respect the cited stiffness constructs and IFM.

Other studies having measured the biomechanical performance of locking plates for A3 fractures report stiffness constructs of 466 $N.mm^{-1}$ (Högel et al., 2012), however in this study much less IFM was reported (1 mm compared to our 10 mm) possibly due to the lower loads and loading frequency (350 N at 10 mm/min). Kuhn et al. 2014a measured the same MDTP against the DTN in a test setup using one proximal spherical joint and a cardan joint at the distal end. The MDTP averaged at 213 $N.mm^{-1}$ and 0.39 $Nm.deg^{-1}$ for axial and torsional stiffness, respectively, falling into a similar range as in the current

study (155 $N.mm^{-1}$ and 0.71 $Nm.deg^{-1}$). Stiffness constructs for the DTN were equally as similar: 888 (Kuhn) versus 823 (present) $N.mm^{-1}$ for axial stiffness, and 1.83 (Kuhn) against 1.33 $Nm.deg^{-1}$ (present).

Snow et al. (2008) reported compressive stiffness values two times greater than those reported in this study (1500 $N.mm^{-1}$) for a an LCP. Their study consisted of a dynamic compression plate over a simulated 10 mm fracture gap in osteoporotic composite bone (Synbone®, Malans, Switzerland). Forces of 350 N were applied over 5 Hz producing a loading frequency of 1750 $N.s^{-1}$ compared to our 35 $N.s^{-1}$, despite the use of weaker osteoporotic composite, the higher loading frequency (50-fold higher) can produce a far higher stiffness construct. It is important to note also that Snow et al. used samples of a different length and diameter to ours as well as with different material properties, all of which play a role in mechanical stiffness.

The MDTP-1 sample demonstrated the highest stiffness values for 700 N testing in Phase-3 but on closer inspection of this sample, it became clear that this was due to contact between the proximal and distal fragments causing a sudden increase in stiffness construct and therefore falsifying the average.

Compressive vs torsional stiffness

Preliminary torsional stiffness (Phase-0) did not seem to have an influence on calculated stiffness constructs during later testing phases – samples demonstrating high torsional stiffness in Phase-0 did not continue to do so in Phases 1-3. However, this is not the case for compressive stiffness where samples such as the DTN-4 and MDTP-1 carry their stiffness through to Phase-1 of testing.

We notice, however, that samples presenting low compressive stiffness demonstrate a high torsional stiffness, and vice versa, particularly in Phase-2 where all MDTP samples display high compressive stiffness values whereas the DTN samples exhibit high torsional stiffness values, both differences proving to be statistically significant. The MDTP-1 sample displays the highest torsional stiffness for Phases 1 and 2 (at 4 Nm only for Phase-2) and DTN-8 shows the lowest torsional stiffness in Phases-1 and 2 (at 8 Nm only for Phase-1). Both of these samples exhibited the opposite behaviour during compression testing.

Compressive stiffness depends primarily on the surface area over which the force is applied, whereas torsional stiffness depends on the moment of inertia. For a given area to which a *torsional* load is applied, it is the distance of this area from the axis of rotation which will dictate whether the stiffness is higher or lower. It may therefore be the factors linked to the differing osteotomies and implant positions may explain the inverse relationship between compressive and torsional stiffness, related to load axis and implant position rather than sample geometry. This will be evaluated in the following chapter.

One explanation for the differences between compressive and torsional stiffness for the DTN samples is related to the positioning of the screws and the 0.8 mm gap left from the difference in screw

and pilot hole –diameter (3.2 mm and 4 mm, respectively). If the screws are placed against the proximal edge of the nail (Figure 78a), this will prevent movement in the vertical axis and result in high compressive stiffness but low torsional stiffness as there is still room for the nail to move medio-laterally. In this case there is still scope for the nail to move in the vertical axis but due to the quasi-static loading frequencies used in this study (0.05 Hz and 0.1 Hz), this is unlikely.

A screw placed against the medial or lateral border of the screw hole (Figure 78b) will result in (for example) high positive torsional stiffness but low negative torsional stiffness and low compressive stiffness. If the screw is perfectly placed at the centre of the screw hole (Figure 78c), movement is permitted in the proximo-distal and medio-lateral axes.

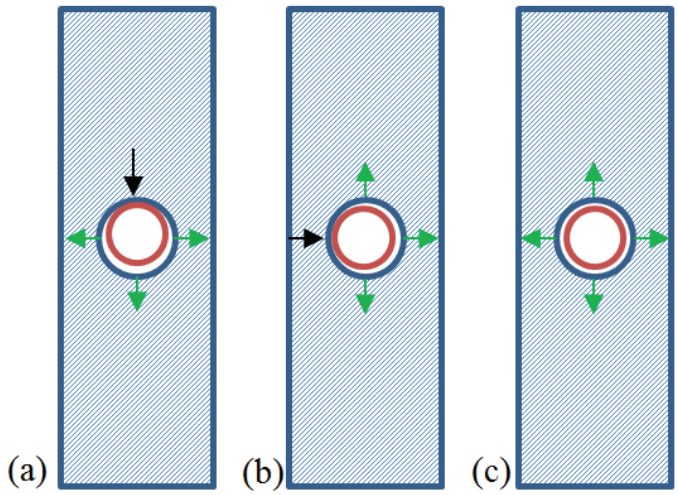

Figure 78: Screw placement examples influencing construct stiffness. The black arrows represent where the screw is blocked against the DTN; the green arrows indicate where movement is possible

Due to the local artefacts around the screws and implant in the CT scans it is not possible to measure the screw position with the current data. However, x-ray images could be taken in order to assess this. Unfortunately, during a surgical procedure in living patients, the surgeons have little scope to control screw positioning at this level of precision.

Limitations

There are still many parameters of the setup that were not controlled for (but have been evaluated in Chapter 2), such as setup stiffness, sample placement, potential PMMA influences, and sample placement-replacement. It is therefore not possible to state whether inter-sample differences for a specific phase of testing are due to the bone-implant construct, or to variations in test setup. The torsion test setup was little studied prior to the main series of testing taking place due the nature of the test setup (difficult to modify) and the initial tests from chapter 2 showing that the PMMA stiffness was little affected by torsional loads.

The boundary conditions for the compression test setup consisted of two spheres placed at the proximal and distal ends of the sample which drastically reduced parasitic torques influencing the sample's mechanical behaviour and makes for a reproducible test setup, for example in the case of numerical model development. Ideally, a 6-axis sensor would be used to measure the parasitic reactions. For torsional testing, force and torque transducers were used and z-axis displacement and rotation were recorded; however, the fixation of the sample extremities leaves four unknown components.

In Phase-2 of testing, the lateral cortex of all samples was cut using a 0.5 mm coping saw. However, the tightening of the sample in the machine clamps repeatedly caused vertical forces to be detected by the force transducer. During torsional testing, compressive forces of -5 N to -6 N were applied per cycle. At the start of each test, the actuator automatically regulates itself to apply -5 N to the sample. In light of this, after clamping the sample in the testing machine, the actuator was manually repositioned until a compressive force between 0 N and -5 N was detected by the load cell. In some cases, this resulted in the contact of the proximal and distal fragments of the lateral cortex; in other cases the gap was maintained. Nonetheless, this signifies that the boundary conditions were not identical for all samples and this may explain the high standard deviations witnessed in all samples.

The MDTP-1 continuously proved low in compressive construct stiffness, however in this sample the simulated osteotomy was atypical with the distal cut being parallel to the distal articular surface whereas the standard procedure would be to cut the osteotomy at an incline. The sample was cut in such a way after a failed attempt at creating an osteotomy template; it was nonetheless kept in the MDTP sample group to maintain the $n = 8$ samples per implant group after the two reserve samples (X-1 and X-2 were required to replace a DTN sample). The osteotomy may explain why the MDTP-1 sample displays the lowest stiffness constructs for Phase-1 and Phase-2 of testing and will have slightly falsified the average stiffness calculated for the MDTP implant group. Nonetheless, this will require further investigation as the MDTP-1 sample displayed very little IFM across the fracture gap in Phases 1 and 2 of testing.

Initially, we had planned to evaluate the outcome measures using displacement data collected from the markers placed on the machine clamps; however these data appeared to present lower stiffness constructs (and higher displacement levels) than the machine data. The machine data takes into account all the gaps and deformation of the machine clamps between the displacement transducer and the sample while the cameras. It would therefore be expected that lower displacement be registered by the cameras as the markers were placed directly above the sample. In light of this, only the machine data was used. It is possible that the machine manufacturer applies a scaling factor to the displacement transducer in order to account for its position being far from the sample. Displacement data may therefore be exaggerated; in this case, the difference is constant, at approximately 0.2 mm (Figure 79). We can,

however, observe and be reassured by the similar pattern that the machine and marker data follows, indicating that it is a systematic, rather than random, error differentiating the two.

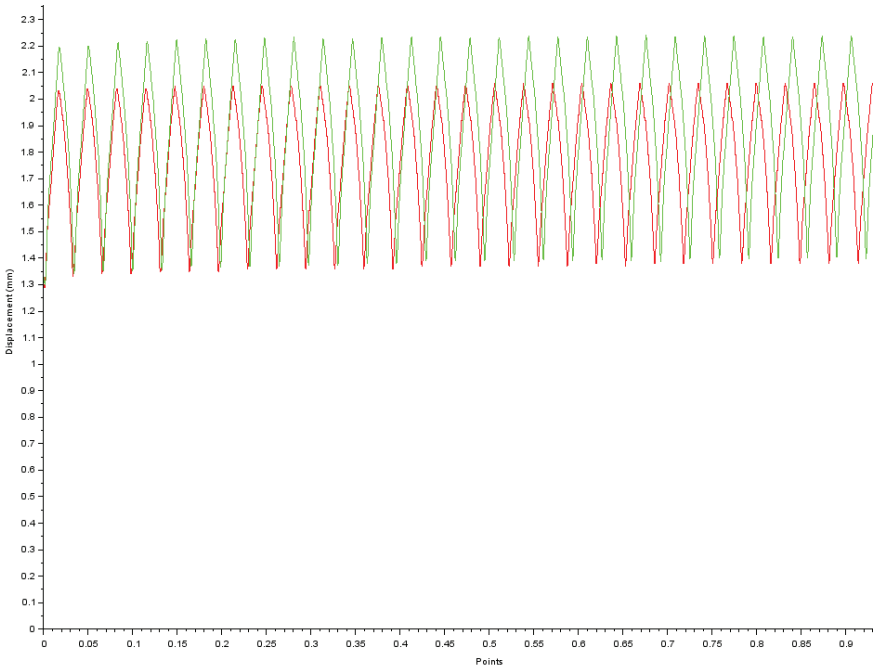

Figure 79: Differences in machine (red) and marker (green) displacement during compression testing.

It may have been equally as relevant to film the anterior side of the DTN samples during Phase-3 compression testing as the DTN implant is inserted into the medial malleolus. It is therefore possible that any fracture gap movement would be observed on the lateral or anterior faces. This might be reflected in Figure 74 where the DTN samples demonstrate tensile strain on the medial tibia; on the contrary, the compressive strain may lie on the lateral side.

For all samples, only the distal 40% of the sample was visualised and correlated, although the cited stiffness constructs are based on the entire sample with its PMMA embedding. This decision was made in order to increase post-processing speed (by decreasing the image size) and to be able to apply a finer speckle pattern for more precise strain calculation. However, this results in the loss of information of the entire sample and may have helped to explain the extra-ordinary stiffness results displayed for the MDTP-1 sample.

Only two samples were taken for DIC during each phase of testing to represent the corresponding implant group. As the osteotomy size and shape were not correctly controlled for, the results presented should be considered with caution as it is difficult to generalise for all samples based on the results here presented. Further work in this domain is planned to perform DIC analyses on all samples and subject the strain results to statistical testing in order to try to explain the differences between inter and intra –sample group results.

6. Conclusion

In light of the results presented from IFM in Phases 1 and 2, it seems clear that the DTN can be considered for MWO. Its IFM results (<1 mm) remain below the 2 mm threshold (Billard et al. 2014; Gruszka et al., 2017, Nyary and Scammell, 2018), and although the positive and negative ε_{yy} levels were greater than that observed in the MDTP sample and across a more concentrated area. The use of the MDTP for A3 fractures is discouraged, in agreement with previous studies (Kuhn et al., 2014a; Sathiyakumar et al., 2014), due to its weak resistance against both compressive and torsional loads, and an increased need for secondary surgery.

Fracture gap movement, although generally higher for the DTN samples in Phases 1 and 2, still remained <1 mm – this result in particular questions the significant difference observed between the DTN and MDTP samples for the calculated compressive stiffness construct.

Perspectives

Using the CT scans taken of the healthy and instrumented samples (at Phase-1), the next step is to evaluate the geometric, material, and loading properties of all samples in order to try and explain the differences in stiffness constructs stated in the current chapter. Factors relating to the samples, surgical technique and test setups will be analysed.

No measurement of the fracture/osteotomy gap reduction was performed during torsional testing due to time constraints; however, further analyses of this data are planned to measure the shear movement by comparing the positive and negative x-direction movements of the proximal and distal fragments.

Chapter 4: Geometrical study and statistical analysis of parameters influencing bone-implant construct stiffness

1. Introduction

During the biomechanical tests carried out at the UMC Mainz, Computer Tomography scans of all samples were carried out before and after implantation of each sample. This was done to be able to quantify the geometric properties of all bone-implant constructs and measure the influential parameters likely to have an effect on their stiffness. The results detailed in Chapter 3 show that the boundary conditions could have a large influence on the sample stiffness if they are not controlled for. Testing setups and protocols were controlled to the greatest possible extent based on the time frame and available materials dedicated to the project. The aim of this part of the project is to identify the key factors having the greatest influence on sample stiffness through statistical analyses. Geometric as well as material and test setup properties are quantified and tested.

2. CT scan to 3D reconstruction

2.1. Computer tomography (CT) scanning

Computer tomography is a three-dimensional imaging technique often used in clinical settings to visualise a 3D area of the body. CT scans are essentially a series of 2D images taken through x-ray imaging; the x-ray source sends multiple rays towards a detector, the number of x-rays received by the detector give an insight to the density of the material being scanned. The lower the number of x-rays detected, the greater the density of the material, and vice versa; this technique allows clinicians and scientists to differentiate between different materials of the same object such as cortical and trabecular bone, or a soft tissue and a tumour. The 3D images are represented as volumes commonly referred to as slices; slices are made up of voxels – essentially 2D pixels with a depth component.

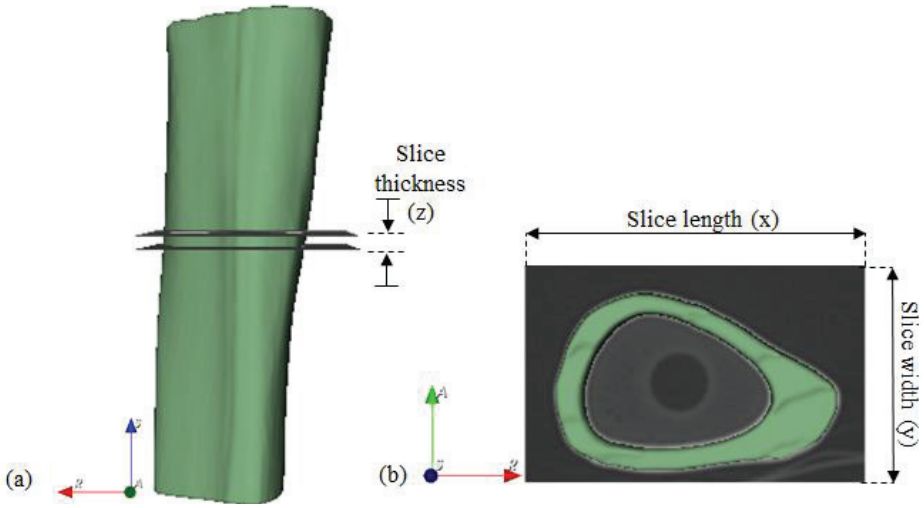

Figure 80: CT scan slice components. The tibial diaphysis is used as an example.

The performance characteristics of a CT scanner depend on slice thickness (the z-component of the x-ray image) and the slice resolution (the number of voxels making up the x and y –components) (Figure 80). At the UMC Mainz, the CT Brilliance iCT scanner (Philips Ltd, Hambourg, Germany), was used to scan all samples, one voxel corresponding to 0.96 x 0.96 x 0.67 mm.

Implant CT scans

In order to obtain uniform models of each of the implants used in this study, a CT scan for all the implants was carried out. The scans were imported into 3D Slicer (version 4.10.2; Fedorov et al., 2012) where a threshold of 2313 to 3071 was applied to obtain only the implant geometries. Once the geometries had been selected and corrected for artefacts, the meshes were exported to Meshlab (version 2016, Cignoni et al., 2008) non-manifold edges and vertices were identified and corrected for.

Mesh smoothing took place using the Taubin smooth (Taubin, 1995) and quadratic edge collapse (QEC) decimation techniques, respectively. The meshes were then refined using the Butterfly subdivision method. Nodes regrouping a high number of adjacent elements were subdivided at the midpoint to add extra nodes. After each of these procedures Taubin smoothing and QEC were reapplied. Isolated elements were located and deleted; hole in the mesh were also located and subsequently filled. The mesh around the filled holes was then separately treated using the above procedure. Following this treatment, the DTN consisted of a total of 14,000 tetrahedral elements, and the MDTP 20,000 (Figure 81).

Figure 81: Final models of the DTN (a) and MDTP (b).

2.2. 3D model reconstruction

2.2.1. CT scan segmentation

The CT scans performed before implantation (healthy samples) and after implantation (implanted samples) were segmented in 3D Slicer. The healthy samples consisted of three materials to segment, while the implanted samples consisted of four. A summary of these materials can be found in Table 9. The thresholds used relate to the greyscale levels were determined by importing the scans into ITK-SNAP (Yushkevich et al., 2006; www.itksnap.org) software and running a Gaussian mixed evaluation of the different greyscale levels (Figure 82).

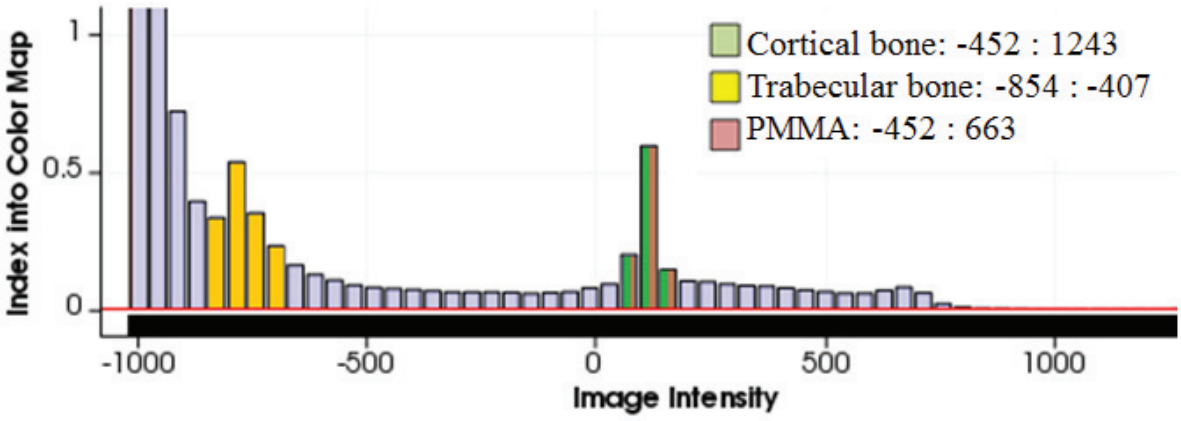

Figure 82: Greyscale level identification of the different elements for segmentation.

.

Table 9: Parameters used for the segmentation of the different bone-implant construct components.

Material	Healthy samples (number)	Instrumented samples (number)
PMMA embedding resin	18	16
Cortical bone	18	16
Trabecular bone	18	N/A
Implant (Titanium)	N/A	16

Trabecular bone was not segmented in the implanted samples due to high artefacts resulting from the metal implants in the CT scanner. All areas in proximity to the implant were affected by artefacts, rendering the identification of the different materials (cortical and trabecular bone) very difficult. Cortical bone was nonetheless segmented but highly affected areas were manually reconstructed based on surrounding areas less impacted by the artefacts.

2.2.2. Reconstruction

The same procedure as described in §2 was applied to the scanned Sawbones® in order to obtain whole bone models.

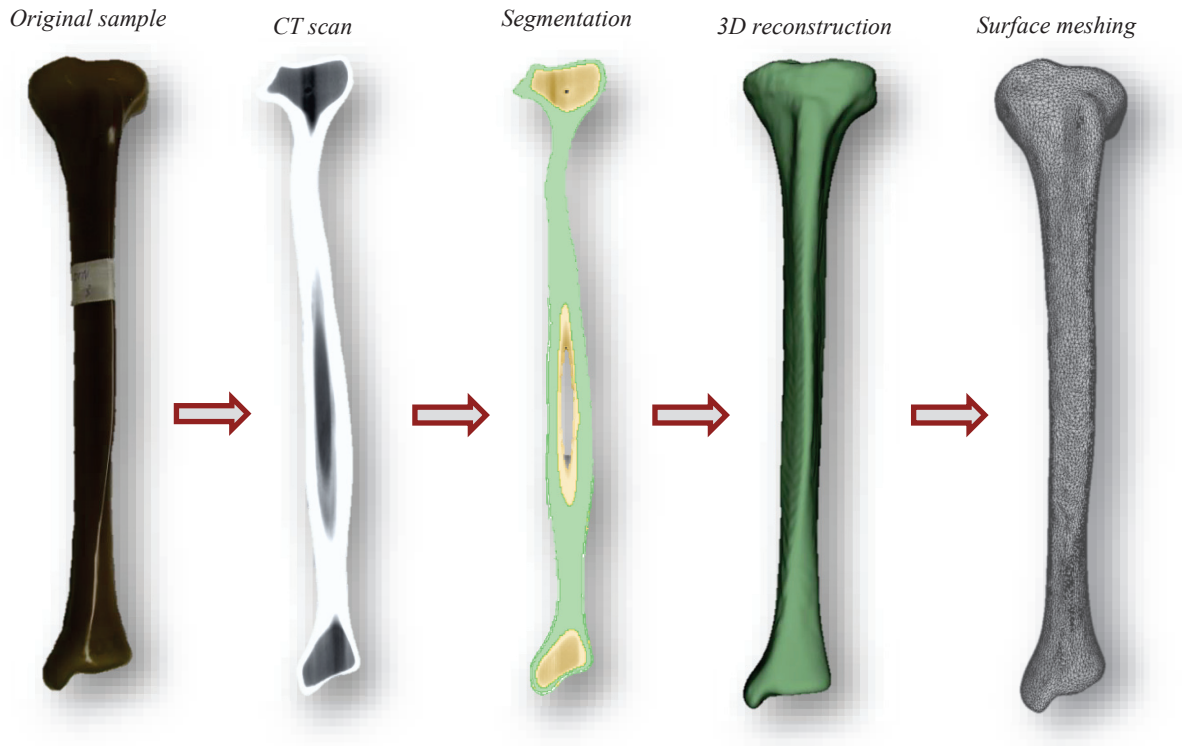

Figure 83: Sample digitalisation procedure.

3. Coordinate systems

3.1.1. Tibial landmark identification

The International Society of Biomechanics (ISB) recommendations for anatomical landmarks (Wu et al., 2002) on the tibia include the lateral and medial malleoli, the inter-malleolar point (midpoint on an imaginary line connecting the lateral and medial malleoli), the tibial tuberosity, the lateral and medial condyles, and the intercondylar point (midpoint on an imaginary line connecting the lateral and medial condyles). Due to the osteotomy at the distal end of the tibia and the possibility that the implant may have altered the position of the distal fragment, only landmarks on the proximal tibia were chosen as these were considered not to change before and after the osteotomy.

User-defined landmarks were used to place all samples in the same coordinate system in order to facilitate the comparison between geometrical measures. Using the CloudCompare open source software (version 2, https://www.danielgm.net/cc/), geometric structures were fitted to the regions of interest of the tibia. The software permits the user to select a region of interest which is then transformed into a point cloud with a user-specified number of points (for this study, n = 1 million). A shape is then fitted to this point cloud; the options involve a cylinder, square, sphere, torus or cone. Multiple variations of the same shape are fitted to the point cloud using the Random Sample Consensus shape detection method (Schnabel et al., 2007) and the user can select the shape, which they consider to best represent the region of interest; geometric properties of this shape can then be exported.

Bone coordinate system

Three geometric features were identified on the proximal tibia: 1/ a cylinder representing the axis of the diaphysis, 2/ a plane covering the tibial plateau, and 3/ a reference point representing the midpoint between the barycentre of each outer extremity of the lateral and medial condyles (Figure 84). The z-axis represented as the normal between the x and y axes (following the right-hand thumb rule) was calculated by taking the cross product of the x and y axes. Finally, the vertical axis of the sample was defined as the z-axis with the x-axis represented the medio-lateral axis and the y-axis being the antero-posterior axis.

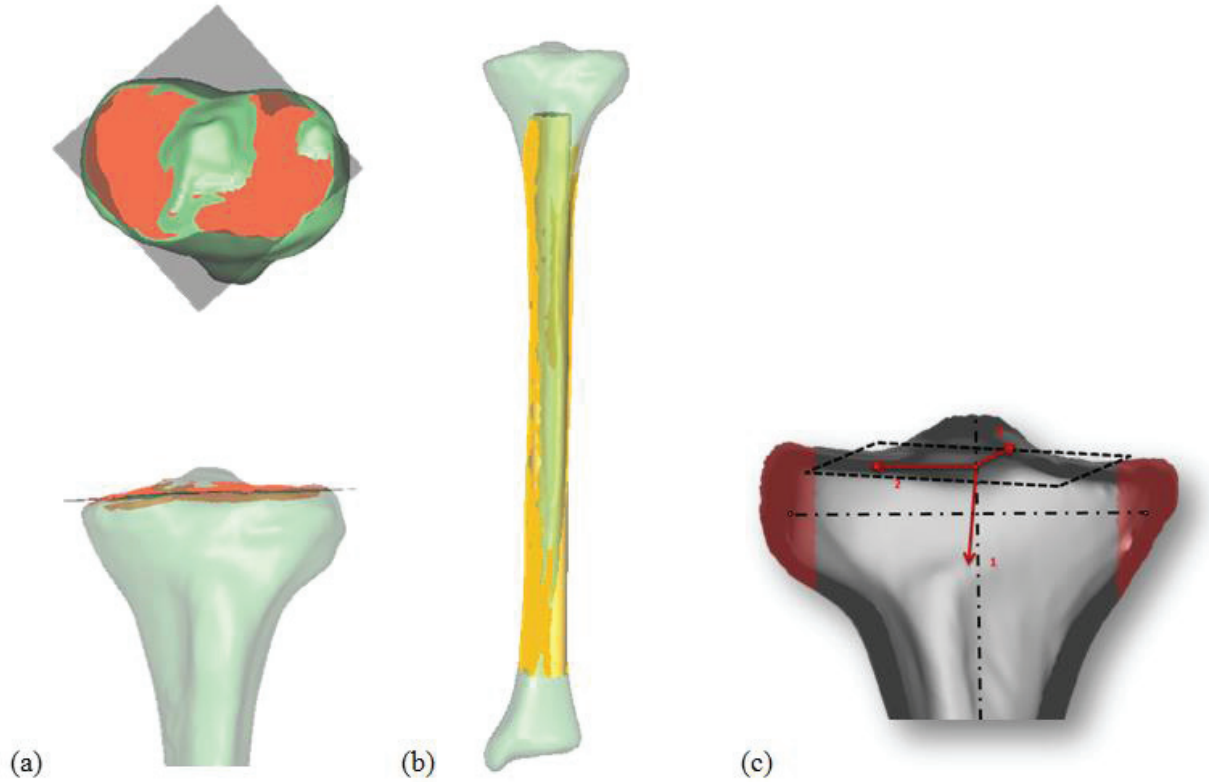

Figure 84: Geometries used for axis definition. The tibial plateau modelled as a plane (a), and the diaphysis as a cylinder (b); Bone coordinate system definition (c) with three axes based upon the intersection of the diaphysis axis with the tibial plateau plane.

Implant coordinate system

Given the very different geometry between the DTN and the MDTP, easily distinguishable landmarks were required. For simplicity's sake, the most proximal, the most distal, and the most lateral point on all implants were identified (Figure 85).

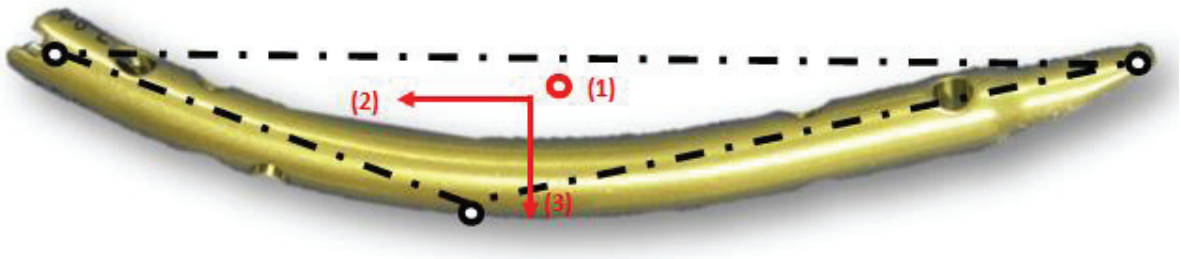

Figure 85: DTN implant coordinate system with three axes based upon the normal axis to the centre of the three identified points (1; y-axis), the axis joining the proximal and distal extremities of the implant (2; z-axis), and the normal axis of the first two (3; x-axis).

Loading axis coordinate system

The loading axis in compression testing was experimentally defined by a hole in the PMMA created during the embedding process. The location of this hole remained constant within the PMMA but the sample had a possibility to move slightly within the template during potting. The loading axis was defined by the line connecting the proximal and distal loading points (Figure 86).

During compression testing, the distal loading point was the 9 mm diameter opening of the Sawbones® on the distal articular surface, present from manufacturing. Performing the reconstruction of this entry point in a reproducible manner on the implanted samples was not possible owing to artefacts from the metal implants. In order to retain the same method for the distal loading point, three geometric shapes were created on the distal tibia to generate a loading point (Figure 86b) with the distal entry point being modelled as a planar surface following the selection of a zone of points around this area (Figure 86a). For torsional testing, the axis of rotation was considered to be the sample's vertical axis.

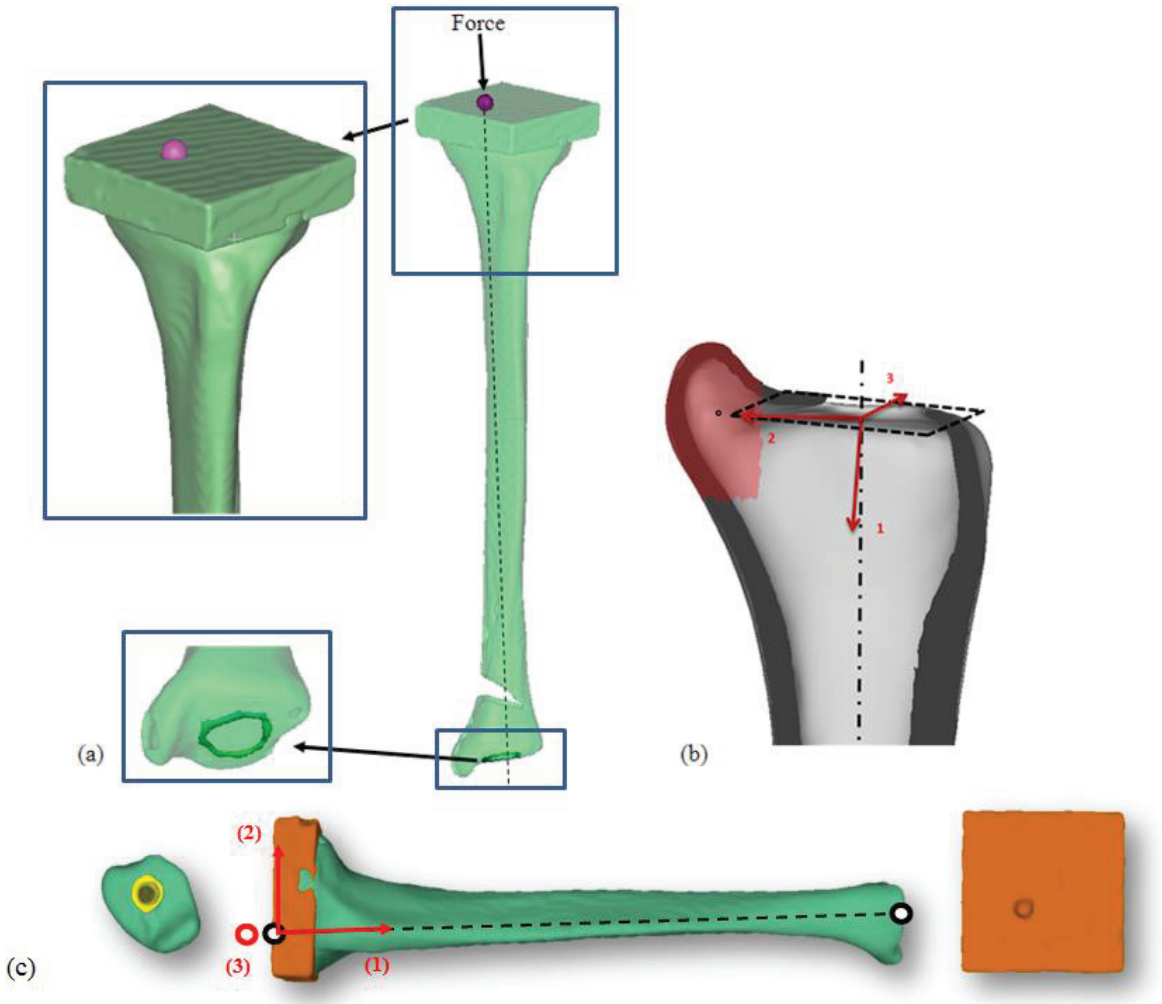

Figure 86: Geometries used for axis definition. The proximal load application point modelled as a sphere (a, above), and the distal loading point modelled as a plane (a, below); the barycentre of the area used for the medial malleolus (b). The loading axis coordinate system (c), calculated by taking the connecting line between the loading points (1; z-axis), the horizontal planar axis of the PMMA block (2; x-axis), and the normal axis to the two latter axes (3; y-axis).

4. Influencing parameters

Five influential factors were identified for the healthy samples in compression, seven factors for torsion, and 11 (10 for the MDTP) for the implanted samples. For factors relating to the geometry of the bone and the implant, and the test setup, it was necessary to identify a series of reliable landmarks, easily recognisable on all samples.

– *Loading axis position / central axis*

All samples were embedded in PMMA using a custom-made template to ensure the repeatability of this procedure. The proximal embedding was done with the addition of a 8 mm hole placed at 10 mm medial and posterior to the centre point of the PMMA block; as aforementioned, this position sought to replicate the 60:40 % loading differences during compression between the medial and lateral condyles of the tibial plateau, respectively (Rastetter et al., 2016; Moewis et al., 2018). Nonetheless, a 3 mm gap was still possible along the frontal axis of the tibia (cf. chapter 2). The reliability of the loading position in the medio-lateral axis is therefore compromised.

Figure 87: Loading (red) and central (blue) axis differences.

It was considered that the most distal point of the loading and central axes fell at the same point on the tibia and that the distance between these two axes was greatest at the superior surface of the PMMA (Figure 87). The angle (θ) between the axes was calculated using the following equation:

$$\theta = \text{acos}\left(\frac{Ux \times Vx + Uy \times Vy + Uz \times Vz}{\|\vec{u}\|.\|\vec{v}\|}\right)$$

Equation 1

Where U and V represent the three components of the loading and central axes, respectively. The torsional loading axis (axis of rotation) is considered as the sample's central/vertical axis (indicated in blue in Figure 87).

– *PMMA thickness*

Following results presented in Chapter 2 on the thickness of PMMA and its influence on construct stiffness due to the low stiffness of this material, the thickness of the PMMA layer at the load application point was investigated. Prior to this, the contact point of the metal sphere was analysed. Given the constant diameter of the sphere, the constant diameter of the drilled hole in the PMMA yet its varying depth, it was possible in some cases that the metal sphere was in contact only with the upper border of the drilled hole, or in other cases – the base of the drilled hole (Figure 88). The criterion could change the thickness of the PMMA layer above the cortical bone.

Sphere contact was measured using the following equation:

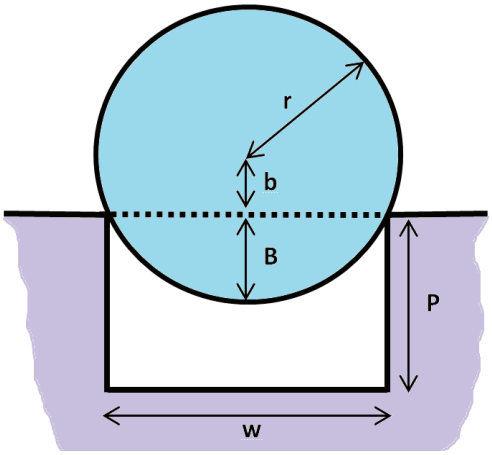

Figure 88: Schema diagram demonstrating the calculation of sphere-PMMA contact.

$$B = r - \sqrt{r^2 - \frac{w^2}{2}}\ , if\ B < P\ then\ border\ contact; if\ B > P\ then\ base\ contact$$

Equation 2

Where B is the linear portion of the sphere radius situated inside the drilled hole, b is the remaining portion the radius in that same position; the diameter and depth of the hole are represented by w and P, respectively. The PMMA thickness at the loading point was then measured by taking the distance P in Figure 88 using the measuring tool in 3D Slicer.

– *Material volumes*

In Slicer3D, the total material volume consists of the mean of all voxels included in the segmentation of that material. The total volume of the PMMA and cortical bone were used for both healthy and implanted samples. Trabecular bone volume was only taken for the healthy samples; this information was not available in implanted samples due to metal artefacts in the CT scan. The volume of the implant was considered to be constant and therefore negligible to this analysis.

– *Material densities*

As with material volume, material density for PMMA and cortical bone was extracted from the segmented parts in both healthy and implanted samples. Information on trabecular bone volume was only collected in healthy samples. The mean density for each segmented element was exported from 3D Slicer.

– *Implant position*

The implants' position was measured with respect to the distance from the lateral inner cortex. Experience from previous experiments at the UMC hypothesised that if the DTN is in contact with the inner cortex of the sample, a higher stiffness construct is produced due to the friction between the

implant and the bone material (trabecular or cortical bone). To analyse this, the minimal distance between the implant and the cortical bone was taken in the region between the two proximal screws of the DTN. The choice of this region allowed for the repeatability of the selected area for analysis. Distance was calculated with respect to the cortical layer as no trabecular segmentation was possible for the implanted samples.

This procedure was only carried out for the DTN. It was assumed that the MDTP was in complete contact with the out cortex of the medial tibia. This parameter was measured by using a realignment procedure described hereafter.

- Implant realignment

The segmented implants and screws from the current CT scans contained many artefacts and were therefore replaced with previously segmented implant; hereafter referred to as the clean implant). The realignment procedure took place in Meshlab using the brutal iterative closest point method. This module allows the user to select two geometrically similar forms and realign one form to its target form; in this case, the clean implant was set to be aligned with the segmented implant relative to the test sample.

Realignment of the implants (Figure 89) meant that the position and orientation of the implant within the sample could be calculated without the parasitic influence of artefacts that gave the segmented implant an inexact shape that varied between samples whereas we know that the shape remains constant. The image in Figure 89 is an example of the realignment with the DTN-1 sample with a maximum error of 0.03 and this is mainly located where the screws are. In the segmented model, the screws are present whereas in the clean model there are no screws; hence, realignment error is greatest here.

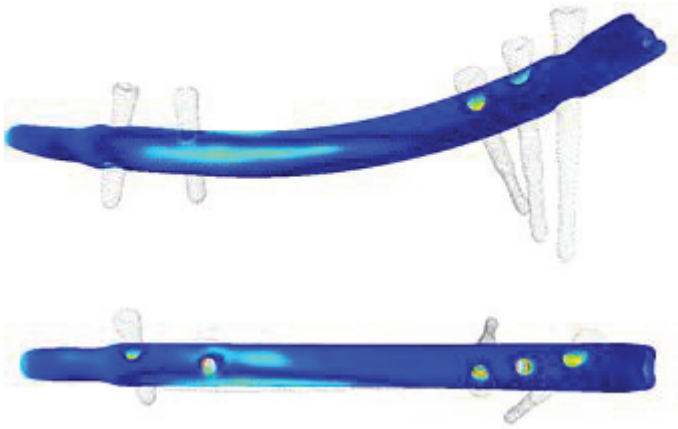

Figure 89: The alignment of two geometrically identical implants. The colours are based on mesh-to-mesh realignment; blue represents low error while red represents high alignment error.

– *Lateral cortex area*

Simulation of the medial wedge opening osteotomies was manually performed without a template to ensure that the same amount of lateral cortex material was remained. The CT scans were used to measure the area of the intact lateral cortex. This area was identified by scrolling through the sample CT images from distal to proximal; the first slice in which the lateral and medial cortices were not connected (Figure 90) was considered as the smallest remaining area.

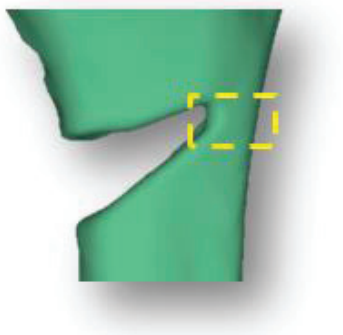

Figure 90: Lateral cortex area measurement from CT scan data.

– *Healthy sample stiffness construct (phase-0 stiffness)*

Since the calculated stiffness constructs for the healthy samples varied (cf. Chapter 3), it was deemed important to consider this for the implanted samples.

– *Screw insertion index*

All screws proximal to the osteotomy were bi-cortically inserted whereas in the distal epiphysis were targeted at better reflecting their insertion in the human body. Screws in the distal epiphysis are chosen at a shorter length than the measured insertion hole in order to prevent the exiting of the screw on the lateral side of the tibia and penetrating the tibio-fibular syndesmosis or tibio-fibular joint.

Whether a screw crosses just one or two cortical layers will influence its purchase in the bone sample. All distal screws were therefore categorised as being completely mono-cortical, partially bi-cortical (entry into the lateral cortical layer but no complete penetration), or completely bi-cortical; Each screw was given a score 0, 1, or 2, based on the above criteria, respectively. The mean of the four scores was calculated and normalised between 0 and 1 to provide a screw insertion index for each sample.

– *Moment of inertia index (parameters for torsion)*

For torsion, the rotational axis was considered to pass through the central axis of the PMMA. The embedding of the composite bone sample was not necessarily in the centre of the PMMA block.

In each of the segmented specimens, the distance from the central/vertical axis of the sample (considered as being the axis of the cylinder representing the tibial diaphysis in Figure 84b) to the central axis of the PMMA block was calculated. As well as the distance from the barycentre of the lateral cortex to the sample central axis and to the rotational axis (Figure 91a). The distance from the barycentre of

the section of the implant covering the osteotomy to the load axis was also calculated (Figure 91b). In addition to this modified parameter, the quantity, surface area, and diagonal section of PMMA were included in the analysis. The reason behind the choice of these variables is based on the calculation of the area moment of inertia.

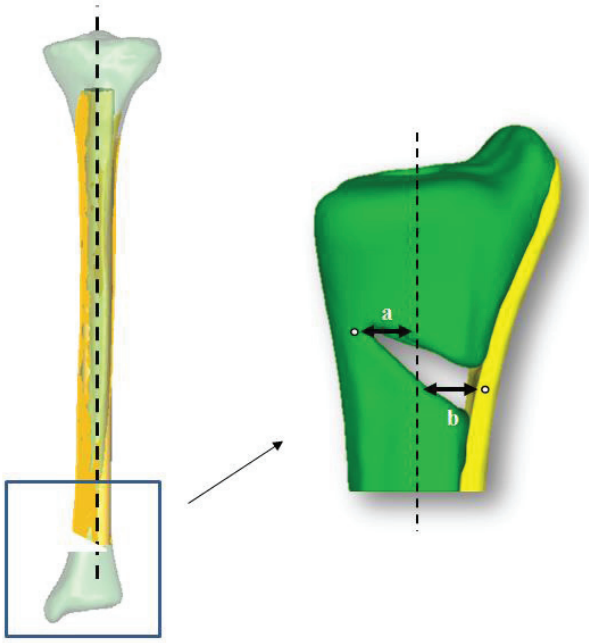

Figure 91: Schema diagram indicating the distance from the lateral cortex barycentre to the loading axis (a) and from the barycentre of the implant covering the osteotomy to the loading axis (b). The dashed line represents the sample rotational axis.

The surface area (S_PMMA), volume (Vol_PMMA) and diagonal cross section (D_PMMA) of the proximal PMMA block were also included in the additional parameters concerning torsional testing (Figure 92).

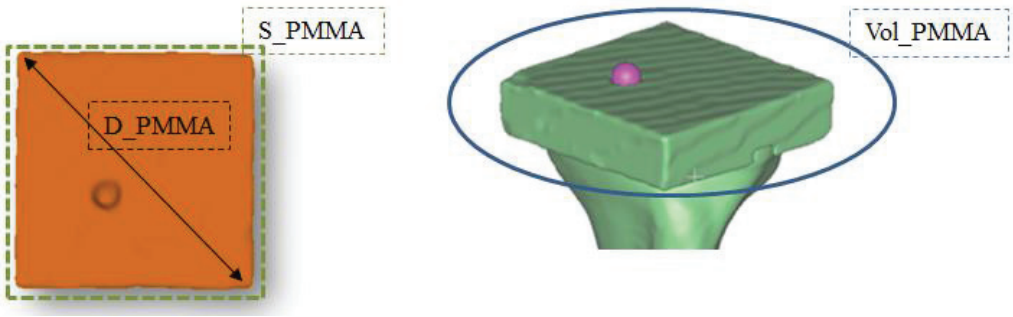

Figure 92: Additional parameters for torsion tests concerning the proximal PMMA embedding.

5. Statistical analyses

Correlation coefficients (Pearson's Product-Moment) are presented below and where possible, simple or multiple linear regressions were conducted to explain the maximum percentage of variation in measured stiffness. Analyses are performed by phase of testing, load type, load level and implant group. Finally, four summary tables are presented which highlight the evolution of the most influential parameters across from testing phases 0-3. A summary of the statistical procedure is given in Figure 93.

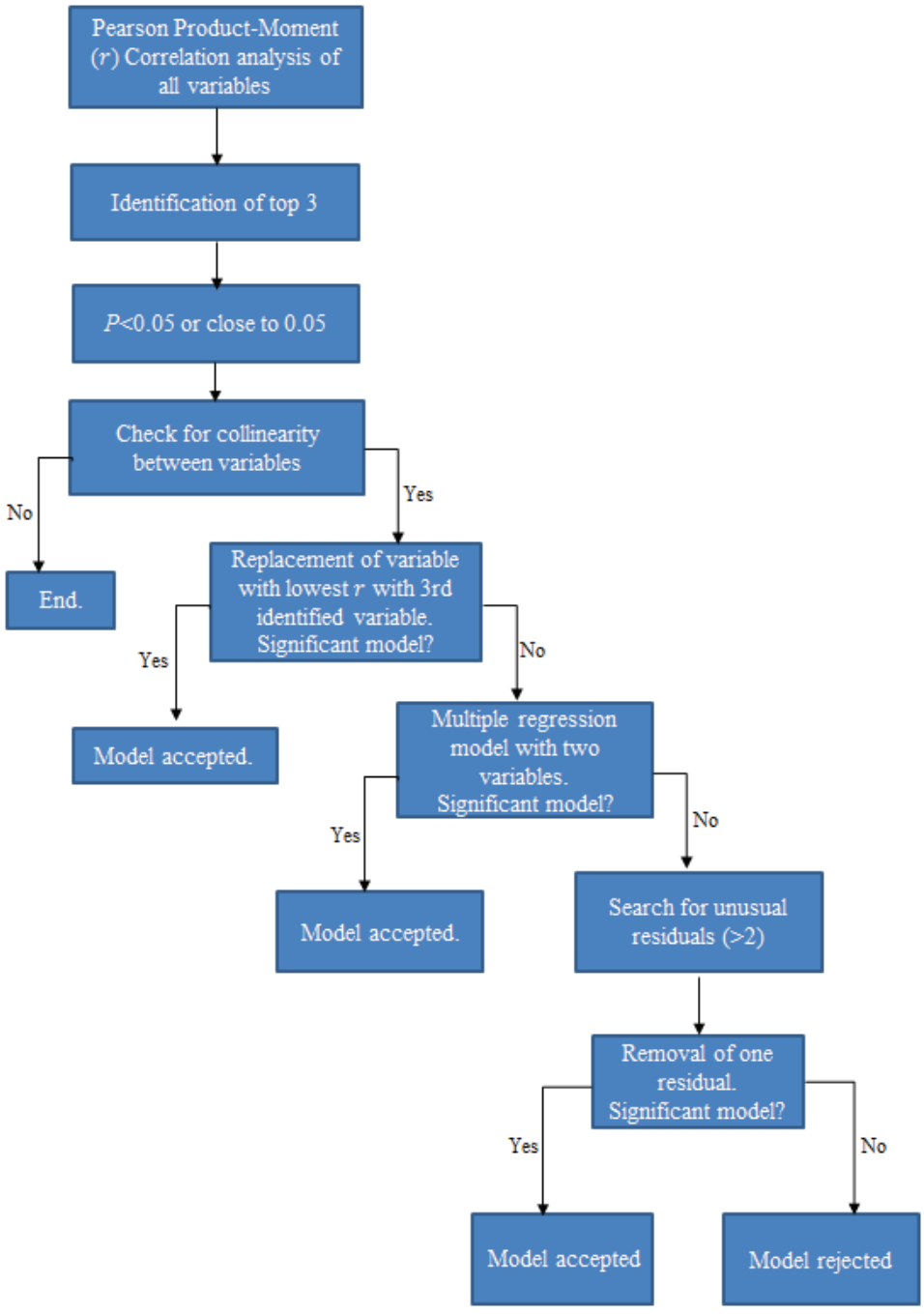

Figure 93: Statistical procedure for the identification of influential variables.

In order to measure the influence of each of the above mentioned parameters for healthy and implanted samples on the calculated stiffness constructs, a multiple regression model was targeted. A summary table of the different parameters and their likely areas of influence is given below (Table 10).

Nine variables related to the sample were identified, three parameters related to the test setup, and two parameters related to the surgical technique. Some parameters, such as PMMA surface area, are specific to torsional testing and are not included in compression results analyses.

Table 10: All input parameters for the regression models and their respective contexts. Abbreviated names used in the statistical analyses are also given.

Parameter		Healthy sample stiffness influence*		Implanted sample stiffness influence			
				DTN		MDTP	
		C	T	C	T	C	T
Sample-related parameters	PMMA thickness (PMMA)	✓	✓	✓	✓	✓	✓
	Cortical layer density (Rho_Cort, Rho_Spongy, Rho_PMMA)	✓	✓				
	Material volume (Vol_Cort, Vol_Spongy)	✓	✓				
	PMMA surface area (S_PMMA)		✓				✓
	PMMA diagonal cross section (D_PMMA)		✓				✓
	PMMA volume (Vol_PMMA)		✓				✓
	Healthy sample stiffness (K0)			✓	✓	✓	✓
	LC area (Lat_Cortex)			✓	✓	✓	✓
Setup-related parameters	Distance from the barycentre of LC to sample Z axis (D_LC_SampleZ)						✓
	Distance from the barycentre of LC to rotational axis (D_LC_Load)						✓
	Loading axis position (Load_axis)	✓	✓	✓	✓	✓	✓
Surgery-related parameters	Distance from the implant barycentre to load axis (D_Implant_Load)		✓				✓
	Implant position (Pos_Implant)			✓	✓		
	Screw index			✓	✓	✓	✓

* C = compression; T = torsion

Normal data distribution was measured using the Shapiro-Wilk test and verified with P-P plots. Homoscedasticity was evaluated using Levene's test and qualitatively assessed with a scatterplot of the residuals. All linear regressions were based on an ordinary least squares model.

5.1. Differences between implant groups

The identified parameters were tested for difference between the implant groups to see whether any differences may explain the significant differences found between groups in chapter 3. Significant differences were found for lateral cortex thickness with the DTN group containing the greatest thickness (DTN median: 55.3 mm² [range: 49-68]; MDTP median: 44.3 mm² [range: 43-50]; $P = 0.001$). Although no significant differences were found in favour of the DTN for stiffness construct during Phases 1 and 2 of testing, this difference in lateral cortex area may explain the advantage that the DTN has over the MDTP for compressive stiffness.

A second variable where a significant difference was found between the implant groups was the distance between the barycentre if the implant section covering the osteotomy gap and the loading axis (D_Implant_Load). The mean distance from the MDTP to the loading axis was much high than that of the DTN (DTN: 8.04±0.94 mm; MDTP: 17.2±0.67 mm; $P = 0$). This parameter was only entered into the correlation models for torsional stiffness.

5.2. Phase-0

Compression

Firstly, the stiffness of the healthy samples was investigated using five parameters. A correlation matrix of all parameters was calculated to individually assess the correlations between all variables (Figure 94). This was carried out to evaluate collinearity between variables, identify a subsample of variables shown to have a high influence on stiffness, and verify the linearity of all variables. Tests for normal distribution and homoscedasticity were also performed.

All data followed a normal distribution ($P > 0.05$) except the cortical density variable ($P = 0.01$); all variables were seen to have an equal variance distribution.

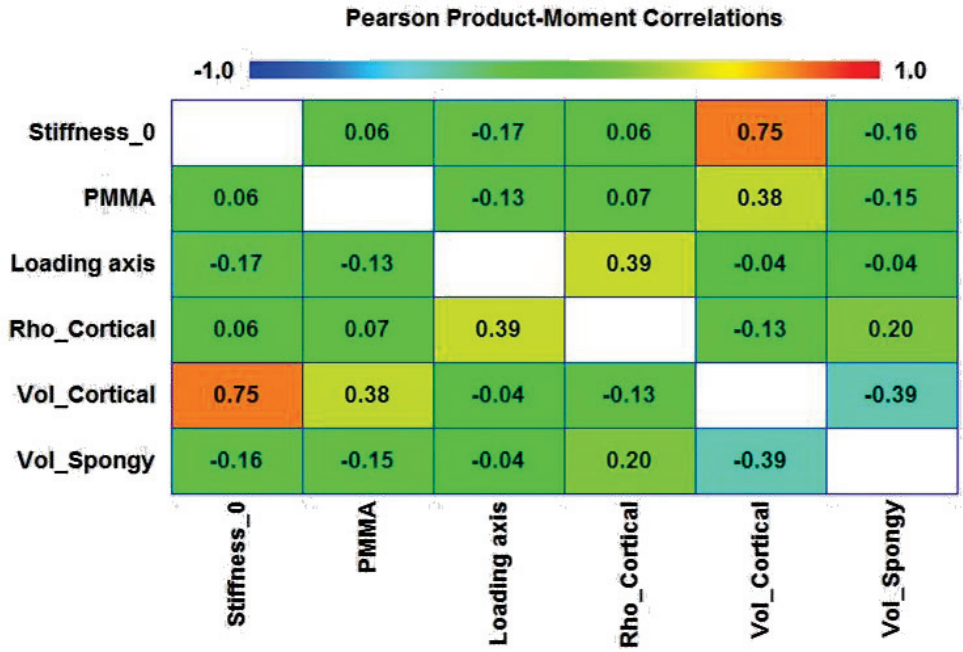

Figure 94: Pearson Product-Moment correlations for independent and dependent variables in Phase-0 of testing.

We know that no causality exists between the variables, despite correlations being found (for example between the volume of cortical layer and the PMMA thickness). Other correlations, such as between the volume of cortical and trabecular bone (R^2 = -0.39) may be true due to a widening in geometry at the bone epiphyses where cortical thickness decreases, this area is filled with more trabecular bone. The greatest correlation related to the healthy sample stiffness construct is the cortical volume (R^2 = 0.75); indeed osteoporosis literature states that the predictor of bone strength is its cortical thickness (Augat and Schorlemmer, 2006; Rausch et al., 2013; Nguyen et al., 2018).

Loading axis position and trabecular volume are both negatively correlated with sample stiffness, indicating that an increase in loading axis distance from the sample's central axis and an increase in trabecular bone will lead to a decrease in stiffness construct. Given the low correlation coefficients (R^2 = -0.06), PMMA thickness and cortical density were not considered influential to sample stiffness. Although the correlation coefficients are not high, these results seem logic as digressing from the central axis will lead to an unequal force distribution and result in bending; an increase in quantity of trabecular bone is related to a decrease in cortical bone, offering less rigidity to the sample.

The linearity of the samples is qualitatively verified through a matrix of correlation plots (Figure 95). A clear linear correlation between sample stiffness and cortical volume can be observed. For the other variables, however, as the Pearson Product-Moments expressed, there is little to no linearity between the independent and dependent variables.

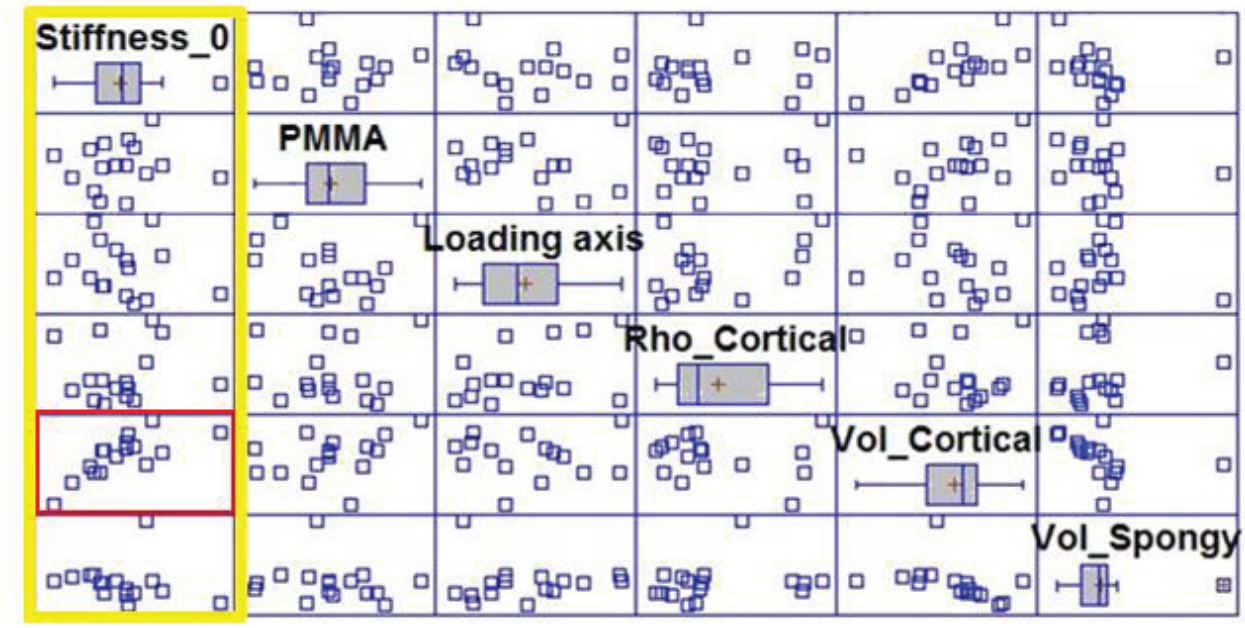

Figure 95: Matrix scatterplot of all variables for Phase-0 of testing.

The correlation between stiffness construct and cortical volume for healthy samples was further investigated by running a simple linear regression of the two variables. Linear regression output equations are expressed as the following:

$$Y = a + bx + MAE$$

Equation 3

Where Y is the dependent variable, a is the intercept of Y when x=0, b is the gradient of the regression line, and MAE represents the mean absolute error.

A first simple linear regression included all 16 observations and produced a statistically significant model ($P < 0.01$) which explained 54% (R^2 adjusted for model degrees of freedom (DOF)) of the variation in sample stiffness.

$$Stiffness_0 = -4386.66 + 0.033 \times Cortical\ volume + 90.23$$

Equation 4

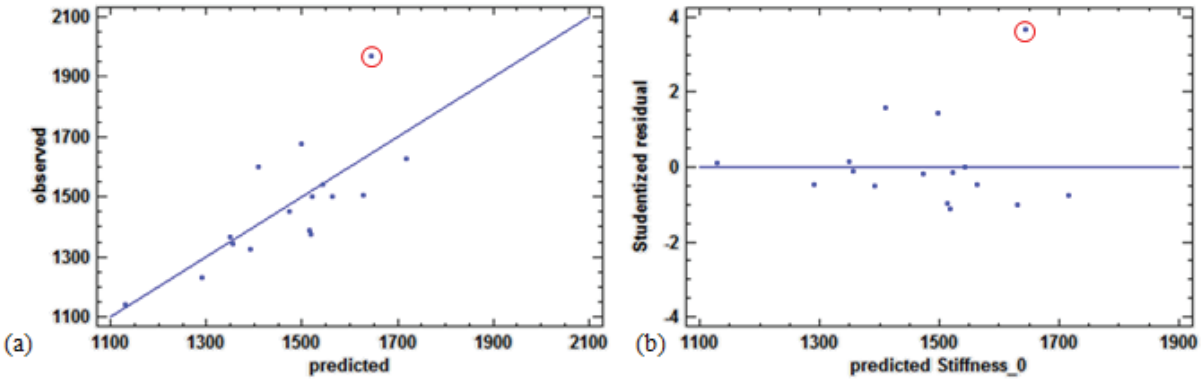

Figure 96: Linear regression observed versus predicted (a) and studentised residuals versus predicted (b) for all observations (n = 16) of healthy sample stiffness (Phase-0). Points circled in red indicate outliers.

A refined model was then run by repeatedly running the regression while removing the identified outlying point in the residual analysis. Finally, removing three observations resulting in $n = 15$ produced a more significant model ($P < 0.01$) explaining 58% (R^2_{adj}) of the variation in healthy sample stiffness construct ($R^2 = 60\%$).

$$Stiffness_0 = -3215.6 + 0.026 \times Cortical\ volume + 63.27$$

Equation 5

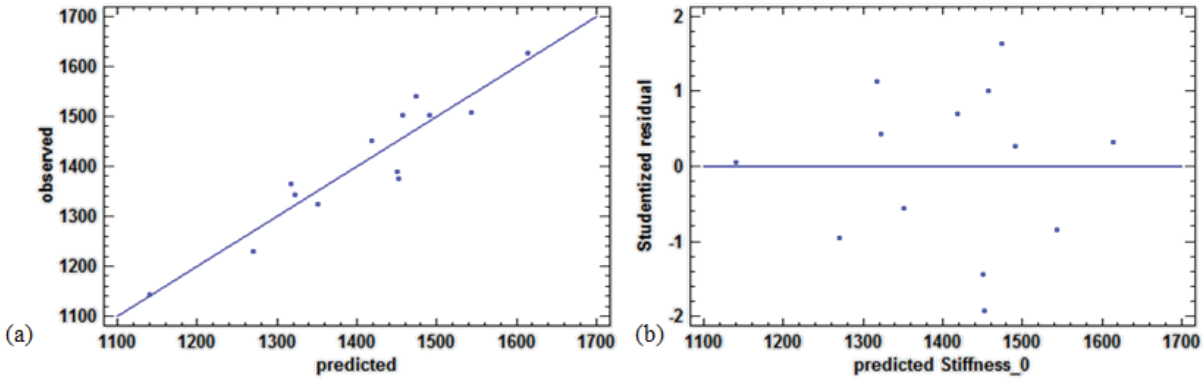

Figure 97: Multiple linear regression observed versus predicted (a) and studentised residuals versus predicted (b) for 15 observations of healthy sample stiffness (Phase-0).

A multiple linear regression was nonetheless run to gain an insight into the differing influences of experimental parameters on sample stiffness construct. Trabecular bone volume was omitted from these analyses due to collinearity with the measured cortical bone volume. This left four parameters for the model input: PMMA thickness, cortical bone volume, loading axis /central axis distance, and cortical density.

The first multiple linear regression run, included all variables ($n = 4$) and all observations ($n = 16$). A statistically significant model was produced ($P < 0.01$), but only cortical volume came through as a statistically significant parameter. This model explained 66% (R^2_{adj}) of the variation in sample stiffness ($R^2 = 75\%$).

$$K_0 = -6771.59 - 63.51 \times \text{PMMA} \ - 10.73 \times \text{Loading axis} \ + \ 14.23 \times \text{Rho\_Cortical} \ + \ 0.032 \times \text{Vol\_Cortical} \ + \ 58.48$$

Equation 6

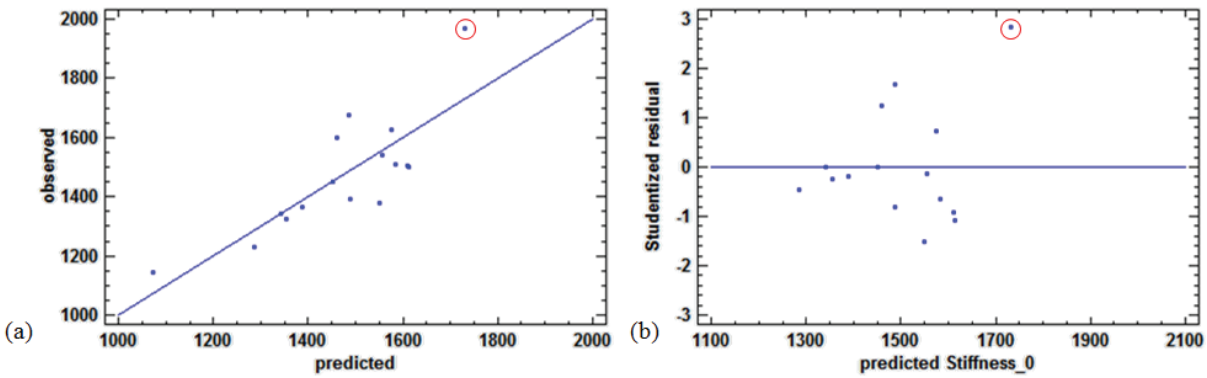

Figure 98: Multiple regression observed versus predicted (a) and studentised residuals versus predicted (b) for all observations (n = 16) of healthy sample stiffness. Points circled in red indicate outliers.

The model was then refined by removing outlier observations (circled in red in Figure 98; having a studentised residual greater than 3) and removing cortical density (Rho_Cortical) due to having a high *P*-value; incidentally this was also the only variable with a non-normal data distribution. The final model, presenting statistical significance ($P < 0.01$) consisted of 15 observations and 3 variables: PMMA thickness ($P = 0.39$), Loading axis ($P = 0.74$) and cortical volume ($P < 0.01$) and resulted in an R^2 (adjusted for DOF) of 65% (standard $R^2 = 63\%$).

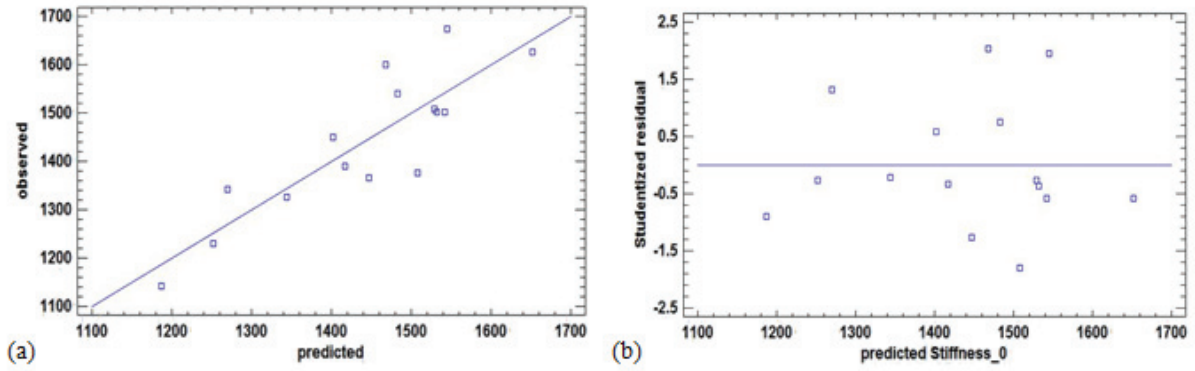

Figure 99: Multiple regression observed versus predicted (a) and studentised residuals versus predicted (b) for 10 observations of healthy sample stiffness.

$$Stiffness_0 = -3377.3 \ - \ 42.16 \times \text{PMMA} - 2.93 \times \text{Loading\_Axis} + \ 0.029 \times \text{Vol\_Cortical} \ + \ 61.54$$

Equation 7

In the end, the simple linear regression analysing cortical volume as an explicative variable of sample stiffness accounted for 54% of the variability in the healthy sample stiffness; furthermore, this value was significant. By introducing more variables and running a multiple regression, the ensemble of these variables explained 65% of the stiffness variability. Adding three extra variables only increased

the R^2_{adj} by 11% and therefore begs the question of whether these three additional variables are at all influential; moreover, none of the variables alone was found to be significant in the multiple regression model.

In further statistical analyses, where no unusual residuals were identified, none were removed.

5.3. Phase 1 Compression

DTN

The same procedure as described above for the healthy sample stiffness variables was repeated for all instrumented sample test stiffness constructs. Due to the volume of variables, correlation coefficient tables and matrices are not presented here but can be found in the appendix (§5).

350 N compression

On closer inspection of the variables, we noticed that the implant position displayed a quadratic relationship with the stiffness construct (Figure 100). Following this finding, the value representing implant position was squared in order to make it linear.

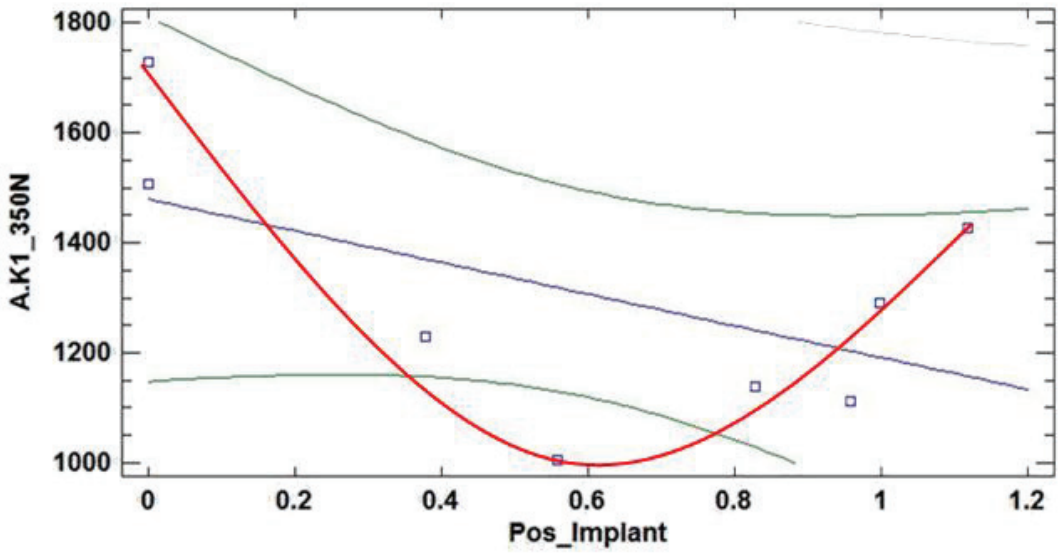

Figure 100: The quadratic relationship between implant position and stiffness at 350 N in Phase-1 of testing.

In Phase-1 of testing, healthy sample stiffness (K0) and lateral cortex area (Lat_Cortex) were found to have the greatest influence on resulting stiffness (K0: r = 0.79, $P = 0.01$; Lat_Cortex: r = 0.52, $P = 0.19$). However there was also a high level of collinearity detected between these variables (r = 0.74, $P = 0.03$) and therefore lateral cortex area was replaced by loading axis distance from the central sample axis (Loading_axis; r = -0.4, $P = 0.32$). The combination of these two variables produced a statistically significant model ($R^2 = 0.74$, $R^2_{adj} = 0.64$, $P = 0.03$).

$$DTN\ K1_{350N} = 690.65 - 24.67 \times Loading\_axis + 0.68 \times K0$$

Equation 8

700 N compression

At 700 N loading, the loading axis became more influential (r = -0.77, P = 0.02) along with PMMA thickness (PMMA; r = -0.71, P = 0.04); however collinearity was again present between these variables (r = 0.72, P = 0.04) and hence healthy samples stiffness replaced PMMA thickness (r = 0.48, P = 0.2). Statistically significant multiple regression models were produced for the following combinations of variables:

Loading_axis & K0 (R^2 = 0.75, R^2_{adj} = 0.66, P = 0.03; Figure 101).

$$DTN\ K1_{700N} = 1644.07 - 35.31 \times Loading\_axis + 0.24 \times K0 + 61$$

Equation 9

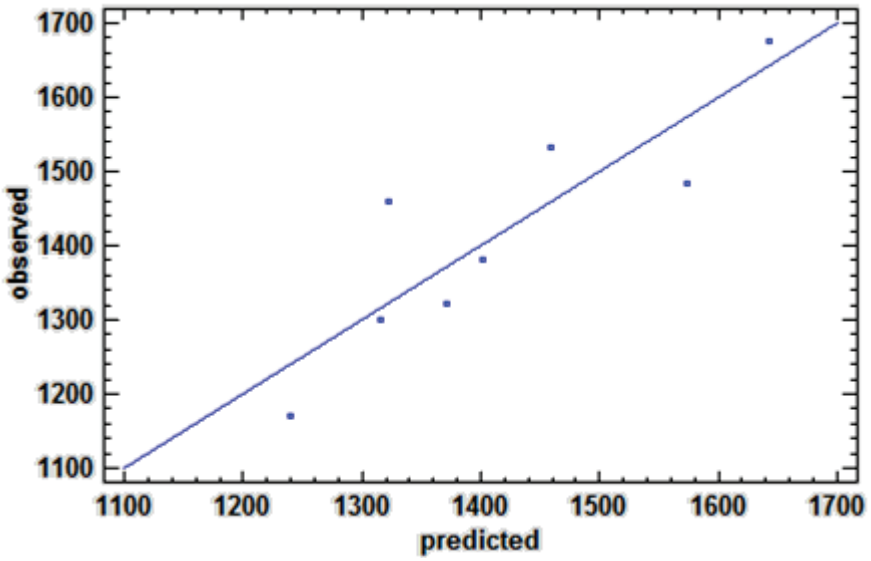

Figure 101: Observed versus predicted graph for the multiple linear regression of K0 and loading axis explaining variability in 700 N stiffness of the DTN during Phase-1 of testing.

PMMA thickness & K0 (R^2 = 0.71, R^2_{adj} = 0.6, P = 0.04; Figure 102)

$$\text{DTN}\ K1_{700N} = 2524.52 - 209.32 \times PMMA + 0.27 \times K0 + 66$$

Equation 10

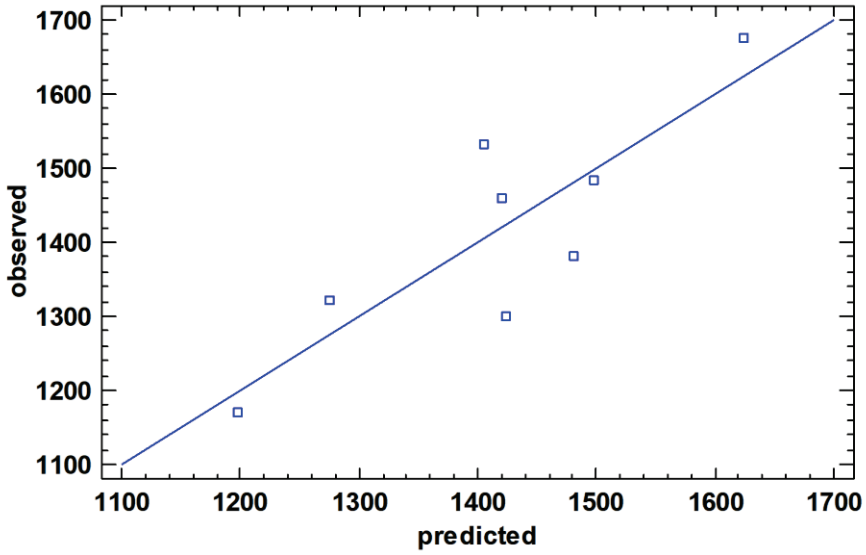

Figure 102: Observed versus predicted graph for the multiple linear regression of K0 and PMMA thickness explaining variability in 700 N stiffness of the DTN during Phase-1 of testing.

MDTP

350 N compression

For Phase-1 350 N, stiffness construct appeared to be mainly influenced by healthy sample stiffness (r = 0.59, *P* = 0.12) and lateral cortex area (r = 0.34, *P* = 0.41), however a collinearity issue was again found between these data for the MDTP results (r = 0.74, *P* = 0.03) and therefore loading axis replaced lateral cortex area (r = -0.27, *P* = 0.52). No significant regression model was produced.

700 N compression

A similar pattern is observed at 700 N loading where loading axis has the highest influence (r = -0.53, *P* = 0.18) followed by K0 (r = 0.46, *P* = 0.23). PMMA thickness (r = 0.46, *P* = 0.23) was entered into a regression model to replace K0 but no significant regression was observed.

5.4. Phase 2 Compression

DTN

350 N Compression

Phase-2 of testing at 350 N was again strongly influenced by healthy sample stiffness (r = -0.73, *P* = 0.03) and lateral cortex area (r = -0.65, *P* = 0.07); however this latter variable shows collinearity issues with K0 and is therefore replaced with implant position (r = 0.41, *P* = 0.3). The combination of K0 and implant position produced an almost significant regression model (R^2 = 0.64, R^2_{adj} = 0.54, *P* = 0.07). Healthy sample stiffness alone was entered into a simple linear regression model and demonstrated a better R^2 value of 0.73 as well as a significant model (R^2_{adj} = 0.54, *P* = 0.04).

$$DTN\ K2_{350N} = 1327.17 - 0.28 \times K0 + 55.5$$

Equation 11

700 N Compression

At 700 N, the calculated correlation coefficients were neither particularly high nor significant for any of the input parameters. Healthy sample stiffness and lateral cortex produced coefficients of -0.42 and -0.43, respectively, but were far from significant (P = 0.3 for both). No regression model was attempted.

MDTP

350 N Compression

In Phase-2 of testing at 350 N for the MDTP samples, a significant model was produced by entering K0 into a simple regression model (R^2 = 0.72, R^2_{adj} = 0.53, P = 0.04), the regression graph is given in Figure 103. No other variables demonstrated significance.

$$K2_{350N} = -1147.72 + 1.61K0 + 106$$

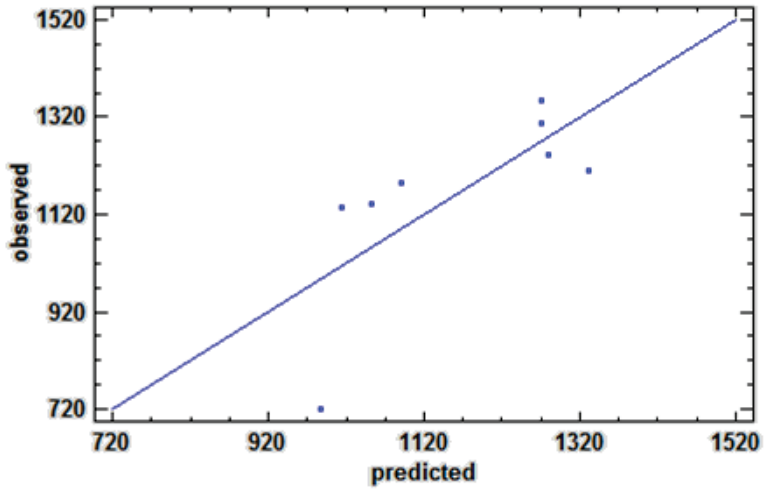

Figure 103: Observed versus predicted graph for the simple linear regression of K0 explaining variability in 350 N stiffness of the MDTP during Phase-2 of testing.

700 N Compression

At 700 N, only K0 was seen to have a medium correlation with test stiffness (r = 0.47, P = 0.24). No other variables presented a correlation coefficient < 0.3 and hence no regression models were produced.

5.5. Phase 3 Compression

DTN

350 N Compression

In Phase-3 of testing at 350 N for the DTN, PMMA thickness appears to have strong influence on measured stiffness construct (r = -0.68, P = 0.06) and was coupled with screw index (having the second highest correlation coefficient: r = -0.39, P = 0.34) in a multiple regression model but no significant model was developed (P > 0.05).

700 N Compression

At 700 N it was again PMMA thickness being the most influential parameter (r = -0.54, *P* = 0.16) followed by loading axis (r = -0.5, *P* = 0.2) but collinearity was present between the two variables leading to the replacement of loading axis by screw index (r = -0.43, *P* = 0.26). Nonetheless, no significant model was produced.

MDTP

350N Compression

For the MDTP samples, loading axis and screw index produced a significant model (R^2 = 0.71, R^2_{adj} = 0.6, *P* = 0.04; Figure 105) however loading axis alone also proved to be significant in a simple linear regression model (R^2 = 0.73, R^2_{adj} = 0.53, *P* = 0.04; Figure 104) while screw index did not (*P* = 0.07).

Loading axis (simple linear regression)

$$MDTP\ K3_{350N} = 231.36 - 3.92 \times Loading\_axis + 8.6$$

Equation 12

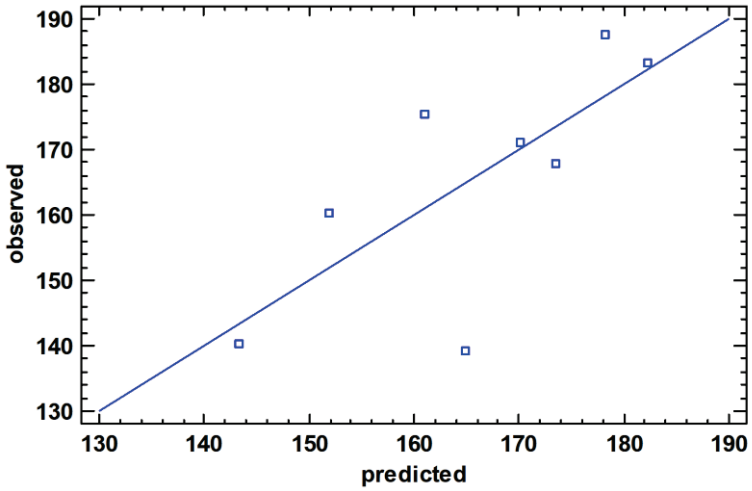

Figure 104: Observed versus predicted graph for the simple linear regression of loading axis explaining variability in 350 N stiffness of the MDTP during Phase-3 of testing.

Loading axis & Screw index

$$MDTP\ K3_{350N} = 201.65 - 2.95 \times Loading\_axis + 35.99 \times Screw\_Index + 6.2$$

Equation 13

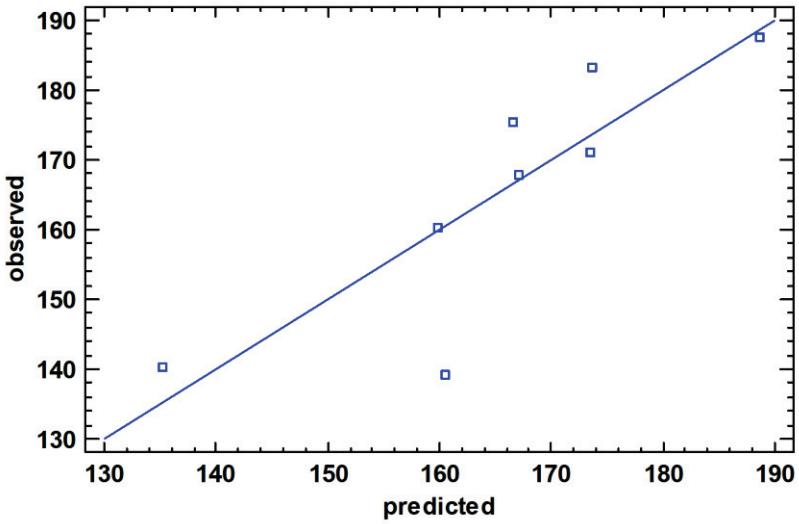

Figure 105: Observed versus predicted graph for the multiple linear regression of loading axis and screw index explaining variability in 350 N stiffness of the MDTP during Phase-3 of testing.

700 N Compression

The same pattern is seen at 700 N with loading axis and screw index presenting high correlation coefficients (r = -0.65 and 0.62, respectively) however neither were significant at the 95% level. A multiple regression model failed on significant due to an overly high residual (-6.16). On removing this observation (decreasing the model degrees of freedom from 8 to 7, including the constant), the model became highly significant ($R^2 = 0.97$, $R^2_{adj} = 0.96$, $P < 0.01$; DTN-4 sample; Figure 106).

$$K3_{700N} = 226 - 4.53 \times Loading\_axis + 32.36 \times Screw\_index + 2.59$$

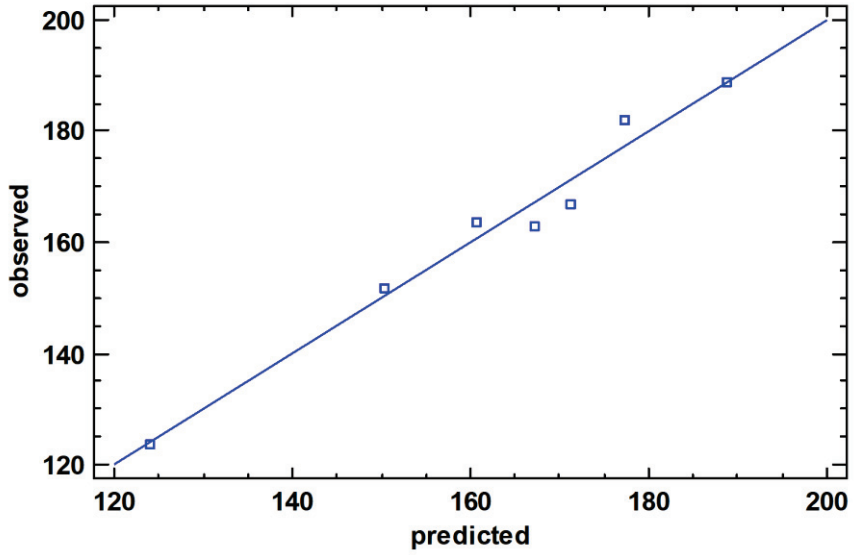

Figure 106: Observed versus predicted graph for the multiple linear regression of loading axis and screw index explaining variability in 700 N stiffness of the MDTP during Phase-3 of testing.

Incidentally, the removal of this observation also provoked a significant simple linear regression model to be observed for loading axis ($R^2 = -0.86$, $R^2_{adj} = 0.83$, $P < 0.01$; Figure 107). This was not true for screw index which remained insignificant ($P = 0.09$), suggesting that loading axis remains largely the most influential variable for explaining variations in stiffness at 700 N for Phase-3 of testing for the MDTP instrumented samples.

$$K3_{700N} = 253.1 - 5.39 \times Loading\_axis + 6.89$$

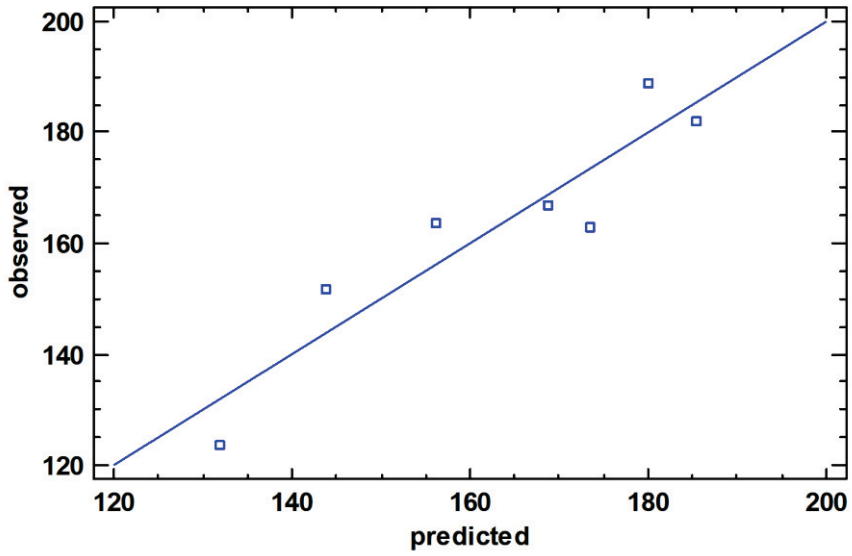

Figure 107: Observed versus predicted graph for the simple linear regression of loading axis explaining variability in 700 N stiffness of the MDTP during Phase-3 of testing.

For all phases of compression testing, it is the loading axis in particular which maintains a high influence on compressive stiffness. For phases 1-3, the initial stiffness of the healthy sample was also seen to have a large effect on later stiffness constructs. Finally, for Phases 1 & 2, the lateral cortex area also appears to play an important role in bone-implant construct stiffness.

5.6. Phase 0 Torsion

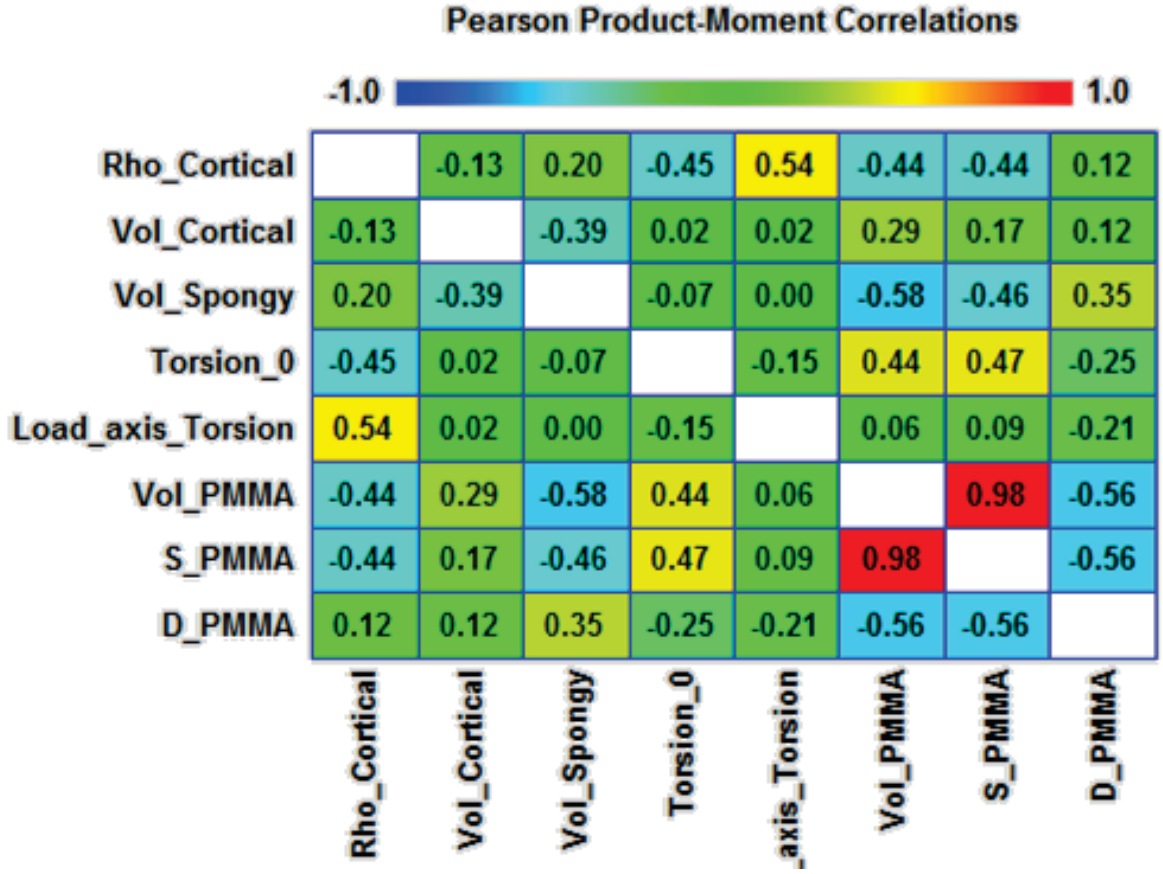

Figure 108: Pearson Product-Moment correlations for all variables included in the torsional stiffness analysis for healthy samples.

Correlation analysis showed medium negative correlation between torsional stiffness and cortical density (R^2 = -0.45) as well as medium positive correlations between stiffness and PMMA volume and surface (R^2 = 0.44 and 0.47, respectively). However, on further investigation into these variables, none of the correlations presented as significant. It is therefore not possible to comment on the factors influencing torsional stiffness in whole Sawbones® samples. Variations in calculated stiffness constructs are due to aspects that were not measured in this study, for example pre-strain applied to the sample on placing it in the testing machine.

Incidentally, on comparing the correlation coefficients between all input parameters, a high significant correlation was seen between PMMA volume and surface area (Vol_PMMA and S_PMMA; r = 0.98, P = 0), a logical relationship owing to Pythagoras' Theorem. In light of this finding, Vol_PMMA was removed from all further analyses, S_PMMA remained.

5.7. Phase 1 Torsion

DTN

4 Nm Torsion

In Phase-1 of testing at 4 Nm for samples instrumented with a DTN, no significant correlations were found ($P > 0.05$). The two highest Pearson Product-Moment correlation coefficients were lateral cortex area (r = 0.55, $P = 0.16$) and loading axis distance from the sample central axis (r = -0.61, $P = 0.11$). These variables were entered into a multiple regression model but no significance was observed.

8 Nm Torsion

At 8 Nm testing, three input parameters were identified: loading axis (r = 0.6, $P = 0.12$) and screw index (r = 0.67, $P = 0.06$). When integrated into a regression model, no significant relationship was displayed ($P = 0.1$).

MDTP

4 Nm Torsion

For the MDTP samples, the distance between the vertical axis of the sample and the loading axis proved statistically significant in a simple regression model ($R^2 = 0.51$, $R^2_{adj} = 0.43$, $P = 0.04$). No other significant model using a combination of parameters was developed.

$$MDTP\ K1_{4Nm} = 9.59159 - 0.356182 \times D\_Implant\_Load + 0.2$$

Equation 14

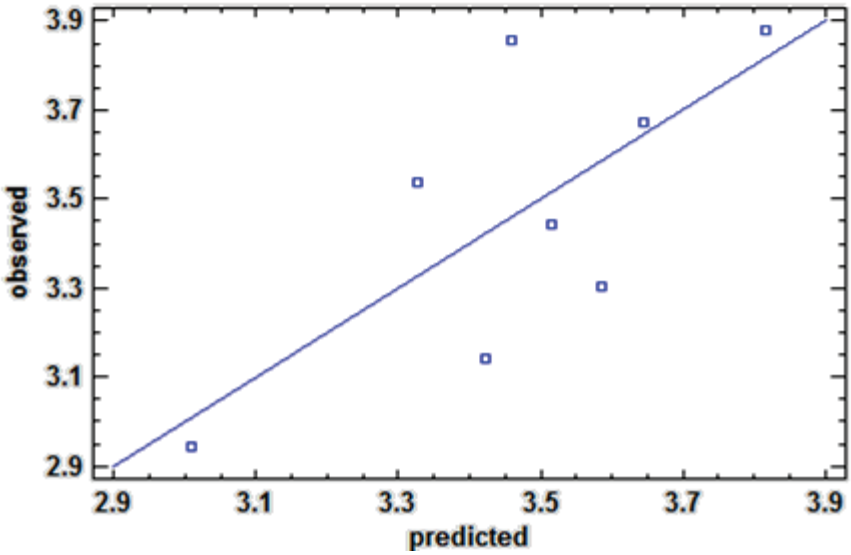

Figure 109: Observed versus predicted graph for the simple linear regression of distance from the implant to the rotational axis explaining variability in 4 Nm stiffness of the MDTP during Phase-1 of testing.

8 Nm Torsion

At 8 Nm on the other hand, none of the input variables appeared close to significance and no significant regression model was produced.

5.8. Phase 2 – Torsion

DTN

4 Nm Torsion

In Phase-2 of testing at 4 Nm the distance from the barycentre of the lateral cortex to the vertical axis of the sample (r = -0.52, $P = 0.19$) and the PMMA surface area (S_PMMA; r = -0.62, $P = 0.1$) were identified. An almost significant regression model as produced ($R^2 = 0.65$, $R^2_{adj} = 0.51$, $P = 0.07$). One residual (relating to the DTN-3 sample) was identified as being an outlier (residual: -2.02) and once removed, a significant model was produced ($R^2 = 0.78$, $R^2_{adj} = 0.67$, $P = 0.049$).

$$DTN\ K2_{4Nm} = 2.29947 - 0.000129876 \times S\_PMMA + 0.00721402 \times Distance\_LatCortex\_SampleZ\_SQ + 0.1$$

Equation 15

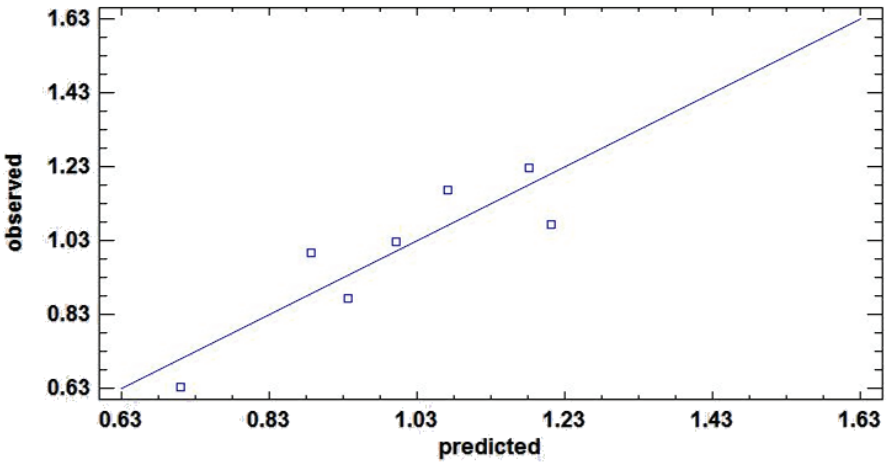

Figure 110: Observed versus predicted graph for the multiple linear regression of the PMMA surface area and distance from the lateral cortex to the rotational axis explaining variability in 4 Nm stiffness of the DTN during Phase-2 of testing.

8 Nm Torsion

At 8 Nm torsion, the lateral cortex area and screw index displayed the highest correlations (Lat_Cortex: r = 0.44, P = 0.28; Screw index: r = 0.53, $P = 0.18$) but they were not high enough to produce a significant regression model.

MDTP

4 Nm Torsion

In Phase-2 of testing for the MDTP samples, at 4 Nm only PMMA thickness was seen to have a correlation with test stiffness (r = 0.49, $P = 0.21$), no statistical significance was found and no other parameters appeared to have a correlation coefficient greater than 0.4. In light of this, no regression model was attempted.

8 Nm Torsion

At 8 Nm loading, the distance between the barycentre of the lateral cortex and the loading axis (r = 0.51, $P = 0.2$), and between the samples' vertical axis and the loading axis (r = -0.48, $P = 0.23$)

displayed good correlation coefficients but no significance was found nor was a regression model developed.

5.9. Phase 3 Torsion

DTN: 8 Nm Torsion

For Phase-3 of torsional testing, multiple parameters demonstrated a good correlation, yet none proved to be significant alone (Table 11) and no combination of the different variables resulted in a significant multiple regression model.

Table 11: Pearson Product-Moment correlation coefficients for variables influencing torsional stiffness for 8 Nm testing in Phase-3 for the DTN samples.

Variable	Pearson's r	P-value
PMMA thickness	0.55	0.16
Load_axis	0.54	0.17
D_implant_Load	-0.54	0.17
K0	0.45	0.26

MDTP: 8 Nm Torsion

The final phase of testing for MDTP samples saw the healthy sample stiffness play a relatively large role in explaining the variations among Phase-3 torsional stiffness constructs (r = -0.66, P = 0.08). When coupled with the distance between the implant and the loading axis, a significant regression model was produced (R^2 = 0.7, R^2_{adj} = 0.6, P = 0.047).

$$MDTP\ K3_{8Nm} = 2.04931 - 0.0407597 \times D\_Implant\_Load - 0.104153 \times K0 + 0.02$$

Equation 16

6. Statistical analyses for instrumented samples

For each implant group and test type (compression/torsion), correlation coefficient tables show the development of the top 5-6 variables across all testing phases. The chosen variables related to instrumented samples are therefore not always relevant in Phase-0.

6.1. DTN in compression

During compression testing of the DTN samples, there is a general decrease in the influence of healthy sample stiffness (K0) between Phases 1-3 while PMMA thickness becomes more important (Table 12). Lateral cortex area also becomes more dominant between Phase-1 and -2 however in Phase-1, an increase in cortex area leads to an increase in stiffness, while in Phase-2 the inverse relationship is displayed. The weight of the loading axis steadily decreases while screw index becomes more important. Implant position remains relatively stable throughout Phases 1-3.

Table 12: Evolution of Pearson product-moment correlation coefficients for the DTN samples during compression testing.

Variable	Correlation coefficient						
K0	/	**0.79**	0.48	**-0.73**	**-0.42**	-0.31	0.05
PMMA	-0.03	-0.31	**-0.71**	-0.38	-0.39	**-0.68**	**-0.54**
Lat_Cortex	/	**0.52**	-0.08	**-0.65**	**-0.43**	/	/
Loading_Axis	-0.09	-0.4	**-0.77**	-0.3	-0.39	-0.37	-0.5
Screw Index	/	-0.2	-0.26	-0.19	-0.36	**-0.39**	**-0.46**
Pos_Implant	/	-0.32	-0.21	0.41	-0.35	0.34	-0.21
	Phase-0	Phase-1 350N	Phase-1 700N	Phase-2 350N	Phase-2 700N	Phase-3 350N	Phase-3 700N

6.2. MDTP in compression

For the MDTP samples (Table 13), healthy sample stiffness increases from Phase-1 to Phase-2 for 350 N loading, but decreases in Phase-3. PMMA thickness has a mediocre influence throughout Phase 0-2 but then becomes insignificant in Phase-3. Lateral cortex area appears to be more important at 350 N in Phases1-2 but is less critical at 700 N compression. Loading axis position decreases from Phase0-2 but increases sharply for Phase-3; screw index only appears to be significant in Phase-3 of testing.

Table 13: Evolution of Pearson product-moment correlation coefficients for the MDTP samples during compression testing.

Variable	Correlation coefficient						
K0	/	**0.59**	**0.46**	**0.72**	**0.47**	0.37	0.2
PMMA	0.21	-0.15	0.35	-0.2	-0.13	0.06	0.01
Lat_Cortex	/	**0.34**	0.31	**0.46**	0.21	/	/
Loading_Axis	-0.55	-0.27	**-0.53**	-0.09	**-0.22**	**-0.73**	**-0.65**
Screw Index	/	0.26	-0.13	0.08	0.14	**0.68**	**0.62**
	Phase-0	Phase-1 350N	Phase-1 700N	Phase-2 350N	Phase-2 700N	Phase-3 350N	Phase-3 700N

6.3. DTN in torsion

In torsional testing for the DTN samples' (Table 14) lateral cortex area seems to play a role in increasing stiffness in Phase-1 but has the opposite effect in Phase-2. Screw index decreases in importance from Phase-1-3 but displays a relatively high relationship with stiffness at 8 Nm in Phases 1 and 2. Loading axis position demonstrates a general increase in dominance over Phases 0-3 but in Phase-2 shows a negative relationship while in other phases it is positive. The distance from the lateral cortex to the loading axis (D_LC_Load) becomes less important between Phase -1 and -2 while the distance from the lateral cortex to the sample's vertical axis (D_LC_SampleZ) increases its negative relationship with construct stiffness until Phase-2 8Nm where there is a positive correlation. The PMMA surface area (S_PMMA) generally increases from phases 0-2 but decreases in Phase-3.

Table 14: Evolution of Pearson product-moment correlation coefficients for the DTN samples during torsion testing.

Variable	Correlation coefficient					
Lat_Cortex	/	**0.55**	0.12	-0.05	**-0.44**	/
Screw Index	/	-0.11	**0.67**	0.17	**0.53**	0.05
Loading axis	-0.15	0.26	0.6	-0.34	-0.09	**0.54**
D_LC_Load	/	**-0.61**	-0.03	-0.05	0.32	/
D_LC_Sample Z	/	-0.28	**-0.48**	**-0.52**	0.32	/
S_PMMA	0.47	-0.44	-0.22	**-0.62**	-0.31	0.34
	Phase-0	Phase-1 4Nm	Phase-1 8Nm	Phase-2 4Nm	Phase-2 8Nm	Phase-3 8Nm

6.4. MDTP in torsion

The MDTP samples during torsional testing (Table 15) saw a decrease in the influence of PMMA surface area from phases 0-3, in particular in Phase-2 where the correlation coefficient is highly insignificant. The distance from the implant to the loading axis at the level of the osteotomy (D_Implant_Load) decreases in importance, especially in Phase-2 4 Nm testing where there is no correlation. The distance from the lateral cortex to the sample vertical axis (D_LC_SampleZ) shows a decrease in correlation from Phase 1-2. Healthy samples stiffness globally increases from Phase 1-3 but does not appear influential in Phase-2 of testing. The distance from the lateral cortex to the load axis (D_LC_Load) only displays an interesting correlation in Phase-2 at 8 Nm.

Table 15: Evolution of Pearson product-moment correlation coefficients for the MDTP samples during torsion testing.

Variable	Correlation coefficient					
S_PMMA	0.47	**-0.43**	**-0.49**	0.03	-0.05	-0.35
D_Implant_Load	/	**-0.72**	-0.44	0.06	**-0.48**	**-0.54**
D_LC_SampleZ	/	0.5	-0.15	**0.34**	0.13	/
K0	/	-0.08	**-0.48**	**-0.33**	-0.3	**-0.66**
D_LC_Load	/	0.01	0.07	-0.05	0.51	/
	Phase-0	Phase-1 4Nm	Phase-1 8Nm	Phase-2 4Nm	Phase-2 8Nm	Phase-3 8Nm

7. Discussion

Multiple parameters were identified and quantified for use in a statistical model in an attempt to explain the variation in stiffness constructs measured from testing in Chapter 3. The number of explanatory variables varied depending on the test and implant type.

Phase-0 (stiffness of healthy composite bones)

Results from Chapter 3 found a relatively high variation (13%) in measured compressive stiffness of the healthy samples despite the fact that the Sawbones® should exhibit very similar mechanical properties. Nonetheless, as previously discussed in chapter 3, this level of variation does not differ greatly from that reported by Heiner et al. (2008).

Cortical volume appeared to be a highly influential factor explaining the variation in stiffness of the healthy samples. However, the measured cortical volume was based on the numerical segmentation process. In our segmentation method, the proximal PMMA and cortical layer had to be reconstructed manually due to almost identical greyscale levels meaning that the program could not automatically detect and differentiate the cortical layer from the PMMA (cf. §2.2). An intra and inter – observer reliability study is required to quantify the extent to which cortical volume differs due to segmentation errors.

Phases 1-3 (stiffness of implanted samples)

On comparing the evolution of the correlation coefficients it would appear that the variables having a high influence on the more stable implanted constructs (Phase-1) did not necessarily continue to dominate once the samples were made less stable by fracturing the lateral cortex (Phase-2) and simulating an A3 fracture (Phase-3). For example, healthy sample stiffness seemed particularly influential in Phases 1-2 of compression testing for both implants, while the lateral cortex area seemed to principally affect the DTN samples. In Phase-3, healthy sample stiffness had less of an impact and it was setup & surgical technique -factors that had the greatest influence on construct stiffness, such as PMMA thickness, loading axis and screw index.

The deviation of the loading axis from the sample's vertical axis creates bending moments and will results in lower stiffness and greater displacement than pure compression. As for the lateral cortex area, following beam theory mechanics, increasing the lateral cortex area will increase the rigidity of the sample and provide greater resistance against compressive and torsional loads. The screw index relates to how well the implant is bound to the sample. A high screw index is linked to a higher level of bi-cortical screw insertion. The Young's modulus of trabecular bone is lower than that of cortical bone (in Sawbones®: 0.155 GPa against 16.7 GPa). Screws which are only mono-cortical will be less well anchored into the sample than bi-cortical screws and result in greater movement between fragments (and hence producing lower stiffness constructs).

For torsional stiffness, the influencing factors change both within and between testing phases. The distance from the implant to the load axis at the level of the osteotomy/fracture, although presenting the strongest correlation in Phase-1 at 4 Nm, does continue to increase its global influence from Phases 1-3 for the MDTP samples. For the DTN samples, there is no specific variable that progressively increases or decreases throughout the testing phases other than screw index for the DTN samples.

The highly significant difference found between the distances from the implant to the loading axis for the DTN and the MDTP is simply related to the positioning itself. Plates are always externally placed on bone while nails and intramedullary meaning that they often fall into (or close to) the natural loading axis of the bone. The lesser the distance from the load, the lower the resulting moment arm and therefore mechanical work necessary for the implant to support the loads.

Unexplained factors

The angle of the osteotomy measured in Phases 1-2 may have had an influence in the calculated stiffness constructs. In particular, we noticed that the MDTP-1 sample had a different osteotomy compared to the other samples and also exhibited different results following compression and torsional testing. The osteotomy zone in the CT scans was affected by artefacts from the implant and it was therefore not possible to measure the angle using a reliable method. It may, however be possible in the future to measure the angle with standard 2D radiography and include this parameter in the statistical analyses.

Influencing factors related to temperature or air pressure may have caused slight differences in the collected machine data. Nonetheless, testing was started at approximately the same time every day, switching the machine on around 30-45 minutes before testing, and three test runs with a sample from a previous study were performed before beginning the tests. This was carried out to stabilise air pressure and movements within the test setup to avoid differences in data being linked to the testing machine. Nonetheless, a certain level of variation in results may stem from the difference in test setups, for example from screws not being tightened with a torque key allowing sample movement, especially during the torsion tests.

Limitations

The compression setup was largely tested and optimised prior to testing whereas the torsion test setup was not well controlled for. This may explain the variations observed in the type of relationship of a given variable with torsional stiffness as there were external factors present which may have influenced measured stiffness. In particular, correlation results relating to Phase-2 of torsional testing tend to show the opposite relationship than in other testing phases. This may be linked to the fact that neither 4 Nm nor 8 Nm stiffness results tested positive for normality (according to the Shapiro-Wilk test), and that the contact between the lateral cortex fragments was not constant.

For testing phases 1-3 only a maximum of eight observations were used in the correlation and regression calculations, indicating just eight degrees of freedom (DoF) available for each model. Where two variables were used to develop a multiple regression model, the DoF drops to seven. Issues with such few observations may lead to the decrease in the precision of the generated regressions and their use outside of this testing context. One study (Babyak, 2004) has suggested using 10-15 observations per input variable for multiple regressions and therefore in our study the use of two independent variables to explain one dependent variable would require 30-45 observations. Nonetheless, a certain level of confidence can be attributed to the displayed models as the adjusted R^2 values were often high and not overly deviating from the R^2 value by more than 0.1 on average. However, it is due to the low number of observations that generally only the Pearson Product-Moment correlation coefficients were analysed. Furthermore, the linearity of certain regression models (for example Figure 103 for the MDTP at 350 N loading) is questionable and can only be confirmed or rejected by including more observations in the model.

There were several cases in which collinearity was detected between the two most influential variables according to the Pearson Product-Moment Correlation Coefficient, and the second highest of the two variables were omitted from regression analyses so to respect the linear regression model assumptions. We know, however, that there is no causality behind these correlations and it may be that more significant regression models would have been produced if there had not been this issue of collinearity. Given the significant difference found between lateral cortex areas between the two implant groups, this parameter may in fact be very influential and further processing of these results may consider expressing certain variables in a different manner so to avoid collinearity problems and include it in the regression models. One way of doing this would be to employ a principal component analysis that regroups variables with high covariance. This was not performed in the current study as we wished to observe each variable individually.

The parameters related to the implant position and sample geometry were measured from CT-scan data of all samples in Phase-1 of testing with the lateral cortex of the osteotomy still intact. The assumption was therefore made that the value of these variables did not change throughout the further testing phases. However, by cutting through the lateral cortex and then opening this area into an A3 fracture, mobility was added to the sample, allowing slight rotation around the sample Y and Z –axes. This is only true for the DTN sample due to the 0.8 mm gap between screw and screw hole –diameter. This problem is not present in the MDTP owing to the use of locking screws fixed into the plate.

8. Conclusion

Although certain factors described above may vary in reality (such as physiological loading axis) from patient to patient depending on different morphologies, the results from the current study demonstrate the effect that external factors can have on measured stiffness constructs, in particular in unstable constructs. For future biomechanical testing for orthopaedic implants, it is strongly recommended that the test boundary conditions be controlled to the maximum of the experimenter's ability in order to decrease variation within results and be more confident that the displayed results truly reflect the bone-implant sample. Furthermore, where stable bone-implant constructs are tested, composite bone sample stiffness should be measured prior to fracture simulation and implantation verified that this does not influence measured bone-implant construct.

With respect to surgical technique, it is easier said than done to control the factors stated here in the implant-related variables. Nonetheless, it is important to note that factors such as implant position and screw index do have an influence on construct stiffness and may be indicators of secondary fracture or implant failure. The screw index, in particular, appears to be important concerning the MDTP. Although it is not possible to ensure the bi-cortical insertion of all screws due to their anatomical position, we cannot ignore that this parameter influences stiffness and therefore also IFM. This is of specific interest for axial stiffness of the MDTP and torsional stiffness of the DTN.

Chapter 5: Influence of screw type on local bone deformation

In the scope of developing a numerical model from the CT-scans taken in Chapter 3 to digitally replicate the tests performed, it was important to obtain data that can be used to later evaluate the model with respect to contact type used for the screws. In light of this, an additional study was carried out to assess the strain levels and patterns around the around head on the external cortex of Sawbones® during compressive loading.

1. Introduction

Bone remodelling is dictated by mechanical stimuli (Wolff's Law; Frost, 1994) and works through feedback loops: more bone tissue is developed in response to higher strain rates and, inversely, this bone tissue is reabsorbed following a decrease in strain applied to bone (Ruff et al., 2006). The Mechano-Regulatory-Pathway theory highlights the fact that it is the surrounding environment which influences the type of cells that are generated around a facture site (Prendergast et al., 1997; Lacroix and Prendergast, 2002) with fluid flow and mechanical strain being the most influential factors.

The exact level of strain required to stimulate bone production has not been precisely quantified; however, multiple studies have attempted to find approximate values (Claes et al., 1997; Frost, 1992; Robling and Turner, 2009). Strains between 1500 and 3000 microstrains (με) are considered excessive causing mechanical fatigue damage; but bone remodelling then quickly takes place to counteract these effects. Above 3000 με, failure due to fatigue can occur; whereas when the strain on the bone is less than 50-100 με, this is considered as "disuse" and bone reabsorption occurs (Isidor and Flemming, 2006). These levels of με required by bone for remodelling to take place have been confirmed by Duncan and Tuner (1995) but the latter study suggested slightly higher levels of strain before the risk of failure comes into play.

Normal strain is often thought to be the main criterion for the stimulation of bone remodelling whereas shear strain is considered harmful to the generation of callus tissue. While both of these points are true, there is nonetheless equilibrium to be found between normal and shear strain where the latter is not harmful to bone remodelling (Klein et al., 2003). Shear strain may in fact not harmful to bone regeneration so long as it does not override the level of normal strain (Epari et al., 2006).

Orthopaedic implants are used to reduce bone fractures. Most implants consist of either an intramedullary nail or a locking compression plate supported by a number of orthopaedic screws. The

number of screws depends on multiple factors such as fracture site and the patient's bone quality (Tada et al., 2003). These screws have a close effect on bone remodelling (Haase & Rouhi, 2013) as they are in direct contact with the bone and therefore provide mechanical stimulus by transferring load to the bone. The torque applied to the screw during insertion can also cause local bone deformation as a peak of compression is applied on the bone around the screw head (Reynolds et al., 2013). An optimal insertion torque based on bone quality has not been estimated and surgeons carry out this procedure based on biomechanical feedback.

The aim of this study is to evaluate the effect of screw-related boundary conditions on the types of deformation consequently applied to the cortical bone and to quantify them. This study was carried out with application to implants used for distal tibia fracture reduction with the main objective of analysing the influence of screw geometry and insertion level and on bone remodelling potential.

2. Method

2.1. Samples

Composite bone samples (medium size left tibiae, item No: #3401, Sawbones®, Malmö, Sweden) were taken from a previous study at the Biomechanical Laboratory of the University Medical Centre, Mainz, Germany, and cut to leave only the lower portion of the diaphysis. The samples had previously been used in a study to test the mechanical performance of surgical reduction implants for distal tibia fractures. No plastic deformation other than the simulated fracture had been recorded. More detailed information on the previous studies can be found in Kuhn (2014a,b). All mechanical hardware was explanted from the samples leaving only the composite bone with its drilled holes for screw insertion.

The samples had previously been implanted with either an External Tibia Nail (ETN, Synthes®, Switzerland), Distal Tibia Nail (DTN, Mizuho®, Japan), or Medial Distal Tibial Plate (MDTP, Synthes®, Switzerland). One of each screw type from each of these implants was collection, leaving a total of four different implant screws (Figure 111). A summary of the screws geometric properties are listed in Table 16. All implant screws are made of the same material: titanium alloy for medical usage (Ti6Al4V) with a Young's modulus of 110-130 GPa (Niinomi, 1998).

Table 16: Geometric properties for each implant screw used.

Sample	Length (mm)	Diameter (mm)	Material	Screw head	Thread profile
DTN distal	43	4	Ti6Al4V	Threaded	Trapezoidal
ETN	36	4	Ti6Al4V	Rounded	Trapezoidal
MDTP cortical	40	2.7	Ti6Al4V	Rounded	Triangular
MDTP locking	30	2.7	Ti6Al4V	Threaded	Triangular
Sawbones ® tibia	375	50 – 60	Epoxy resin	N/A	N/A

Figure 111: The four different orthopaedic screws used in this study.

Screws were inserted into their respective pre-drilled holes using a manual screwdriver. The pre-drilled holes from the previous study acted as an insertion guide for each screw type meaning that all screws were inserted on the medial side of the tibia. The insertion hole for the ETN screw had to be drilled (⌀ 3.5 mm) in the diaphysis as the insertion points for these screws are only found in the proximal and distal metaphyses. All screws were long enough to ensure a bi-cortical insertion. The DTN and ETN screws were inserted at a torque of 1 Nm and 2 Nm (choice of torque is discussed later), respectively. The screws for the MDTP were inserted to the start of the screw head for locking screws, and to the end of the screw thread for the cortical screws. This was to reproduce the position of the compression plate acting upon the screw in a post-operative situation (Figure 113).

The sample was then covered with a black and white speckle pattern in preparation for digital image correlation (DIC) measurements. Still images of the samples were then recorded before and after screw insertion in order to verify the level of pre-strain caused by screw insertion.

Custom-made metal rods were attached to the force transducer (1 kN transducer). Two types of rod were made: one as an inversed "U" to apply the force onto the shaft of the screw in the medullary cavity as per the DTN and ETN Figure 112a). The second rod was cut to leave a thin flat edge used to apply the force onto the neck (MDTP locking screw, Figure 113b-d) or the head (MDTP locking screw, Figure 112b-c) of the screw for example in the case of the MDTP (Figure 113).

The DTN distal screw was tested in three different insertion configurations, all of which were subjected to the same intramedullary loading setup (Figure 112). The threaded screw head was completely inserted into the sample leaving: <1 mm protruding from the cortical layer (DTN-0; Figure 112b); 1 mm of the screw head protruding (DTN-1; Figure 112c); and 2 mm of the head protruding (DTN-2; Figure 112d. These configurations were used to replicate what may be the reality in surgical situations where either the cortical bone is too tough to fully insert the screw head or, on the contrary, where the cortical bone is too weak to support the high torque levels produced when tightening the screw and may trigger cortical crack development leading to secondary fractures.

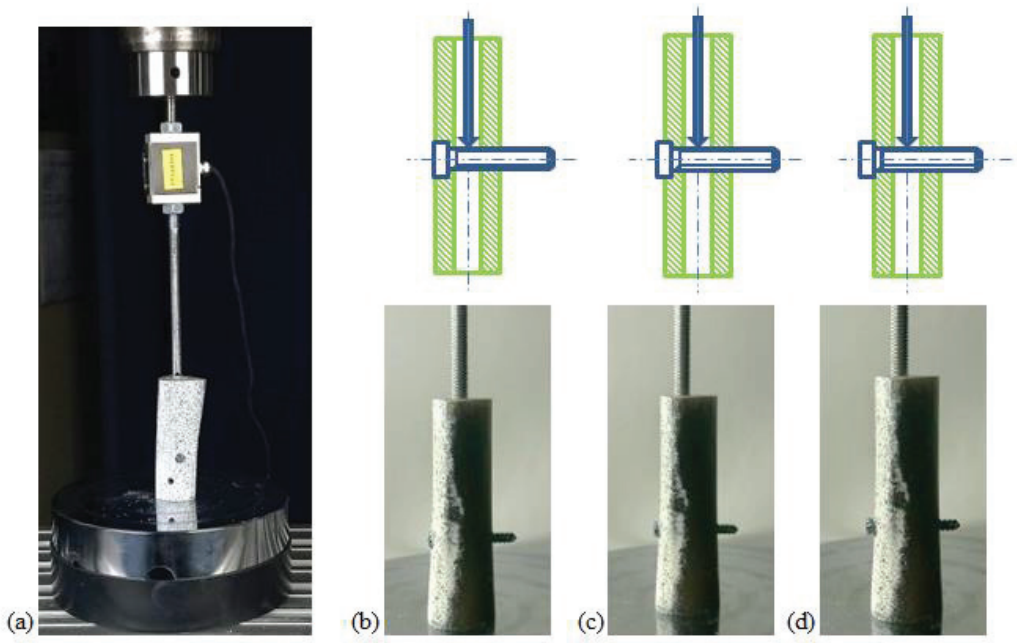

Figure 112: Test setups for intramedullary (a) compression application to the screw as schematic diagrams and experimental photos (b-d). Different setups are shown for the intramedullary screws: DTN-0 (b; fully inserted), DTN-1 (c; 1 mm protruding)

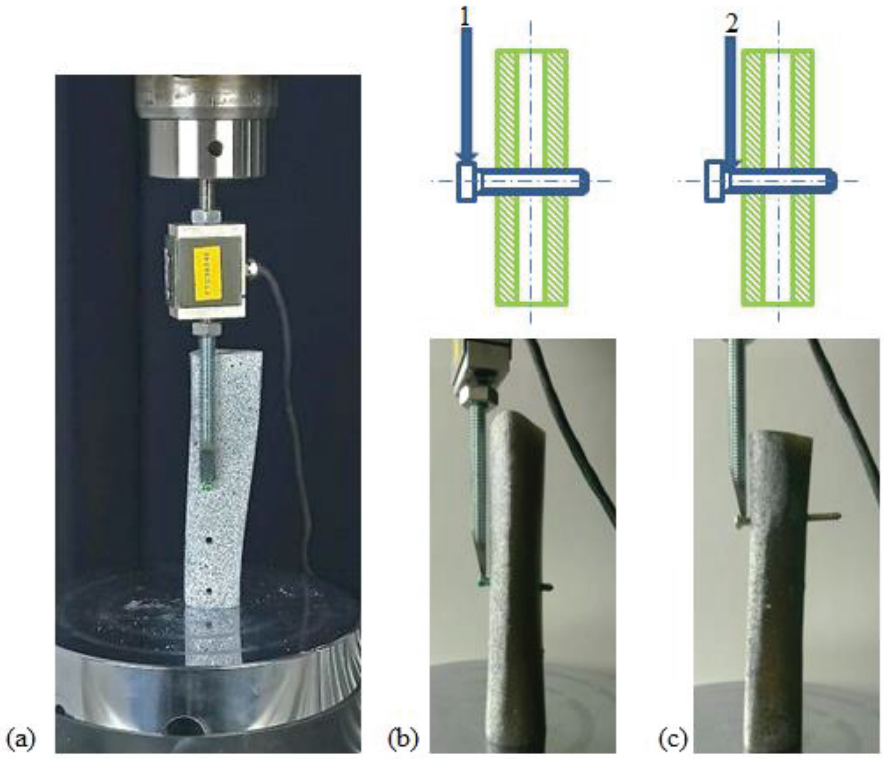

Figure 113: Test setups for external (a) compression application to the screw as a schematic diagram and experimental photos (b). Different setups are shown for the MDTP screws: 1/ MDTP locking screw (b; load application on the screw head), and 2/ MDTP cortical (c; load application on the neck of the screw).

2.2. Data Analysis

An incremental compressive force of 0-700 N was applied to the samples at a loading frequency of 0.05 Hz over 10 cycles. Two identical cameras (GO-5100M-USB, JAI®, Grosswallstadt, Germany) were placed to face the sample, at a divergence of 10° and at a distance of 0.75 m from the sample. Both cameras were simultaneously activated to film the sample during 10 compression cycles at a sampling frequency of 10 Hz. Each screw was tested three times.

Digital Image Correlation was used to calculate the local deformation around the screw head using the image data collected by the cameras; this was carried out using specialised DIC software (Vic3D version 8, Correlated Solutions Inc., South Carolina, USA). A region of interest (ROI) was defined around the screw insertion site and a starting point for correlation placed on a black point of the speckle pattern (Figure 114a). The pattern and step size were 15 and 5 pixels, respectively; the image pixel size was calculated to be 0.1 mm. The first image for all analyses was systematically an image of the sample in question with no screw insertion, and the second image always with the screw inserted before any compressive loading. The remaining images for correlation were those recorded during loading.

Data were extracted by generating a nodal disc on the 3D correlation with the centre of the disc being at the centre of the screw head (Figure 114c). The radius of the nodal disc and the number of points varied between test samples depending on the amount of correlated area around the screw head.

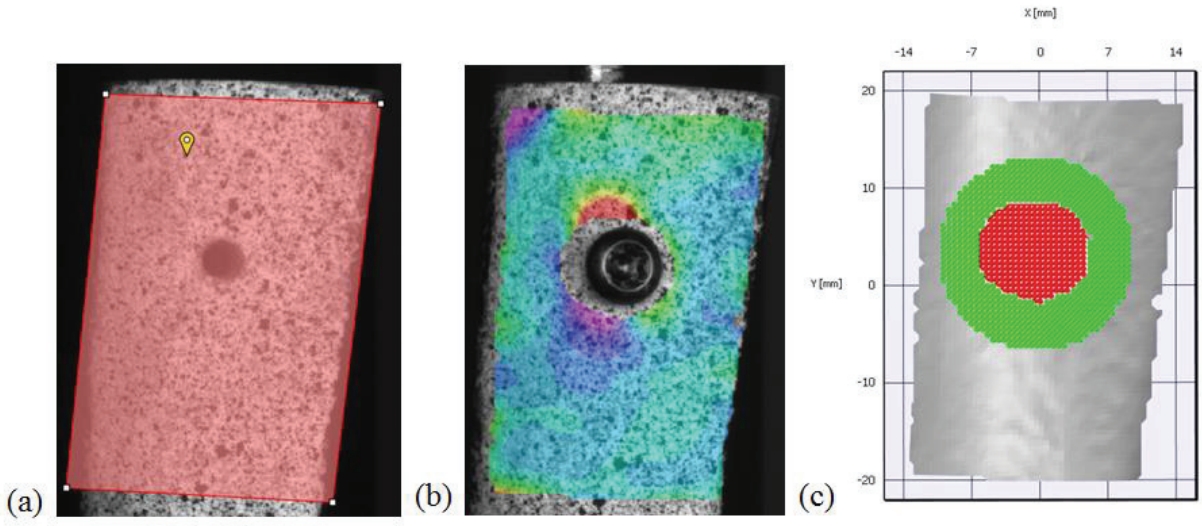

Figure 114: Identification of the ROI (a), the correlation result (b), and the placement of the nodal disc on the correlated surface. Points in red refer indicate no correlated surface (no data); points in green are placed on the correlated surface.

2.3. Data Processing

An in-house script was written in Scilab (version 5.5.2) which processed the strain data exported from Vic3D. The maximum and minimum vertical normal (ε_{yy}) strain levels calculated by Vic3D were identified and each associated to one image file. The ten image files were then further processed. In the grid area, the outer edges were prone to having high deformation levels due to edge side effects produced from the width of the applied grid during the DIC; these areas were eliminated from the data processing procedure. Data were slightly smoothed and projected onto a 2D best fit plane around the screw head.

Once the data had been transformed, a horizontal x-axis was defined and the data were divided into segments of 2° from the 0° x-axis (Figure 115a); within each segment, a local maximum and minimum were located by tracing a line in the centre of this segment. The points of this line were calculated by interpolation using the kriging method (Trochu, 1993). The local maximum, minimum and mean strain were later used to calculate the global maximum & minimum and mean were identified.

Values within a third of one standard deviation of the mean value were identified across all areas around the screw head where high strain values could be located, allowing the angular distance over which the mean positive (Figure 115b, top) or negative (Figure 115b, bottom) strain to be located. One third of one standard deviation was chosen as the cut-off point as this allowed for the maximum amount of information to be collected, while eliminating parasitic deformation from edge effects, for example. The exported data included the angle (with respect to the x-axis) at which the maximum and minimum is located, the distance from the grid centre, and angular range over which this value can be located.

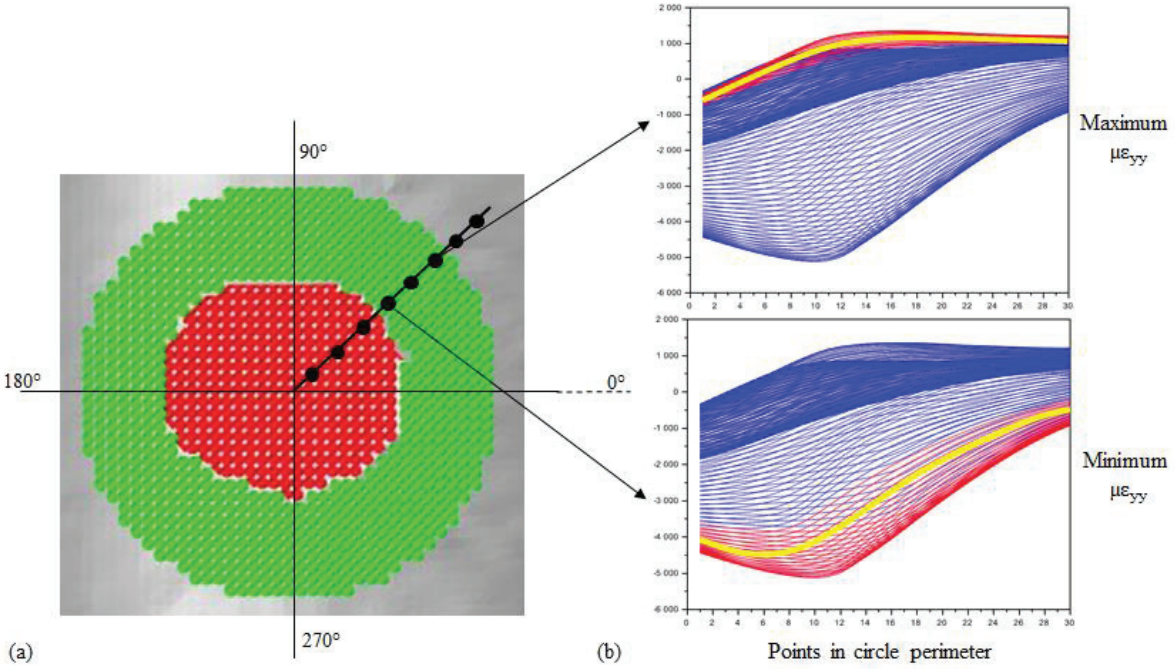

Figure 115: Definition of axes and of segments within which the maximum, minimum and mean strain was located (a). The identification of the mean maximum (b, top) and minimum (b, bottom) strain ± 1/3SD; strain variation as a function of polar coordinates of the nodal grid with maximum and minimum zones highlighted in red.

3. Results

Four different screws (one of which was tested in 3 different configurations) were subjected to compression testing. Exported deformation variables included vertical normal strain (ε_{yy}) and shear strain (ε_{xy}). No other deformation variables were used due to artefacts resulting from parasite speckle pattern edge effects. No statistical analyses were carried out due to small sample size. For the MDTP screws, data analysis was only undertaken for the lower hemisphere (180-360°) of the nodal disc during loading as the metal rod for force application hid the upper hemisphere speckle pattern (Figure 113a).

The applied scale in Figure 116 to Figure 119 was based on 75% of the maximum positive and negative ε_{yy} (-0.002 and +0.001 ε) and ε_{xy} (-0.0014 and +0.0026 ε), respectively. This scale has the effect of amplifying or reducing the highlighted area of positive or negative deformation. In cases where multiple positive or negative strain zones are identified, the zone where the maximum strain can be located is underlined.

Vertical normal strain (ε_{yy})

Vertical normal pre-strain (Figure 116) is mainly distributed across four clear zones consisting of two positive and two negative deformation zones (Figure 116a-d). This is true for all samples except the MDTP screws where only one negative zone is identified in the cortical (Figure 116e) and locking screw, and just one positive zone in the locking screw (Figure 116f).

In samples where two maximum or two minimum ε_{yy} zones are observed, these tend to be located at opposing sides of the screw head, with the exception of the ETN screw where the ε_{yy} zones appear to be at right angles (Figure 116d). For the MDTP locking screw (Figure 116f), the sole maximum and minimum deformation zones are at opposing sides. For the DTN-0 screw configuration, overlapping of the maximum and minimum ε_{yy} is witnessed for the pre-strain, likely due to the range in which the strain values were identified where within any one segment both levels of ε_{yy} can be seen.

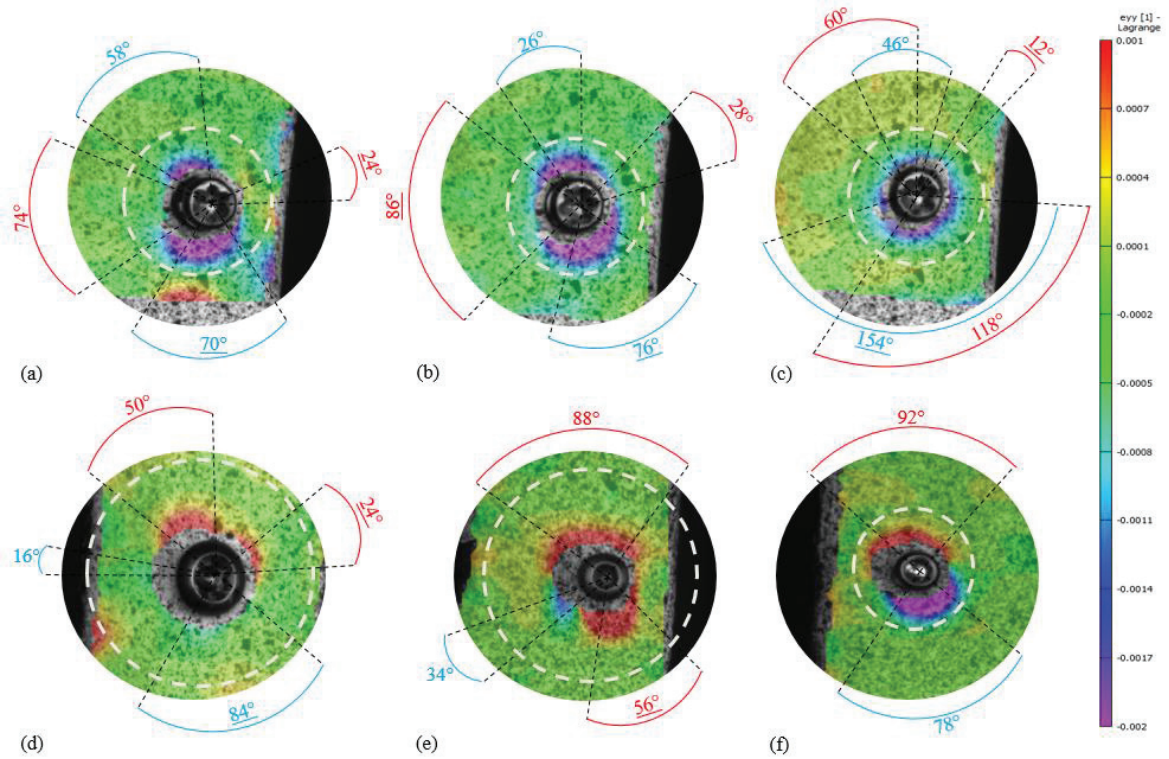

Figure 116: Qualitative positive and negative εyy pre-strain distributions for the DTN-2 (a), DTN-1 (b), DTN-0 (c), ETN (d), MDTP Cortical (e), and MDTP Locking (f) screws after insertion. The white dashed circle represents the zone in which the nodal grid was superimposed.

During loading (Figure 117) the DTN-2 and -1 screw configurations maintain four clear ε_{yy} zones (two maximum and two minimum) but over a smaller range indicating an increase in strain concentration in that area (Figure 117a-b). The maximum ε_{yy} shifts from to the right to the left of the screw head in the DTN-2 sample. In the DTN-1 screw configuration, the maximum and minimum ε_{yy} zones remain in the same area but over a smaller range (maximum pre-strain: 132-218°, loading: 160-212°; minimum pre-strain: 248-324°, loading: 244-302°).

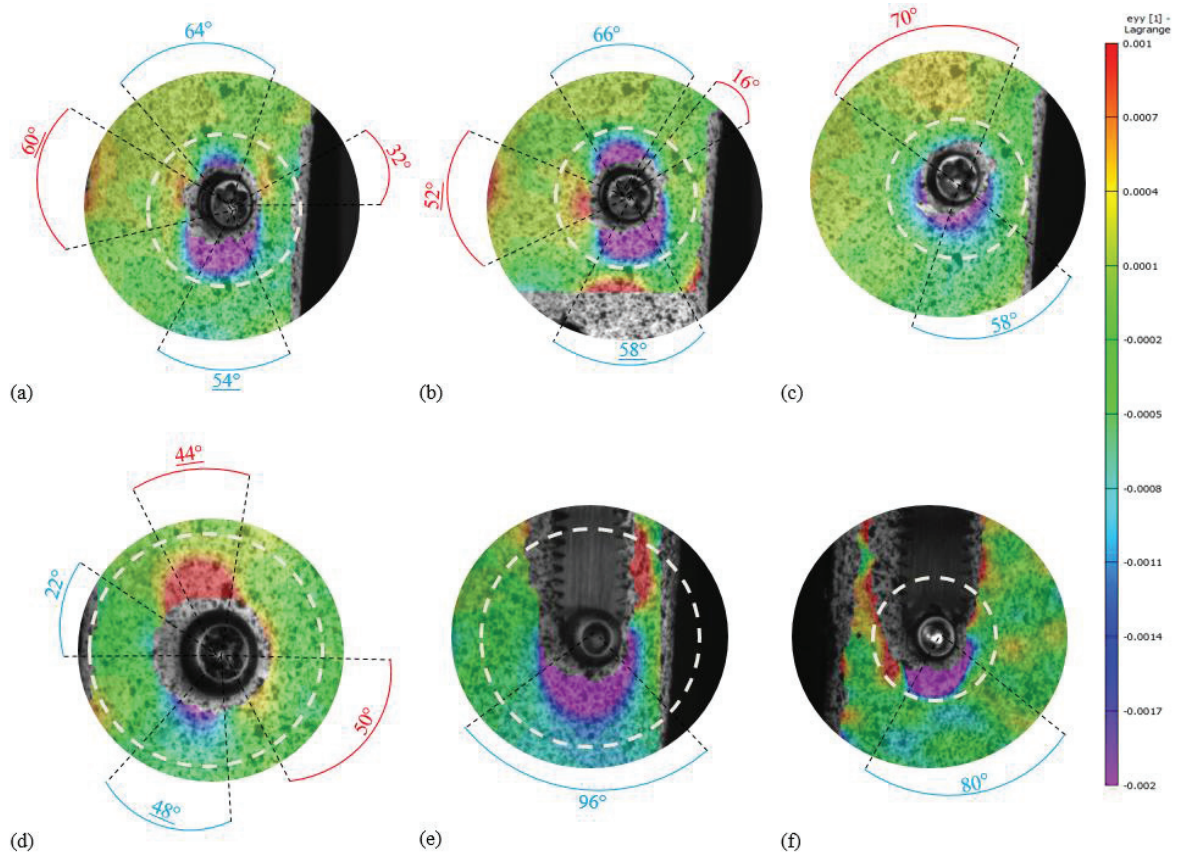

Figure 117: Qualitative strain distribution at maximum negative εyy strain levels at -690 N loading for the DTN-2 (a), DTN-1 (b), DTN-0 (c), ETN (d), MDTP Cortical (e), and MDTP Locking (f) screws. The white dashed circle represents the zone in which the nodal grid was superimposed.

The DTN-0 screw shows two opposing and one smaller zone of maximum ε_{yy}; minimum ε_{yy} is located below (Figure 116c); in particular, the minimum ε_{yy} zone seems to be concentrated over a smaller area below and immediately around the screw head, the highest level of maximum ε_{yy} is over the smallest range above the screw head. The DTN-0 sample minimum ε_{yy} zone reduces in size almost by three-fold from pre-strain (Figure 116c) loading (Figure 117c). Four zones can also be seen around the ETN screw due to both screw insertion and loading. Minimum ε_{yy} is located below the screw head while maximum ε_{yy} is observed above the screw head.

The MDTP cortical screw exhibits a relatively large range of maximum ε_{yy} at screw insertion (pre-strain, Figure 116e) with the highest value being located in the zone 260-326°, while during loading (Figure 117e) no maximum ε_{yy} is identified in the analysed area. The minimum ε_{yy} range increases to almost three times from 200-234° (pre-strain) to 194-290° (loading). The MDTP locking screw demonstrates almost no change in minimum ε_{yy} range; as with the cortical screw, no maximum ε_{yy} is recorded (Figure 117f).

Shear normal strain (ε_{xy})

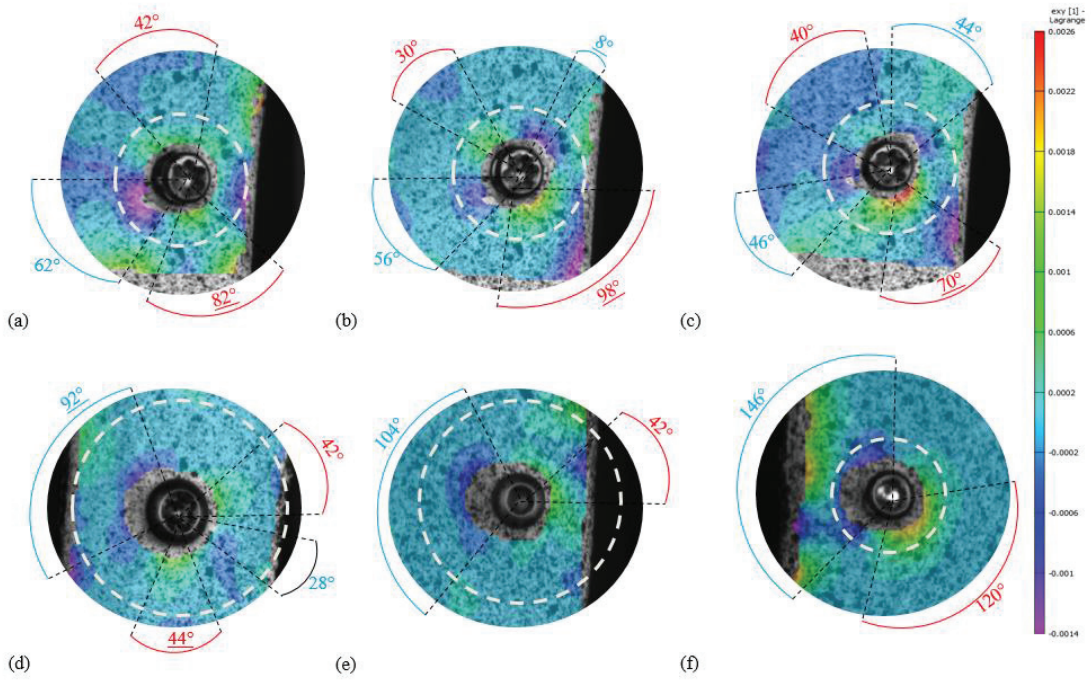

Figure 118: Qualitative positive and negative εxy pre-strain distributions for the DTN-2 (a), DTN-1 (b), DTN-0 (c), ETN (d), MDTP Cortical (e), and MDTP Locking (f) screws. The white dashed circle represents the zone in which the nodal grid was superimposed.

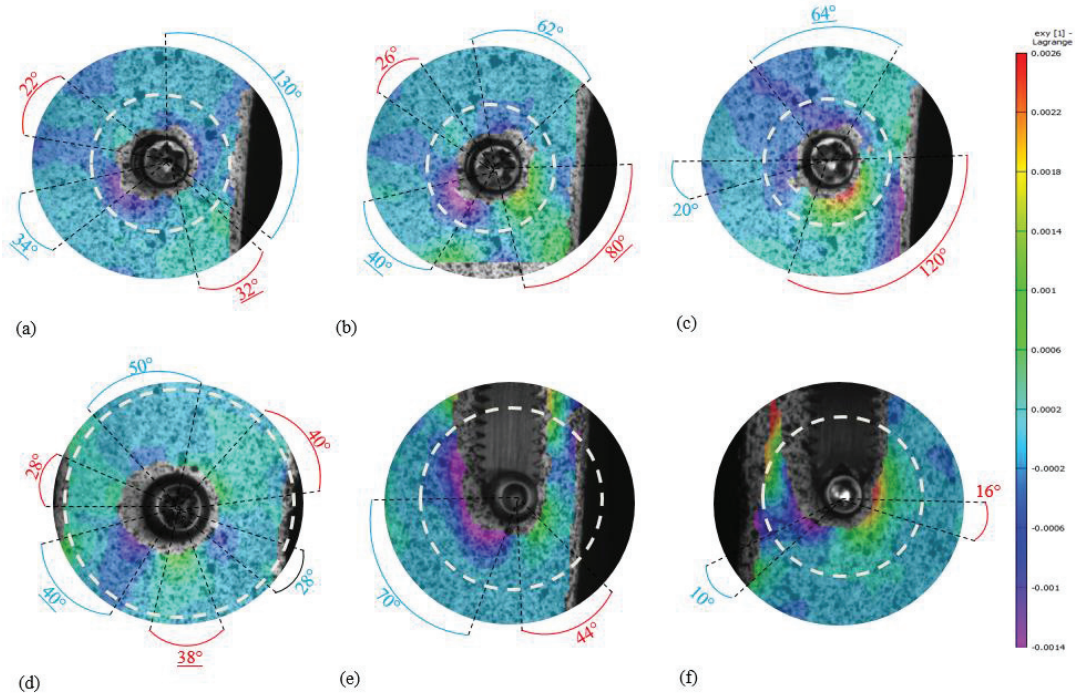

Figure 119: Qualitative strain distribution at maximum negative εxy strain levels during loading for the DTN-2 (a), DTN-1 (b), DTN-0 (c), ETN (d), MDTP Cortical (e), and MDTP Locking (f) screws. The white dashed circle represents the zone in which the nodal grid was superimposed.

The DTN-2 screw configuration presents one minimum ε_{xy} zone and two maximum – which are located at opposite ends of the screw head (Figure 118a). This increases to four defined ε_{xy} zones during loading (Figure 119a) with the addition of a minimal ε_{xy} zone opposite to the original zone. The maximum ε_{xy} zones become more concentrated as does the original minimum ε_{xy} zone, whereas the second minimum ε_{xy} zone is located over a wide range, but strain levels remain in the same regions around the screw head.

The DTN-1 sample demonstrates four zones (two maximum and two minimum) both for pre-strain (Figure 118b) and loading (Figure 119b) analyses. Strains of the same pole are found at opposing ends of the screw head, and during loading two dominant concentrated zones are identified: one maximum and one minimum, both below the screw head. The minimum ε_{xy} zone shifts to its polar opposite between pre-strain and loading, also increasing in range. The maximum ε_{xy} remains in the 270-360° quadrant, decreasing slightly in range.

Four zones can also be identified for the DTN-0 pre-strain observations in similar areas as the DTN-1 screw (Figure 118b-c). During loading the maximum ε_{xy} merges to one zone below the screw head where the highest shear strain levels are located; the greatest minimum ε_{xy} zone is located opposite to this maximum zone both during pre-strain and loading, it covers a greater area during loading (Figure 119c). One could argue that the second, smaller minimum ε_{xy} zone can merge with the greater minimum ε_{xy} zone; however, based on the analysis parameters, two separate zones are identified.

The ETN presents two opposing minimum ε_{xy} zones and two maximum ε_{xy} zones during pre-strain (Figure 118d), increasing to three during loading (Figure 119d). The zones are located in alternating order (maximum followed by minimum ε_{xy}). The highest minimum ε_{xy} decreases in range by 50% between pre-strain and loading. Maximum ε_{xy} remains relatively unchanged before and during loading.

Both MDTP screws demonstrate one maximum and one minimum ε_{xy} zone for screw-related pre-strain (Figure 118e-f) and under loading (Figure 119e-f). Contrary to ε_{yy}, where multiple strain zones are present, the maximum ε_{xy} zones tend to be located below the screw head with the minimal ε_{xy} zones above the screw head. The differences between pre-strain and loading demonstrate a reduction in range for minimum $\varepsilon_{xy;}$ whereas the maximum range remains the same, but is transferred to below the screw head for the cortical screw. The MDTP locking screw experiences a large decrease in minimum and maximum ε_{xy} range, becoming more concentrate during loading.

The graphical representation of ε_{yy} (Figure 120; Figure 121) and ε_{xy} show the pre-strain levels in blue and are completed by total strain during loading, in red. In certain cases, no strain during loading

is added to the graph implying that the pre-strain was greater than or equal to the total strain measured during loading.

The highest levels of maximum ε_{yy} can be observed in the MDTP Cortical screw where an average of 2322 με was calculated, and all of which is due to pre-strain. The ETN screw also exhibits relatively high levels of ε_{yy} of which 67% is accounted for by pre-strain. The DTN screw configurations seem less sensitive to dominant vertical pre-strain with 67%, 9%, and 3% being accounted for by pre-strain in the DTN-2, -1, and -0, respectively. The MDTP locking screw displays relatively low levels of ε_{yy}, 78% of which are related to pre-strain. An increase in DTN screw head insertion therefore seems to reduce initial strain before loading; whereas screws that are less inserted into the cortical layer produce higher levels of vertical pre-strain.

Maximum ε_{xy} is highly present in the all DTN screw setups, exceeding ε_{yy} values by more than 20-fold in one case (DTN-0: 115 $\mu\varepsilon_{yy}$ against 2422 $\mu\varepsilon_{xy}$). Loading seems to have a greater impact on ε_{xy} levels where the screw head is further inserted into the sample. Values for ε_{xy} for then ETN and MDTP cortical screw are solely due to pre-shear strain and do not exceed 50% for the ε_{yy} levels. Shear strain for the MDTP locking screw is 2.5 times greater than ε_{yy} and, as with the ETN and MDTP cortical screw; it is entirely dominated by pre-strain.

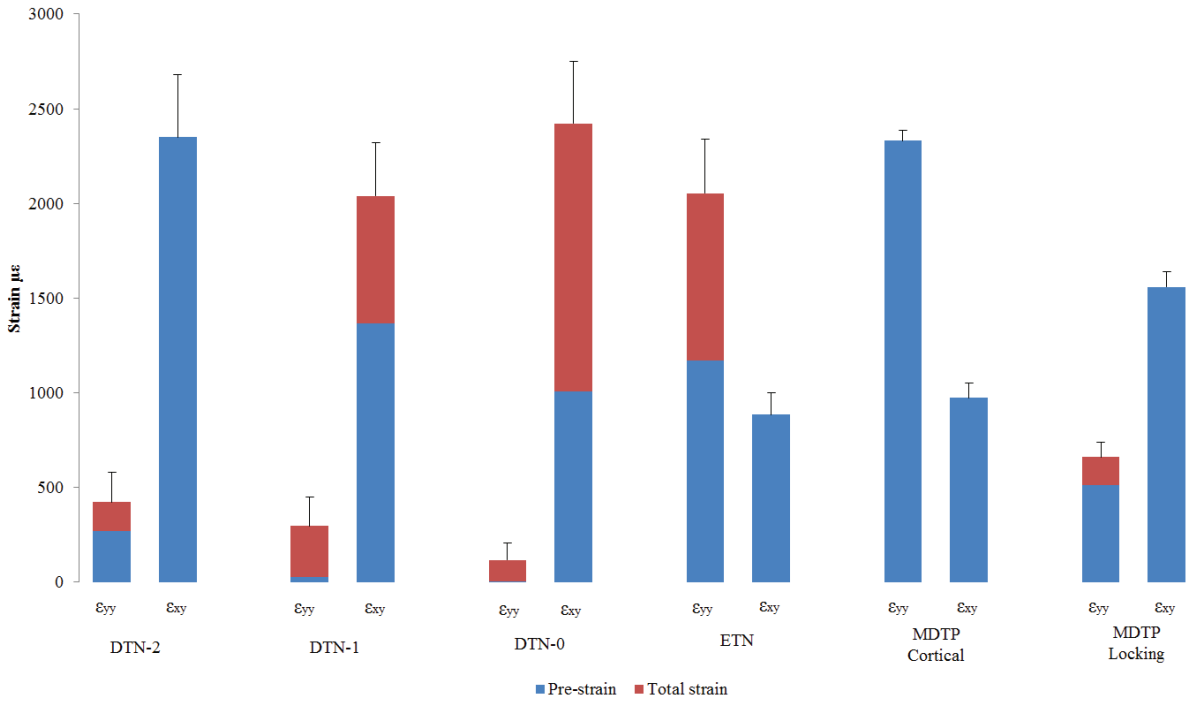

Figure 120: Proportions of mean + 1SD positive pre and total normal (εyy) and shear (εxy) -strain before and during loading. Where no total strain is presented, the pre-strain was observed as higher than the total strain.

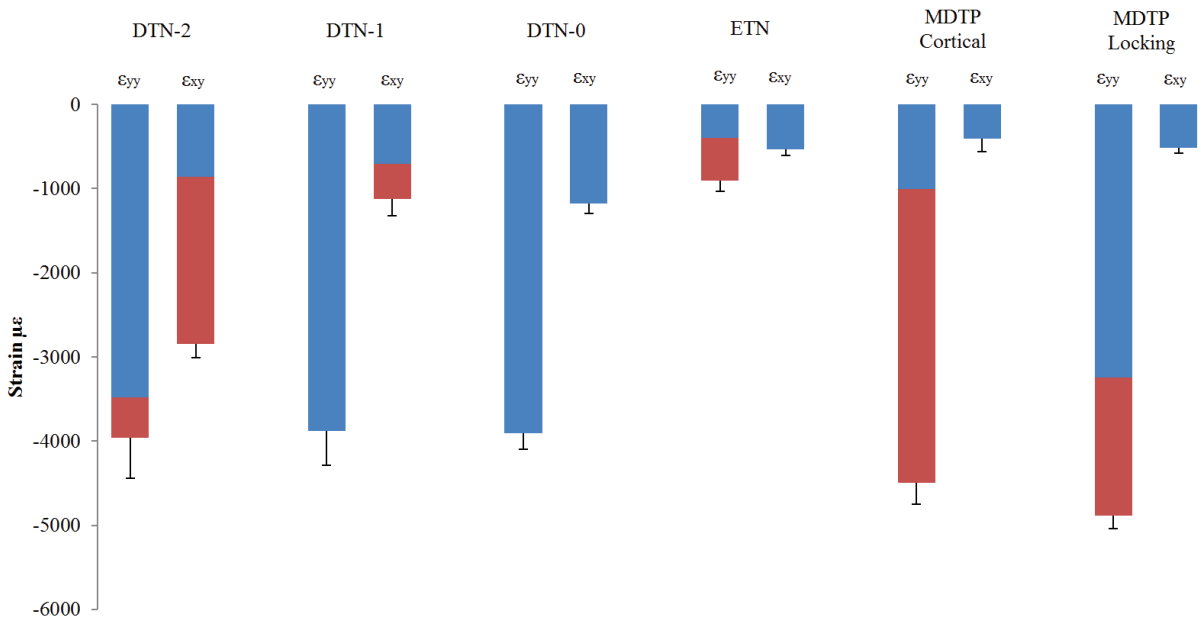

Figure 121: Proportions of mean + 1SD negative pre and total vertical (εyy) and shear (εxy) -strain before and during loading. Where no total strain is presented, the pre-strain was observed as higher than the total strain.

The DTN screws all reach a similar level of negative ε_{yy} (DTN-2: -3958 με, DTN-1: -3880 με, DTN-0: -3911 με), only the DTN-2 sample is not entirely dominated by pre-strain, which nonetheless accounts for 88% of total ε_{yy}. The ETN screw displays low levels of ε_{yy} (-905 με), pre-strain accounting for 44% of total strain. The MDTP samples demonstrate the highest level of ε_{yy} (cortical screw: -4492 με and locking screw: -4885 με) of which 22% and 66% are due to pre-strain, respectively.

Minimum ε_{xy} is less present than maximum ε_{xy} reaching a high of -2849 με in the DTN-2 sample, 30% of which is represented by pre-shear strain. The DTN-1 and -0 samples exhibit similar levels of ε_{xy} (-1123 με and -1178 με, respectively), in which 63% for the DTN-1 is due to pre-strain where as in the DTN-0 configuration the ε_{xy} is 100% pre-strain. This indicates that an increase in screw insertion decreases total negative shear strain but increases its pre-strain. The ε_{xy} for the ETN is dictated by pre-strain at around 50% (-487 με) of the ε_{yy} measured. In the MDTP screws, very little shear strain is observed (cortical: -412 με, locking -514 με) compared to the measured ε_{yy}.

Dominance of minimum ε_{xy}, exceeding minimum ε_{yy}, is witnessed in none of the samples.

4. Discussion

Normal and shear deformation patterns and values for screw types for DTN (3 configurations), ETN and MDTP implants were evaluated using a 700 N compression test setup. Quasi-static loads (0.05 Hz loading frequency) were applied directly to the screw body for the DTN and ETN screws, while for the MDTP screws the load was applied to the screw head (locking screw) or neck (cortical screw). The highest ε_{yy} levels were found in the MDTP cortical and ETN screws, the greatest minimum ε_{yy} levels were observed in the MDTP cortical and locking screws. Highest maximum ε_{xy} values were found in DTN-0 and DTN-2 samples, while the highest minimum ε_{xy} were recorded in the DTN-2 sample.

An increase in maximum ε_{yy} concentration was observed in all samples from screw insertion to loading, except for the MDTP screw where no positive ε_{yy} was measured after screw insertion.

The increase in positive strain range between the DTN, ETN and MDTP locking screws may be related to the fact that the external screw head creates a greater moment arm, generating compression below and tension above the screw head. Tensile strain has been shown to have a positive effect on bone modelling when compared to compressive strain but at a slower rate (Zhong et al., 2011).

Shear strain has been suggested to not be harmful to the bone remodelling process, provided that ε_{xy} levels do not exceed ε_{yy} levels (Klein et al., 2003; Epari et al., 2006). For negative strain measurements, the ε_{yy} remained constantly greater than the ε_{xy} indicating that normal, healthy remodelling would take place in these zones. For positive strain however, shear strain surpassed vertical strain for all DTN screw configurations and also the MDTP locking screw. In these cases, healing around these areas may be delayed. As compressive (negative) strain largely dominated shear strain in the majority of cases, it may be of interest to take this into account in rehabilitation programmes enabling negative vertical strain to be transmitted to different areas of the screw insertion or healing site allowing for a more efficient healing process.

The high vertical pre-strain levels relative to total strain during loading for the DTN screw may be explained by the diameter of the drilled hole for screw insertion (3.2 mm) and the diameter of the screw head (cone shaped from 4 mm to 5 mm). The total insertion of the screw head generates a global compression all around the insertion site leading to minimum strain, and this may explain the low minimum ε_{yy} levels recorded, linked to the fact that the strain is more equally distributed. High ε_{yy} pre-strain levels without the effects of loading are of interest concerning the bone remodelling that can take place while the patient is still susceptible to be immobile directly after the operation (Watanabe et al., 2000). This can be beneficial to patients who already have mobility problems; however, this should also be treated with caution and over-loading may occur faster in these scenarios during weight-bearing (such as that observed in the MDTP screws), increasing the risk of implant failure particularly in patients with

compromised bone quality (Varga et al., 2017). The ETN screw however, demonstrated higher minimum pre-shear strain than pre-vertical strain.

The highest minimum ε_{yy} levels during loading are found in the MDTP cortical and locking screw samples. This can be related to their geometry as screws with a smaller diameter and triangular threads have been found to transmit higher forces to neighbouring bone (Haase and Rouhi, 2013) when compared to trapezoidal or rectangular threads. The small diameter and external loading point may also explain the higher minimum ε_{yy} levels observed in the cortical screw as more force is transmitted to the bone sample.

In certain cases, qualitative observation in Figure 116 to Figure 119 show high strain close to the screw head but also to the border of the correlated area. Such zones were omitted from results and considered as edge side effects, not related to the screw insertion or loading; this was analysed on a case-by-case basis, strain zones were considered as valid if the strain originated from the screw head and if the highest concentrated area of that zone was closest to the screw head. If the highest concentrated strain zone originated at the edge of the correlated area, the zone was regarded as an edge effect.

The decision to assess only the lower 180° of the MDTP screw strain during loading was based on the identification of high strain levels located in a non-correlated area due to the interpolation method used in the data processing. We felt it was wiser to simply evaluate an area where only a correlated zone of quality would be taken into account (see example of undesired zone in Figure 119f). This may, however, lead to missing data for example for the MDTP cortical screw during loading (Figure 8e) where the negative ε_{xy} is observed before 180°. We cannot say for sure whether this is due to edge effects or sample deformation due to loading.

Not all screws were inserted with the same torque. The torque level of 1 Nm for DTN-0 screw head insertion was chosen based on the 1.5 Nm used when inserting the green locking screws into the MDTP. The 1.5 Nm are based on the titanium plate surgical procedure and therefore a lower rotational force was selected for cortical bone. The 2 Nm for the ETN screw was the lowest torque level measured when inserting the screw. This may be due to the new hole drilled for screw insertion, the hole was tapped by the screw insertion creating high friction levels whereas for the other samples, the insertion holes had already been tapped and subjected to loading.

In-vivo forces would be higher than 700 N and also applied at a higher frequency but they would also be distributed over an average of 5 screws depending on the implant type. The loading frequency in the current study equated to 70 $N.s^{-1}$; whereas a person of 70 kg walking at a normal speed would induce a loading frequency of 420 $N.s^{-1}$. This latter calculation is based on loads of 1.2x body weight, equivalent to 840 N in a 70kg patient (Hamill and Knutzen, 2008) and a walking frequency of 2 Hz (Cavagna and Franzetti, 1986). Nonetheless, one would not

expect a newly post-operative patient to walk at the usual rate of 2 Hz nor to be full weight-bearing.

Research has also suggested that it is not only the level of strain applied to the bone, but also the rate at which it is applied. The example used in the literature (McLeod and Rubin, 1992) states that a strain of 500 με applied at a rate of 1 Hz, is relatively harmless. However, the same level of strain applied at a frequency of anywhere between 10 to 60 Hz can promote bone remodelling, demonstrating an inverse relationship between strain magnitude and rate (Rubin and McLeod, 1994). Future studies may wish to integrate varying load application rates to their protocols.

4.1. Limitations

One might imagine that strain levels would be even higher in the uncorrelated area surrounding the screw head as it is the initial area which receives the force transfer from the screw. The areas close to the screw head for all screw types were, however, unable to be correlated. In order to be able to apply DIC closer to the screw head, a finer speckle pattern would need to be used and a smaller ROI defined. Incidentally, DIC was impossible above the screw head for the MDTP screws due to the rod used to apply the force which blocked the camera view of this area.

The loads applied to the screws were not pure compressive loads and a six-axis sensor would have been necessary to evaluate the other forces and moments applied. During testing, a bending effect was applied to the screw due to its bi-cortical insertion in the Sawbones® sample, and slight rotation of the sample was also observed however neither of these components was measured.

The values cited in this study for strain levels and angle ranges are taken from an in-house code which was based on finding the maximum positive and negative strain exported from the Vic3D software. A zone around this area within one third of standard deviation of the maximum strain was defined. The use of one third of standard deviation (SD) was used after initially choosing an area based on SD/2 which we perceived to be too broad allowing low values to be included in the analysis. A more robust method may have been to carry out a sensitivity analysis in order to find the optimum percentage to use for each sample.

Sawbones have been validated as being a sound substitute for cadaver bones, but they are based on a young male aged around 30, of height 183 cm and weight 90kg, in good health (Heiner et al., 2008; Gardner et al., 2010). Using these products as specimens does not give us the global picture of the influence of screw types on human cortical bone as it omits the elderly and post-menopausal women, for example who are at a greater risk of fracture and may receive an implant. As cortical thickness is a strong indicator of bone strength (Ammann and Rizzoli, 2003), future research should consider carrying out a similar study based on elderly patients and the use of weakened (composite) bone where screw

purchase may be compromised due to a decrease in cortical thickness and quality in this population (Tada et al., 2003).

The use of composite bone was chosen based on the supposed macro-homogeneity of the geometry and material properties; nonetheless, multiple test series (n = 5) were required before consistent results were able to be exploited. We can be confident in the use of Sawbones® on a macro-level with respect to mechanical behaviour during macro-loading; however, in light of the problem encountered, questions can be asked on the validity of Sawbones® at a micro-structural level with respect to observed deformation patterns. Factors such as pre-strain, screw insertion torque, and metal rod (for force application) length and diameter were all progressively controlled in the study. Authors wishing conduct similar studies are advised to increase the number of tests carried out on each sample and also to carefully dedicate time to controlling boundary conditions.

Only DIC was used to calculate the strain tensors in this study. DIC has been evaluated and found to provide satisfactory results for strain measurements in composite materials in comparison with strain gauge measurements (Hensley et al., 2017; Rogge et al., 2013). The use of DIC allows the experimentally measure the strain on the surface of the cortical bone; however, we are not able to gain information regarding the effect of mechanical hardware on trabecular bone. This would be possible through finite element analysis (FEA) (Epari et al., 2006; Haase and Rouhi, 2013; Lacroix and Prendergast, 2002).

5. Conclusion

Although these results may not be conclusive enough to weigh the decision between screw options – this being more importantly based on the patient and the wound – it offers information on screw-related boundary conditions for new implant development. Pre-strain linked to screw insertion levels seems to play a large role in the compressive and tensile deformations transmitted to the outer surface of the cortical layer. The use of numerical simulation would allow for an insight into what happens across the entire cortical and trabecular bone, an aspect that is not readily available by use of experimental techniques. Furthermore, where pre-strain is non-negligible, pre-stress is also likely to be important.

It is also interesting to note that any projects involving the numerical modelling of these here-mentioned implants should take into account the screw type. As noted in the present study, the deformation patterns around the screw head vary depending on screw head geometry (threaded vs non-threaded) and the load application point (intramedullary or external). Screws are modelled as basic cylinders should consider taking into account the level of screw head insertion so that the relevant deformation patterns are reproduced.

Conclusion

The aim of this research project was to assess the feasibility of the Distal Tibia Nail as an orthopaedic fixation device for supra malleolar osteotomies performed using the medial wedge opening technique. To date, only external plates are offered to support this type of osteotomy and there is little research dedicated to the biomechanical study of SMOT. The only specific biomechanical research found was from Ettinger et al. (2018) who compared the biomechanical behaviour of four different plates for MWO, and Nha et al. (2016) who investigated the safe zone for MWO. The Distal Tibia Nail has already proven to be a solid option for A3 distal tibia fractures in previous research by Kuhn et al. (2014a,b) and this implant is currently in clinical trials in Japan.

Test setup – Chapter 2

Firstly, a preliminary study was conducted to characterise the testing environment in both the compression and torsion test setups. For compression testing, the underlying point was the use of PMMA as a potting material for biomechanical samples. While easy to produce and mould to any form, it in fact has an equivalent compressive stiffness construct to than of a Sawbones® medium-sized tibia. Other factors were also found to strongly influence measured stiffness, such as loading contact point, removal and replacement of the sample, and the applied loading axis. It was, in particular the PMMA thickness and the loading axis to which the most attention was drawn in further testing scenarios leading to the development of a template to ensure the repeatability of the sample embedding method.

Biomechanical testing – Chapter 3

A series of 18 left medium-sized composite tibiae were tested under low levels of compression (350 N) and bi-directional torsion (±4 Nm). Heiner et al. (2008) is the only author to have tested fourth generation Sawbones® samples under compressive and torsional loads, finding a standard deviation of 9.3% between samples. A different test setup was used in our study and 13% SD was observed between samples.

A total of 16 samples were then attributed to either a DTN (n=8) or MDTP (n=8) implant and a MWO was simulated in all samples. The composite bones underwent low and high compression (350 N, 700 N) and torsion (4 Nm, 8 Nm) testing and bone-implant stiffness construct was measured. The same procedure was performed after creating a fracture in the lateral cortex of the osteotomy, and finally by simulating an A3 fracture.

Although a significant difference was observed between stiffness constructs of the two groups, the measured interfragmentary movement remained below 1 mm and it is therefore possible to conclude that the DTN could be a viable option for MWO fixation. Results from the A3 fracture simulation were

in agreement with data from Kuhn et al., (2014b) in that the MDTP is not a safe option for unstable extra-articular distal tibia fractures.

Statistical analyses – Chapter 4

The penultimate part of this project was to use all collected data from tested samples to measure a series of influencing parameters thought to have an impact on measured stiffness from the biomechanical tests. All healthy samples were reconstructed, as were samples with a MWO osteotomy and implant. CT scans of the instrumented samples were locally affected by metal artefacts from the implants and this made the reconstruction of trabecular bone impossible from CT scanning.

The identified parameters were used as input variables into a statistical analysis of Pearson Product-Moment correlation coefficients to assess their effect on sample stiffness. In the case of one or more variables being statistically significant at the 95% level during correlation, a combination of maximum two variables were entered into a multiple regression model to ascertain to what extent they together influenced stiffness results.

Results varied between the DTN and MDTP groups, as well as between the compression and torsion tests. Healthy sample stiffness was found to have a non-negligible influence on measured stiffness, supporting the idea that the original stiffness construct of Sawbones® samples can create a bias on later results. For compression testing, the loading axis position and PMMA thickness appeared to be continuously influential throughout all testing phases. For torsional testing, the position of the sample and the implant with respect to the loading axis also proved to be important factors. Again, these results support findings from the preliminary study in Chapter 2, highlighting the need to control test boundary conditions in order to reduce parasitic influence on stiffness measurements.

Screw influence on bone strain – Chapter 5

An investigative study was carried out to assess the different strain levels and patterns transmitted to the outer cortical surface of Sawbones® by the screws specifically used for distal tibia fractures. A secondary objective of this study was to obtain this information for later use for the evaluation of a numerical model.

Compressive loads of 700 N were applied to the screws in a loading situation equivalent to that applied in reality with an implant. Normal and shear strain levels were recorded using DIC. Maximum εyy was often overtaken by maximum εxy; whereas minimum εyy remained higher than minimum εxy which offers a more favourable situation for bone remodelling. Different screw head boundary conditions produce very strain patterns and levels and this should be accounted for in the development of a numerical model with respect to the specific modelling of the screws.

Perspectives

Using the CT scan reconstructions, numerical models are planned to be developed in order to imitate the test conditions used in the experimental work presented here. This will firstly be performed for compression testing.

Digital image correlation was little used, compared to collected data, in this project due to the necessarily time needed to process the collected images; however this is planned for future work and will contribute to the validation of a numerical model.

Results could be improved for the setup for torsional testing as this was possibly an error source in the measured stiffness constructs. Further work is required to produce an experimental procedure for which we can quantify the setup stiffness and measure the influence of different setup parameters, similar to the work carried out for the compression setup.

This study brought new insights into the experimental factors influencing outcome measures in the testing of orthopaedic devices and confirmed the possibility of the DTN implant being used for the fixation medial wedge osteotomies.

References

Ahmad, M.A., Sivaraman, A., Zia, A., Rai, A., Patel, A.D. Percutaneous locking plates for fractures of the distal tibia: Our experience and a review of the literature. *J Trauma* 2012; **72**(2): E81-E87.

Ammann, P., Rizzoli, R. Bone strength and its determinants. *Osteoporosis Int* 2003;**14**: 13–18. doi:10.1007/s00198-002-1345-4

Augat, P., & Schorlemmer, S. The role of cortical bone and its microstructure in bone strength. *Age and Ageing 2006*; **35** Suppl 2: ii27–ii31. https://doi.org/10.1093/ageing/afl081

Babyak, M.A., What You See May Not Be What You Get: A Brief, Nontechnical Introduction to Overfitting in Regression-Type Models, *Psychosom Med* 2004; **66**:411-421.

BAUER, R., KERSCHBAUMER, F., POISEL, S. Orthopädische Operationslehre. Becken und untere Extremität, Teil 2. 1995. Georg Thieme Verlag : Stuttgart.

Beaman, D., & Gellman, R. Distal Tibial Varus. *Foot and Ankle Clin* 2012; **17**(1):83–93. https://doi.org/10.1016/j.fcl.2011.11.002

Bennell, K., & Brukner, P. Preventing and managing stress fractures in athletes. *Phys Ther Sport* 2005; **6**(4):171–180. https://doi.org/10.1016/j.ptsp.2005.07.002

Billard, R. Développement d'un implant à géométrie variable pour le traitement des fractures du fémur proximal chez les personnes âgées (Phd thesis). Université de Grenoble 2014. Retrieved from https://tel.archives-ouvertes.fr/tel-00987969/document

Bishop, J. A., Campbell, S. T., Eno, J.-J. T., & Gardner, M. J. Knee Pain After Intramedullary Nailing of Tibia Fractures: Prevalence, Etiology, and Treatment. *J Am Acad Orthop Surg* 2018; **26**(18):e381–e387. https://doi.org/10.5435/JAAOS-D-18-00076

Brinkman, J.-M., Hurschler, C., Agneskirchner, J., Lobenhoffer, P., Castelein, R. M., & van Heerwaarden, R. J. Biomechanical testing of distal femur osteotomy plate fixation techniques: the role of simulated physiological loading. *J Exp Orthop* 2014; **1**. https://doi.org/10.1186/s40634-014-0001-1

Casstevens, C., Toan ,L., Archdeacon, M.T., Wyrick, J.D.. Management of extra-articular fractures of the distal tibia: intramedullary nailing versus plate fixation. *J Am Acad Orthop Surg* 2012; **20**(11): 675-683

Cavagna, G. A. and Franzetti, P. The determinants of the step frequency in walking in humans. *The Journal of Physiology* 1986; **373**(1): 235–242. doi: 10.1113/jphysiol.1986.sp016044.

Chen, A., Gupte, C., Akhtar, K., Smith, P., & Cobb, J. The Global Economic Cost of Osteoarthritis: How the UK Compares. *Arthritis*, 2012; https://doi.org/10.1155/2012/698709

Cignoni, P., Callieri, M., Corsini, M,, Dellepiane, M. Ganovelli, F., Ranzuglia, G. MeshLab: an Open-Source Mesh Processing Tool. Sixth Eurographics Italian Chapter Conference 2008: 129-136.

Claes, L., Augat, P., Suger, G., Wilke, H.J. Influence of size and stability of the osteotomy gap on the success of fracture healing. *J. Orthop. Res* 1997; **15**: 577–584. doi: 10.1002/jor.1100150414

Clarke, B. Normal bone anatomy and physiology. *Clin. J. Am. Soc. Nephrol*. 2008; **3** Suppl 3: S131-139. https://doi.org/10.2215/CJN.04151206

Court-Brown, C.M., McBirnie, J. The epidemiology of tibial fractures. *J Bone Joint Surg Br* 1995; **77**:B417-B421

Crockett, J. C., Rogers, M. J., Coxon, F. P., Hocking, L. J., & Helfrich, M. H. Bone remodelling at a glance. *J. Cell Sci.* 2011: **124**(7): 991–998. https://doi.org/10.1242/jcs.063032

Colin, F., Gaudot, F., Odri, G., & Judet, T. Supramalleolar osteotomy: techniques, indications and outcomes in a series of 83 cases. *Orthop Traumatol Sur Res* 2014; **100**(4): 413–418. https://doi.org/10.1016/j.otsr.2013.12.027

Dahabreh, Z., Calori, G. M., Kanakaris, N. K., Nikolaou, V. S., & Giannoudis, P. V. A cost analysis of treatment of tibial fracture nonunion by bone grafting or bone morphogenetic protein-7. *Int Orthop* 2009: **33**(5): 1407–1414. https://doi.org/10.1007/s00264-008-0709-6

Duncan, R. L., & Turner, C. H. Mechanotransduction and the functional response of bone to mechanical strain. *Calcified Tissue Int* 1995; **57**(5): 344–358. https://doi.org/10.1007/BF00302070

Egloff, C., Hügle, T., & Valderrabano, V. Biomechanics and pathomechanisms of osteoarthritis. Swiss Medical Weekly 2012; **142**: w13583. https://doi.org/10.4414/smw.2012.13583

Epari, D.R., Taylor, W.R., Heller, M.O., Duda, G.N. Mechanical conditions in the initial phase of bone healing. *Clin Biomech* 2006; **21**(6): 646-655. doi: 10.1016/j.clinbiomech.2006.01.003

Ettinger, S., Schwarze, M., Yao, D., Ettinger, M., Claassen, L., Stukenborg-Colsman, C., et al. Stability of supramalleolar osteotomies using different implants in a sawbone model. *Arch Orthop Traum Sur* 2018; **138**(10): 1359–1363. https://doi.org/10.1007/s00402-018-2981-2

Fedorov, A., Beichel, R., Kalpathy-Cramer, J., Finet, J., Fillion-Robin, J-C., et al. 3D Slicer as an Image Computing Platform for the Quantitative Imaging Network. *Mag Res Imag* 2012 **30**(9):1323-41. PMID: 22770690.

Fouad, H. Effects of the bone-plate material and the presence of a gap between the fractured bone and plate on the predicted stresses at the fractured bone. *Med Eng Phys* 2010; **32**(7): 783–789. https://doi.org/10.1016/j.medengphy.2010.05.003

Frost, H. M. Perspectives: bone's mechanical usage windows. *Bone and Mineral* 1992; **19**(3): 257–271. doi: 10.1016/0169-6009(92)90875-E.

Gardner, M.P., Chong, A.C.M., Pollock, A.G., Wooley, P.H. Mechanical evaluation of large-sized fourth-generation composite femur and tibia models. *J Biomed Eng* 2010; **38**(3): 613-620.

Golovakha, M. L., Orljanski, W., Benedetto, K.-P., Panchenko, S., Büchler, P., Henle, P., & Aghayev, E. Comparison of theoretical fixation stability of three devices employed in medial opening wedge high tibial osteotomy: a finite element analysis. *BMC Musculoskel Dis* 2014; **15**, 230. https://doi.org/10.1186/1471-2474-15-230

Gomez-Benito, M.J., Fornells, P., Garcia-Aznar, J.M., Seral, B., Seral-Iñnigo, F., Doblare, M. Computational comparison of reamed versus undreamed intramedullary tibial nails. *J Orthop Res* 2007; **25**(2): 191-200.

Grassi, L., & Isaksson, H. Extracting accurate strain measurements in bone mechanics: A critical review of current methods. *J Mech Behav Biomed Mater* 2015; **50**: 43–54. https://doi.org/10.1016/j.jmbbm.2015.06.006

Grassi, L., Väänänen, S. P., Amin Yavari, S., Jurvelin, J. S., Weinans, H., Ristinmaa, M., … Isaksson, H. Full-Field Strain Measurement During Mechanical Testing of the Human Femur at Physiologically Relevant Strain Rates. *J Biomech Eng* 2014; **136**(11): 111010-111018. https://doi.org/10.1115/1.4028415

Greenfield, J., Kuhn, S., Mehler, D., Puel F., Rommens, P.M. Biomechanical evaluation of a new treatment method for distal tibia fractures, *Computer Methods Biomech Biomed Eng* 2015; **18**(sup1): 1952–1953. doi: 10.1080/10255842.2015.1069582.

Gruszka, D., Arand, C., Greenfield, J., Nowak, T. E., Kuechle, R., Kuhn, S., & Rommens, P. M. (2017). Is the novel olecranon tension plate a valid alternative to tension band wiring of olecranon fractures? A biomechanical study on cadaver bones. *Arch Orthop Traum Sur*; **137**(12): 1651–1658. https://doi.org/10.1007/s00402-017-2760-5

Gueorguiev, B., & Lenz, M. Why and how do locking plates fail? *Injury* 2018; **49**: S56–S60. https://doi.org/10.1016/S0020-1383(18)30305-X

Haase, K., Rouhi, G. Prediction of stress shielding around an orthopedic screw: using stress and strain energy density as mechanical stimuli. *Computers in Biology and Medicine* 2013; **43**(11): 1748–1757. doi: 10.1016/j.compbiomed.2013.07.032.

Haddadi, H., Belhabib, S. Use of rigid-body motion for the investigation and estimation of the measurement errors related to digital image correlation technique. *Opt Lasers Eng* 2008. **46**:185–196.

Hammil, J., and Knutzen, K. Biomecahnical basis of human movement, 3rd edition 2008. Lippincott, Williams & Wilkins: London

Hansen, M., Mehler, D., Hessmann, M.H., Blum, J., Rommens, P.M. Intramedullary stabilisation of extraarticular proximal tibial fractures: A biomechanical comparison of intramedullary and extramedullary implants including a new proximal tibia nail (PTN). *J Orthop Trauma* 2007; **21**(10): 701-709.

Hasenboehler, E., Rikli, D., Babst, R. Locking compression plate with minimally invasive plate osteosynthesis in diaphyseal and distal tibial fracture: A retrospective study of 32 patients. *Injury* 2007; **38**(3): 365-370.

Hazarika, S., Chakravarthy, J., Cooper, J: Minimally invasive locking plate osteosynthesis for fractures of the distal tibia: Results in 20 patients. *Injury* 2006; **37**(9):877-887.

Heckman, J. D., & Sarasohn-Kahn, J. The economics of treating tibia fractures. The cost of delayed unions. *Bulletin (Hospital for Joint Diseases (New York)* 1997; **56**(1): 63–72.

Heiner, A.D. Structural properties of fourth-generation composite femurs and tibias. *J Biomech* 2008; **41**: 3282-3284.

Helgason, B., Gilchrist, S., Ariza, O., Chak, J. D., Zheng, G., Widmer, R. P., et al. (2014). Development of a balanced experimental-computational approach to understanding the mechanics of proximal femur fractures. *Med Eng Phys*; **36**(6), 793–799. https://doi.org/10.1016/j.medengphy.2014.02.019

Hensley, S., Christensen, M., Small, S., Archer, D., Lakes, E., Rogge, R., 2017. Digital image correlation techniques for strain measurement in a variety of biomechanical test models. *Acta Bioeng Biomech* 2017; **19**: 187–195.

Högel, F., Gerber, C., Bühren, V., & Augat, P. (2013). Reamed intramedullary nailing of diaphyseal tibial fractures: comparison of compression and non-compression nailing. *Eur J Trauma Emerg Surg* 2013; **39**(1): 73–77. https://doi.org/10.1007/s00068-012-0237-3

Horn, J., Linke J.H., Höntzsch B.L., et al. Angle stable interlocking screws improve construct stability of intramedullary nailing of distal tibia fractures: a biomechanical study. *Injury* 2009; **40**(7): 767–771. https://doi.org/10.1016/j.injury.2009.01.117

Hunter, D. J., Schofield, D., & Callander, E. The individual and socioeconomic impact of osteoarthritis. *Nat. Rev. Rheumatol* 2014; **10**(7): 437–441. https://doi.org/10.1038/nrrheum.2014.44

Isidor, F., Influence of forces on peri-implant bone. *Clin Oral Implants Res* 2006 ; **17** Suppl 2 : 8–18. doi: 10.1111/j.1600-0501.2006.01360.x

Kanakaris, N. K., & Giannoudis, P. V. The health economics of the treatment of long-bone non-unions. *Injury* 2007; **38**: S77–S84. https://doi.org/10.1016/S0020-1383(07)80012-X

Katsoulis, E., Court-Brown, C., & Giannoudis, P. V. Incidence and aetiology of anterior knee pain after intramedullary nailing of the femur and tibia. *J Bone Joint Surg (British Volume)* 2006; **88**(5): 576–580. https://doi.org/10.1302/0301-620X.88B5.16875

Kitaoka, H. B., Alexander, I. J., Adelaar, R. S., Nunley, J. A., Myerson, M. S., & Sanders, M. Clinical rating systems for the ankle-hindfoot, midfoot, hallux, and lesser toes. *Foot Ankle Int* 1994; **15**(7): 349–353. https://doi.org/10.1177/107110079401500701

Khoury, A., Liebergall, M., London, E., Mosheiff R. Percutaneous plating of distal tibial fractures. *Foot Ankle Int* 2002; **23**(9): 818–824

Kim, S.-H., Chang, S.-H., & Jung, H.-J. The finite element analysis of a fractured tibia applied by composite bone plates considering contact conditions and time-varying properties of curing tissues. *Compos Struct* 2010; **92**(9), 2109–2118. https://doi.org/10.1016/j.compstruct.2009.09.051

Klein, P., Schell, H., Streitparth, F., Heller, M., Kassi, J.-P., Kandziora, F., Bragulla, H., Haas, N.P., Duda, G.N., 2003. The initial phase of fracture healing is specifically sensitive to mechanical conditions. *J. Orthop. Res* 2003; **21**: 662–669. doi: 10.1016/S0736-0266(02)00259-0

Kluess, D., Soodmand, E., Lorenz, A., Pahr, D., Schwarze, M., Cichon, R., et al. A round-robin finite element analysis of human femur mechanics between seven participating laboratories with experimental validation. *Computer Methods in Biomechanics and Biomedical Engineering* 2019; **22**(12), 1020–1031. https://doi.org/10.1080/10255842.2019.1615481

Knupp, M., Pagenstert, G., Valderrabano, V., & Hintermann, B. Osteotomien zur Entlastung der Varusarthrose im oberen Sprunggelenk. *Operative Orthopädie Und Traumatologie* 2008; **20**(3), 262–273. https://doi.org/10.1007/s00064-008-1308-9

Kobayashi, H., Kageyama, Y., & Shido, Y. Treatment of Varus Ankle Osteoarthritis and Instability With a Novel Mortise-Plasty Osteotomy Procedure. *J Foot Ankle Surg* 2016; **55**(1): 60–67. https://doi.org/10.1053/j.jfas.2015.06.011

Kuhn, S., Hansen, M., Rommens, PM. Extending the indications of intrameduallary nailing with the Expert Tibial Nail®. *Acta Chirurgiae Orthopaedicae et Traumatologiae Cechobl* 2008; **75**: 77-78.

Kuhn, S., Dietz, S-O., Appelmann, P., Rothenbach, E.C., Rommens, P.M. Intramedullary nailing of distal tibial fractures. *Minerva Orthop Traumatol* 2012; **63**: 45-59.

Kuhn, S., Appelmann, P., Pairon, P., Mahler, D., Rommens, P.M. The retrograde tibial nail: presentation and biomechanical evaluation of a new concept in the treatment of distal tibia fractures. *Injury Int J Care Injured* 2014a; **455**: S81-S86.

Kuhn, S., Appelmann, P., Mehler, D., Pairon, P., Rommens, P.M. Retrograde tibial nailing: a minimally invasive and biomechanically superior alternative to angle-stable plate osteosynthesis in distal tibia fractures. *J Orthop Surg Res* 2014b. **9**(35): DOI:10.1186/1749-799X-9-35

Kuhn S., Appelmann, P., Pairon, P., Mehler, D., Hartmann, F., Rommens, P.M. A new angle stable nailing concept for the treatment of distal tibia fractures. *Int Orthop (SICOT)* 2014c; **38**(6): 1255-1260.

Lacroix, D. and Prendergast, P. J. A mechano-regulation model for tissue differentiation during fracture healing: analysis of gap size and loading. *J Biomech* 2002; **35**(9): 1163–1171.

Lanyon, L. E. Functional strain in bone tissue as an objective, and controlling stimulus for adaptive bone remodelling. *Journal of Biomechanics* 1987; **20**(11): 1083–1093. doi: 10.1016/0021-9290(87)90026-1

Lee, W.-C., Moon, J.-S., Lee, K., Byun, W. J., & Lee, S. H. Indications for supramalleolar osteotomy in patients with ankle osteoarthritis and varus deformity. *J Bone Joint Surg Am* 2011; **93**(13): 1243–1248. https://doi.org/10.2106/JBJS.J.00249

Li, B., Yang, Y., Jiang, L-S. Plate fixation versus intramedullary nailing for displaced extra-articular distal tibia fractures: a system review. *Eur J Orthop Surg Traumatol* 2015; **25**: 53-63.

Lobenhoffer, P., Agneskirchner, J.D. Improvements in surgical technique of valgus high tibial osteotomy. *Knee Surg Sports Traumatol Arthrosc* 2003;**11**(3):132–138.

Luepongsak, N., Amin, S., Krebs, D. E., McGibbon, C. A., & Felson, D. The contribution of type of daily activity to loading across the hip and knee joints in the elderly. *Osteoarthritis and Cartilage* 2012 ; **10**(5): 353–359. https://doi.org/10.1053/joca.2000.0511

Ma, C.-H., Wu, C.-H., Tu, Y.-K., & Lin, T.-S. Metaphyseal locking plate as a definitive external fixator for treating open tibial fractures--clinical outcome and a finite element study. *Injury* 2013; **44**(8), 1097–1101. https://doi.org/10.1016/j.injury.2013.04.023

MacLeod, A., Simpson, A. H. R. W., & Pankaj, P. Experimental and numerical investigation into the influence of loading conditions in biomechanical testing of locking plate fracture fixation devices. *Bone Joint Res* 2018; **7**(1): 111–120. https://doi.org/10.1302/2046-3758.71.BJR-2017-0074.R2

Marsell, R., & Einhorn, T. A. The biology of fracture healing. *Injury* 2011; **42**(6): 551–555. https://doi.org/10.1016/j.injury.2011.03.031

Martel-Pelletier, J. Pathophysiology of osteoarthritis. *Osteoarthritis and Cartilage* 1998; **6**(6): 374–376. https://doi.org/10.1053/joca.1998.0140

Mauffrey, C., McGuinness, K., Parsons, N., Achten, J., Costa, M.L. A randomised pilot trial of "locking plate" fixation versus intramedullary nailing for extra-articular fractures of the distal tibia. *J Bone Joint Surg Br* 2012; 94:B704-708

McLeod, K. J. and Rubin, C. T. The effect of low-frequency electrical fields on osteogenesis. *J Bone Joint Surg Am* 1992; **74**(6): 920–929.

Miller, F., Girardi, H., Lipton, G., Ponzio, R., Klaumann, M., Dabney, K.W. Reconstruction of the dysplastic spastic hip with peri-ilial pelvic and femoral osteotomy followed by immediate mobilization. *J Pediatr Orthop* 1997;**17**:592–602. doi: 10.1097/01241398-199709000-00005

Moewis, P., Checa, S., Kutzner, I., Hommel, H., & Duda, G. N. Physiological joint line total knee arthroplasty designs are especially sensitive to rotational placement – A finite element analysis. *PLoS ONE* 2018; **13**(2).

Nguyen, A.-D., Boling, M. C., Levine, B., & Shultz, S. J. Relationships Between Lower Extremity Alignment and the Quadriceps Angle. *Clin J Sport Med* 2009; **19**(3): 201–206. https://doi.org/10.1097/JSM.0b013e3181a38fb1

Nha, K. W., Lee, S. H., Rhyu, I. J., Kim, H. J., Song, J. G., Han, J. H., et al.. Safe Zone for Medial Open-Wedge Supramalleolar Osteotomy of the Ankle: A Cadaveric Study. *Foot Ankle Int* 2016; **37**(1): 102–108. https://doi.org/10.1177/1071100715597438

Niinomi, M. Mechanical properties of biomedical titanium alloys. Mat Sci Eng 1998; **243**(1): 231–236. https://doi.org/10.1016/S0921-5093(97)00806-X

Niinomi, M., Nakai, M.. Titanium-based biomaterials for preventing stress shielding between implant devices and bone. *Int J Biomat* 2011, Article ID 836587, 10 pages, http://dx.doi.org/10.1155/2011/836587

Nourisa, J., & Rouhi, G. Biomechanical evaluation of intramedullary nail and bone plate for the fixation of distal metaphyseal fractures. *J Mech Behav Biomed Mater* 2016; **56**: 34–44. https://doi.org/10.1016/j.jmbbm.2015.10.029

Nyary, T., & Scammell, B. E. Principles of bone and joint injuries and their healing. *Surgery - Oxford International Edition* 2018; **36**(1): 7–14. https://doi.org/10.1016/j.mpsur.2017.10.005

Oh, J.-K., Sahu, D., Ahn, Y.-H., Lee, S.-J., Tsutsumi, S., Hwang, J.-H., et al. Effect of fracture gap on stability of compression plate fixation: a finite element study. *J Orthop Res* 2010; **28**(4): 462–467. https://doi.org/10.1002/jor.20990

Oken, O. F., Yildirim, A. O., & Asilturk, M. Finite element analysis of the stability of AO/OTA 43-C1 type distal tibial fractures treated with distal tibia medial anatomic plate versus anterolateral anatomic plate. Acta Orthopaedica Et Traumatologica Turcica 2017; **51**(5): 404–408. https://doi.org/10.1016/j.aott.2017.09.003

Op Den Buijs, J., & Dragomir-Daescu, D. Validated finite element models of the proximal femur using two-dimensional projected geometry and bone density. *Comput Methods Programs Biomed 2011*; **104**(2): 168–174. https://doi.org/10.1016/j.cmpb.2010.11.008

Pacific Research Laboratories, Inc., 2016. Sawbones® Biomechanical Test Materials Catalogue. www.sawbones.com [Accessed 20th October 2016].

Pagenstert, G. I., Hintermann, B., Barg, A., Leumann, A., & Valderrabano, V. Realignment surgery as alternative treatment of varus and valgus ankle osteoarthritis. Clin Orthop Related Res 2007; **462**: 156–168. https://doi.org/10.1097/BLO.0b013e318124a462

Pairon, P., Ossendorf, C., Kuhn, S., Hofmann, A., Rommens, P.M. Intramedullary nailing after external fixation of the femur and tibia: A review of advantages and limits. *Eur J Trauma Emerg Surg* 2015. **41**: 25-38.

Palanca, M., Brugo, T. M., & Cristofolini, L. Use of digital image correlation to investigate the biomechanics of the vertebra. *J Mech Med Biol* 2015; **15**(2): 1540004. https://doi.org/10.1142/S0219519415400047

Peng, H., Wang, S., & Wang, X. Consistency and asymptotic distribution of the Theil–Sen estimator. *J. Stat. Plan. Inference* 2008; 1**38**(6): 1836–1850. https://doi.org/10.1016/j.jspi.2007.06.036

Inman, V.T., Ralston, H.J., Todd, F. *Human Walking*. Baltimore, London: Williams & Wilkins, 1981.

Prendergast, P. J., Huiskes, R., & Søballe, K. Biophysical stimuli on cells during tissue differentiation at implant interfaces. *J Biomech* 1997; **30**(6): 539–548. https://doi.org/10.1016/S0021-9290(96)00140-6

Probe, R. A. Lower extremity angular malunion: evaluation and surgical correction. *J Am Acad Orthop Surg* 2003; **11**(5): 302–311.

Racine, J., & Aaron, R. K. Pathogenesis and epidemiology of osteoarthritis. *Rhode Island Medical Journal (2013)*, *96*(3), 19–22.

Raisz, L. G. Pathogenesis of osteoporosis: concepts, conflicts, and prospects. *J Clin Invest* 2005; **115**(12): 3318–3325. https://doi.org/10.1172/JCI27071

Raja Izaham, R. M. A., Abdul Kadir, M. R., Abdul Rashid, A. H., Hossain, M. G., & Kamarul, T. Finite element analysis of Puddu and Tomofix plate fixation for open wedge high tibial osteotomy. *Injury* 2012; **43**(6): 898–902. https://doi.org/10.1016/j.injury.2011.12.006

Rastetter, B. R., Wright, S. J., Gheduzzi, S., Miles, A. W., & Clift, S. E. The influence of tibial component malalignment on bone strain in revision total knee replacement. *Proceedings of the Institution of Mechanical Engineers. Part H, Journal of Engineering in Medicine* 2016; **230**(6), 561–568. https://doi.org/10.1177/0954411916638684

Rausch, S., Klos, K., Gras, F., Skulev, H. K., Popp, A., Hofmann, G. O., & Mückley, T. Utility of the Cortical Thickness of the Distal Radius as a Predictor of Distal-Radius Bone Density. Arch Trauma Res 2013; **2**(1): 11–15. https://doi.org/10.5812/atr.10687

Reilly, D. T., & Burstein, A. H. The elastic and ultimate properties of compact bone tissue. *Journal of Biomechanics* 1975 ; **8**(6), 393–405. https://doi.org/10.1016/0021-9290(75)90075-5

Reynolds, K.J., Cleek, T.M., Mohtar, A.A., Hearn, T.C., Predicting cancellous bone failure during screw insertion. *J Biomech* 2013; **46**: 1207–1210. doi: 10.1016/j.jbiomech.2013.01.021

Rho, J. Y., Ashman, R. B., & Turner, C. H. Young's modulus of trabecular and cortical bone material: ultrasonic and microtensile measurements. *J Biomech* 1993; **26**(2): 111–119.

Robling, A. G. and Turner, C. H. Mechanical Signaling for Bone Modeling and Remodeling. *Crit Rev Eukar Gene* 2009; **19**(4): 319–338.

Rogge, R.D., Small, S.R., Archer, D.B., Berend, M.E., Ritter, M.A. Validation of Digital Image Correlation Techniques for Strain Measurement in Biomechanical Test Models. *ASME. Summer Bioengineering Conference* 2013; **1A** doi: 10.1115/SBC2013-14540

Rubin, C. T. and McLeod, K. J. (1994) 'Promotion of bony ingrowth by frequency-specific, low-amplitude mechanical strain', *Clinical Orthopaedics and Related Research*, (**298**), pp. 165–174.

Ruff, C., Holt, B., Trinkaus, E., Who's afraid of the big bad Wolff?: "Wolff's law" and bone functional adaptation. *Am J Phys Anthropol* 2006; **129**: 484–498. doi: 10.1002/ajpa.20371

Sathiyakumar, V., Thakore, R. V., Ihejirika, R. C., Obremskey, W. T., & Sethi, M. K. Distal tibia fractures and medial plating: factors influencing re-operation. *International Orthopaedics* 2014; **38**(7), 1483–1488. https://doi.org/10.1007/s00264-014-2345-7
Schindelin, J., Arganda-Carreras, I. & Frise, E. et al. Fiji: an open-source platform for biological-image analysis. *Nature methods* 2012; **9**(7): 676-682, PMID 22743772, doi:10.1038/nmeth.2019

Schnabel, R., Wahl, R., Klein, R. Efficient RANSAC for Point-Cloud Shape Detection. *Computer Graphics Forum* 2007, **26**(2):214-226.

Soraganvi, P., Anand-Kumar, B., Rajagopalakrishnan, R., & Praveen-Kumar, B. Anterior Knee Pain after Tibial Intra-medullary Nailing: Is it Predictable? *Malaysian Orthopaedic Journal* 2016; **10**(2): 16–20. https://doi.org/10.5704/MOJ.1607.004

Small, SR., Malinzak, RA., Rogge, RD., Archer, DB., Oja, JW. Berend ME. Digital Image Correlation Analysis of Tibial Loading in Rotating Platform Total Knee Arthroplasty. *Conference paper of the Orthopaedic Research Society* 2013: Texas.

Snow, M., Thompson, G., & Turner, P. G. A mechanical comparison of the locking compression plate (LCP) and the low contact-dynamic compression plate (DCP) in an osteoporotic bone model. *J Orthop Trauma* 2008; **22**(2): 121–125. https://doi.org/10.1097/BOT.0b013e318160c84c

Spahn, G., Kirschbaum, S., & Kahl, E. Factors that influence high tibial osteotomy results in patients with medial gonarthritis: a score to predict the results. *Osteoarthritis and Cartilage* 2006; **14**(2): 190–195. https://doi.org/10.1016/j.joca.2005.08.013

Symon, K. R. 1971. *Mechanics*. Addison-Wesley Publishing Company. ISBN: 0201073927

Sztefek, P., Vanleene, M., Olsson, R., Collinson, R., Pitsillides, A. A., & Shefelbine, S. Using digital image correlation to determine bone surface strains during loading and after adaptation of the mouse tibia. *J Biomech* 2010 ; **43**(4) : 599–605. https://doi.org/10.1016/j.jbiomech.2009.10.042

Tada, S., Stegaroiu, R., Kitamura, E., Miyakawa, O., Kusakari, H. Influence of implant design and bone quality on stress/strain distribution in bone around implants: a 3-dimensional finite element analysis. *Int J Oral Max Impl* 2003; **18**(3): 357–368.

Takakura, Y., Tanaka, Y., Kumai, T., & Tamai, S. Low tibial osteotomy for osteoarthritis of the ankle. Results of a new operation in 18 patients. *J Bon Joint Surg Br* 1995; **77**(1): 50–54.

Taubin, G. Curve and surface smoothing without shrinkage. In Proceedings of IEEE International *Conference on Computer Vision* 1995: 852–857. https://doi.org/10.1109/ICCV.1995.466848

Tayton, E., Evans, S., O'Doherty, D. 2010. Mapping the strain distribution on the proximal femur with titanium and flexible-stemmed implants using digital image correlation. *J Bone Joint Surg*. **92**-B:1176–1181.

Väänänen, S. P., Amin Yavari, S., Weinans, H., Zadpoor, A. A., Jurvelin, J. S., & Isaksson, H. Repeatability of digital image correlation for measurement of surface strains in composite long bones. *J Biomech* 2013; **46**(11): 1928–1932. https://doi.org/10.1016/j.jbiomech.2013.05.021

Väistö, O., Toivanen, J., Kannus, P., & Järvinen, M. Anterior knee pain after intramedullary nailing of fractures of the tibial shaft: an eight-year follow-up of a prospective, randomized study comparing two different nail-insertion techniques. *J Trauma* 2008; **64**(6): 1511–1516. https://doi.org/10.1097/TA.0b013e318031cd27

Wähnert, D., Stolarczyk, Y., Hoffmeier, K. L., Raschke, M. J., Hofmann, G. O., & Mückley, T. Long-term stability of angle-stable versus conventional locked intramedullary nails in distal tibia fractures. BMC Musculoskel Dis 2013; **14:** 66. https://doi.org/10.1186/1471-2474-14-66

Wu, G., Siegler, S., Allard, P., Kirtley, C., Leardini, A., Rosenbaum, D., … Stokes, I. ISB recommendation on definitions of joint coordinate system of various joints for the reporting of human joint motion—part I: ankle, hip, and spine. *J Biomech* 2002; **35**(4): 543–548. https://doi.org/10.1016/S0021-9290(01)00222-6

Yushkevich, P.A., Piven, J. Hazlett, H.C., Smith, R.G., Ho, S. et al. User-guided 3D active contour segmentation of anatomical structures: Significantly improved efficiency and reliability. *Neuroimage* 2006; **31**(3):1116-28.

Zelle, B.A, Bhandari, M., Espiritu, M., Koval, K.J, Zlowodzki, M. Treatment of distal tibia fractures without articular involvement: A systematic review of 1125 fractures. *J Orthop Trauma* 2006; **20**: 76-79.

Zhang, J., Ebraheim, N., Li, M., He, X., Schwind, J., Liu, J., & Zhu, L. External fixation using locking plate in distal tibial fracture: a finite element analysis. *Europ J Orthop Surg Traumatol* 2015; **25**(6): 1099–1104. https://doi.org/10.1007/s00590-015-1604-7

Zhang, Q.-H., Cossey, A., & Tong, J. Stress shielding in periprosthetic bone following a total knee replacement: Effects of implant material, design and alignment. *Med Eng Phys* 2016; **38**(12): 1481–1488. https://doi.org/10.1016/j.medengphy.2016.09.018

Zhong, Z., Zeng, X.-L., Ni, J.-H., Huang, X.-F. Comparison of the biological response of osteoblasts after tension and compression. *Eur J Orthop* 2011; **35**(1): 59-65.

Summary in French
Résumé en français

Chapitre 1 : Introduction

Anatomie de la jambe

La jambe est composée de deux os: le tibia et le péroné – ce dernier ne portant que 10% du poids du corps passant par la jambe (Hammil and Knutzen, 2008); ces deux os sont connectés par une membrane nommée la syndesmose. Le tibia se décompose en trois parties (Trafton, 2009) : deux épiphyses (proximale et distale), et la diaphyse au centre de l'os. L'épiphyse distale s'articule avec le talus pour créer l'articulation de la cheville.

L'arthrose & les ostéotomies correctives

Chez les personnes atteintes d'une difformité osseuse de la jambe (due à une mauvaise consolidation osseuse suite à une fracture, ou bien des difformités existantes à la naissance), l'arthrose précoce de la cheville est fréquente (Beaman et al., 2012). L'arthrose est une maladie dégénérative qui touche principalement le cartilage articulaire et conduit à une croissance de l'os sous-chondral qui mène à la réduction de l'espace intérieur de l'articulation. Les conséquences de cette maladie comprennent des douleurs lors des activités quotidiennes (telles que la marche) et une réduction de mobilité.

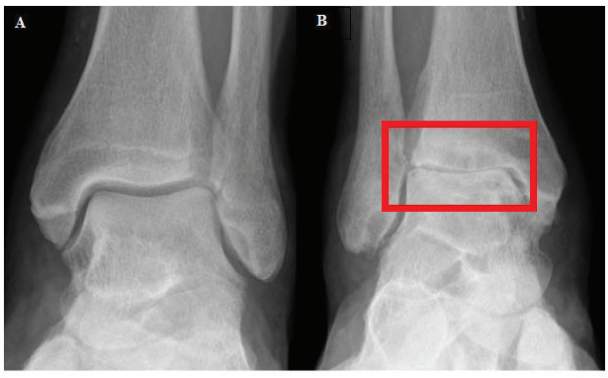

Figure 122: Radiographies d'une cheville saine (a) et avec de l'arthrose (b). En rouge, contact d'os sous-chondral lié à la réduction de l'écart articulaire. Image adaptée de l'étude TARVA: www.anklearthritis.co.uk

Afin d'éviter l'arthrose précoce, les patients souffrant d'une déformation tibiale sont soignés par « ostéotomie corrective » (Lee et al., 2011). Cette procédure chirurgical s'appuie sur l'enlèvement d'un

morceau d'os en forme de cale de la partie médiale du tibia (Medial Wedge Opening Osteotomy ; MWO). Le but de cette opération est de redresser le tibia et réaligner les surfaces articulaires de la cheville afin de mieux répartir les charges passant par cette articulation.

Les fractures du tibia distal

La fracture la plus fréquente est de type A3 d'après la classification de l'organisation AO, c'est-à-dire extra-articulaire et instable. Les fractures du tibia distal proviennent essentiellement d'un choc violent ou d'une chute (plus commune chez les personnes âgées ; Court-Brown and McBirnie, 1995). La réduction d'une fracture du tibia distal se fait souvent à l'aide d'un implant pour réunir les fragments osseux, soit par une plaque externe (Medial Distal Tibia Plate, MDTP, Synthes®, aussi utilisée pour fixer des ostéotomies correctives) soit par un clou centromédullaire. Un clou centromédullaire récent, spécifique au tibia distal, est encore en période d'essais cliniques : le Distal Tibia Nail (DTN ; Mizuho®).

Objectif

L'objectif de cette thèse est d'évaluer la faisabilité du DTN pour la fixation des ostéotomies correctives du tibia distal. Une étude de la configuration d'essai a d'abord été menée ; ensuite des os composites ont été instrumentés avec un implant suite à la simulation d'une ostéotomie. Ces échantillons ont été soumis à différents tests biomécaniques.

Chapitre 2 : Etude préliminaire des méthodes et configurations d'essai

Introduction

Notre première tâche fut d'évaluer la configuration retenue pour les essais, c'est-à-dire de de quantifier les sources d'incertitudes (conditions au limites, positionnement du spécimen etc.) influant le comportement mesuré (MacLeod et al., 2018). Les essais ont eu lieu au laboratoire de biomécanique du CHU de Mayence, Allemagne.

Configurations d'essai

Tous les essais ont été réalisés dans une configuration identique, avec du PMMA aux extrémités pour maintenir les échantillons dans les mors et fournir une surface plane utile au chargement en compression. Pour l'essai en compression, un effort de compression ponctuel est appliqué à l'aide d'une bille (liaison rotule) sur la surface du PMMA en partie proximale du spécimen ; l'encastrement de la partie distale

menant au blocage des six degrés de liberté a été modifié pour réaliser une seconde liaison rotule en zone distale (Figure 123).

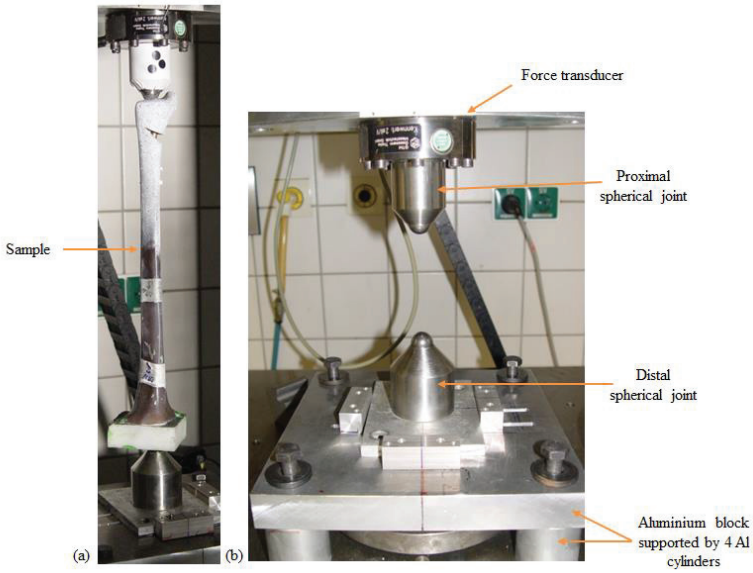

Figure 123: Une nouvelle configuration d'essai avec une liaison double-rotule avec (a) et sans (b) échantillon.

Sources d'erreur

Cinq sources d'incertitude ont été identifiées dans la préparation des essais à mener : la résine PMMA utilisée pour l'emboîtement des échantillons (son épaisseur et sa composition), le chargement (point de contact et axe du chargement), et la reproductibilité du positionnement de l'échantillon dans la machine d'essai.

La raideur de la pièce en PMMA s'avère plus faible que celle de l'os, et participe donc d'une manière non négligeable à la raideur globale mesurée par la machine d'essai. De même l'axe de chargement influence la raideur mesurée. Et la reproductibilité du positionnement doit être améliorée pour diminuer la variabilité de la raideur mesurée de l'échantillon.

Conclusion

Suite aux essais menés dans cette partie, l'influence du PMMA sur la mesure de la raideur de l'échantillon sera réduite. L'axe de chargement sera contrôlé pour tous les échantillons grâce à la conception d'un montage pour mouler le PMMA sur l'os de manière répétitive. Finalement, pour limiter la variabilité de raideur liée au positionnement des échantillons dans la machine, les essais pour chaque type de sollicitation, quel que soit le niveau de chargement, seront réalisés d'une façon consécutive.

Chapitre 3 : Evaluation biomécanique d'un nouvel implant pour des ostéotomies correctives supra-malléolaires

Introduction

Actuellement la fixation par plaque est la seule option chirurgicale suite à une ostéotomie corrective supra-malléolaire. Ce type de fixation a été évalué par Ettinger et al. (2018) and Nha et al. (2016). Un nouvel implant, le DTN, s'offre une performance biomécanique plus intéressante que celle de la plaque pour la fixation des fractures du tibia distal. L'objectif de ce chapitre a été de réaliser des tests biomécaniques sur des os composites après simulation d'une ostéotomie fixée par MDTP ou DTN.

Méthodes

16 échantillons (8 par type d'implant) ont été soumis à des tests biomécaniques de compression et de torsion. Quatre phases d'expérimentation ont été réalisées : (i) Phase-0, os « sains » ou intègre i.e. sans ostéotomie ni implant, (ii) Phase-1, os instrumentés après simulation d'une ostéotomie, (iii) Phase-2, rupture du cortex latéral de l'ostéotomie, (iv) Phase-3, simulation d'une fracture de type A3. Les données de la machine d'essai sont utilisées pour calculer la raideur, et la corrélation d'images réalisées à l'aide des deux caméras filmant l'échantillon permet le calcul du mouvement inter-fragmentaire (IFM).

Résultats & Discussion

La Phase 0 permet de quantifier la variabilité de raideur liée aux éléments du montage (positionnement, PMMA, os composite sain), qui semblent peu en compression et en torsion. En Phase-1, la variabilité de raideur est très faible (82 $N.mm^{-1}$) tant en compression (Figure 124) qu'en torsion (0.2 $Nm.deg^{-1}$). En Phase-2, le MDTP réalise un montage significativement plus raide que le DTN en compression, pour un IFM toujours faible (<1 mm) ; en revanche, le DTN est significativement plus raide en torsion (Figure 125). En Phase-3, le DTN offre un montage toujours plus raide que celui réalisé avec une plaque, tant en compression qu'en torsion.

Conclusion

Malgré les différences de raideurs parfois significatives entre les fixations d'ostéotomie par DTN ou plaque en compression, l'IFM reste très faible. Le DTN peut donc être considéré comme une option pour la fixation des ostéotomies correctives. De plus le comportement en torsion d'une fixation par DTN s'avère souvent plus favorable, or cette sollicitation est délétère pour le remodelage osseux. Enfin, pour les fractures de type A3, les résultats de l'étude actuelle sont comparables à ceux des recherches précédentes, montrant que la plaque n'est pas adaptée pour ce type de fracture.

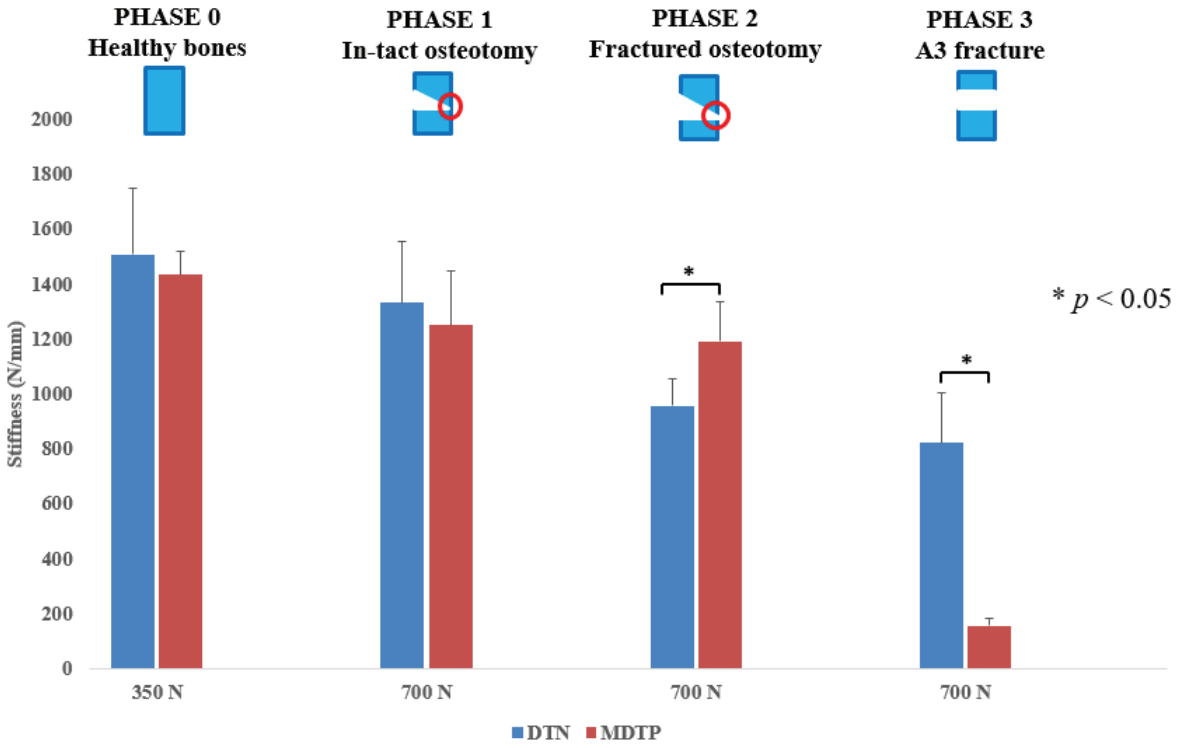

Figure 124: Raideurs en compression des deux types de fixation (par DTN et MDTP) pour chaque phase de test.

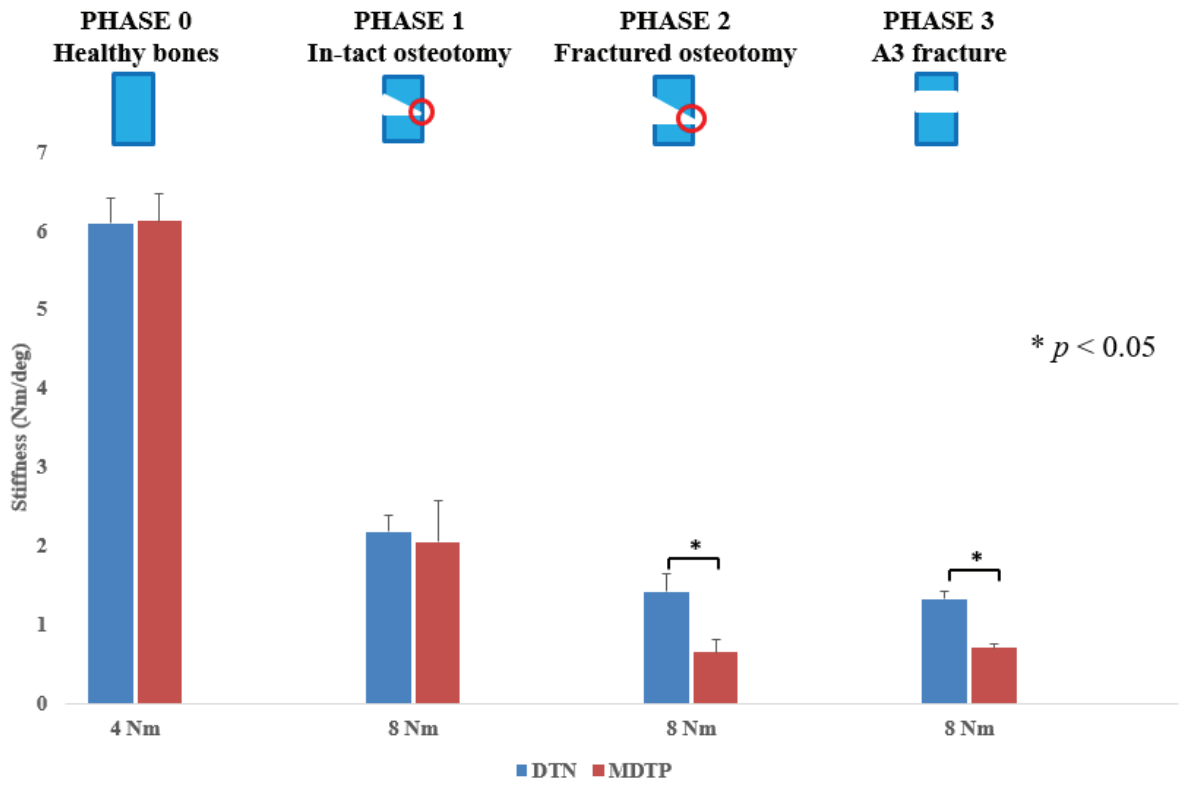

Figure 125: Raideurs en torsion des deux types de fixation (par DTN et MDTP) pour chaque phase de test.

Chapitre 4 : Etude géométrique et analyse statistique des conditions aux limites influençant la raideur de l'ensemble os-implant

Introduction

Suite à l'étude publiée par MacLeod et al. (2018) soulignant l'influence des conditions limites sur les résultats d'essais expérimentaux, une étude statistique a été menée afin d'identifier les paramètres ayant une influence majeure sur les raideurs obtenues.

Paramètres géométriques

Les paramètres retenus sont classés dans trois catégories :
1/ Echantillon : épaisseur du PMMA, densité et volume des différentes parties (os cortical, os trabéculaire, PMMA), raideur des os sains, aire du PMMA et du cortex latérale (CL).
2/ Configuration d'essai : distances du barycentre du CL à l'axe de chargement et à l'axe longitudinal de l'os, distance de l'axe de chargement à l'axe longitudinal de l'os.
3/ Implant : distance du barycentre de l'implant à l'axe de chargement, position de l'implant dans l'os (DTN uniquement), position des vis.

Analyses Statistiques

Du fait du faible nombre d'échantillons, les coefficients de corrélation (Pearson Product-Moment) ont été analysés afin d'identifier les paramètres ayant le plus d'influence, ainsi que les paramètres liés par une relation linéaire. Des régressions multiples sur deux variables indépendantes ont été réalisées pour les variables ayant un coefficient de Pearson élevé et significatif.

Conclusion

La variation trouvée entre les raideurs exposées au Chapitre 3 s'explique en partie par quelques paramètres. En Phase-0, la variabilité des raideurs s'explique en compression par l'axe de chargement, en torsion par la surface du PMMA. Pendant les Phases 1 & 2, la raideur après ostéotomie & instrumentation s'explique essentiellement par la raideur initiale des échantillons ; en torsion la position des vis et la position de l'implant par rapport à l'axe de chargement sont les paramètres importants.

Chapitre 5 : Influence de l'implant et des vis sur la déformation locale de l'os

Introduction

Le remodelage osseux est lié en particulier à la déformation osseuse. Entre 2000 et 4000 micro-déformations, l'os se fatigue mais le remodelage osseux répare rapidement les endommagements. Après une fixation osseuse par implant, les vis assurent la liaison mécanique entre l'os et l'implant, elles contribuent donc à la déformation à l'os et réalisent le stimulus nécessaire pour le remodelage. L'objectif de cette étude est de comparer les niveaux de déformation transférés à l'os selon le type de vis, en s'appuyant sur les implants et leurs vis utilisés pour des fractures du tibia distal.

Méthodes

Trois implants ont été évalués : le Distal Tibia Nail (CTN), l'Expert Tibia Nail (ETN), et le Medial Distal Tibial Plate (MDTP). Un type de vis propre à chacun des implants a été inséré dans un échantillon d'os composite. Pour simuler la sollicitation transmise par le DTN et l'ETN, une tige en métal appuie sur le corps de la vis à l'intérieur de l'os. Pour les vis du MDTP, une tige appuie sur la tête ou le fût de la vis en fonction du type de vis. Le chargement en compression s'élève à 700 N pour une fréquence de 0.05 Hz. Deux caméras ont filmé l'échantillon afin de quantifier la déformation de la surface osseuse par stéréo-corrélation.

Résultats & Discussion

La pré-déformation liée à l'insertion des vis était élevée pour toutes les vis, représentant un pourcentage important de la déformation totale après chargement en compression. Des niveaux excessifs de déformation négative verticale (compression locale) et de cisaillement ont été relevés pour les vis du MDTP et du DTN (Figure 127). Les vis de l'ETN et du MDTP réalisent les valeurs maximales de compression positives (traction locale) (Figure 126). Les niveaux élevés de déformation pour les vis du MDTP s'expliqueraient par la géométrie différente de ces vis, qui ont un diamètre et un filetage plus petit. Les vis de l'ETN présentent une large tête qui ne se visse pas dans l'os.

Conclusion

La pré-déformation provoquée par l'insertion des vis dans l'os peut être très importante et contribuer au remodelage osseux. En particulier, ce paramètre pourrait être intéressant pour des personnes âgées ou des personnes avec une mobilité réduite. Le niveau et la répartition des déformations varient selon le type de vis, ce qui devrait être pris en compte pour des études basés sur des modèles numériques.

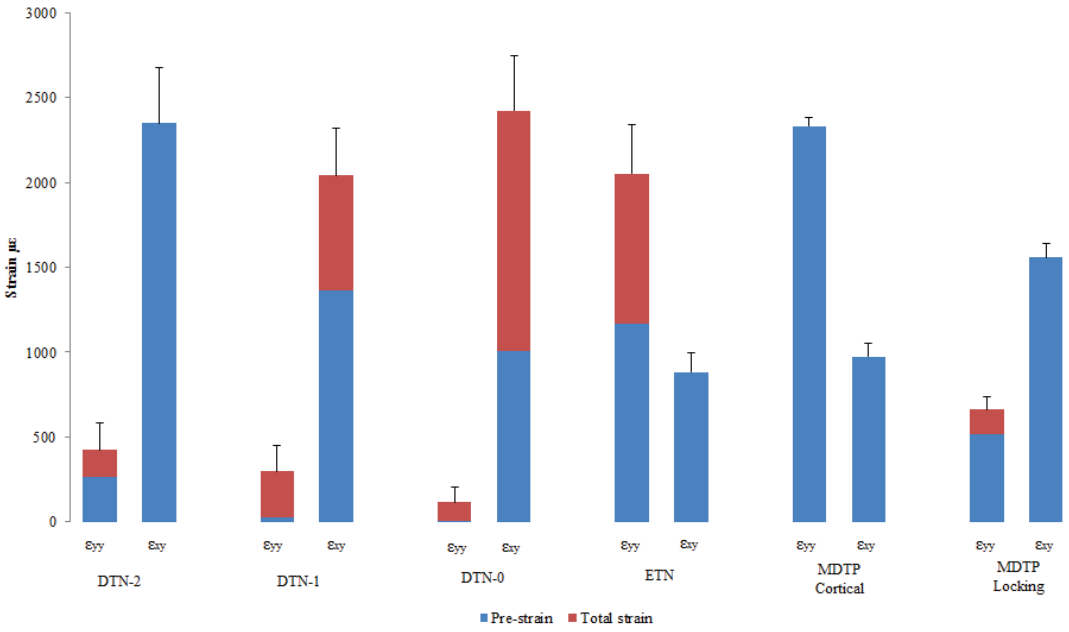

Figure 126: Déformation maximale (normale et en cisaillement) pour tous les échantillons.

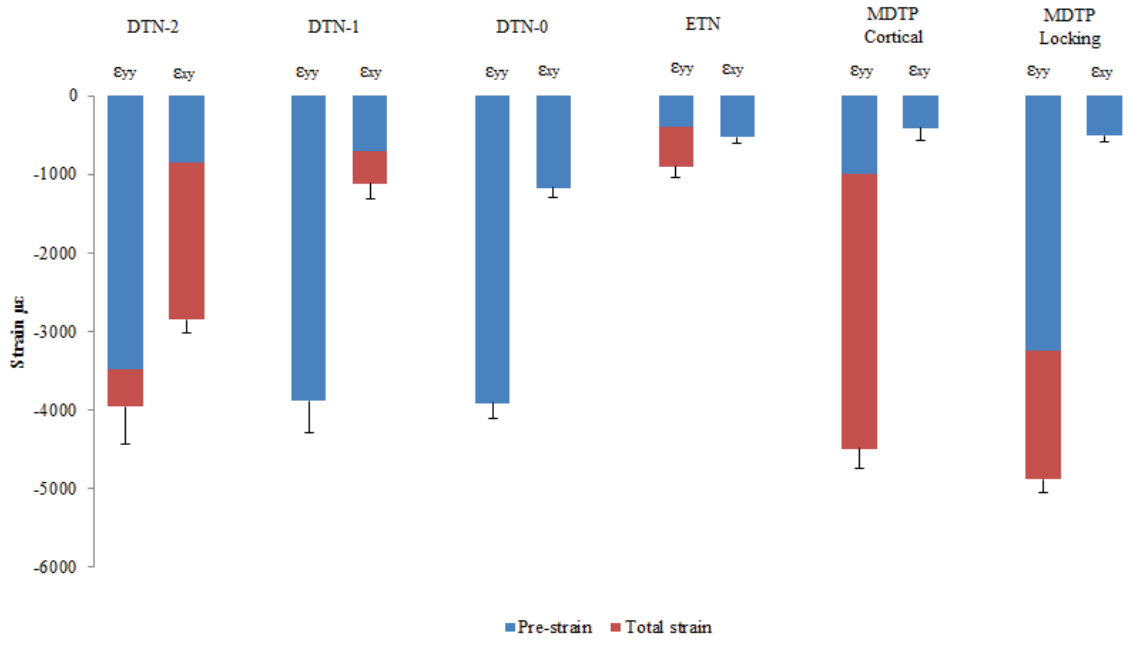

Figure 127: Déformation maximale (normale et en cisaillement) pour tous les échantillons.

Conclusion générale

L'objectif principal de ce projet a été d'évaluer l'utilisation du DTN pour la fixation des ostéotomies correctives supra-malléolaires. La configuration d'essai pour la compression a été étudiée en détail afin de l'optimiser et d'identifier des sources de variabilité. Le PMMA et l'axe de chargement ont été identifiés comme influant la raideur mesurée de l'échantillon. Ensuite, seize os composites ont été soumis à des tests biomécaniques de compression et de torsion, avant (Phase 0) et après instrumentation par DTN ou MDTP (Phases 1, 2 et 3). Ces trois phases d'essai ont permis de tster les implants pour des configurations à l'instabilité croissante de l'ensemble os-implant. La raideur de l'échantillon, les mouvements inter-fragmentaires (IFM) et la déformation à la surface externe de l'os ont été mesurés.

Malgré des différences de raideur parfois significatives entre des groupes d'implant, l'IFM reste en dessous de 2 mm pendant les Phases 1 & 2 : cela signifie que ces différences en raideur ont une cause autre que l'IFM. A l'issue de ces essais, le DTN semble être une véritable option pour la fixation des ostéotomies correctives ; cet implant peut être avantageux chez des patients ayant une vascularisation compromise (telles que les personnes âgées) où la pose d'une plaque n'est pas adaptée.

Une analyse statistique a été menée afin d'identifier les paramètres expérimentaux influant la raideur mesurée. Ces paramètres changent en fonction de l'implant et de la configuration, même si la raideur initiale des os composites semble avoir toujours une grande influence sur la raideur des os instrumentés. D'autres facteurs tels que l'épaisseur du PMMA, l'axe de chargement, la position de l'implant et de l'échantillon par rapport à l'axe de chargement, peuvent contribuer à la variabilité des résultats finaux. L'analyse statistique n'a pas pu expliquer la majorité de la variabilité des raideurs mesurées en torsion. Il est donc recommandé que les futures études basées sur des essais biomécaniques s'appuient sur une analyse préalable des conditions d'essai afin d'identifier des sources de variabilité.

Les perspectives de ce projet comprennent le développement d'un modèle numérique calibré sur les essais effectués ici et à la géométrie reconstruite à partir de l'imagerie effectuée au cours de cette étude.

Appendix

1. Supplementary data related to Chapter 1

1.1. Complementary options to biomechanical testing

The use of cameras to film a sample is widely used (Horn et al., 2009; Guerorguiev et al., 2011; Hogel et al., 2012; Kuhn et al., 2014a) to obtain information on interfragmentary movement of the

fracture gap. This can be carried out by placing markers on the sample and tracking them using public or private software. This method is easy to put into practice and provides data that is less affected by external factors such as the experimental setup.

The use of cameras as a complementary measurement method can also be employed to indirectly measure strain through digital image correlation. This technique requires two cameras, each at a divergence of 10-15° facing the sample. A speckle pattern is applied to the sample (not affecting its mechanical or material properties) and the points are then tracked.

1.2. Principles of digital image correlation

The concept of DIC is the tracking of multiple points which make up a speckle pattern applied to a sample. The displacement and deformation of all points gives information of the displacement and deformation of specific zones of a sample or, indeed, the entire sample. Points from image "n" are compared to a reference image which is either the first image recorded (often relating to a static position with no deformation), or the previous image (n-1). The use of two cameras is to obtain a three-dimensional image, as is the case with sight in human beings. The reconstruction of a 3D object requires at least two images. These acquired images are two-dimensional, whereas our object is three-dimensional; this indicates that by recording an environment in 2D, we lose information related to the third dimension (Boufama, 1994). 3D reconstruction seeks to calculate this lost dimension.

The 3D reconstruction is complicated by the fact that two cameras looking at the same object but from different positions will not always see the same image. The object can be identified but the visualised surface is not the same; the greater the angle of view between the cameras, the greater the disparity between the observed surface of a same object. Furthermore, a second object hidden behind the primary object may be visible to one camera but not the other. It is therefore important that the view of both cameras covers a sufficient shared surface in order to match points between two images. It is therefore important that the divergence angle between the two cameras lies within the range of 10° - 30°.

Monochrome images are necessary in order for the correlation algorithm to compare the levels of greyscale between two images and identify the speckle points thanks to a high contrast between the point and background -colour. The user-defined area of interest (AOI) is specified as the zone to be correlated and is divided into squares known as facets. Each facet is made up of $M \times N$ pixels and a b-cubic spline interpolation to estimate greyscale levels between pixels. DIC seeks to re-identify each facet in each image to be correlated. The speckle points within the facet are analysed every n number of pixels, this parameter is known as the step size and the initial size of the facet is known as the pattern size.

The similarity between two images is analysed using the zero normalised cross correlation (ZNCC). The ZNCC criterion is based on the addition and multiplication of greyscale levels between two images. The closer this criterion tends towards the value of 1, the greater the similarity between the two images.

$$C = \frac{\sum_{i \in D} (f(X_i) - \bar{f}) \times (g(x_i) - \bar{g})}{\sqrt{\sum_{i \in D} \left(f(X_i) - \bar{f}\right)^2 \times \sum_{i \in D} (g(x_i - \bar{g})^2}}$$

Suppl. Equation 1: Zero normalised cross correlation
Equation adapted from Correlated Solutions technical data (Correlated Solutions, Inc., USA)

Greyscale levels are represented in the above equation by $\bar{f}$ and $\bar{g}$, stating the grey level for each pixel i of the surface to be correlated D. The greyscale of coordinates X (reference image) and x (image to be correlated) are given by the functions f and g, respectively.

All pixels in the surface D for correlation are analysed, meaning that images with a greater resolution will provide more detailed information on surface displacements and deformations.

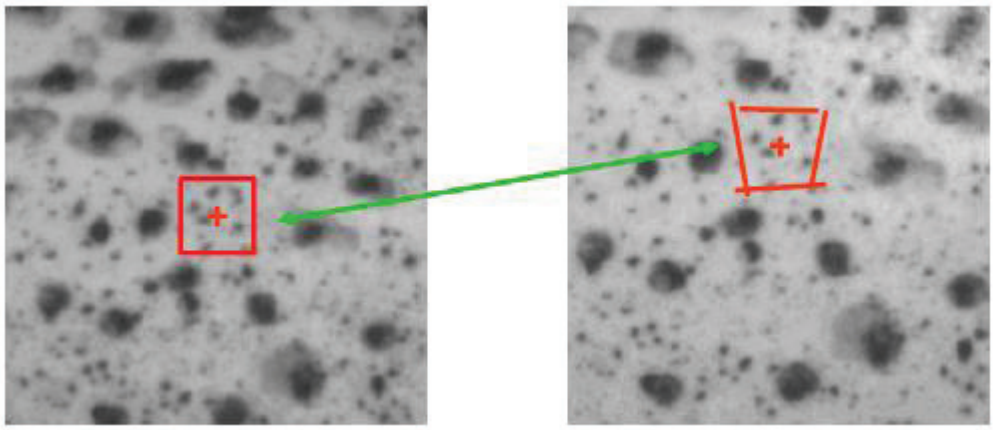

Suppl. Figure 1: Example of how the speckle pattern within a facet can be displaced and deformed.
Images adapted from Correlated Solutions technical data (Correlated Solutions, Inc., USA).

In order for a DIC system to work, the environment first needs to be calibrated to calculate the position of each camera with respect to the sample. This is done using a pre-defined calibration grid consisting of a series of points that are detectable by the DIC software. The size and spacing of the points is known and therefore the software can calculate the spatial position of the cameras relative to the sample being tested.

2. Supplementary data related to chapter 2

2.1. Inserts for PMMA compression

A supplementary study was performed to test the use of metallic inserts in the PMMA with the aim of distributing the applied load over a greater area and therefore minimising the concentration of stress and deformation in a localised area.

Two Sawbones® samples were embedded in PU resin and subjected to incremental compressive loads of 700 N were applied using a double ball joint setup (Suppl. Figure 2) at a frequency of 0.05 Hz over 30 cycles. A speckle pattern was applied to the composite one sample and the distal third of the bone was analysed using DIC.

Suppl. Figure 2: Test setup used to measure the stiffness construct of a Sawbones® sample with and without the use of metal proximal and distal metal inserts.

Testing took place at the LBMC laboratory (Lyon) using the Instron 8800 servohydraulic testing machine. The composite bones were tested in alternating order to allow the PMMA to return to its original state (Suppl. Table 1).

Suppl. Table 1: Testing order for the different configurations used for each sample

Test	Sawbones® sample	Insert location(s)
1	1	Distal
2	2	Proximal and distal
3	1	Proximal and distal

4	2	Distal
5	1	None
6	2	None

2.2. Results

PMMA characterisation

In order to calculate the Young's modulus of PMMA with the same composition as that used during all testing (2:1 powder to liquid ratio), a cuboid (dimensions: 16 x 16 x 101 mm) was created from the resin and subjected to incremental compression testing of 700 N at 0.05 Hz over 30 cycles. The cuboid was covered with a black and white speckle pattern for DIC analysis. Markers were placed on the superior and inferior joints of the testing machine to measure the displacement.

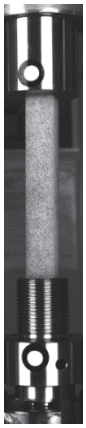

Suppl. Figure 3: Test setup for PMMA compression testing to characterise its mechanical properties.

The machine data were processed using the same method described in Chapter 2 (Data Processing). DIC data were processed using Vic3D (version 8, Correlated Solutions, Inc., USA). The DIC processed data was exported as extensometer data (strain: $\Delta L/L_0$) and minimal principal strain (e_2). Young's modulus was calculated and average strain was observed.

The force of 700 N was applied over an area of 256 mm² giving a maximal pressure of 2.73 MPa; the maximum strain recorded by the extensometer was $-7.5e^{-4}$. The resulting Young's modulus was therefore calculated to be 3.6 GPa.

Strain and displacement distributions show an uneven spread of deformation throughout the sample. Compressive strain is first concentrated in the top-left corner of the sample while tensile strain is observed in the top right. Poisson's ratio was also calculated and found to be at 0.27.

2.3. Discussion

Comparing this figure with Young's moduli cited in the literature, this figure is 4 fold lower than the compressive elastic modulus for Sawbones® (cited at 16.7 GPa; Pacific Laboratories, Inc., 2016). These findings further support the notion that the use PMMA will contribute to stiffness values

in a parasitic manner. Furthermore, the Young's modulus calculated in this supplementary study will provide useful information for the numerical simulation of tests carried out in order to account for the PMMA embedding.

The uneven strain distribution leads us to believe that the PMMA surface across which the force was applied was not entirely flat, and therefore our calculations should be treated with caution as strain levels may be lower when compression is equally applied across the whole surface.

To verify our tests, three separate extensometers were applied to the correlated in Vic3D (Suppl. Figure 4). This was in order to check the level of strain measured over the cross-section of the sample at maximal force (-700 N). A difference of 0.00075 can be observed between the three extensometer positions, further highlighting the fact that compressive force was not equally applied across the proximal surface.

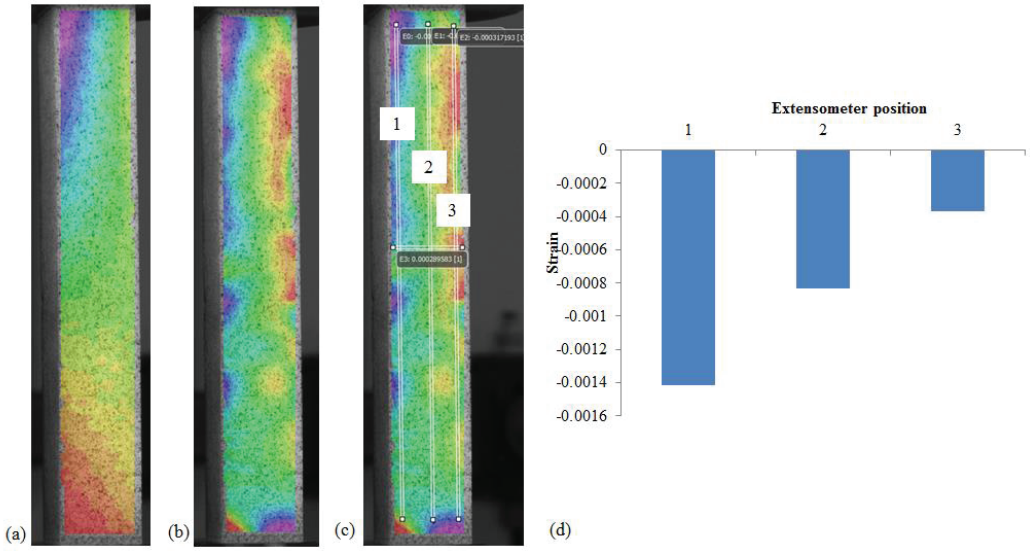

Suppl. Figure 4: DIC of PMMA block subjected to 700 N compression; results of vertical displacement (a), minimal principal strain (b) with extensometer placement (c) and variation (d) to assess average strain.

The small dimensions of the PMMA block used in this study with respect to the force applied may have resulted in bending or buckling; although this was not observed, we plan to carry out a second test with the same boundary conditions but using a larger sample with true planar surfaces.

3. Supplementary data related to chapter 3

Suppl. Table 2: Camera settings for all tests

Samples	Test	Camera resolution (pixels)	Equivalent pixel size (mm²)	Camera offset (x , y) (pixels)	Camera divergence angle
Whole Sawbones (Phase 0)	Compression 350 N at 0.1 Hz	320 x 1250	0.0721	1024 , 250	16°

	30 cycles				
	Torsion ±4 Nm at 0.1 Hz 30 cycles	512 x 1000	0.0707	1264 , 400	16°
Corrective osteotomy (Phase 1)	Compression 350 N at 0.1 Hz 700 N at 0.05 Hz 30 cycles	384 x 1100	0.0742	1104 , 450	20°
	Torsion ±4 Nm at 0.1 Hz ±8 Nm at 0.05 Hz 30 cycles	544 x 1000	0.0706	992 , 400	18°
Corrective osteotomy (Phase 2)	Compression 350 N at 0.1 Hz 700 N at 0.05 Hz 30 cycles	384 x 1100	0.0742	880 , 450	16°
	Torsion ±4 Nm at 0.1 Hz ±8 Nm at 0.05 Hz 30 cycles	544 x 1000	0.0706	992 , 400	18°
A3 Fracture (Phase 3)	Compression 350 N at 0.1 Hz 700 N at 0.05 Hz 30 cycles	384 x 1100	0.0742	1072 , 350	17°
	Torsion ±8 Nm at 0.05 Hz 30 cycles	576 x 1000	0.0699	1024 , 400	20°

3.1. The Theil-Sen estimator

The use of the Theil-Sen estimator was preferred over the least squares method as this procedure is less sensitive to outliers, using the median, rather than the mean, of all points. The Theil-Sen estimator is calculated by taking the median of all the slopes between two points of a cloud. Paired points are first computed, pairing one point with all remaining points and taking the slope between the paired points. This pairing procedure is carried out until all points have been paired with all over points.

$$\tilde{\beta}_n = \left\{ b_{i\,j} : b_{i\,j} = \frac{Y_j - Y_i}{x_j - x_i}, if\ x_i \neq x_j, 1 \leq i < j \leq n \right\}$$

Equation 17

Where $\tilde{\beta}_n$ is the Theil-Sen estimator for $b_{i\,j}$ points the slope is calculated by subtracting the Y-coordinates of point i from point j and diving this by the subtraction of the X-coordinates of point i from point j. Point j must always be greater than point i unless these points lie on the same x-coordinate.

3.2. DIC for healthy samples

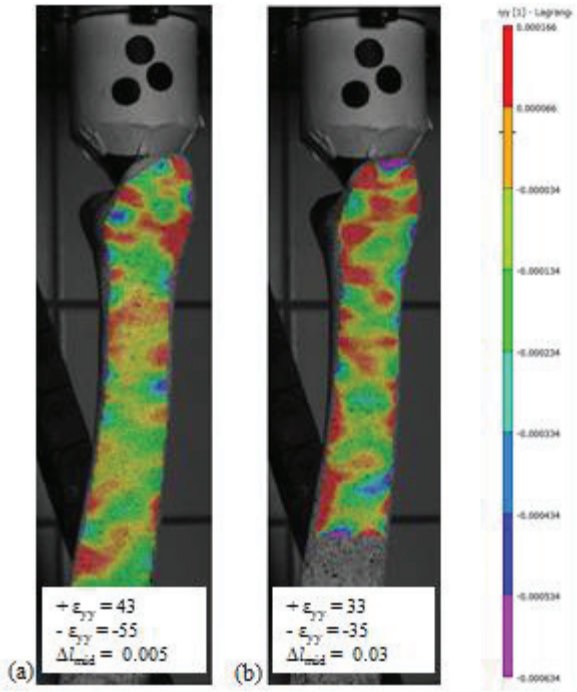

Suppl. Figure 5: Vertical strain maps for the DTN-1 and DTN-4 samples during Phase-0 compression testing at 350 N. Images are taken at 300 N loading.

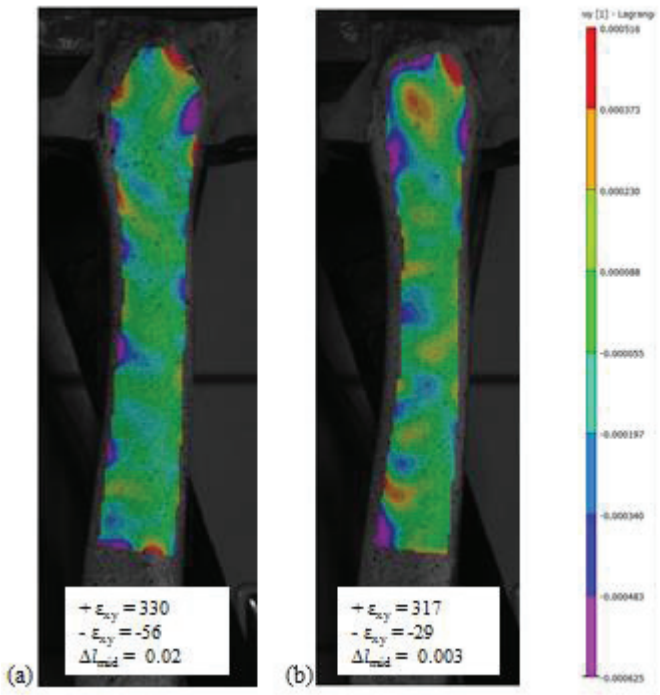

Suppl. Figure 6: Shear strain mapping for the MDTP-2 and MDTP-7 samples during Phase-0 of testing at ±4 Nm torsion. Images are taken at 3.5 Nm loading.

During Phase-0 of testing for both torsion and compression testing, little deformation is observed across all samples. In compression testing, the tensile forces seem more widespread in the DTN4 sample (K = 1968 $N.mm^{-1}$) despite its greater stiffness compared to the DTN-1 sample. Nonetheless, the detected positive and negative vertical strain in this sample is lower than in the DTN-1 sample (max $\mu\varepsilon_{yy}$ = 43 and -33; min $\mu\varepsilon_{yy}$ = -35 and -55, respectively).

Shear strain levels during torsional testing are also very low and the observed strain distributions shown in Suppl. Figure 6 may in fact be related to edge side effects. Levels of -56 $\mu\varepsilon_{xy}$ and -29 $\mu\varepsilon_{xy}$ are observed for negative ε_{xy}, and 33 and 32 $\mu\varepsilon_{xy}$ for positive ε_{xy}; values are stated for the MDTP-2 and MDTP-7 samples, respectively.

4.3. Evaluation of abnormal standard deviations from machine data

Phase-1 Compression testing, MDTP-6 sample

On running a closer inspection of this sample, we notice that cycles 11-13 do not appear normal (Suppl. Figure 7). The cause of this disturbance is unknown as no errors were identified during testing or implantation of this sample.

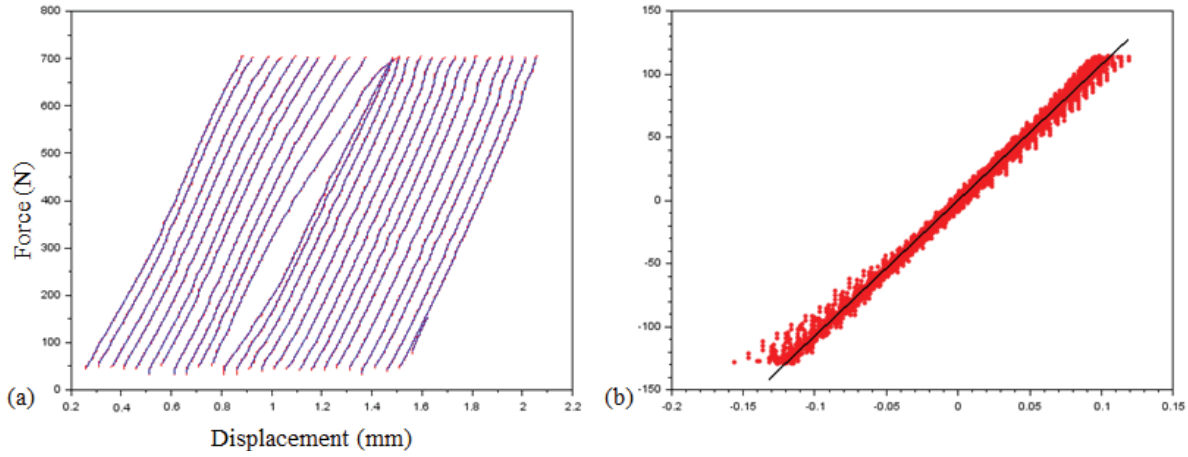

Suppl. Figure 7: Force-displacement (a) and goodness of fit curves for the Plate-6 sample.

Phase-1 Torsional testing, MDTP-7

Particularly high standard deviations can be seen in the Plate-7 sample when compared to other samples. This also becomes apparent when closely analysing the data cycle by cycle (Suppl. Figure 8). This figure below shows the torque-angle curve and points for line of best fit graphs for Plate-7 (Suppl. Figure 8a) and Plate-8 (Suppl. Figure 8b). The zone for stiffness calculation is indicated on the graphs (2±1 Nm) and on comparing the two samples, it is clear that the data above 2 Nm for Plate-7 does not follow a linear pattern.

This may again be related to testing machine parameters such as clamp tightening and sample position in the testing machine; especially as such high standard deviations are not evident in phases 2 and 3 for this sample.

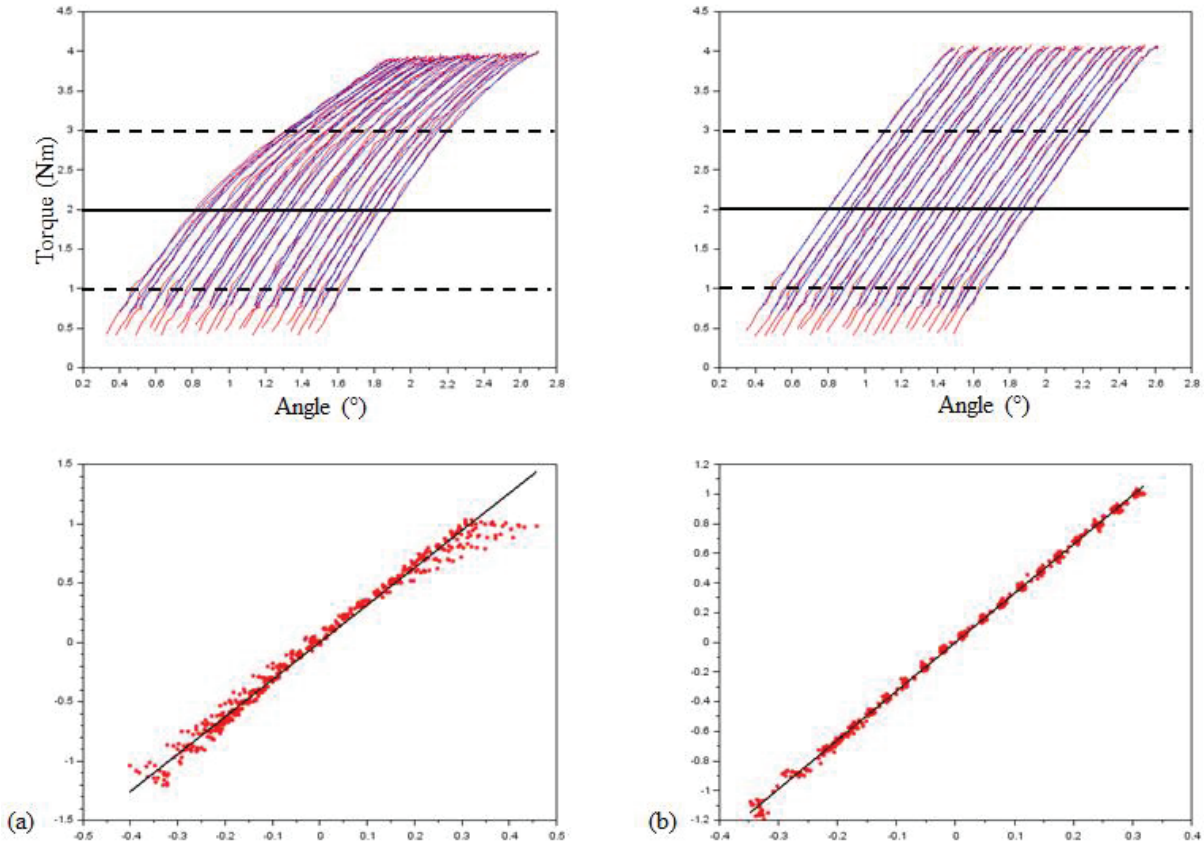

Suppl. Figure 8: Torque-angle and goodness of fit graphs for the Plate-7 and Plate-8 samples during ±4 Nm loading tests.

Phase-2 Compression testing 700 N, DTN-7

The DTN-7 when measured in the "Fracture" configuration. By observing the graphs in Suppl. Figure 9, it is clear that there were problems in the data collection for this sample. No comments were made during the testing of this sample. The stiffness value taken for statistical analysis (calculated from the Theil-Sen estimator) is not influenced by this abnormality and estimates a high stiffness falling in the correct range when compared to the other DTN samples (DTN-7: 1035 N.mm-1; DTN sample range: 778 – 1095 $N.mm^{-1}$). Nonetheless, the data from the "Implant" configuration are used for visual comparison against other samples in Suppl. Figure 9 in order to demonstrate a figure truer to reality.

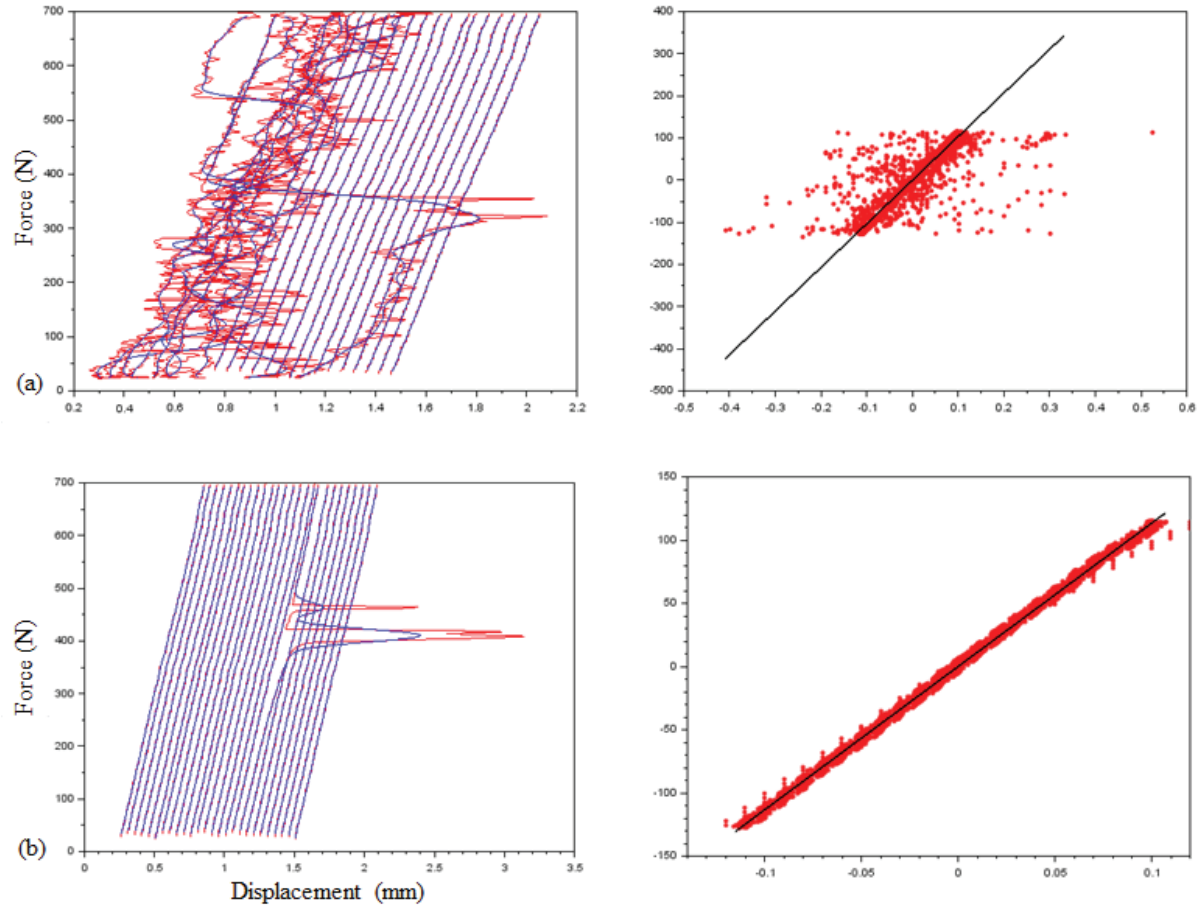

Suppl. Figure 9: Force-displacement (left) and goodness of fit (right) curves for the DTN-7 sample in the Fracture (a) and Implant (b) configurations.

Phase-2, Torsional testing at 4Nm, DTN-1, -2, and -5

Closer investigation of the DTN-1, -2, and -5 shows non-linear stiffness curves (Suppl. Figure 10) in which a first linear curve is displayed up to 1 Nm, followed by either a plateau (e.g. DTN-1, Figure…a) or a very gentle increase in stiffness until approximately 1.5 Nm. This is mimicked by the goodness of fit curves which all deviate largely from the line of best fit over the first 50% of the points used for stiffness calculation. The plateaus in in the stiffness curves may be a result of insufficient tightening of the sample in the testing machine clamps.

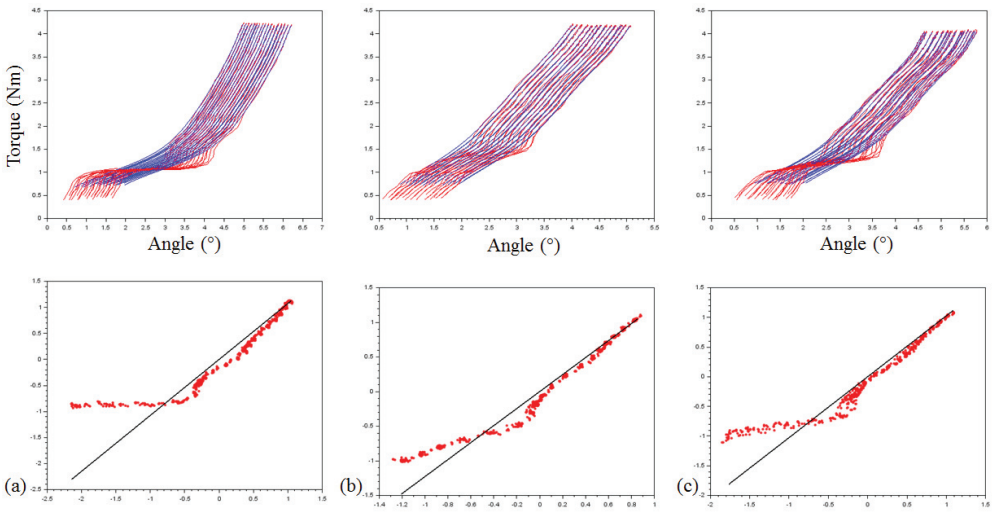

Suppl. Figure 10: Torque-angle and goodness of fit graphs for the DTN-1, -2, and -5 samples during ±4 Nm loading in Phase-2 of testing.

Phase-2 Torsional testing 8Nm

The MDTP samples 4-8 exhibit high standard deviations compared to the DTN samples and on looking more closely at the stiffness curves, it becomes evident that the stiffness construct of these samples is less stable (Suppl. Figure 11). Variations in the torque-angle and … curves can be seen throughout the entire torque range for positive stiffness Suppl. Figure 11b) and also at low torque levels for the negative stiffness (Suppl. Figure 11c). The points fitted to the line of best fit for stiffness calculation highlight this variation. In particular, the slope of the line is steeper for the DTN-1 sample (indicating a higher stiffness), but between the positive and negative values for the same sample (Plate-5), there is not an equal stiffness construct. Positive torque results in a stiffness construct of 0.78 $Nm.^{-1}$ which is twice as high as the negative torque at just 0.36 $Nm.^{\circ-1}$.

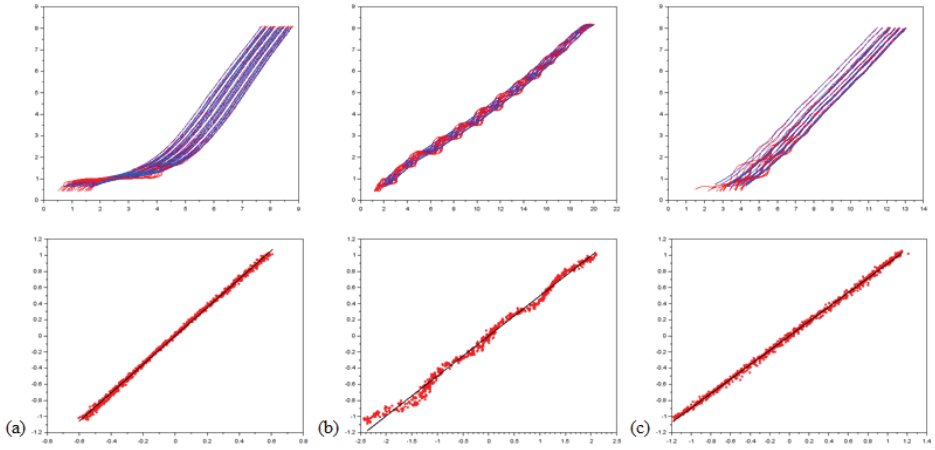

Suppl. Figure 11: Torque-angle (top) and goodness of fit (bottom) curves for the DTN-1 (a), Plate-5 positive torsion (b), and Plate-5 negative torsion (c) samples.

4. Supplementary data related to chapter 5

Correlation coefficients and correlation matrices for all instrumented testing phases (1-3) are presented. For correlations based on input parameters for torsional stiffness, the analyses are split into two parts, one for the sample-related factors, and one for the implant & experiment –related factors. This was done to render the graphs more legible and reduce the number of variables in each correlation.

Phase-1 350 N Compression: DTN

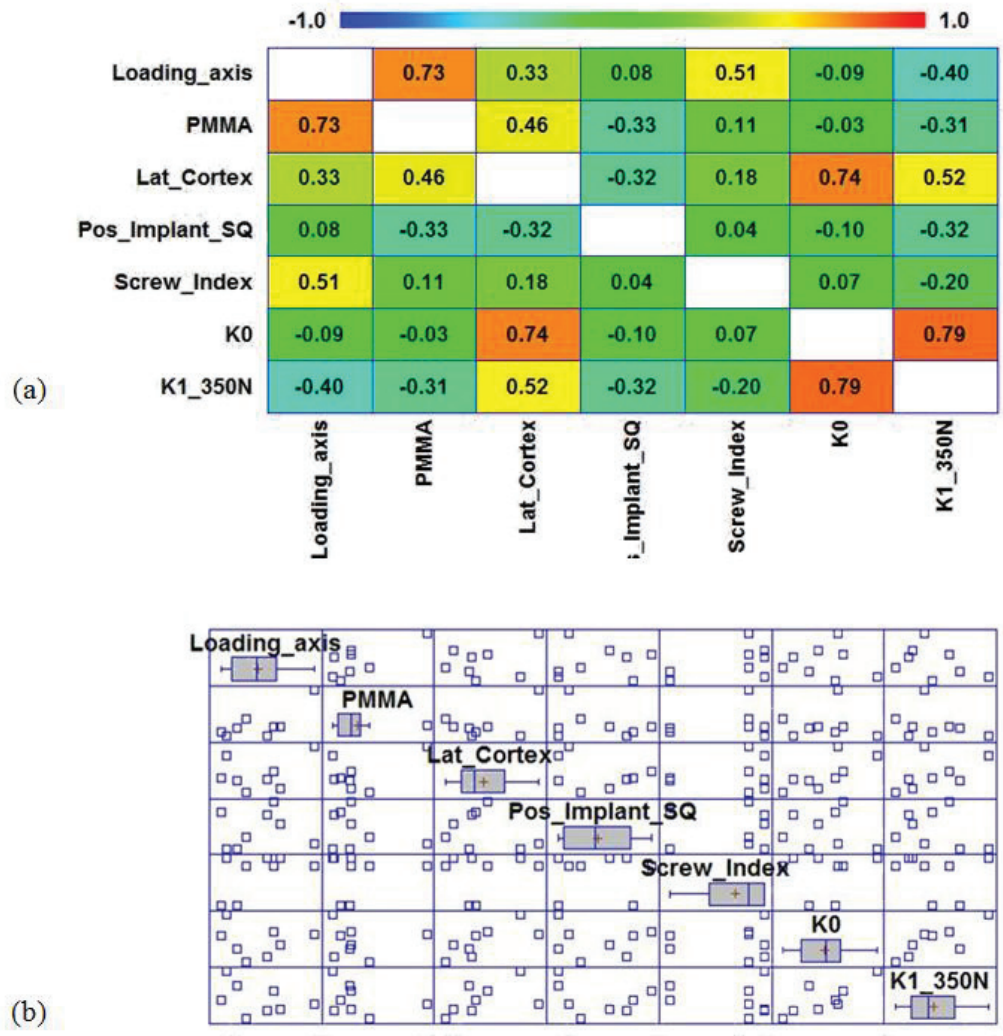

Suppl. Figure 12: Correlation coefficients (a) and matrices for the DTN samples at 350 N compression, Phase-1.

Phase-1 350 N Compression: MDTP

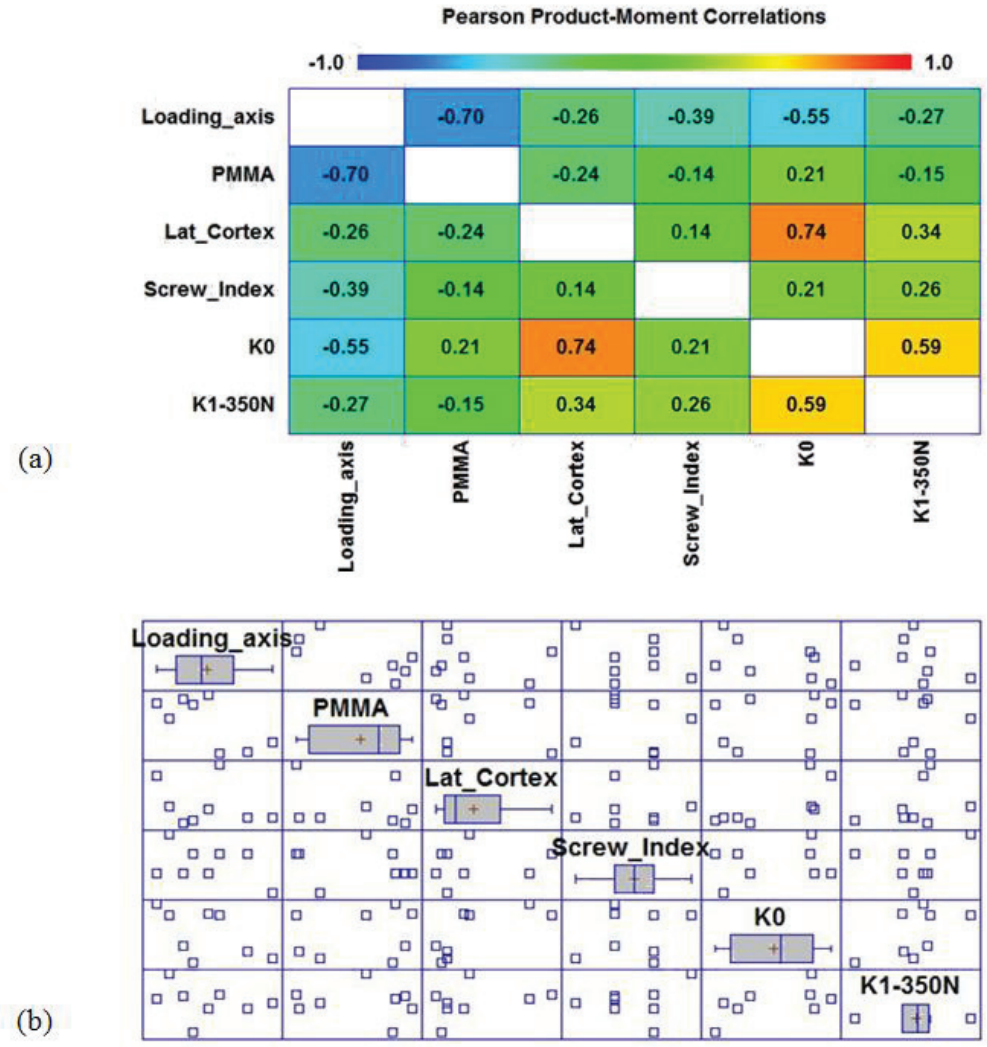

Suppl. Figure 13: Correlation coefficients (a) and matrices for the MDTP samples at 350 N compression, Phase-1.

Phase-1 700 N Compression: DTN

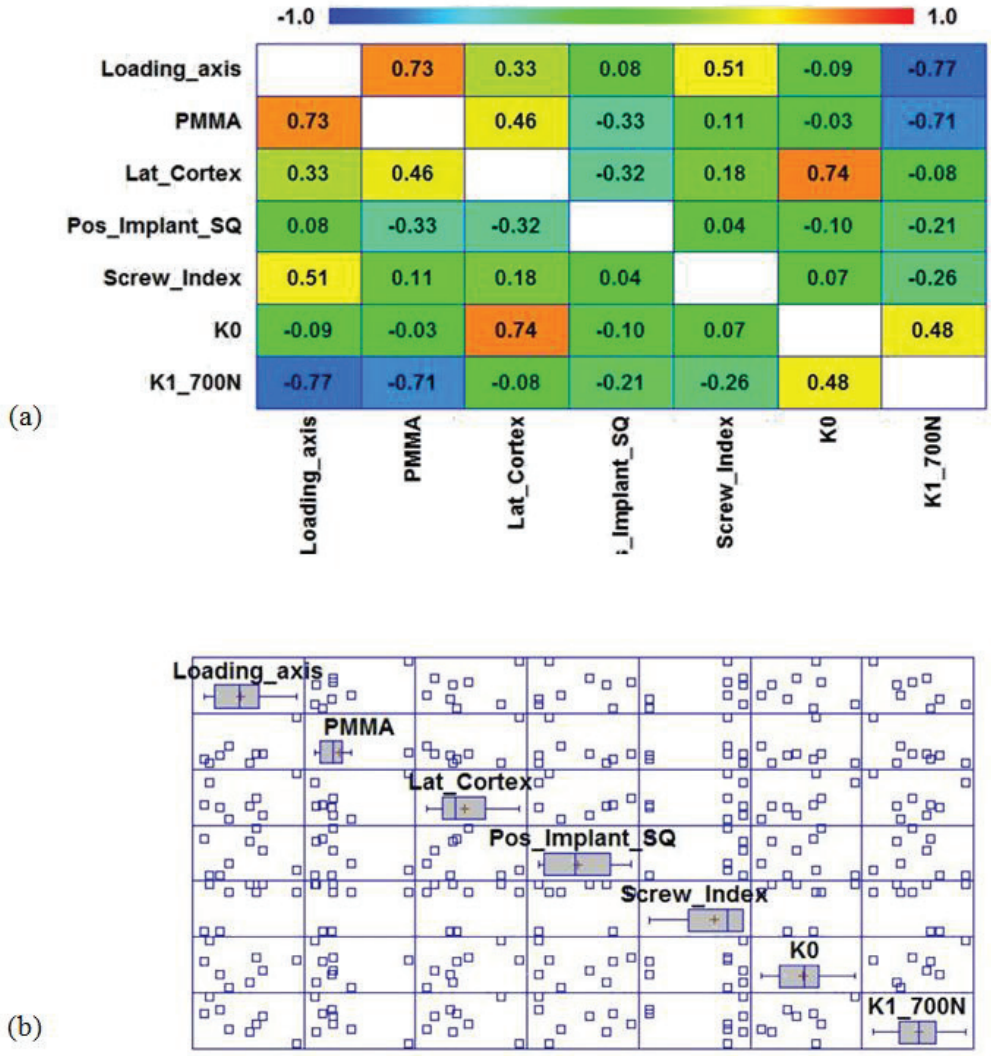

Suppl. Figure 14: Correlation coefficients (a) and matrices for the DTN samples at 700 N compression, Phase-1.

Phase-1 700 N Compression: MDTP

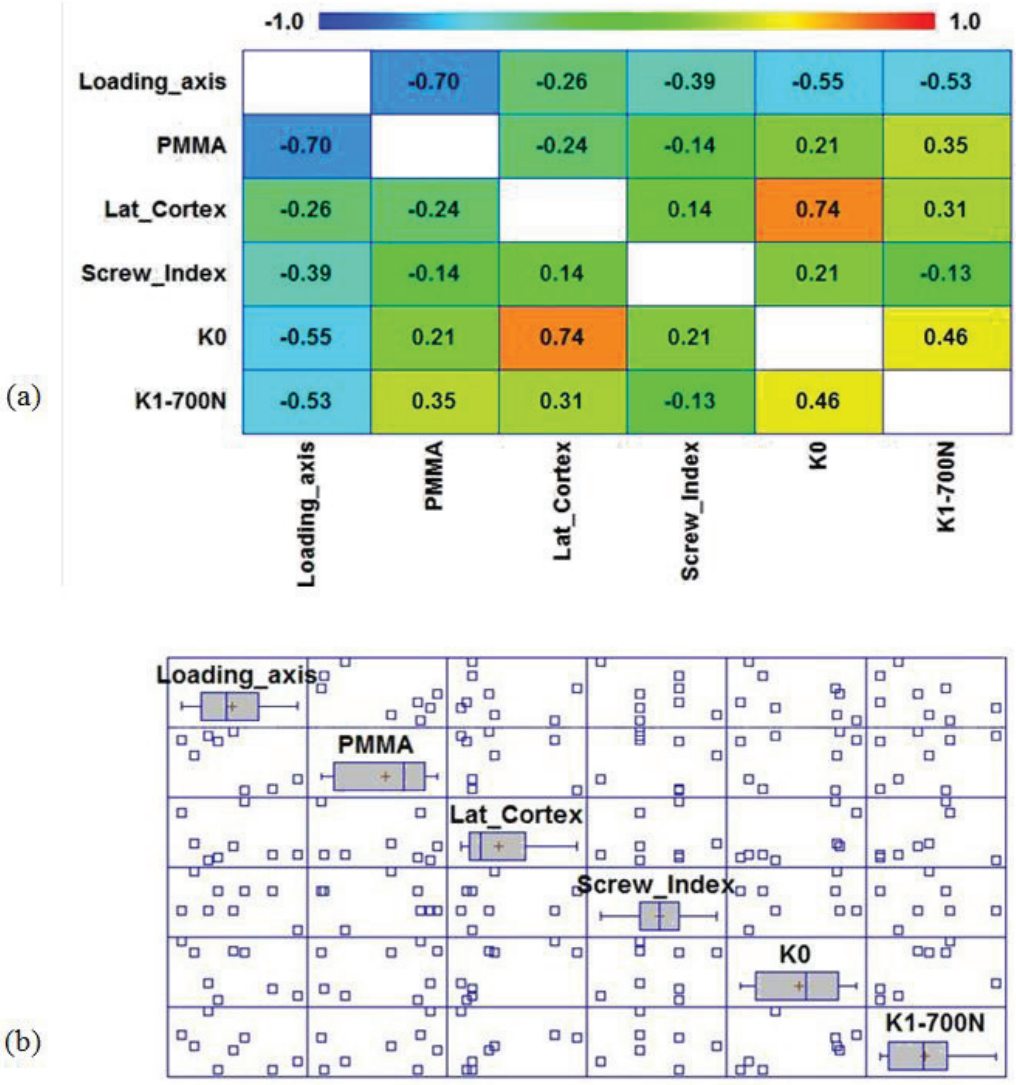

Suppl. Figure 15: Correlation coefficients (a) and matrices for the MDTP samples at 700 N compression, Phase-1.

Phase-1 4 Nm Torsion: DTN

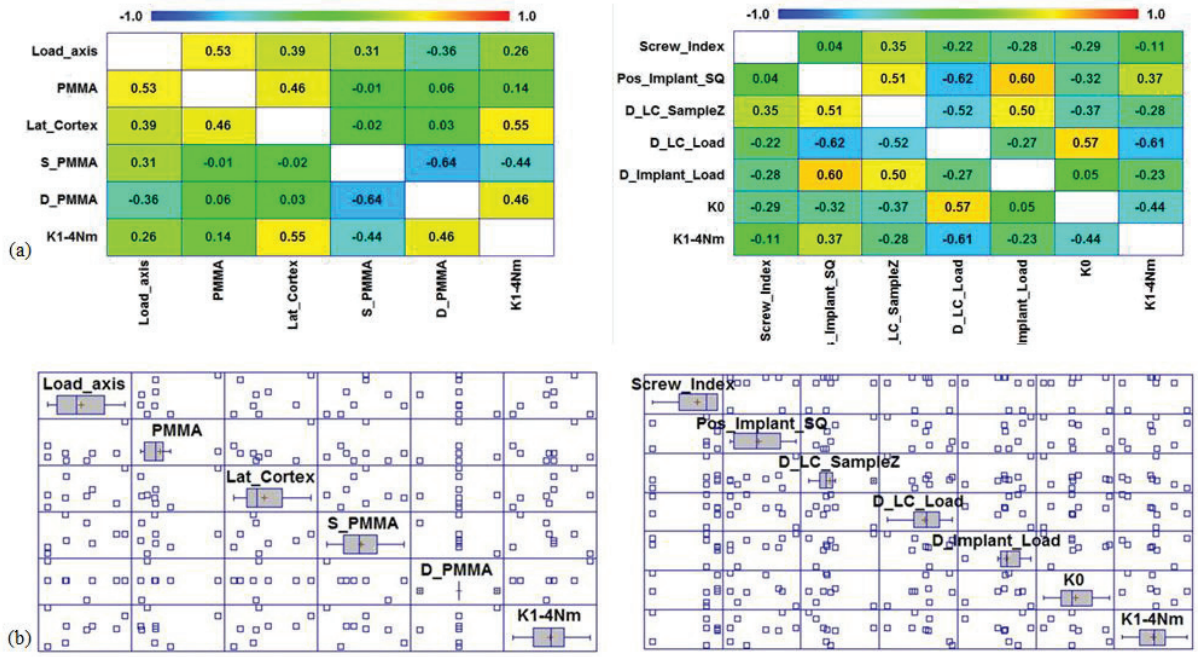

Suppl. Figure 16: Correlation coefficients (a) and scatter plots (b) for the DTN samples at 4 Nm torsion. Phase-1 of testing.

Phase-1 4 Nm Torsion: MDTP

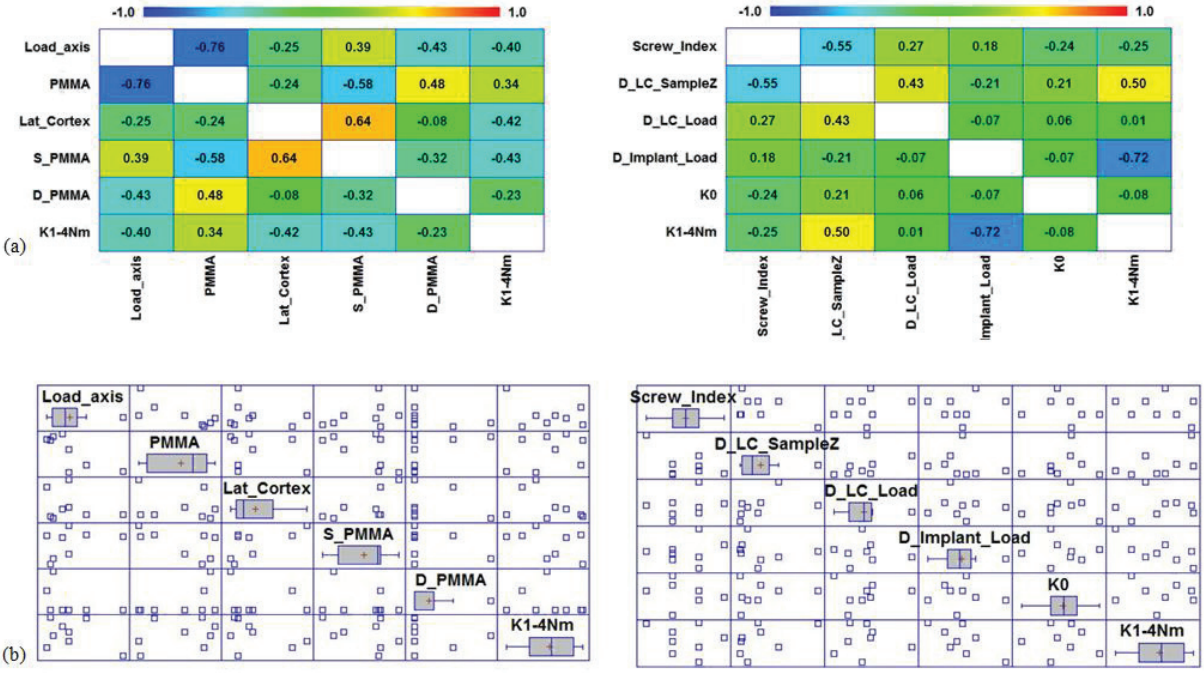

Suppl. Figure 17: Correlation coefficients (a) and scatter plots (b) for the MDTP samples at 4 Nm torsion. Phase-1 of testing.

Phase-1 8 Nm Torsion: DTN

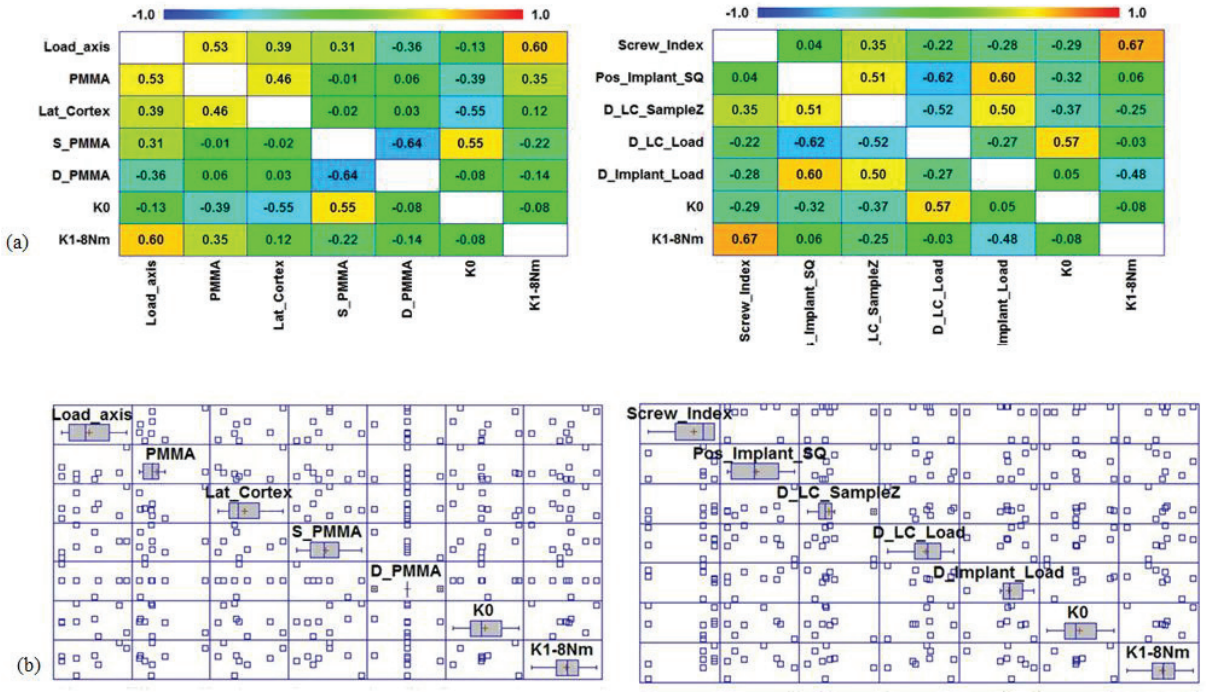

Suppl. Figure 18: Correlation coefficients (a) and scatter plots (b) for the DTN samples at 8 Nm torsion. Phase-1 of testing.

Phase-1 8 Nm Torsion: MDTP

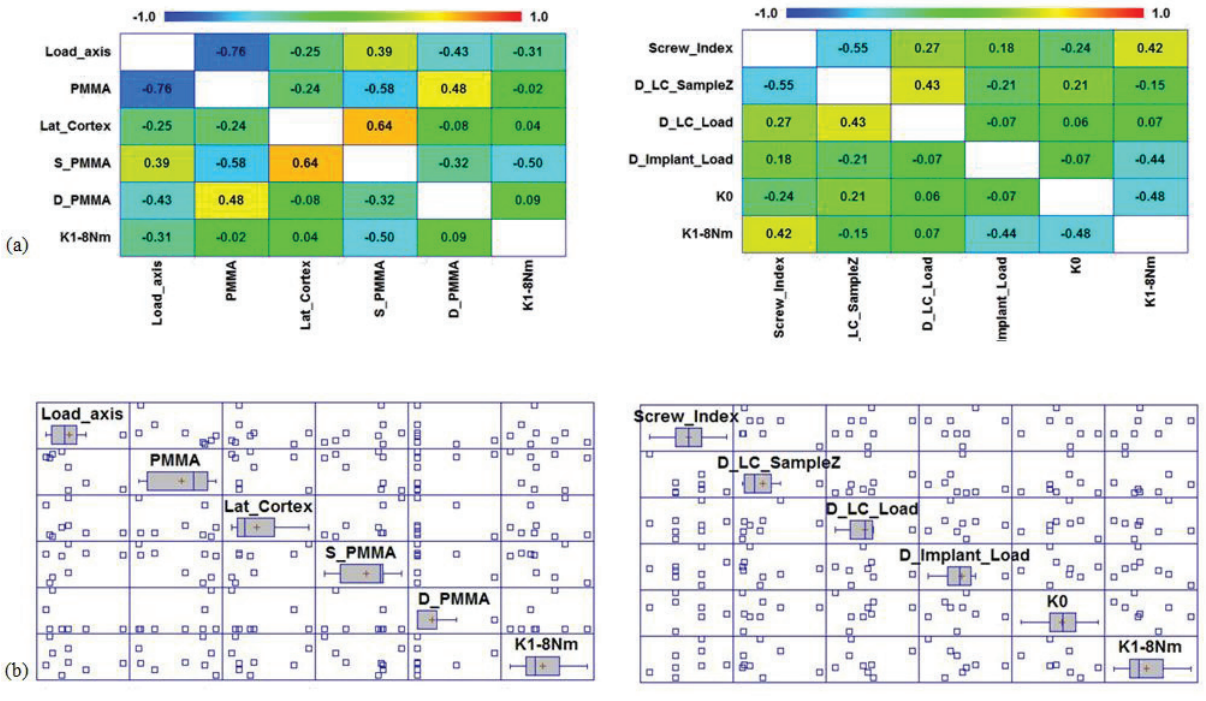

Suppl. Figure 19: Correlation coefficients (a) and scatter plots (b) for the DTN samples at 8 Nm torsion. Phase-1 of testing.

Phase-2 350 N Compression: DTN

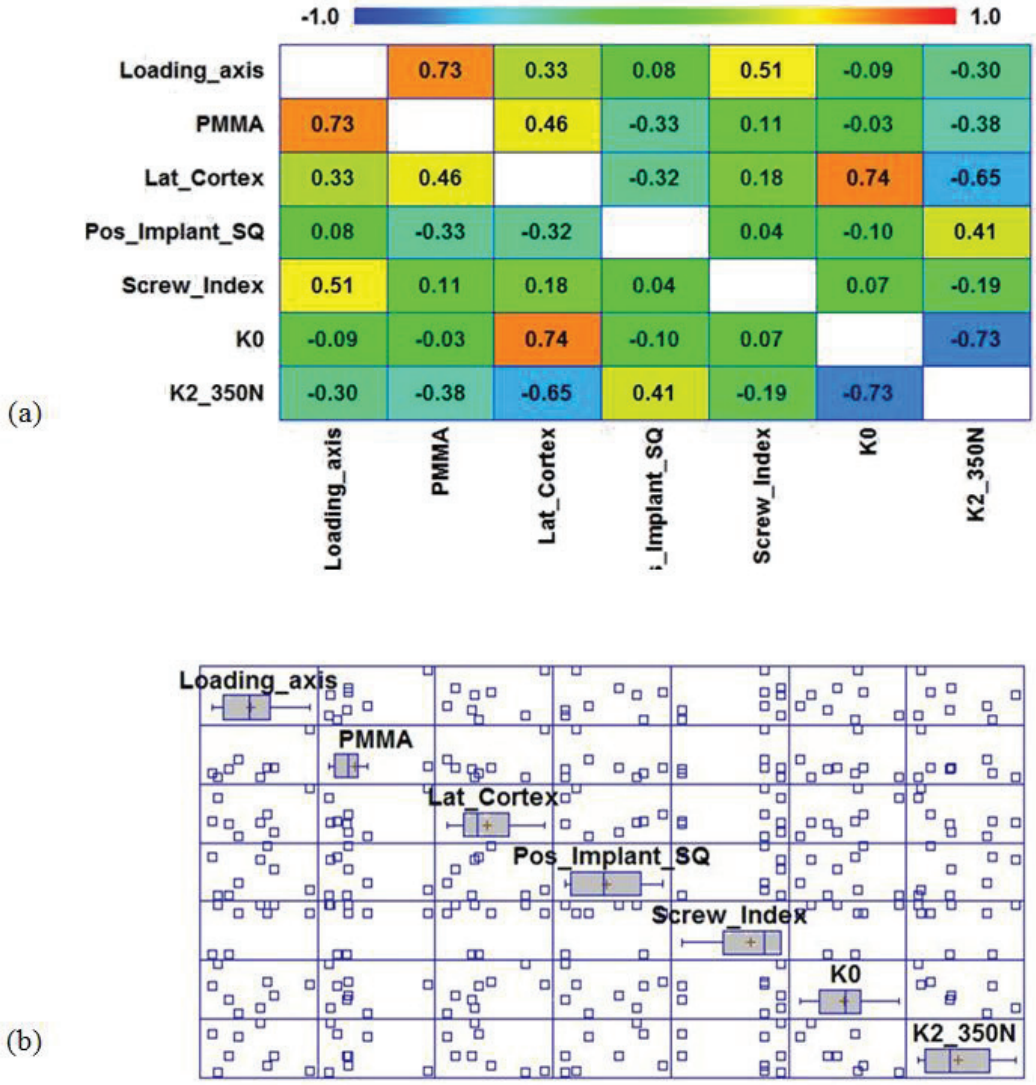

Suppl. Figure 20: Correlation coefficients (a) and matrices (b) for the DTN samples at 350 N compression, Phase-2.

Phase-2 350 N Compression: MDTP

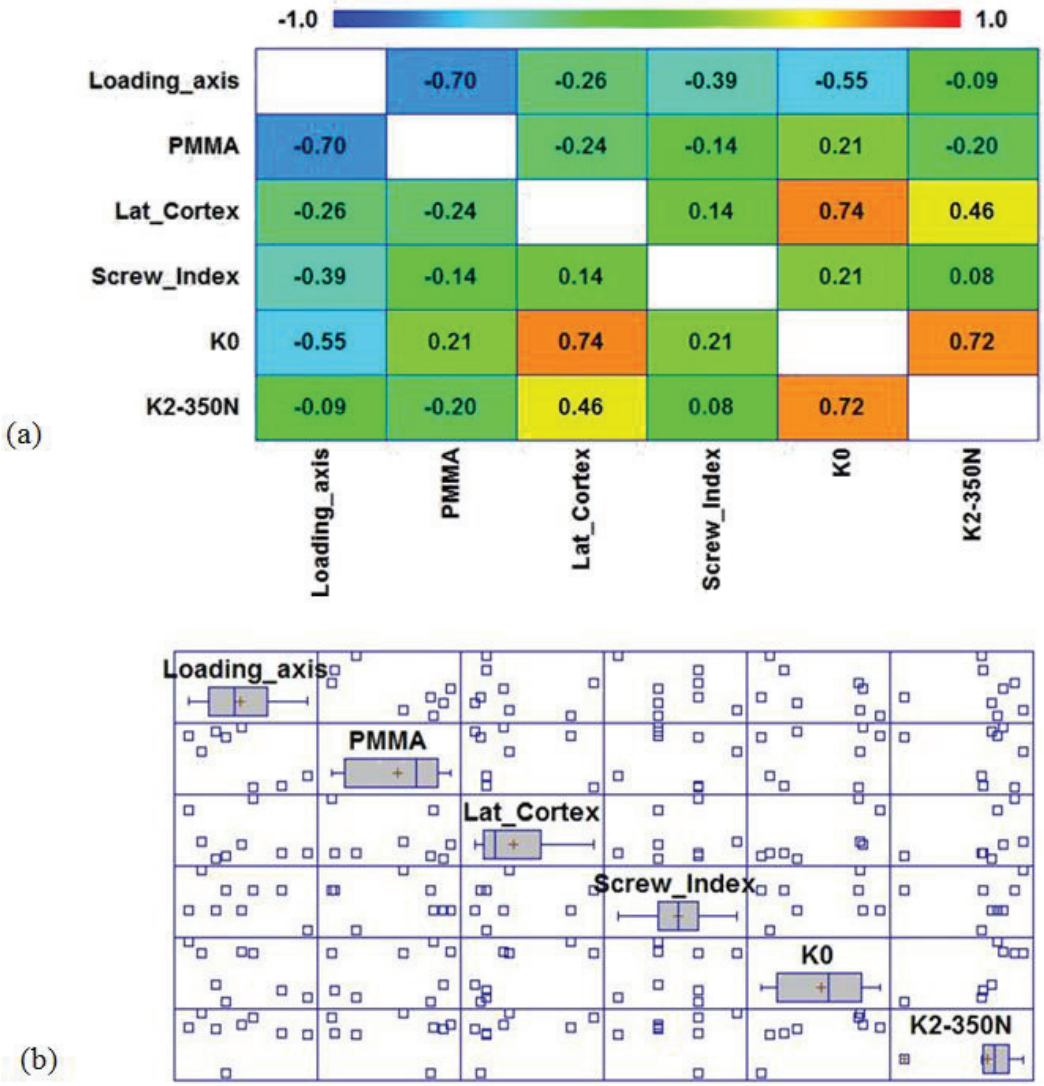

Suppl. Figure 21: Correlation coefficients (a) and matrices (b) for the MDTP samples at 350 N compression, Phase-2.

Phase-2 700 N Compression: DTN

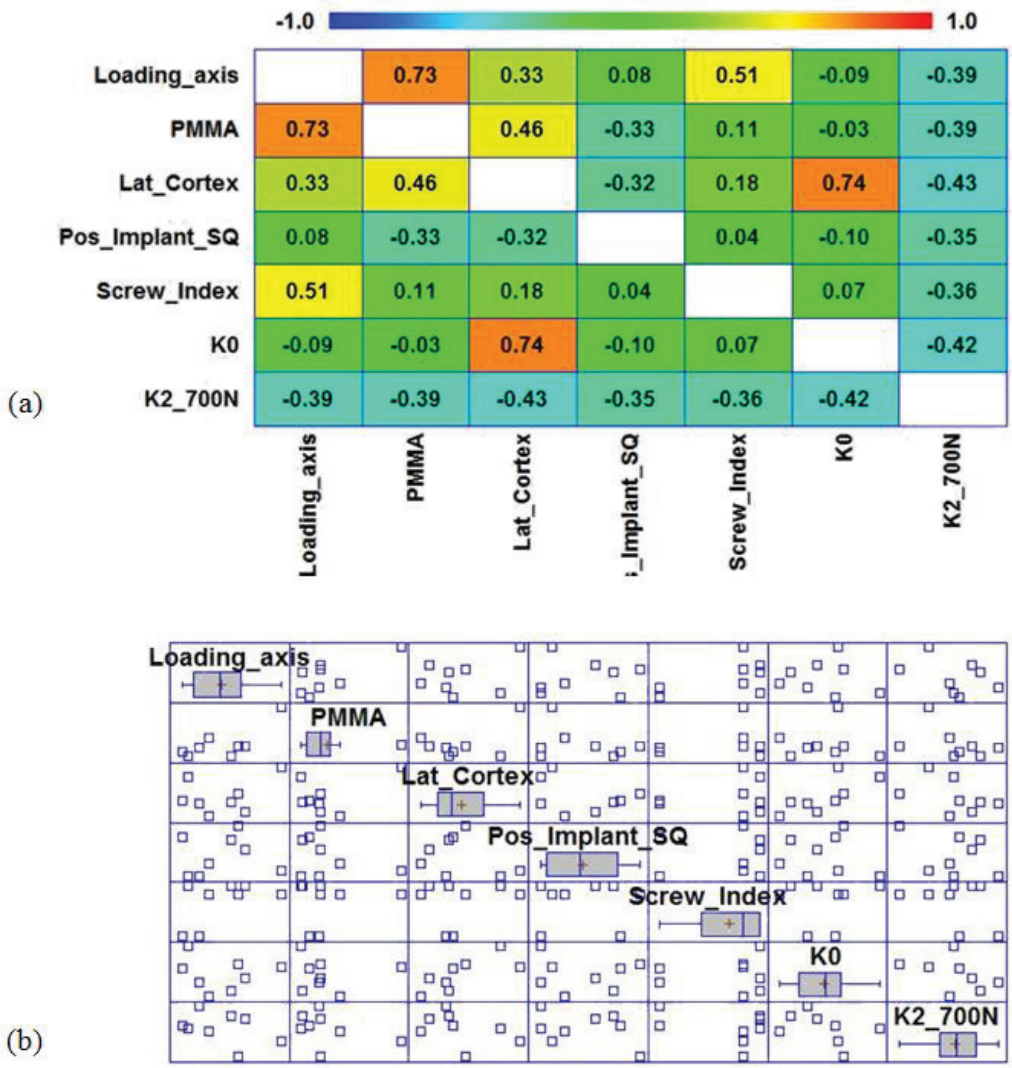

Suppl. Figure 22: Correlation coefficients (a) and matrices (b) for the DTN samples at 700 N compression, Phase-2.

Phase-2 700 N Compression: MDTP

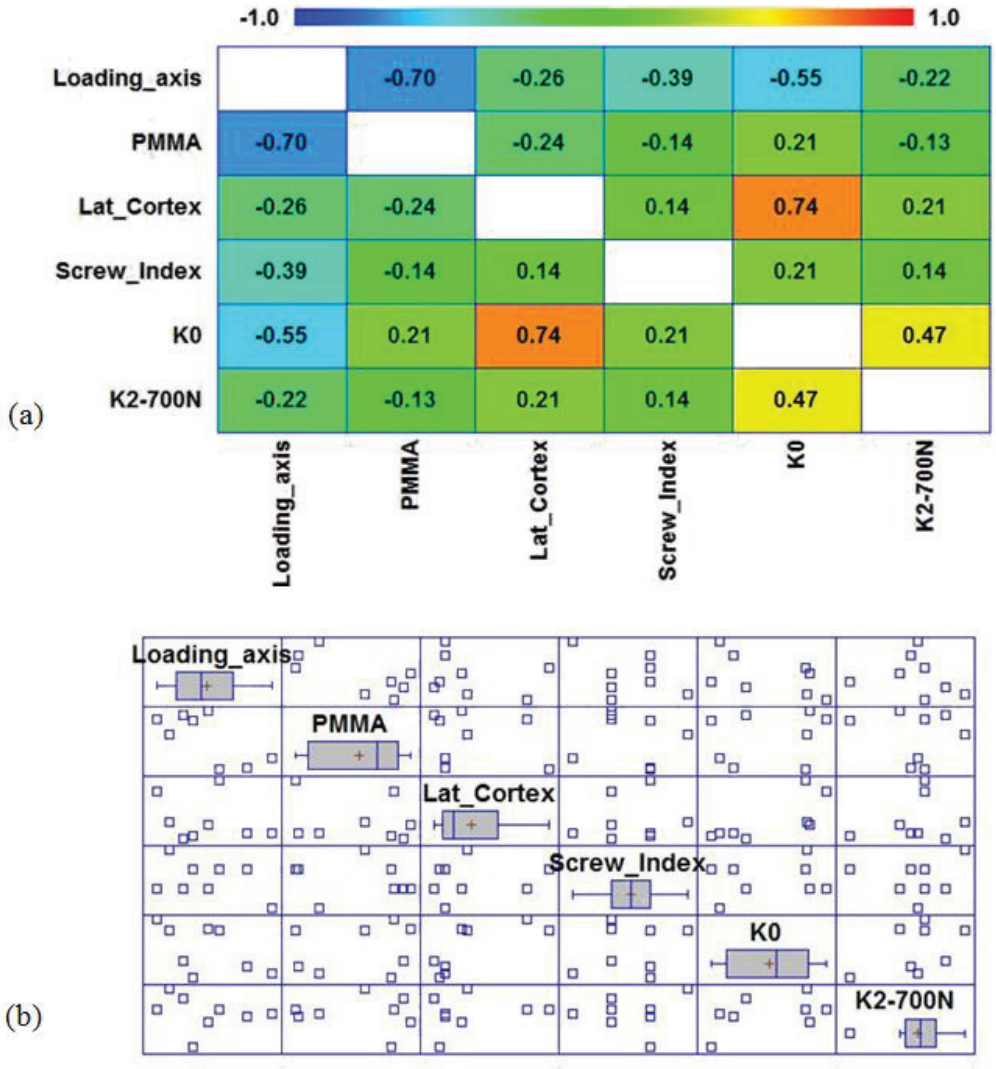

Suppl. Figure 23: Correlation coefficients (a) and matrices (b) for the MDTP samples at 700 N compression, Phase-2.

Phase-2 4 Nm Torsion: DTN

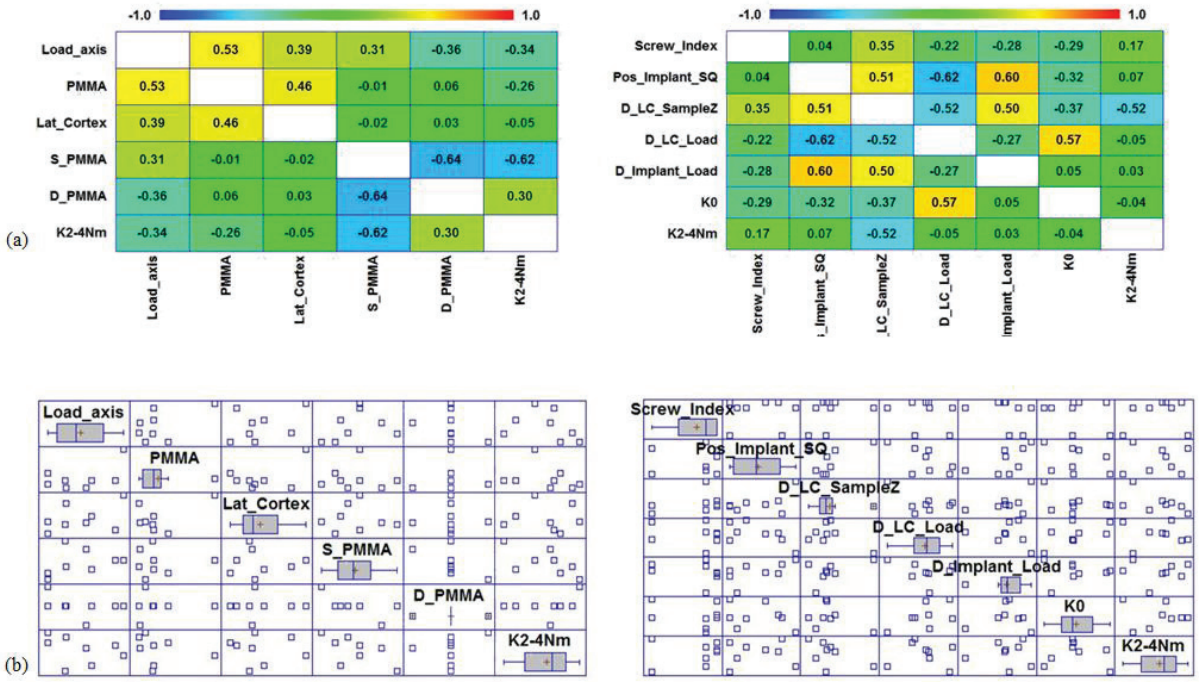

Suppl. Figure 24: Correlation coefficients (a) and scatter plots (b) for the DTN samples at 4 Nm torsion. Phase-2 of testing.

Phase-2 4 Nm Torsion: MDTP

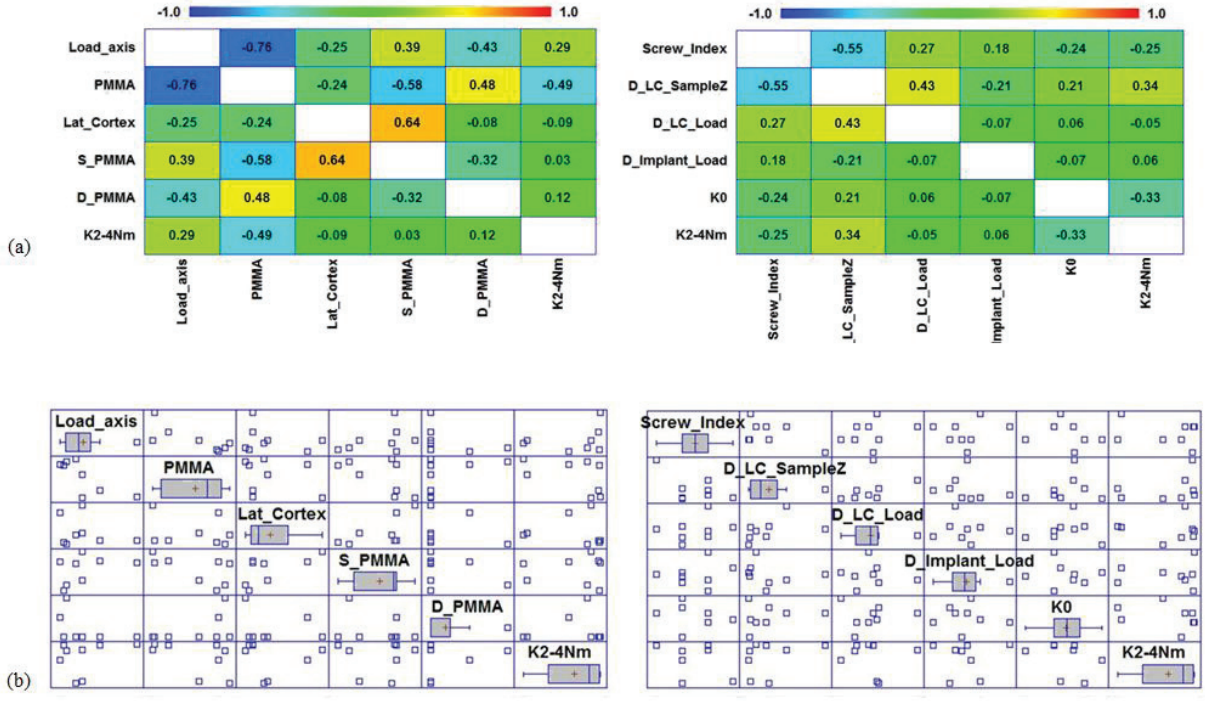

Suppl. Figure 25: Correlation coefficients (a) and scatter plots (b) for the MDTP samples at 4 Nm torsion. Phase-2 of testing.

Phase-2 8 Nm Torsion: DTN

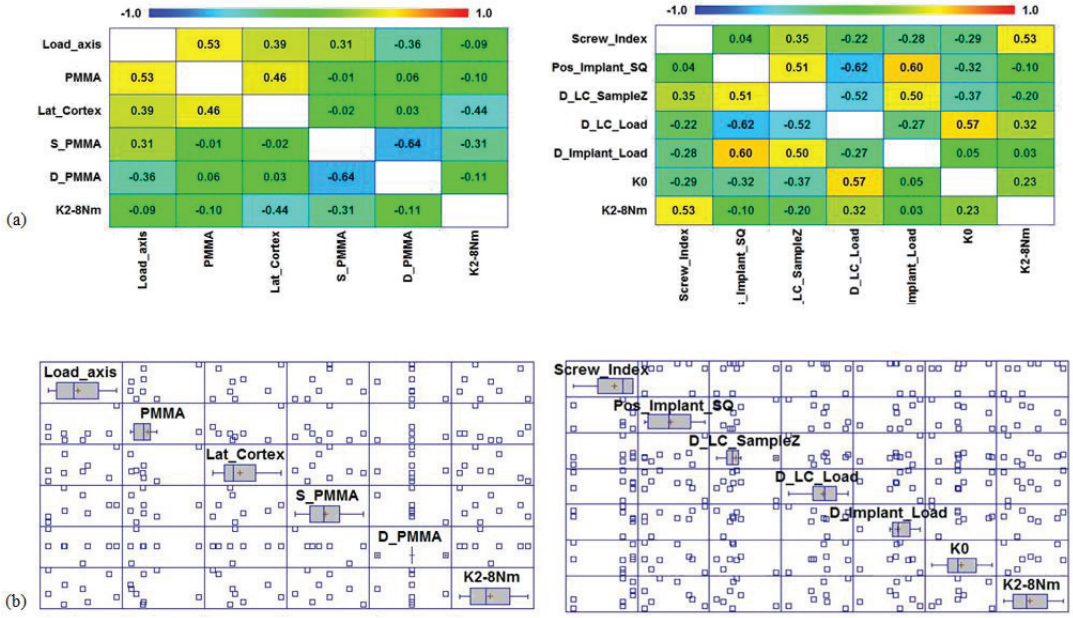

Suppl. Figure 26: Correlation coefficients (a) and scatter plots (b) for the DTN samples at 8 Nm torsion. Phase-2 of testing.

Phase-2 8 Nm Torsion: MDTP

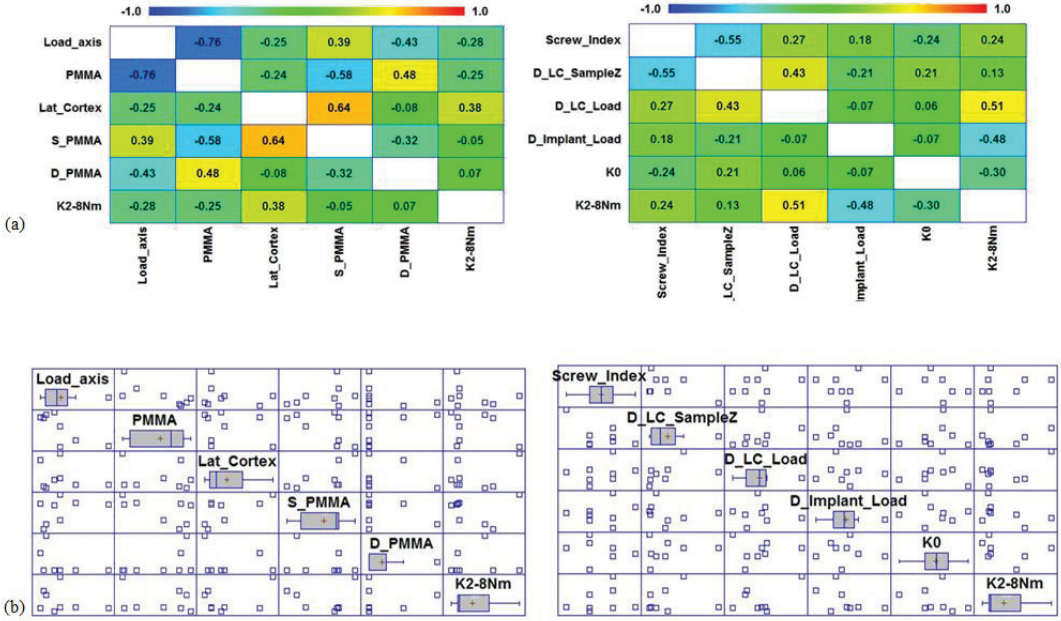

Suppl. Figure 27: Correlation coefficients (a) and scatter plots (b) for the MDTP samples at 8 Nm torsion. Phase-2 of testing.

Phase-3 350 N Compression: DTN

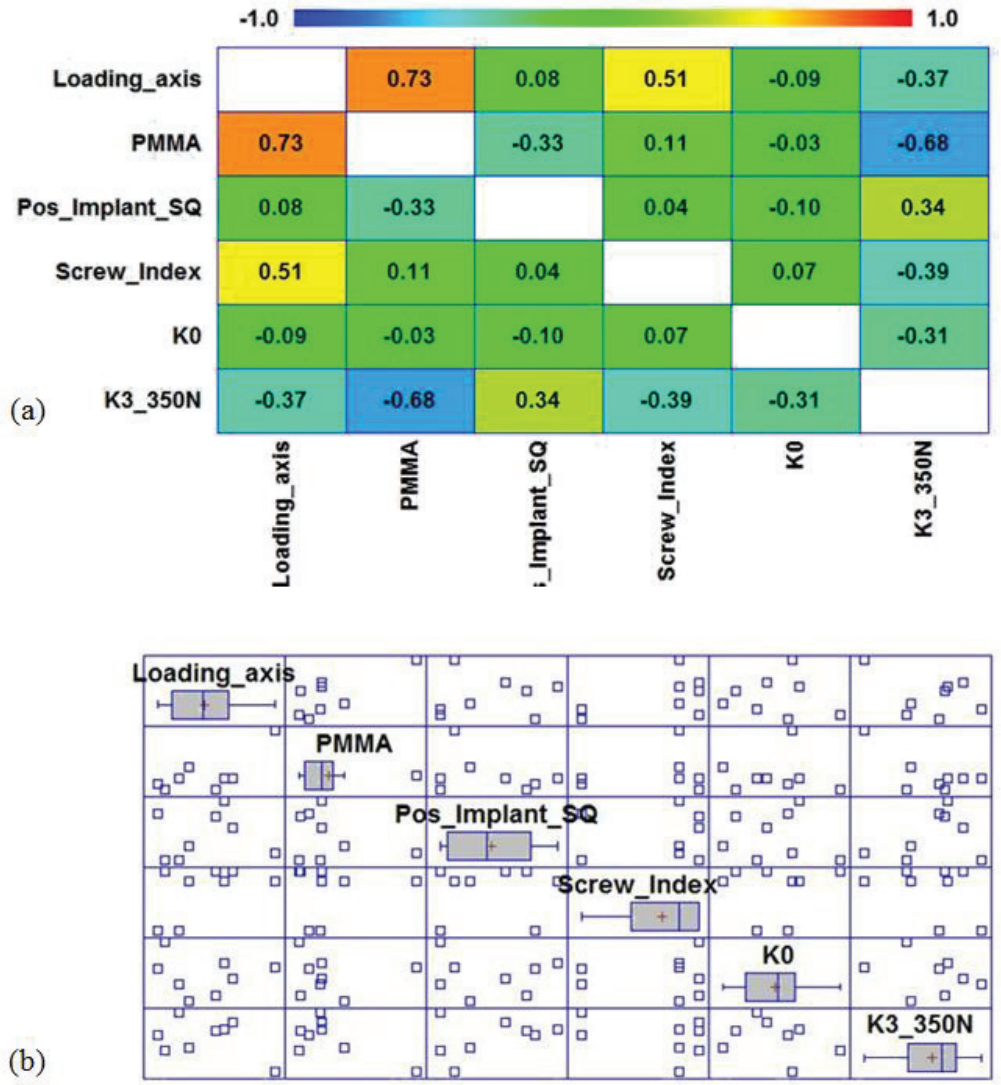

Suppl. Figure 28: Correlation coefficients (a) and matrices (b) for DTN samples at 350 N compression during Phase-3 of testing.

Phase-3 350 N Compression: MDTP

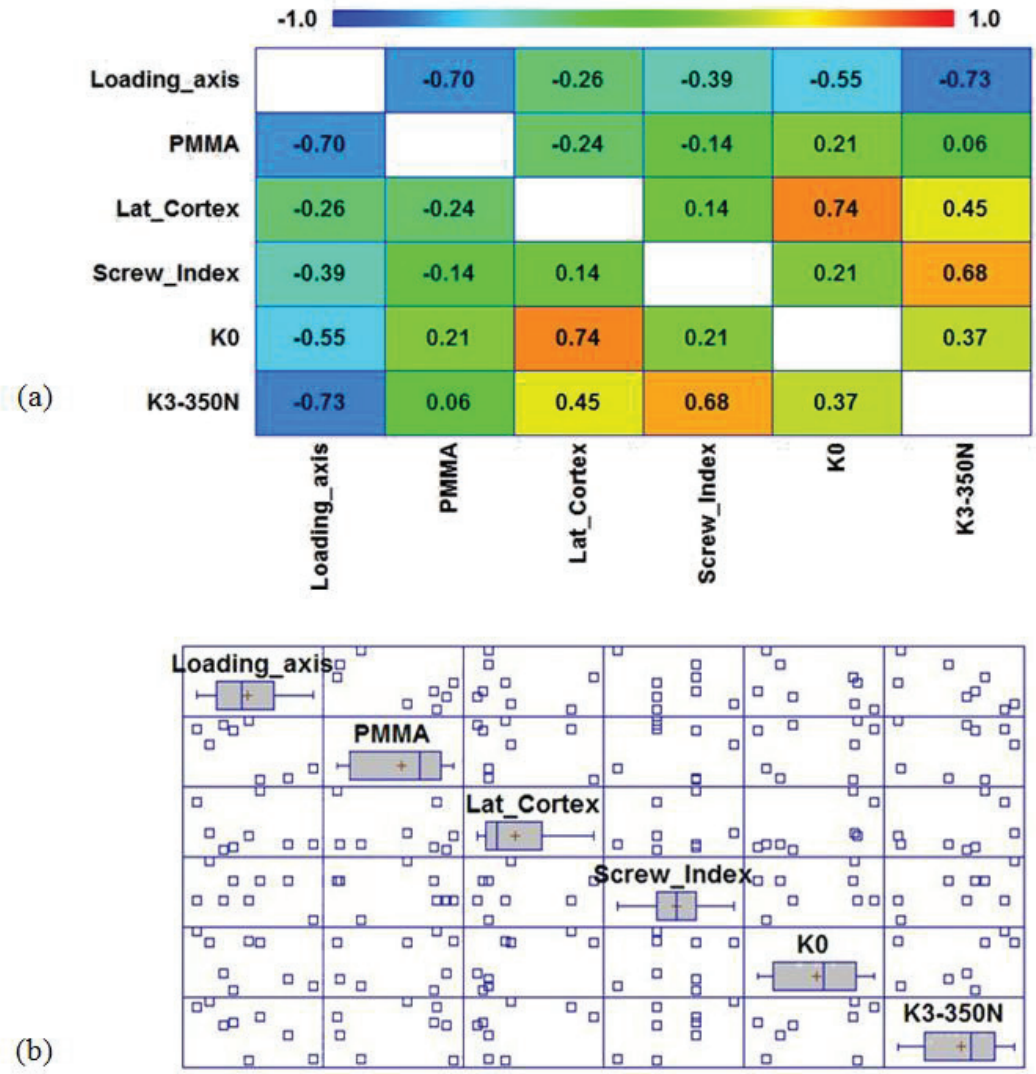

Suppl. Figure 29: Correlation coefficients (a) and matrices (b) for MDTP samples at 350 N compression during Phase-3 of testing.

Phase-3 700 N Compression: DTN

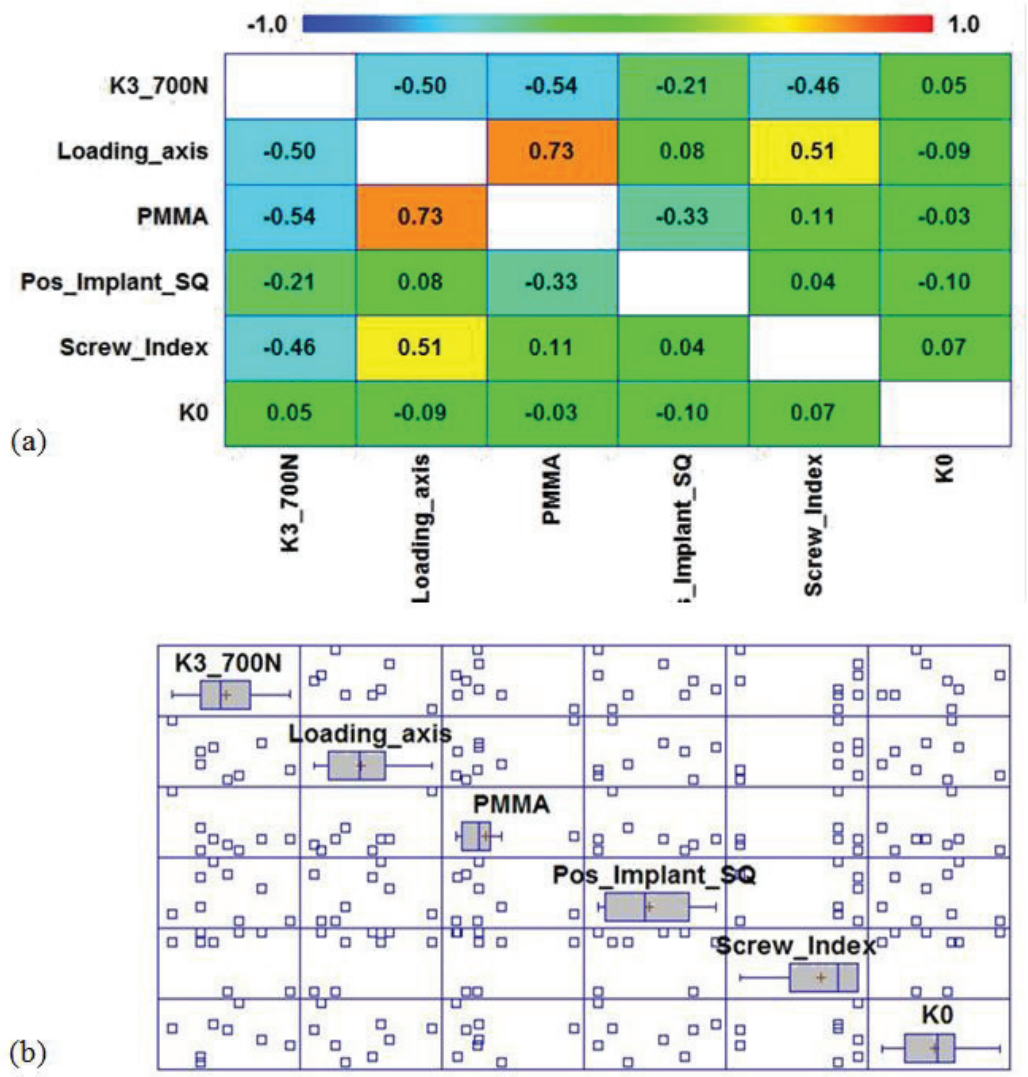

Suppl. Figure 30: Correlation coefficients (a) and matrices (b) for DTN samples at 700 N compression during Phase-3 of testing.

Phase-3 700 N Compression: MDTP

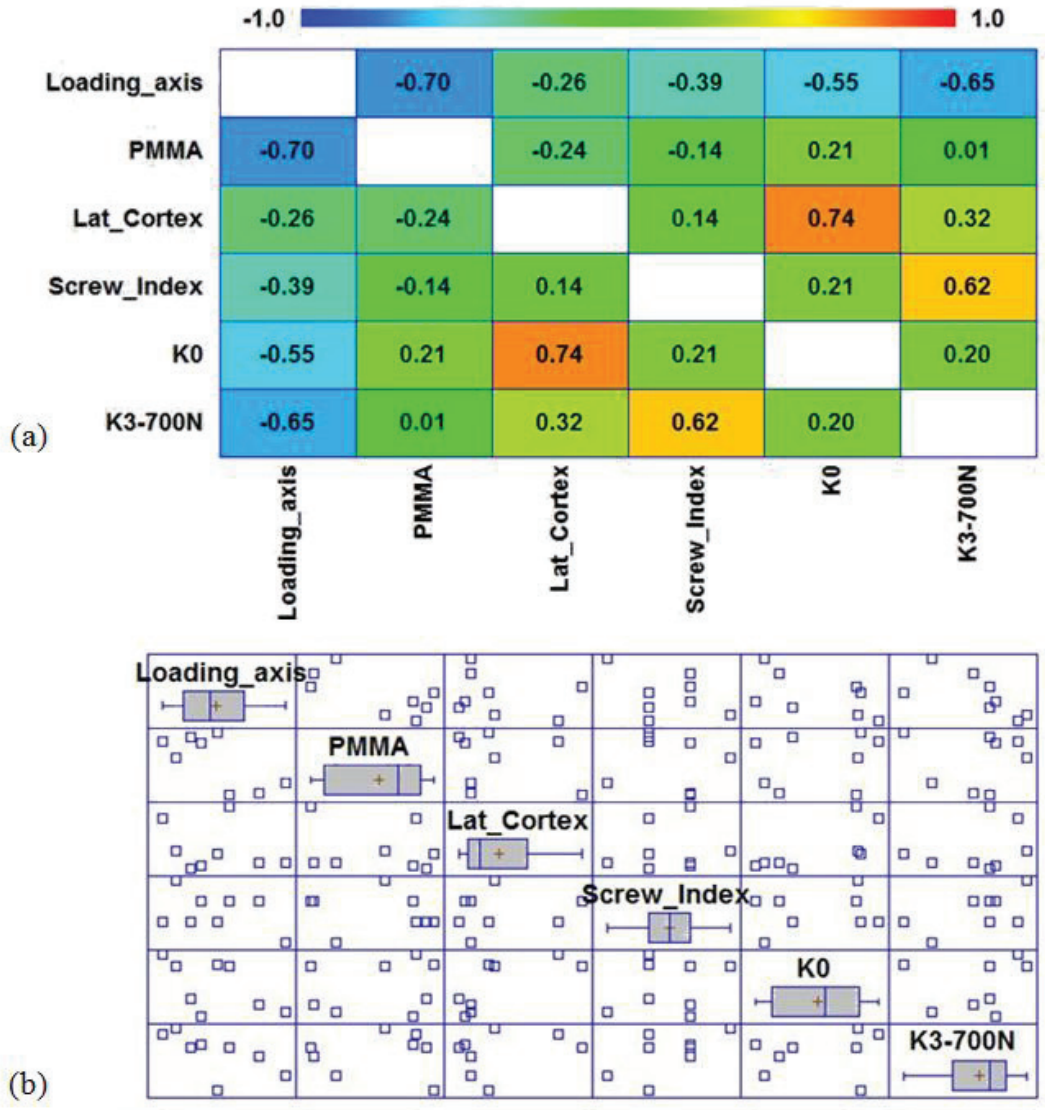

Suppl. Figure 31: Correlation coefficients (a) and matrices (b) for MDTP samples at 700 N compression during Phase-3 of testing.

Phase-3 8 Nm Torsion: DTN

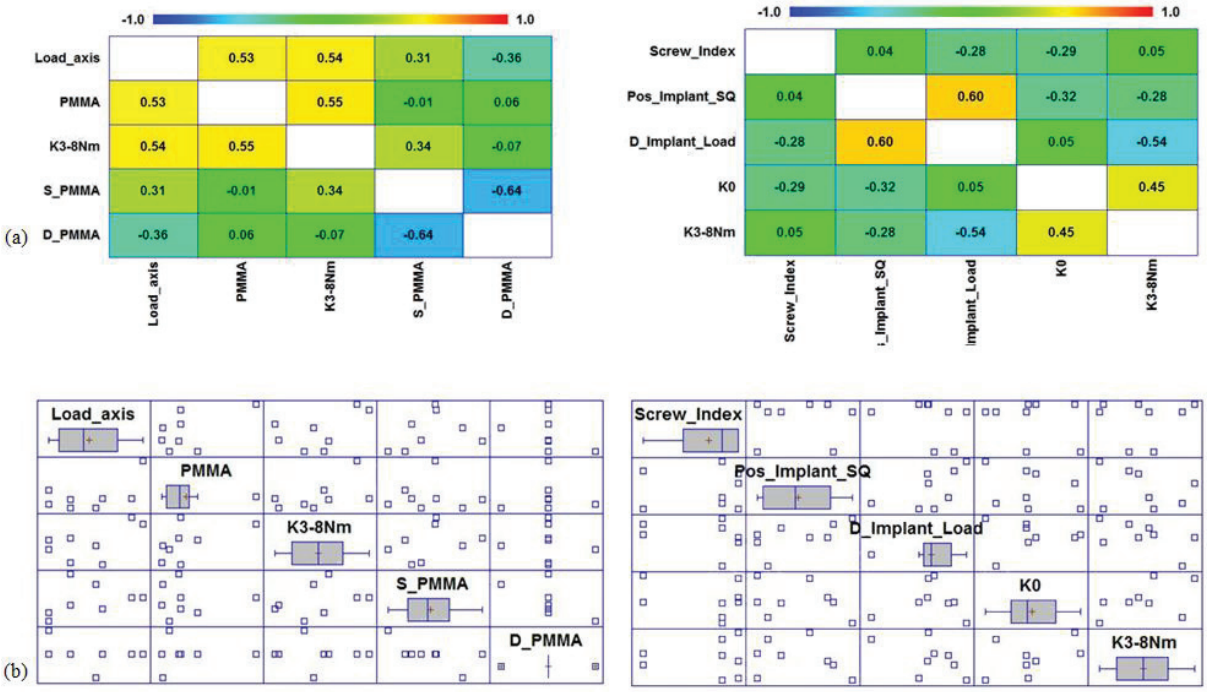

Suppl. Figure 32: Correlation coefficients (a) and scatter plots (b) for DTN samples at 8 Nm torsion in Phase-3 of testing.

Phase-3 8 Nm Torsion: MDTP

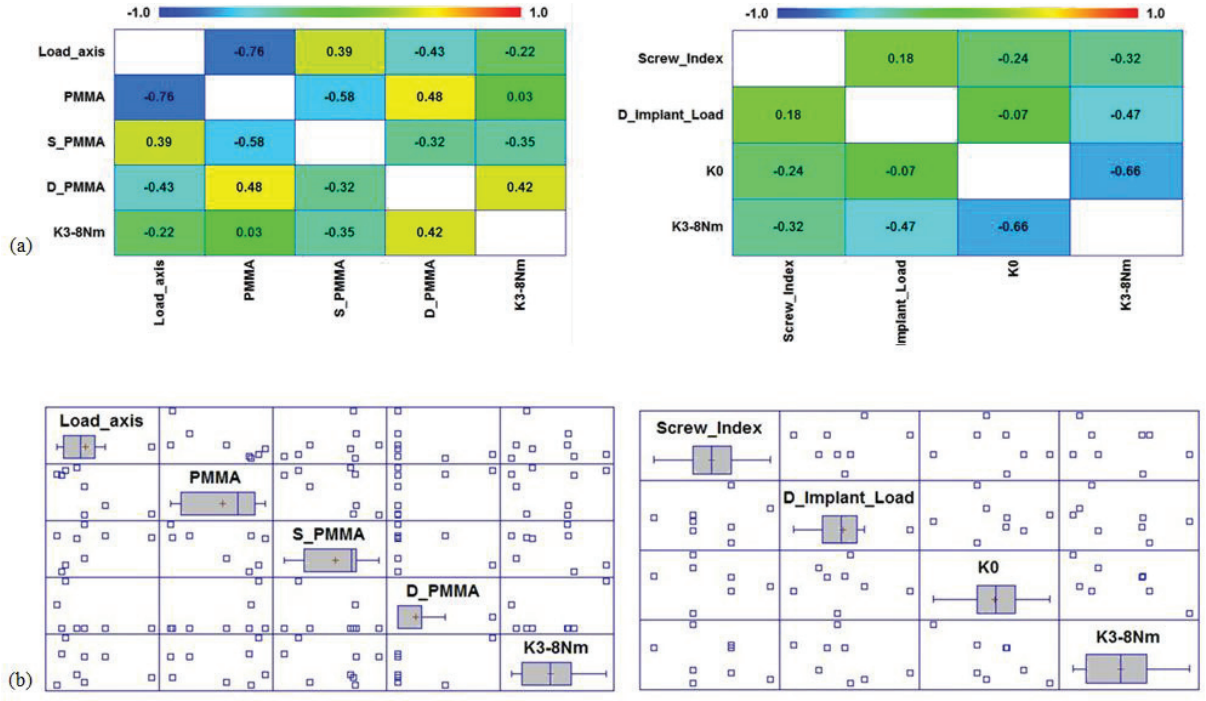

Suppl. Figure 33: Correlation coefficients (a) and scatter plots (b) for MDTP samples at 8 Nm torsion in Phase-3 of testing